

2006

The numerical simulation of turbulent boundary layers and film cooling

Kunlun Liu
Iowa State University

Follow this and additional works at: <https://lib.dr.iastate.edu/rtd>

 Part of the [Mechanical Engineering Commons](#)

Recommended Citation

Liu, Kunlun, "The numerical simulation of turbulent boundary layers and film cooling " (2006). *Retrospective Theses and Dissertations*. 1278.
<https://lib.dr.iastate.edu/rtd/1278>

This Dissertation is brought to you for free and open access by the Iowa State University Capstones, Theses and Dissertations at Iowa State University Digital Repository. It has been accepted for inclusion in Retrospective Theses and Dissertations by an authorized administrator of Iowa State University Digital Repository. For more information, please contact digirep@iastate.edu.

The numerical simulation of turbulent boundary layers and film cooling

by

Kunlun Liu

A dissertation submitted to the graduate faculty
in partial fulfillment of the requirements for the degree of

DOCTOR OF PHILOSOPHY

Major: Mechanical Engineering

Program of Study Committee:
Richard H. Pletcher, Major Professor
Eric S. Weber
Francine Battaglia
John C. Tannehill
Michael G. Olsen

Iowa State University

Ames, Iowa

2006

Copyright © Kunlun Liu, 2006. All rights reserved.

UMI Number: 3217292

INFORMATION TO USERS

The quality of this reproduction is dependent upon the quality of the copy submitted. Broken or indistinct print, colored or poor quality illustrations and photographs, print bleed-through, substandard margins, and improper alignment can adversely affect reproduction.

In the unlikely event that the author did not send a complete manuscript and there are missing pages, these will be noted. Also, if unauthorized copyright material had to be removed, a note will indicate the deletion.

UMI[®]

UMI Microform 3217292

Copyright 2006 by ProQuest Information and Learning Company.

All rights reserved. This microform edition is protected against unauthorized copying under Title 17, United States Code.

ProQuest Information and Learning Company
300 North Zeeb Road
P.O. Box 1346
Ann Arbor, MI 48106-1346

Graduate College
Iowa State University

This is to certify that the doctoral dissertation of
Kunlun Liu
has met the dissertation requirements of Iowa State University

Signature was redacted for privacy.

Major Professor

Signature was redacted for privacy.

For the Major Program

DEDICATION

I would like to dedicate this dissertation to my wife Jie without her support I would not have been able to complete this work.

TABLE OF CONTENTS

| | |
|--|------|
| LIST OF TABLES | viii |
| LIST OF FIGURES | ix |
| NOMENCLATURE | xvi |
| ABSTRACT | xix |
| CHAPTER 1. INTRODUCTION | 1 |
| 1.1 Motivation and Outline of the Research | 1 |
| 1.2 Dissertation Organization | 6 |
| CHAPTER 2. A NEW FRACTIONAL STEP METHOD FOR COMPRESS- | |
| IBLE NAVIER-STOKES EQUATION | 8 |
| 2.1 Introduction | 9 |
| 2.2 Governing Equations for Large Eddy Simulation | 12 |
| 2.3 Governing Equations for Direct Numerical Simulation | 15 |
| 2.4 Quasi-Newton Iteration | 15 |
| 2.4.1 Preconditioning | 17 |
| 2.4.2 Fractional Step Factorization | 19 |
| 2.4.3 Numerical Procedure | 27 |
| 2.5 Validation of Numerical Method | 30 |
| 2.5.1 Case1: Adiabatic Turbulent Boundary Layer | 30 |
| 2.5.2 Case2: Turbulent Boundary Layer with Heat Transfer | 31 |
| CHAPTER 3. BOUNDARY CONDITIONS | 41 |
| 3.1 Introduction | 41 |

| | | |
|---|--|-----------|
| 3.2 | A Dynamic Recycling Inflow Condition | 42 |
| 3.2.1 | The Inflow Conditions | 44 |
| 3.3 | Characteristic Boundary Conditions | 45 |
| 3.3.1 | Outlet Characteristic Boundary Conditions For Subsonic Flows | 47 |
| 3.4 | Results And Conclusions | 48 |
| | | |
| CHAPTER 4. AN ANISOTROPIC TURBULENCE: A TURBULENT BOUND- | | |
| ARY LAYER | | 54 |
| 4.1 | Introduction | 54 |
| 4.1.1 | A Brief Summary of Previous Turbulence Theories | 56 |
| 4.1.2 | Motivation for This Study | 58 |
| 4.2 | Theoretical Analysis and Problem Formulation | 59 |
| 4.2.1 | The strong fully developed anisotropic flows cannot be globally homoge- neous without forcing | 59 |
| 4.2.2 | Local Homogeneity | 60 |
| 4.3 | The Validation of the Numerical Method | 62 |
| 4.3.1 | Numerical Method | 63 |
| 4.3.2 | Validation of the Numerical Simulations of the First and Second Order Statistics. | 64 |
| 4.3.3 | Reynolds Stress Budget | 65 |
| 4.4 | Results and Discussion | 66 |
| 4.4.1 | Anisotropic Tensors | 66 |
| 4.4.2 | Two-point Correlations of Velocities | 68 |
| 4.5 | Conclusions | 72 |
| | | |
| CHAPTER 5. COMPRESSIBILITY EFFECTS AND VARIABLE DEN- | | |
| SITY EFFECTS OF TURBULENT BOUNDARY LAYERS | | 92 |
| 5.1 | Introduction | 92 |
| 5.1.1 | Numerical Configurations | 97 |
| 5.2 | Results and Discussion | 97 |

| | | |
|---|--|------------|
| 5.2.1 | Compressibility and Variable Density Effects | 97 |
| 5.2.2 | Favre Average | 101 |
| 5.3 | Conclusion | 103 |
| CHAPTER 6. PROBABILITY DENSITY FUNCTION OF VELOCITY | | |
| FLUCTUATIONS IN A TURBULENT BOUNDARY LAYER | | 115 |
| 6.1 | Introduction | 115 |
| 6.2 | Results and Discussion | 116 |
| CHAPTER 7. LARGE EDDY SIMULATION OF TURBULENT BOUND- | | |
| ARY LAYERS SUBJECTED TO FREE-STREAM TURBULENCE . . . | | 127 |
| 7.1 | Introduction | 127 |
| 7.2 | Model | 129 |
| 7.3 | Results | 134 |
| 7.4 | Conclusions | 136 |
| CHAPTER 8. LARGE EDDY SIMULATION OF DISCRETE-HOLE FILM | | |
| COOLING IN FLAT PLATE TURBULENT BOUNDARY LAYERS . . | | 148 |
| 8.1 | Introduction | 148 |
| 8.2 | Numerical Configurations | 149 |
| 8.3 | Numerical Results | 151 |
| 8.4 | Conclusions | 153 |
| CHAPTER 9. CONCLUSIONS AND RECOMMENDATIONS | | |
| 9.1 | Summary and Contributions | 162 |
| 9.2 | Recommendations for Future Work | 164 |
| 9.2.1 | Future Work Relate to This Dissertation | 164 |
| 9.2.2 | Future Studies | 165 |
| APPENDIX A. GOVERNING EQUATION FOR REYNOLDS STRESS | | |
| ANISOTROPIC TENSOR b_{ij} | | 167 |
| APPENDIX B. LU-SGS SCHEME | | 169 |

APPENDIX C. EXISTENCE OF A STRONG SOLUTION FOR A CLASS

| | |
|---|-----|
| OF NONLINEAR PARABOLIC SYSTEMS | 174 |
| C.1 Introduction | 174 |
| C.2 Notation and Main Ideas | 176 |
| C.2.1 Notation | 176 |
| C.2.2 The Idea of Construction | 177 |
| C.3 Main Theorems | 179 |
| C.3.1 Preliminaries | 179 |
| C.3.2 The Existence of Global and Local Solutions in $B_{m+1}^{s+1,2}(0, T; U)$ | 188 |
| C.4 Conclusion | 204 |
| BIBLIOGRAPHY | 205 |
| ACKNOWLEDGEMENTS | 217 |

LIST OF TABLES

| | | |
|-----------|---|-----|
| Table 4.1 | The categories of the turbulence in terms of the level of anisotropy and non-homogeneity | 55 |
| Table 4.2 | Comparison of parameters used in the incompressible simulation of Spalart (1988), DeGraaff and Eaton (2000), and the present simulations. | 63 |
| Table 6.1 | Table of the corresponding y^+ value of the statistical locations | 117 |
| Table 6.2 | Table of the α , β values of the beta distribution shown by Fig. 6.3 | 119 |
| Table 7.1 | Table of chosen weighting functions | 133 |
| Table C.1 | The relationship between the rescaled system and original system | 201 |

LIST OF FIGURES

| | | |
|------------|--|----|
| Figure 2.1 | Comparison of mean velocity profile in a turbulent boundary layer $Re_{\delta_d} = 2000$ over an adiabatic wall : The solid line is LES results, the dashed line gives a DNS profile by Spalart (1988) and the square symbols are the experiment data by DeGraaff and Eaton (2000). . . . | 33 |
| Figure 2.2 | Comparison of rms of streamwise velocity profile in a turbulent boundary layer $Re_{\delta_d} = 2000$ over an adiabatic wall : The solid line is LES results, the dashed line gives a DNS profile by Spalart (1988), and the square symbols are the experimental data by DeGraaff and Eaton (2000). | 34 |
| Figure 2.3 | Comparison of rms of normal velocity profile in a turbulent boundary layer $Re_{\delta_d} = 2000$ over an adiabatic wall : The solid line is LES results, the dashed line gives a DNS profile by Spalart (1988), and the square symbols are the experimental data by DeGraaff and Eaton (2000). . . | 35 |
| Figure 2.4 | Comparison of rms of normal velocity profile in a turbulent boundary layer $Re_{\delta_d} = 2000$ over an adiabatic wall : The solid line is LES results, the dashed line gives a DNS profile by Spalart (1988). | 36 |
| Figure 2.5 | The downward view of streamwise velocity contours at $Y^+ = 23$ | 37 |
| Figure 2.6 | The downward view of streamwise velocity contours at $Y^+ = 200$ | 37 |
| Figure 2.7 | Mean velocity and temperature profiles in the heated turbulent boundary layer, $T_{wall} = 1.3$. The square symbols are the velocity profile of incompressible turbulent boundary layer by DeGraaff and Eaton (2000), and the circle symbols are the empirical temperature results suggested by Kadar (1981). | 38 |

| | | |
|------------|--|----|
| Figure 2.8 | RMS fluctuation profiles of an heated turbulent boundary layer, $T_{wall} = 1.3$. The circle symbols are the experimental data of the incompressible turbulent boundary layer by DeGraaff and Eaton (2000). | 39 |
| Figure 2.9 | Convergence history of residual errors vs iteration steps in the pseudo-time loops. $T_{wall} = 1.3$, The solid line is the convergence history by the present scheme and dashed line is by the LUSGS scheme. | 40 |
| Figure 3.1 | Comparison of rms profiles by present method in a turbulent boundary layer $Re_{\delta_d} = 2000$ and $T_w = T_{ref}$ with the DNS data reported by Spalart (1988) and the experimental data reported by DeGraaff and Eaton (2000). | 50 |
| Figure 3.2 | Comparison of mean streamwise velocity profiles in a turbulent boundary layer $Re_{\delta_d} = 2000$, $T_w = T_{ref}$: The solid line is LES results, the dashed line gives a DNS profile by Spalart (1988), and the square symbols are experimental data by DeGraaff and Eaton (2000). | 51 |
| Figure 3.3 | Evolution of skin friction: —, Recycling plane was dynamically chosen by equation (3.1), — —, Recycling plane was fixed. — —, Empirical curve is the Ludwig-Tillmann correlation. | 52 |
| Figure 3.4 | Evolution of skin friction: Solid line is mean profile of skin friction from $t = 100 \frac{\delta_d}{U_\infty}$ to $t = 600 \frac{\delta_d}{U_\infty}$, the square symbol is the spanwise average skin friction at $t = 12 \frac{\delta_d}{U_\infty}$, the delta symbol is the spanwise average skin friction at $t = 24 \frac{\delta_d}{U_\infty}$, and the circle symbol is the spanwise average skin friction at $t = 36 \frac{\delta_d}{U_\infty}$ | 53 |
| Figure 4.1 | The comparison of the present mean streamwise velocity profile with the DNS results reported by Spalart (1988) and experimental data reported by DeGraaff and Eaton (2000). | 75 |

| | | |
|-------------|--|----|
| Figure 4.2 | Comparison of the present rms profiles of the turbulence fluctuations with the DNS results reported by Spalart (1988) and experimental data reported by DeGraaff and Eaton (2000). | 76 |
| Figure 4.3 | Reynolds stress budget of u^2 normalized by u_τ^4/ν | 77 |
| Figure 4.4 | Reynolds stress budget of v^2 normalized by u_τ^4/ν | 78 |
| Figure 4.5 | Reynolds stress budget of w^2 normalized by u_τ^4/ν | 79 |
| Figure 4.6 | Reynolds stress budget of $-uv$ normalized by u_τ^4/ν | 80 |
| Figure 4.7 | Comparison of the second invariance of the Reynolds stress anisotropic tensor b_{ij} ($-II_b$), the turbulent production anisotropic tensor \overline{P}_{ij} ($-II_P$), the turbulent dissipation anisotropic tensor $\overline{\varepsilon}_{ij}$ ($-II_D$), and the the turbulent transport anisotropic tensor \overline{T}_{ij} ($-II_T$). | 81 |
| Figure 4.8 | Comparison of the third invariance of the Reynolds stress anisotropic tensor b_{ij} (III_b), the turbulent production anisotropic tensor \overline{P}_{ij} (III_P), the turbulent dissipation anisotropic tensor $\overline{\varepsilon}_{ij}$ (III_D), and the the turbulent transport anisotropic tensor \overline{T}_{ij} (III_T). | 82 |
| Figure 4.9 | The log plot of the $R_{vv}(0, 0, r_z; y_1)$, normalized by $R_{vv}(0, 0, 0; y_1)$, at the three different y_1 locations. | 83 |
| Figure 4.10 | Plot of the $R_{vv}(r_x, 0, 0; y_1)$, normalized by $R_{vv}(0, 0, 0; y_1)$, at the three different y_1 locations. | 84 |
| Figure 4.11 | Plot of $R_{vv}(0, r_y, 0; y_1)$, normalized by $R_{vv}(0, 0, 0; y_1)$, at the three different y_1 locations. | 85 |
| Figure 4.12 | Plot of $R_{ww}(r_x, r_y, 0; y_1)$ normalized by $R_{ww}(0, 0, 0; y_1)$ where $y_1^+ = 56$ | 86 |
| Figure 4.13 | Plot of $R_{ww}(r_x, r_y, 0; y_1)$ normalized by $R_{ww}(0, 0, 0; y_1)$ where $y_1^+ = 178$ | 87 |
| Figure 4.14 | Plot of $R_{ww}(0, 0, r_z; y_1)$, normalized by $R_{ww}(0, 0, 0; y_1)$, at the three different y_1 locations. | 88 |
| Figure 4.15 | Plot of $R_{ww}(r_x, 0, 0; y_1)$, normalized by $R_{ww}(0, 0, 0; y_1)$, at the three different y_1 locations. | 89 |

| | | |
|-------------|---|-----|
| Figure 4.16 | Plot of $R_{ww}(0, r_y, 0; y_1)$, normalized by $R_{ww}(0, 0, 0; y_1)$, at the three different y_1 locations. | 90 |
| Figure 4.17 | R_{ww} and R_{vv} correlations at $Y^+ = 378$ and $Y^+ = 178$. The contour levels range from 0.1 to 0.9 with increments of 0.1. | 91 |
| Figure 5.1 | Comparison of mean streamwise velocity with experimental results reported by Degraaff and Eaton (2000). | 105 |
| Figure 5.2 | Comparison of rms profiles of velocity with the DNS results reported by Spalart (1988). | 106 |
| Figure 5.3 | The plots of $-\overline{u'v'}/U_{\tau,local}$ vs. Y^+ | 107 |
| Figure 5.4 | Plot of the mean density, $\bar{\rho}/\rho_e$, and the RMS of density, $(\overline{\rho'^2})^{1/2}/\rho_e$ as functions of Y^+ | 108 |
| Figure 5.5 | The mean and RMS of dilatation of velocities vs. Y^+ , i.e. $\bar{\theta}$ and $\sqrt{\overline{\theta'^2}}/u_{\tau}$ | 109 |
| Figure 5.6 | Turbulent Mach number, M_t , as functions of y^+ | 110 |
| Figure 5.7 | Turbulent Prandtl number Pr_t as functions of Y^+ , and the test of strong Reynolds analogy as expressed by 5.1. | 111 |
| Figure 5.8 | Comparison of $(\widetilde{u_1} - \bar{u}_1)/u_{\tau}$ | 112 |
| Figure 5.9 | The components of τ_{11} . The solid line is τ_{11} , the dashed line is the τ_{11_t} , the dash-dotted line is τ_{11_c} , and the dash-double-dotted line is τ_{11_F} . The square samples are τ_{22} , The delta samples are τ_{22_t} , the right triangular samples are τ_{22_c} , and the left triangular samples are τ_{22_F} | 113 |
| Figure 5.10 | Comparison of γ and π vs. Y^+ , where the solid line is γ for the case 1, the dash-dotted line is γ for the case 2, the dashed line is π for the case 1, the dash-double-dotted line if π for the case 2. | 114 |
| Figure 6.1 | The PDFs of spanwise velocities. The solid curves are the numerical results, and the dash-dotted curves are the Gaussian distributions having the same mean and variance with the corresponding solid curves. | 123 |

Figure 6.2 The PDFs of normal velocity fluctuations. The solid curves are the numerical results, and the dashed curves are the Gaussian distributions having the same mean and variance with the corresponding solid curves. 124

Figure 6.3 The plot of skewnesses and the Reynolds stress with respect to the normal distance from the wall. The solid and the dashed curves are the one third power of the streamwise velocity and normal vorticity, respectively. i.e. $\gamma_{1\omega_3}^{1/3} = (\frac{\langle(\omega_3 - \langle\omega_3\rangle)^3\rangle}{(\langle(\omega_3 - \langle\omega_3\rangle)^2\rangle)^{3/2}})^{1/3}$ and $\gamma_{1u}^{1/3} = (\frac{\langle(u - \langle u \rangle)^3\rangle}{(\langle(u - \langle u \rangle)^2\rangle)^{3/2}})^{1/3}$ 125

Figure 6.4 The PDF of streamwise velocity fluctuations. The solid curves are the numerical results, and the dash-dotted lines are the beta distributions having the same variance, skewness, mode and maximum value with the corresponding solid curves. 126

Figure 7.1 Comparison of mean velocity profiles in a turbulent boundary layer $Re_{\delta_d} = 2000$: The solid, dash dot, and long dash line are LES results, the dashed dot dot line gives a DNS profile by Spalart (1988) and the circle symbols are experimental data by DeGraaff and Eaton (2000). . . 138

Figure 7.2 Comparison of rms of fluctuations in a turbulent boundary layer $Re_{\delta_d} = 2000$, $TU = 0\%$ and $T_w = T_{ref}$ with DNS profile by Spalart (1988), and the experimental data by DeGraaff and Eaton (2000). 139

Figure 7.3 The plot of nondimensional U_τ vs streamwise direction in a region from $Re_{\delta_d} = 1760$ up to $Re_{\delta_d} = 2100$ 140

Figure 7.4 Plot of Reynolds number based on displacement thickness vs streamwise distance. 141

Figure 7.5 Plot of U_{rms} vs normal distance at $Re_{\delta_d} = 2000$ and $T_w = T_{ref}$ 142

Figure 7.6 The log plot of U_{rms} vs normal distance at $Re_{\delta_d} = 2000$ and $T_w = T_{ref}$. 143

Figure 7.7 Plot of V_{rms} vs normal distance at $Re_{\delta_d} = 2000$ and $T_w = T_{ref}$ 144

Figure 7.8 Plot of W_{rms} vs normal distance at $Re_{\delta_d} = 2000$ and $T_w = T_{ref}$ 145

Figure 7.9 The downward view of streamwise velocity contours at $Y^+ = 23$ and $TU = 5\%$ 146

| | | |
|-------------|--|-----|
| Figure 7.10 | The downward view of streamwise velocity contours at $Y^+ = 200$ and $TU = 5\%$ | 146 |
| Figure 7.11 | The downward view of streamwise velocity contours at $Y^+ = 440$ and $TU = 5\%$ | 146 |
| Figure 7.12 | The downward view of streamwise velocity contours at $Y^+ = 1400$ and $TU = 5\%$ | 147 |
| Figure 8.1 | The numerical configuration for film cooling. | 154 |
| Figure 8.2 | The downward view of numerical mesh in the near hole region. | 155 |
| Figure 8.3 | The downward view of numerical mesh in the near hole region. | 156 |
| Figure 8.4 | The downward of temperature contours at the station $y^+ = 14$, the units of axis are displacement thickness, and the center of the hole is located at $x = 56.5$ | 156 |
| Figure 8.5 | The sideview of temperature contours at the centerline of numerical domain. The unit of axis is displacement thickness, and the center of the hole is located at $x = 56.5$ | 157 |
| Figure 8.6 | The distribution of adiabatic effectiveness on the flat plate in the the case density ratio $DR = 2.0$, blowing ratio $BR = 0.5$, free stream turbulence level $Tu = 0.0$. X is the streamwise direction and Z is the spanwise direction. | 157 |
| Figure 8.7 | The plot of adiabatic effectiveness at the downstream $X/D = 8.75$, where density ratio $DR = 2.0$, blowing ratio $BR = 0.5$ and free stream turbulence level $Tu = 0.0$ | 158 |
| Figure 8.8 | The upstream view of temperature contours at $X = 84$; the unit of axis is displacement thickness, and the center of the hole located at $X/D = 8.75$ | 159 |
| Figure 8.9 | The plot of adiabatic effectiveness following the center line of the flat plate, where density ratio $DR = 2.0$, blowing ratio $BR = 0.5$ and free stream turbulence level $Tu = 0.0$ | 160 |

- Figure 8.10 The plot of adiabatic effectiveness following the center line of the flat plate, where density ratio $DR = 1.6$, blowing ratio $BR = 0.362$, mass flow ratio $MR = 0.58$, and free stream turbulence level $Tu = 0.0$ 161
- Figure B.1 Main control volume with cell center, (i,j,k) , and six neighboring cell centers, labeled as E, W, N, S, U, and D. 173

NOMENCLATURE

Roman Symbols

| | |
|--------------|--|
| D | The diameter of coolant supply pipe |
| E | Cartesian flux vector in the x direction |
| F | Cartesian flux vector in the y direction |
| G | Cartesian flux vector in the z direction |
| L | The length of pipe |
| M | Mach number |
| P | Pressure |
| t | Physics time |
| T | Temperature |
| u | Velocity component in the x direction |
| v | Velocity component in the y direction |
| w | Velocity component in the z direction |
| \mathbf{W} | Vector of primitive variance |
| x | Longitude direction in a Cartesian coordinate frame |
| y | Normal direction in a Cartesian coordinate frame |
| z | Spanwise direction in a Cartesian coordinate frame |
| BR | Blowing ratio ($BR = \frac{U_1}{U_2}$) |
| DR | Density ratio ($DR = \frac{\rho_1}{\rho_2}$) |
| Pr | Prandtl number |
| MR | Mass flow ratio ($MR = \frac{\rho_1 U_1}{\rho_2 U_2}$) |

| | |
|-------------|---|
| TU | Free stream turbulent level |
| Re_d | Reynolds number based on displacement thickness |
| Re_θ | Reynolds number based on momentum thickness |
| u' | Velocity fluctuations in the x direction |
| v' | Velocity fluctuations in the y direction |
| w' | Velocity fluctuations in the z direction |
| T' | Temperature fluctuations |
| p' | Pressure fluctuations |

Greek Symbols

| | |
|-----------------|--------------------------|
| η | Adiabatic effectiveness |
| δ | Boundary layer thickness |
| δ_d | Displacement thickness |
| δ_θ | Momentum thickness |
| ρ | Density |
| ρ' | Density fluctuations |

Subscript

| | |
|--------------|--------------------------|
| c | The coolant property |
| e | The environment property |
| w | Wall property |
| <i>local</i> | The local property |
| ∞ | Free stream property |
| <i>ref</i> | The reference system |

rms Root mean square

i, j, k Indices for Cartesian coordinates

Superscript

N Physical time step

M Pseudo-time step

ABSTRACT

A new finite volume algorithm has been developed to solve a variety of flows by using large eddy simulation and direct numerical simulation. This finite volume algorithm was developed using a dual time stepping approach with a preconditioning technique and a new factorization implementation. The method takes the advantage of pressure-based and density-based methods. Thus, it provides an efficient way to numerically solve the Navier-Stokes equations at the low Mach numbers. The implementation of the numerical scheme was validated by obtaining solutions to a number of flows including turbulent boundary layers with or without heat transfer, turbulent boundary layers subjected to free stream turbulence, and supersonic adiabatic turbulent boundary layers. Good agreement between the present results and benchmark results in the literature was achieved.

In order to generate the inflow conditions for the simulation of turbulent boundary layers, a dynamic recycling method was proposed. It is an improvement over the recycling method proposed by Lund et al., and dramatically reduces the starting-transients of the numerical simulations. In addition, a characteristic boundary condition method was suggested for the outlet boundary conditions of external wall shear flows. Such a non-reflecting boundary condition is a modification of the method introduced by Poinso and Lele (1992).

With the new numerical method and boundary condition technique it is possible to investigate the statistics of turbulence with greater accuracy. Thus, the fluid physics of three different turbulent boundary layers are discussed. These are a turbulent boundary layer without heat transfer, a turbulent boundary layer on a heated wall, and an adiabatic supersonic turbulent boundary layer at Mach number 1.8. The three-dimensional two-point correlations and the one-point turbulent structure tensors of a incompressible turbulent boundary layer have been

investigated and formulated. The results indicate the influence of Reynolds stress and the hairpin vortices on two-point correlations of spanwise or normal velocities. Moreover, the results revealed that the turbulent production makes the major contribution to the anisotropy of the anisotropic tensor b_{ij} compared with turbulent dissipation and transport. The compressible turbulent boundary layers study, that is, the low Mach number turbulent boundary layer with strong heat transfer and the supersonic turbulent boundary layer, is concerned with the strong Reynolds analogy, Van Driest transformation, and the applicability of Morkovin's hypothesis. The results showed that the Van Driest transformation and the strong Reynolds analogy are approximately satisfied for both of the flows, and the local properties collapse to the incompressible statistical curves: the law of the wall and the defect law.

In addition, a numerical algorithm was proposed to calculate a turbulent boundary layer subjected to the free stream turbulence. To reveal the influence of free stream turbulence level on the statistics of the turbulent structure in the boundary layers, turbulence levels of $Tu=0\%$, 5% , and 7.5% were imposed. The influence of the free stream turbulence on the first and second-order statistics has been studied.

Large eddy simulation is applied to an example discrete hole film cooling configuration. The computational domain included the coolant supply tube as well as the main mixing region. A tube L/D of 8 and an injection angle of 35 degrees was employed for two different simulations: one was with a blowing ratio of 0.5 and a density ratio of 2, and the other was with a blowing ratio of 0.362 and a density ratio of 1.6. The numerical results and a comparison with experimental data are presented.

CHAPTER 1. INTRODUCTION

1.1 Motivation and Outline of the Research

The advance of turbine engine technology has led to higher turbine inlet temperatures. This requires active cooling in order to maintain the blades of the turbine engine at a safe temperature, since the excessive high temperature levels will reduce the life of blades and can even cause failure of those blades. Film cooling is a widely used technique to achieve this goal. A number of experiments (Ligrani *et al.* (1994a), Ligrani *et al.* (1994b), Sen *et al.* (1996), and Schmidt *et al.* (1996)) have been reported that examine the performance of film cooling. The purpose of this study is to develop a numerical technique to calculate the film cooling of the turbulent boundary layers. In this configuration, both the external and internal flows need to be simulated, as well as the interaction of the external and internal flows. Since the thermal effectiveness of the heat transfer is considered, the fully compressible Navier-Stokes equation should be calculated. To successfully solve this numerical problem, the numerical method should:

- 1) robustly establish the turbulence,
- 2) accurately achieve the statistical results,
- 3) efficiently converge the residual errors,
- 4) be flexible to the numerical mesh, initial data, and boundary conditions.

In other words, an efficient and accurate solver is desired for the simulation of the turbulent boundary layers including the cases with or without heat transfer or subjected to free-stream turbulence. Moreover, the solver should be able to deal with the internal flows, external flows, and interaction between them.

For the lower Mach number flows, the flow is nearly incompressible and the condition number for the Jacobian matrix J is extremely large. This presents a stiffness problem. In order to achieve a steady convergence of residual errors, this dissertation introduces a new scheme suggested by Liu and Pletcher (2006) which combines the SIMPLE method introduced by Patankar and Spalding (1972), the fractional step method developed by Kim and Moin (1985), and a preconditioning technique by Turkel (1999).

Currently, there are two widely utilized pressure-based methods; the fractional step method (Chorin (1968), Kim and Moin (1985)) and SIMPLE method (Patankar and Spalding (1972)). Both methods solve the pressure Poisson equation instead of the continuity equation to avoid the singularity of the numerical solver. Recently, to simulate the compressible Navier-Stokes equations at the low Mach number limit, a semi-implicit scheme based on the traditional fractional step method has been formulated by Wall *et al.* (2002). However, a fully-implicit solver is desired.

A typical density-based method for the simulation of low Mach number flows is the preconditioning method. Unlike the pressure-based methods which adjust the eigenvalues of the Jacobian matrix by using a left multiplier, the preconditioning methods cluster the eigenvalues of the Jacobian matrix by using a right multiplier. More details on the preconditioning technique can be found in Turkel (1999).

By a preconditioning technique along with a new factorization, the distribution of eigenvalues of the Jacobian are adjusted to cluster near one, which enables the resolved submatrices to be positive definite and hence accelerates the numerical convergence. When the preconditioning is applied, the eigenvalues and eigenvectors of the Jacobian will be modified. To control the numerical instability and the spurious wave reflections at the numerical boundaries, the new characteristic boundary conditions consistent with this method should be formulated. This numerical method and boundary conditions extend the traditional fractional step method to the calculation of the compressible Navier-Stokes equations.

As we know, the inflow conditions have a dramatic effect on numerical simulations of turbulent boundary layers due to the strong convective characteristic of flows with a displacement

thickness Reynolds number as high as 2000. The fluid structures present in the inflow will be transported downstream, but some information may be modified or lost during this transport process so that a finite length, or buffer zone, is required immediately downstream of the inlet for the establishment of realistic turbulent structures. Such a buffer zone adds to the cost of the simulation in terms of CPU resources. In order to establish the downstream turbulent boundary layers robustly, a dynamic recycling method is suggested.

To validate the numerical method and the boundary conditions, a number of turbulent boundary layers were calculated, which were:

- 1) A turbulent boundary layer with the Reynolds number 2000 based on inlet displacement thickness and Mach number 0.02.
- 2) A turbulent boundary layer with the Reynolds number 2000 based on inlet displacement thickness and Mach number 0.04.
- 3) A turbulent boundary layer with the Reynolds number 2000 based on inlet displacement thickness and Mach number 0.06.
- 4) A turbulent boundary layer with the Reynolds number 2000 based on inlet displacement thickness and Mach number 0.1.
- 5) A turbulent boundary layer with the Reynolds number 2000 based on inlet displacement thickness and Mach number 0.8.
- 6) A turbulent boundary layer with the Reynolds number 2000 based on inlet displacement thickness and Mach number 1.8.
- 7) A turbulent boundary layer with the Reynolds number 2000 based on inlet displacement thickness and Mach number 2.2.
- 8) A turbulent boundary layer with the Reynolds number 2000 based on inlet displacement thickness, Mach number 0.1, and heated wall $T_w = 1.3T_e$.
- 9) A turbulent boundary layer with the Reynolds number 2000 based on inlet displacement thickness, Mach number 0.1, and heated wall $T_w = 1.4T_e$.

- 10) A turbulent boundary layer with the Reynolds number 2000 based on inlet displacement thickness, Mach number 0.06, and heated wall $T_w = 1.58T_e$.
- 11) A turbulent boundary layer with the Reynolds number 2000 based on inlet displacement thickness and subjected to the free stream turbulence $Tu = 5\%$. The Mach number is 0.06
- 12) A turbulent boundary layer with the Reynolds number 2000 based on inlet displacement thickness and subjected to the free stream turbulence $Tu = 7.5\%$. The Mach number is 0.06
- 13) A turbulent boundary layer with the Reynolds number 1000 based on inlet displacement thickness and subjected to the free stream turbulence $Tu = 5\%$. The Mach number is 0.06

The selection of the cases was based on the concern about the influence of Mach number on the numerical stability and accuracy and the influence of heat transfer or free stream turbulence on the statistics of turbulent boundary layers.

The success of the numerical method enables us to investigate and analyze the fluid physics of turbulent boundary layers. Several fundamental concepts and mechanisms have been explored, which included the concept of the local homogeneity, the influence of the strong anisotropy on the global homogeneity, the two-point correlations of turbulent boundary layers, and the mechanism of anisotropy of turbulent boundary layers. The research was dedicated to provide the detail information to answer the following question:

- (1) Can the strong fully developed anisotropic turbulence be global homogeneous without the external forcing?
- (2) Must the small scale structures for turbulence with high Reynolds number satisfy the incremental homogeneity?
- (3) What is the three-dimensional structure of two-point correlations and the one-point turbulent structure tensors?

(4) What is the cause of anisotropy for the strong anisotropic turbulence in the turbulent boundary layer?

(5) What is the probability density function (PDF) of the velocities for the turbulent boundary layer, and what causes the non-Gaussian distribution of velocities?

The first question relates to the weak non-homogeneity theory of turbulence which will be introduced in a later chapter. The second question is fundamental to Kolmogorov's K41 theory. Recently, the concept of the local homogeneity was argued by Frisch *et al.* (2005). It is worthwhile to discuss it in order to understand the concept of turbulence. It is known that the hairpin vortices are relevant to turbulent wall shear flows. But the detailed information about this influence on the two-point correlations has not been documented. That is why we asked the third question. The fourth question arises from Lumley's return-to-isotropy theory. In order to understand how the turbulence returns to isotropy, we must know firstly that what is the cause of anisotropy. The last question is central to the statistical theory of the turbulence. The detailed arguments about above questions will be presented in later chapters.

Also, some pure and applied mathematical research about the existence and regularity of the strong solution of a class of nonlinear parabolic equations including the Navier-Stokes equation has been conducted. The original goal of this study was to seek a numerical algorithm which is able to control the numerical instability relative to the nonlinear terms. This research included two aspects: what is the method and how to prove the convergence of the method. It is easy to know that the existence problem is associated with the convergence problem. In other words, if we can construct a Cauchy sequence to converge to a function which holds the equation, then we get the proof of existence. In this sense, the major problems relevant to this study become: (1) What is the method? (2) How to prove the Cauchy-Dirichlet problem of the system? (3) Which space is the solution in? The method was discovered and was examined by the calculation of driven-cavity flows. But the mathematical proofs took the author three years. Finally, the Cauchy-Dirichlet problem for some nonlinear parabolic system was proved. This part is collected into the Appendix.

1.2 Dissertation Organization

Chapter 2 contains the numerical algorithm for the LES and DNS of the full Navier-Stokes equations. The finite volume formulation is used for both schemes. The non-dimensional Navier-Stokes equations for the LES were Favre filtered. In this manner, this algorithm is a fully implicit finite volume method and a combination of the pressure-based and density-based method. A couple of theorems concerning the theoretical foundation of the method are proposed. Numerical procedures are presented in detail.

In Chapter 3, the details of a dynamic recycling method and the boundary and initial conditions are given. This includes a discussion of the inlet buffer zone, the starting transient, and the numerical treatments for the inflow conditions. In addition, a characteristic boundary condition is formulated, which will be utilized as the outlet boundary condition.

The theoretical and numerical results about the fluid physics of turbulent boundary layer are presented in Chapter 4. The three-dimensional two-point correlations and the one-point turbulent structure tensors are formulated. The mechanisms relevant to the anisotropy of the anisotropic tensor b_{ij} are discussed. A proof in this Chapter indicates that the small scale structures of higher Reynolds number turbulence hold the incremental homogeneity. This answers Frisch *et al.* (2005)'s paradox to the concept of the local homogeneity. In addition, in this Chapter, it is also proven that the strong fully developed anisotropic turbulence cannot be globally homogeneous without external forcing.

In Chapter 5, a comparison between two turbulent boundary layers is presented. One is an adiabatic supersonic adiabatic turbulent boundary layer at a Mach number 1.8, and the other is a subsonic turbulent boundary layer with constant wall temperature $T_w = 1.58T_\infty$. The strong Reynolds analogy, Van Driest transformation, and the applicability of Morkovin's hypothesis are tested in this Chapter. The influence of compressible effects on the first and second order of the statistics and the turbulent kinetic energy budget are discussed and reported.

The probability density function (PDF) of the velocities for the turbulent boundary layer are discussed in Chapter 6. The distribution of streamwise, normal, and spanwise velocities is formulated. The major cause of the non-Gaussian distribution of velocities is addressed.

Chapter 7 reports the numerical simulation of turbulent boundary layers subjected to free-stream turbulence. Results with three different free-stream turbulence levels are presented. Comparisons are made with available results in the literature. The effects of free-stream turbulence on the structure of turbulent boundary layers are discussed. Numerical methods used to calculate the turbulent boundary layer are presented.

The calculation of the film cooling of turbulent boundary layers is described in Chapter 8. This includes the numerical configuration, vortex structure, and the thermal effectiveness.

The dissertation is summarized in Chapter 9. The significant contributions of this work are outlined. Recommendations for future study are given.

CHAPTER 2. A NEW FRACTIONAL STEP METHOD FOR COMPRESSIBLE NAVIER-STOKES EQUATION

In order to decouple the temperature, velocity, and pressure in the compressible Navier-Stokes equations, a novel fractional step method is suggested in this dissertation, by which the traditional fractional algorithm has been extended to the simulation of compressible flows. This improvement provides a new way to calculate compressible Navier-Stokes equations. For the simulation of lower Mach number flows, the advantage is outstanding.

The main idea of this method is to adjust the eigenvalues of the Jacobian matrix by using the preconditioning method and a factorization matrix. The preconditioning technique is a widely used applied mathematical method. However, preconditioning is not enough to achieve the diagonal dominance of the Jacobian matrix. Therefore, this dissertation formulates a factorization process. By using this factorization together with the preconditioning method, the Jacobian matrix was decomposed into four parts. And these submatrices can be positive definite, regardless of the Mach number. This provides a robust and efficient way to calculate compressible Navier-Stokes equations.

One of the highlights of this chapter is a theoretical proof of the Kim and Moin (1985)'s suggestion of replacing the inverse operator $\frac{D}{Dt}^{-1}$ by Δt . The proof indicates that it is a second-order accurate approximation. When the time step Δt is small, the validation of this substitution can be explained by perturbation theory (Lee *et al.* (2001)). However, Choi and Moin (1994)'s numerical simulation showed that the fractional step scheme proposed by Kim and Moin (1985) can work fairly well even when Δt is 0.4. This feature cannot be explained by the perturbation theory. Thus, a theory to explain this phenomenon is desired.

For the convenience of mathematical proof, a subspace of \mathbb{R}^3 , Favre space, was introduced.

It is the material volume which is invariant under the Favre average. In this space, the inverse operator of the material derivative was formulated. This inverse operator enables us to explicitly factorize the Jacobian matrix. Although the Favre average was designed for compressible flows, for constant density incompressible flows, the velocity is invariant under the Favre average.

The other purpose of this chapter is to formulate a fractional step method for compressible flows, and deduce an efficient numerical algorithm to solve the compressible Navier-Stokes equations for a wide range of Mach numbers.

2.1 Introduction

Traditional fractional step or projection methods for the incompressible Navier-Stokes equations were introduced by Chorin (1968) and Temam (1969) in the late 1960s. The reformulation of these methods by Kim and Moin (1985) was a milestone in the development of computational fluid dynamics. From then on, the fractional step method has enjoyed widespread popularity in the simulation of incompressible flows since it provides an efficient way to decouple the pressure and velocities, which helps to remove most of the computational difficulties arising from the requirement of a divergence-free velocity. The main idea of the fractional step method is to replace the singular matrix with some proper submatrices by using a factorization technique. These submatrices can be solved easily since they have a better eigenvalue distribution, thereby increasing the speed of numerical convergence. The success of the fractional step method in incompressible flows inspires us to seek an analogous algorithm to improve the calculation of compressible Navier-Stokes equations.

In low Mach number flows, the influence of density fluctuations on the turbulent boundary layer is negligible as long as the mean density remains constant across the boundary layer (Bradshaw (1977)). Therefore, such flows can be treated as incompressible flows and traditional fractional steps method for incompressible flows can be applied. However, the density varies with the distance from the wall once heat transfer is involved, which greatly affects the turbulent structures. As a result, the mean velocity profiles will eventually be deformed

even though the Mach number is small (Nicoud and Bradshaw (2000)). Huang *et al.* (1993) and Nicoud and Bradshaw (2000) suggested using some density-weighted transformations to modify the velocity profiles so that the similarity laws of incompressible flows can be applied to compressible turbulent boundary layers. To accurately capture these phenomena, the overall compressible Navier-Stokes equations should be solved.

In the compressible Navier-Stokes equations, the threefold correlations among temperature, pressure and velocities may produce numerical difficulties at low Mach numbers due to a singularity as the Mach number approaches zero. To be more specific, the coupling between the pressure and velocity in such flows slows the convergence at low Mach numbers. Moreover, the temperature is coupled with the pressure and the velocity through the equation of state and the energy equation. The variation of temperature is associated with the variation of pressure or density, and a sudden change of the temperature in a local region caused by turbulence may induce a large gradient of pressure or density. This tends to slow the numerical convergence, or even worse, cause divergence. Therefore, a decoupling technique is desired for this purpose.

Currently, there are two distinct treatments for low Mach number compressible Navier-Stokes equations: pressure-based methods, and the density-based methods. The pressure-based methods (Karki and Patankar (1989), Bijl and Wesseling (1998), and, Wall *et al.* (2002)) are analogous with the fractional step method for incompressible flows. The difference between them are twofold: firstly, the pressure is determined from a Poisson equation for incompressible flows, but is governed by a Helmholtz equation for compressible flows. Secondly, the traditional fractional step method does not account for the coupling between the temperature and the other two quantities: velocity and pressure. For the incompressible flows, by using the factorization technique, the velocities and pressure are decoupled. Hence, one can determine the velocities and pressure through the fractional-staged schemes. However, for compressible flows, particularly for the flows with strong heat transfer, the coupling between the temperature and velocities makes a major contribution to the compressible effects of flows. How to deal with these compressible effects and handle the stiffness associated with lower Mach number limit has remained elusive. Wall *et al.* (2002) proposed a semi-implicit scheme, which focused more

on the stiffness. The other idea, the density-based method, attempts to cope with both the compressible effects and stiffness.

The density-based methods contains two classes: the preconditioning schemes and the asymptotic schemes. Asymptotic schemes decomposed the pressure into thermodynamic pressure and hydrodynamic pressure by using a perturbation method (Tomboulides and Orzag (1998)). This treatment will accelerate the convergence if the pressure fluctuations are small. As the heat transfer increases, the pressure fluctuations could be the same order of magnitude as the temperature and velocity fluctuations. Thus, perturbation cannot be applied. In this circumstance, preconditioning schemes offer a better way. Unlike the pressure-based methods which adjust the Jacobian matrix by using a right multiplication, a factorization matrix, the preconditioning methods optimize the Jacobian matrix by using a left multiplication (Pletcher and Chen (1993) and Turkel (1999)). A well-designed preconditioning matrix will cluster the eigenvalues, which eventually causes the acceleration of convergence. However, for the simulation of the lower Mach number flows, pressure-based methods give a better numerical performance compared with the density-based methods because of their different pressure solvers.

Furthermore, according to the Ostrowski-Reich theorem (Varga (2000)), the Gauss-Seidel scheme or SOR scheme converges if and only if the Jacobian matrix is positive definite. However, this situation cannot be guaranteed because the eigenvalues corresponding to the continuity equation or the energy equation may be negative or extremely large somewhere, particularly for the low Mach number flows or incompressible flow. The negative eigenvalues will give rise to the divergence of some iterative schemes such as the Gauss-Seidel scheme, Newton Gauss-Seidel scheme, or SOR scheme. In order to overcome this problem, this dissertation proposes a method to optimize the distribution of eigenvalues of the Jacobian matrix by using a right multiplier and a left multiplier. In other words, the method deduced by this paper is a combination of a preconditioning method and a factorization treatment, or a combination of pressure-based and density-based methods.

Precisely, the fractional step method is a kind of factorization treatment to the Jacobian

matrix. Perot (1993) represented the traditional fractional step method for incompressible flow as

$$\begin{bmatrix} \mathbf{A} & G \\ D & 0 \end{bmatrix} \begin{bmatrix} \mathbf{v}^{n+1} \\ p^{n+1} \end{bmatrix} = \begin{bmatrix} \mathbf{r} \\ 0 \end{bmatrix} + \begin{bmatrix} b.c's \\ b.c's \end{bmatrix} \quad (2.1)$$

where submatrices \mathbf{A} contains components from the time discrete derivative, convection and diffusion if the implicit scheme is applied (Perot (1995)). The splitting of the matrix requires the explicit representation of the inverse of \mathbf{A} . Unfortunately, such a representation is still unavailable. Kim and Moin (1985) suggested an approach whereby \mathbf{A}^{-1} is replaced with $\Delta t I$, and I is an identity matrix. This idea works fairly well in a variety of simulations (Kim and Moin (1985), Choi and Moin (1994)), but it has not been proved rigorously. Theoretical research is desired to explain why and how it works.

2.2 Governing Equations for Large Eddy Simulation

In this section, variables in the compressible flows are normalized as follows,

$$\begin{aligned} x_i &= \frac{x_i^*}{L_{ref}} & u_i &= \frac{u_i^*}{U_{ref}} & t &= \frac{t^*}{(L_{ref}/U_{ref})} & \rho &= \frac{\rho^*}{\rho_{ref}} \\ p &= \frac{p^*}{\rho_{ref} U_{ref}^2} & T &= \frac{T^*}{T_{ref}} & e &= \frac{e^*}{U_{ref}^2} & \mu &= \frac{\mu^*}{\mu_{ref}} \\ k &= \frac{k^*}{k_{ref}} & c_v &= \frac{c_v^*}{(U_{ref}^2/T_{ref})} & R &= \frac{R^*}{(U_{ref}^2/T_{ref})} & c_p &= \frac{c_p^*}{(U_{ref}^2/T_{ref})} \end{aligned} \quad (2.2)$$

The reference Mach number is $M_{ref} = U_{ref}/\sqrt{\gamma R^* T_{ref}}$. As usual, the fluid is assumed to be an ideal gas and the non-dimensional equation of state is: $p = \rho RT$. The non-dimensional coefficients of viscosity and thermal conductivity were evaluated as: $\mu = T^n$, where n is assumed to be 0.71. The specific heats, c_p and c_v , and Prandtl number were treated as constant.

In compressible flow, fluid properties may be variable temporally and spatially due to the simultaneous fluctuations in dilatation, heat transfer and mass transfer. A mass-weighted averaging is recommended for the scaling of properties carried by fluid elements which keep the mass conservation. Favre-filtered average (Favre (1983)) was utilized for this purpose.

Consequently, the Favre-filtered compressible Navier-Stokes equations are

$$\frac{\partial \bar{\rho}}{\partial t} + \frac{\partial(\bar{\rho}\tilde{u}_j)}{\partial x_j} = 0 \quad (2.3)$$

$$\frac{\partial(\bar{\rho}\tilde{u}_i)}{\partial t} + \frac{\partial(\bar{\rho}\tilde{u}_i\tilde{u}_j)}{\partial x_j} = -\frac{\partial \bar{p}}{\partial x_i} + \frac{\partial \hat{\sigma}_{ij}}{\partial x_j} - \frac{\partial \tau_{ij}}{\partial x_j} \quad (2.4)$$

$$\frac{\partial(\bar{\rho}\hat{E})}{\partial t} + \frac{\partial[(\bar{\rho}\hat{E} + \bar{p})\tilde{u}_j]}{\partial x_j} = \frac{\partial(\tilde{u}_i\bar{\sigma}_{ij})}{\partial x_j} - \frac{\partial \bar{q}_j}{\partial x_j} - \frac{\partial Q_j}{\partial x_j} - \gamma - \pi - \varepsilon \quad (2.5)$$

The tilde, $\tilde{\bullet}$, stands for the Favre-filtered average. For instance, $\tilde{a} = \frac{\bar{\rho a}}{\bar{\rho}}$. $\hat{E} = c_v \tilde{T} + \frac{1}{2} \tilde{u}_i \tilde{u}_j$, and $\hat{\sigma}_{ij} = \frac{2\bar{\mu}}{Re_r} (\tilde{S}_{ij} - \frac{1}{3} \tilde{S}_{kk} \delta_{ij})$. Moreover, the equation of state becomes

$$\bar{p} = R\bar{\rho}\tilde{T} \quad (2.6)$$

The effects of the small-scale motions are represented in the above equations through the subgrid-scale (SGS) stress tensor, τ_{ij} , in the momentum equation as

$$\tau_{ij} = \bar{\rho}(\widetilde{u_i u_j} - \tilde{u}_i \tilde{u}_j) \quad (2.7)$$

and the SGS terms that are the last four terms on the right hand side of Eq. 2.5 as

$$Q_j = \bar{\rho} c_v (\widetilde{T u_j} - \tilde{T} \tilde{u}_j) \quad (2.8)$$

$$\gamma = \tilde{u}_i \frac{\partial \tau_{ij}}{\partial x_j} \quad (2.9)$$

$$\pi = \overline{p \frac{\partial u_j}{\partial x_j}} - \bar{p} \frac{\partial \tilde{u}_j}{\partial x_j} \quad (2.10)$$

$$\varepsilon = \overline{\sigma_{ij} \frac{\partial u_i}{\partial x_j}} - \hat{\sigma}_{ij} \frac{\partial \tilde{u}_j}{\partial x_j} \quad (2.11)$$

where Q_j is the SGS heat flux vector. The terms γ , π and ε were neglected in the low Mach number flows (Vreman *et al.* (1995)). But in high Mach number flows, these terms must be modeled. Unfortunately, current research results give little guidance on how to model π and ε . Since the target of this chapter is to present an improvement to a numerical scheme, we neglect those terms and assume low Mach number flows here.

The filtered dimensionless viscous stress and heat flux vector are approximated by assuming that the correlations between the fluid properties and the derivatives of the velocity or temperature are weak (Cebeci (1974)). The approximations are

$$\bar{\sigma}_{ij} \approx \hat{\sigma}_{ij} = \frac{2\bar{\mu}}{Re_{ref}} \left(\tilde{S}_{ij} - \frac{1}{3} \tilde{S}_{kk} \delta_{ij} \right) \quad (2.12)$$

and

$$\bar{q}_j \approx \hat{q}_j = -\frac{c_p \bar{\mu}}{Re_{ref} Pr} \frac{\partial \tilde{T}}{\partial x_j} \quad (2.13)$$

where the strain rate tensor is

$$\tilde{S}_{ij} = \frac{1}{2} \left(\frac{\partial \tilde{u}_i}{\partial x_j} + \frac{\partial \tilde{u}_j}{\partial x_i} \right) \quad (2.14)$$

To close the equations, the SGS stress tensor and heat flux vector in the Favre-filtered equations need be modeled. A dynamic model proposed for compressible turbulence by Moin *et al.* (1991) and recommended by Lilly (1992) is implemented.

The anisotropic part of SGS stress tensor based on the grid filter was modeled as

$$\tau_{ij} - \frac{1}{3} \tau_{kk} \delta_{ij} = -2C_d \bar{\rho} \Delta^2 |\tilde{S}| \left(\tilde{S}_{ij} - \frac{1}{3} \tilde{S}_{kk} \delta_{ij} \right) \quad (2.15)$$

So the isotropic part of SGS stress tensor, τ_{kk} , becomes

$$\tau_{kk} = 2C_I \bar{\rho} \Delta^2 |\tilde{S}|^2 \quad (2.16)$$

The isotropic part of SGS stress tensor is neglected because it has a lower order of magnitude than the thermodynamic pressure (Moin *et al.* (1991)). The coefficient, C_d , is computed dynamically by

$$C_d = \frac{\langle L_{ij} M_{ij} \rangle}{\langle M_{kl} M_{kl} \rangle} \quad (2.17)$$

where

$$L_{ij} = \widehat{\bar{\rho} \tilde{u}_i \tilde{u}_j} - \frac{\widehat{\bar{\rho} \tilde{u}_i} \widehat{\bar{\rho} \tilde{u}_j}}{\widehat{\bar{\rho}}} \quad (2.18)$$

$$M_{ij} = -2\hat{\rho} \hat{\Delta}^2 |\hat{S}| (\hat{S}_{ij} - \frac{1}{3} \hat{S}_{kk} \delta_{ij}) + 2\Delta^2 \bar{\rho} |\tilde{S}| (\widehat{\tilde{S}_{ij} - \frac{1}{3} \tilde{S}_{kk} \delta_{ij}}) \quad (2.19)$$

A procedure similar to the modeling of the SGS stress tensor is followed to represent the SGS heat flux vector. Considering the modeling for the eddy diffusivity SGS model, the subgrid-scale heat flux vector can be modeled as

$$\begin{aligned} Q_j &= -\frac{c_p \mu_t}{Pr_t} \frac{\partial \tilde{T}}{\partial x_j} \\ &= -\frac{c_p C_d \bar{\rho} \Delta^2 |\tilde{S}|}{Pr_t} \frac{\partial \tilde{T}}{\partial x_j} \end{aligned} \quad (2.20)$$

where Pr_t is the turbulent Prandtl number and calculated dynamically as

$$Pr_t = -c_p C_d \frac{\langle F_j F_j \rangle}{\langle H_k F_k \rangle} \quad (2.21)$$

where

$$H_j = c_v \left(\widehat{\rho \tilde{u}_j \tilde{T}} - \frac{\widehat{\rho u_j \rho T}}{\hat{\rho}} \right) \quad (2.22)$$

$$F_j = \hat{\rho} \hat{\Delta}^2 |\hat{S}| \frac{\partial \hat{T}}{\partial x_j} - \Delta^2 \left(\widehat{\bar{\rho} |\tilde{S}| \frac{\partial \tilde{T}}{\partial x_j}} \right) \quad (2.23)$$

2.3 Governing Equations for Direct Numerical Simulation

The direct numerical simulation (DNS) is also an important numerical tool widely utilized in the simulation of turbulence. Clearly, the governing equations of DNS are different from the that of LES even if the same reference system is used. The governing equation for the DNS follows:

$$\frac{\partial \rho}{\partial t} + \frac{\partial(\rho u_j)}{\partial x_j} = 0, \quad (2.24)$$

$$\frac{\partial(\rho u_i)}{\partial t} + \frac{\partial(\rho u_i u_j)}{\partial x_j} + \frac{\partial p}{\partial x_i} = \frac{\partial \sigma_{ij}}{\partial x_j}, \quad (2.25)$$

$$\frac{\partial(\rho E)}{\partial t} + \frac{\partial[(\rho E + p)u_j]}{\partial x_j} = \frac{\partial(u_i \sigma_{ij})}{\partial x_j} - \frac{\partial q_j}{\partial x_j}. \quad (2.26)$$

Here, $E = c_v T + \frac{1}{2} u_i u_i$, $\sigma_{ij} = \frac{2\mu}{Re_r} (S_{ij} - \frac{1}{3} S_{kk} \delta_{ij})$, and $q_j = -\frac{c_p \mu}{Re_{r ef} Pr} \frac{\partial T}{\partial x_j}$.

2.4 Quasi-Newton Iteration

The best-known and widely applied method for solving nonlinear equations is the Newton method. There are two main types Newton-like methods; the locally convergent Newton method and the globally convergent Newton method. When the initial guess is sufficiently close to the solution, the locally convergent Newton method, e.g. Kantorovich method (Dennis and Schnabel (1996)), has a quadratic convergence rate. Its convergence strictly depends on an appropriate initial guess, but such a guess is almost impossible for the simulation of complex flows. Alternatively, the quasi-Newton method, which offers a global convergence advantage, enables us to calculate the complicated flows with a rough initial guess. But the price paid is

the convergence rate. Unlike the local method, the quasi-Newton method holds a superlinear convergent rate (Dennis and Schnabel (1996)). For the simulation of complicated flows, like turbulence, superlinear should be a satisfactory convergence speed since the long time behavior of the residual error decays faster than any other linear function. With the quasi-Newton method, the Jacobian matrix will be adjusted by some factorization techniques. In order to achieve the global convergence, a new algorithm is proposed here.

When using a Newton-like method, governing equations can be represented as:

$$J\delta v = -F \quad (2.27)$$

where J is the Jacobian matrix. Usually, for the discretized Navier-Stokes equations, it is hard to guarantee a diagonally dominant Jacobian matrix. The condition number may be extremely huge, unless a very tiny time step is utilized. But the small time step implies a geometrical increase of the cost in terms of CPU time. Moreover, the small time step is not a resolution for incompressible flows due to the singularity of continuity equation. Therefore, the Jacobian matrix must be adjusted. The main idea of this chapter is to determine an appropriate left multiplier P and right multiplier M so that the resolved matrices can be diagonal dominant and positive definite. Thus, an improved solver follows:

$$PJMM^{-1}\delta v = -PF \quad (2.28)$$

Actually, the left multiplier is essentially a preconditioning matrix while the right multiplier provides a factorization.

There are two ways to obtain these Jacobian matrix equations. Without loss of generality, we consider the governing equation for DNS. The first way is to take a variation δ to the left hand side of equations (2.24)~(2.26). The second way is to replace P , u_1 , u_2 , u_3 , and, T with $P + \delta P$, $u_1 + \delta u_1$, $u_2 + \delta u_2$, $u_3 + \delta u_3$ and $T + \delta T$ on the left hand side of equations (2.24) (2.26) respectively. And then neglect the higher order variances. The second method is based on the idea of perturbation. Both method give the following of equations:

$$\frac{\partial}{\partial t}\delta\rho + \frac{\partial}{\partial x_j}\delta(\rho u_j) = -\frac{\partial\rho}{\partial t} - \frac{\partial(\rho u_j)}{\partial x_j}, \quad (2.29)$$

$$\frac{\partial}{\partial t}\delta(\rho u_i) + \frac{\partial}{\partial x_j}\delta(\rho u_i u_j) + \frac{\partial}{\partial x_i}\delta p = -\frac{\partial(\rho u_i)}{\partial t} - \frac{\partial(\rho u_i u_j)}{\partial x_j} - \frac{\partial p}{\partial x_i} + \frac{\partial \sigma_{ij}}{\partial x_j}, \quad (2.30)$$

$$\frac{\partial}{\partial t}\delta(\rho E) + \frac{\partial}{\partial x_j}\delta[(\rho E + p)u_j] = -\frac{\partial(\rho E)}{\partial t} - \frac{\partial[(\rho E + p)u_j]}{\partial x_j} + \frac{\partial(u_i \sigma_{ij})}{\partial x_j} - \frac{\partial q_j}{\partial x_j}. \quad (2.31)$$

Note that, in this study, viscous terms are treat explicitly. In the other words, the Jacobian matrix does not contain the viscous terms. The reason for this is twofold: firstly, keeping the viscous terms in the Jacobian matrix will cause difficulty in the analysis of eigenvalues. Secondly, for the simulation of turbulence, which is usually associated with high Reynolds numbers, the influence of viscous terms on the numerical stability is negligible particularly for the Newton method. With the quasi-Newton method, the Jacobian matrix shall be adjusted by a preconditioning and a factorization technique.

2.4.1 Preconditioning

The preconditioning matrix proposed by Pletcher and Chen (1993) is utilized in this chapter. It is

$$P = \begin{pmatrix} \frac{q}{RC_v} & -\frac{\hat{U}}{RC_v} & -\frac{\hat{V}}{RC_v} & -\frac{\hat{W}}{RC_v} & -\frac{1}{RC_v} \\ -\frac{\hat{T}\hat{U}}{\hat{P}} & \frac{\hat{T}}{\hat{P}} & 0 & 0 & 0 \\ -\frac{\hat{T}\hat{V}}{\hat{P}} & 0 & \frac{\hat{T}}{\hat{P}} & 0 & 0 \\ -\frac{\hat{T}\hat{W}}{\hat{P}} & 0 & 0 & \frac{\hat{T}}{\hat{P}} & 0 \\ \frac{\hat{T}}{\hat{P}}(\frac{q}{RC_v} - 1) & -\frac{\hat{T}\hat{U}}{\hat{P}C_v} & -\frac{\hat{T}\hat{V}}{\hat{P}C_v} & -\frac{\hat{T}\hat{W}}{\hat{P}C_v} & \frac{\hat{T}}{\hat{P}C_v} \end{pmatrix} \quad (2.32)$$

where

$$q = \frac{(\hat{U}^2 + \hat{V}^2 + \hat{W}^2)}{2}$$

Left multiplying both sides of equation (2.27) with this preconditioning matrix, yields

$$\begin{pmatrix} \frac{D}{RDt} & b\frac{\partial}{\partial x} & b\frac{\partial}{\partial y} & b\frac{\partial}{\partial z} & 0 \\ e\frac{\partial}{\partial x} & \frac{D}{Dt} & 0 & 0 & 0 \\ e\frac{\partial}{\partial y} & 0 & \frac{D}{Dt} & 0 & 0 \\ e\frac{\partial}{\partial z} & 0 & 0 & \frac{D}{Dt} & 0 \\ 0 & \frac{\hat{T}R\partial}{C_v\partial x} & \frac{\hat{T}R\partial}{C_v\partial y} & \frac{\hat{T}R\partial}{C_v\partial z} & \frac{D}{Dt} \end{pmatrix} \begin{pmatrix} \delta P \\ \delta U \\ \delta V \\ \delta W \\ \delta T \end{pmatrix} = \begin{pmatrix} -f_1 \\ -f_2 \\ -f_3 \\ -f_4 \\ -f_5 \end{pmatrix}$$

where $b = \frac{\hat{P}}{R} + \frac{\hat{P}}{C_v}$, $e = \frac{\hat{T}R}{\hat{P}}$, and vector $\vec{f} = P\vec{F}$. For simplification, it is represented as

$$\begin{pmatrix} a & bD & 0 \\ eG & C & 0 \\ 0 & B & E \end{pmatrix} \begin{pmatrix} \delta P \\ \delta V_i \\ \delta T \end{pmatrix} = \begin{pmatrix} -f_1 \\ -f_i \\ -f_5 \end{pmatrix} \quad (2.33)$$

where G is the gradient operator, D is the divergence operator, $a = \frac{D}{RDt}$, $E = \frac{D}{Dt}$, $\delta V_i = \begin{bmatrix} \delta U & \delta V & \delta W \end{bmatrix}^{-1}$, $f_i = \begin{bmatrix} f_2 & f_3 & f_4 \end{bmatrix}^{-1}$, $B = \begin{bmatrix} \frac{\hat{T}R\partial}{C_v\partial x} & \frac{\hat{T}R\partial}{C_v\partial y} & \frac{\hat{T}R\partial}{C_v\partial z} \end{bmatrix}$ and

$$C = \begin{pmatrix} \frac{D}{Dt} & 0 & 0 \\ 0 & \frac{D}{Dt} & 0 \\ 0 & 0 & \frac{D}{Dt} \end{pmatrix} = \frac{D}{Dt}I \quad (2.34)$$

Here, $\frac{D}{Dt}$ is a material derivative and I is the identity matrix. Such a preconditioning matrix offers us two advantages: firstly, it transfers the large off-diagonal terms into the diagonal part so that the numerical scheme becomes more robust regardless of how small the Mach number is. Secondly, this preconditioning technique enables us to decouple the temperature and velocities. Clearly, the threefold correlations among temperature, pressure and velocities produce some numerical difficulties especially in the low Mach number flows.

A perturbation analysis could also be performed so that

$$\delta P = R\rho\delta T + RT\delta\rho$$

Under the reference system used in this chapter, $R = \frac{1}{\gamma M_{ref} M_{ref}}$. This implies that the small perturbation on temperature will be greatly magnified by R , and be brought into the momentum equations by δP . This dynamic procedure slows convergence. Moreover, the eigenvalues after preconditioning are U and

$$[U(1 + R) \pm \sqrt{U^2(R - 1)^2 + 4R\alpha^2}]/(2R) \quad (2.35)$$

where $R = \frac{\gamma}{M^2}$ and α is non-dimensional acoustic speed, $\alpha = \sqrt{\gamma RT}$. Obviously, these eigenvalues cluster near 1. Before preconditioning, the eigenvalues are U and $U \pm \alpha$. But it is still possible to have zero or negative eigenvalues in the solver regardless of the Mach

number. In subsonic flows, $U < \alpha$, then $U(1 + R) < \sqrt{U^2(R - 1)^2 + 4R\alpha^2}$. In supersonic flows, the local velocity U must be less than the acoustic speed α somewhere near to the wall. In this region, $U(1 + R) < \sqrt{U^2(R - 1)^2 + 4R\alpha^2}$ certainly. The appearance of negative eigenvalues results in the loss of the positive definite condition. Such non positive eigenvalues produce the numerical difficulty of the quasi-Newton solver, and even cause the divergence of the iterative scheme. Therefore, a proper factorization technique needs to be applied.

2.4.2 Fractional Step Factorization

Denote the matrix M^{-1} in equation (2.28) as

$$M^{-1} = \begin{pmatrix} a - bDC^{-1}eG & 0 & 0 \\ C^{-1}eG & I & 0 \\ -E^{-1}BC^{-1}eG & 0 & 1 \end{pmatrix} \quad (2.36)$$

where I is an identity matrix. Hence, the Jacobian matrix in equation (2.33) can be decomposed into

$$\begin{pmatrix} 1 & bD & 0 \\ 0 & C & 0 \\ 0 & B & E \end{pmatrix} \begin{pmatrix} a - bDC^{-1}eG & 0 & 0 \\ C^{-1}eG & I & 0 \\ -E^{-1}BC^{-1}eG & 0 & I \end{pmatrix} \begin{pmatrix} \delta P \\ \delta u_i \\ \delta T \end{pmatrix} = \begin{pmatrix} -f_1 \\ -f_i \\ -f_5 \end{pmatrix} \quad (2.37)$$

This factorization offers a way to decouple δP , δu_i , and δT . Essentially, this decoupling is a kind of fractional step procedure.

Resolving equation (2.37) requires the formulation of the operator C^{-1} . According to equation 2.34, the inverse of the operator C implies the inverse of the material derivative. But, unfortunately, there is no explicit representation of such an inverse operator of material derivative currently. That is the reason that Kim and Moin (1985) suggested substituting the operator A^{-1} , which is the advection-diffusion part of momentum equation and corresponds to the operator C^{-1} in this chapter, with Δt in their fractional step method for incompressible flows. Choi and Moin (1994) found that such a time difference Δt can be up to 0.4 without reducing the accuracy in their simulation of turbulent channel flow. Perot (1993) analyzed this splitting procedure for incompressible flows.

When Δt is small enough,

$$\frac{1}{\Delta t} \sim \frac{1}{\Delta t} + u_i \frac{1}{\Delta x_i} \quad (2.38)$$

where $\frac{1}{\Delta t} + u_i \frac{1}{\Delta x_i}$ is the discretization of the operator A . But this idea cannot explain the fact that Δt can be up to 0.4 without loss of the accuracy (Choi and Moin (1994)).

In the later part of this section, we will focus on the questions why such a substitution can work well even when Δt is up to 0.4, how we can formulate this inverse operator C^{-1} explicitly, and what is the relationship between the submatrices C^{-1} and $\Delta t \mathbf{I}$.

In order to answer these questions, we need define a subspace of Euclidean space \mathbb{R}^3 , firstly.

Definition 1 Let U be a compact subset of 3 dimensional Euclidean space \mathbb{R}^3 , the set $\{\tau_i(t)\}$ is called fluid element partition of U , FEP, if $\{\tau_i(t)\}$ is a partition of U , $\{\tau_i(t)\}$ are pairwise disjoint, and $\int_{\tau_i(t)} \rho d\tau$ is independent on t . i.e.

$$FEP = \{\tau_i(t) | \tau_i(t) \cap \tau_j(t) = \emptyset \text{ when } i \neq j, U = \cup_i \tau_i \text{ and } \frac{d}{dt} \int_{\tau_i(t)} \rho d\tau = 0\} \quad (2.39)$$

Definition 2 Let $\rho, \phi_j, \rho\phi_j \in L^1(U)$. Denote Favre space, FS, as

$$FS = \{\phi_j | \phi_j = \frac{\int_{\tau_i(t)} d\tau \rho \phi_j}{\int_{\tau_i(t)} d\tau \rho}, \text{ for all } \tau_i(t) \in FEP\} \quad (2.40)$$

Clearly, FEP covers U , since U is compact in \mathbb{R}^3 . Furthermore, FEP is a Lagrangian decomposition of U . $\tau_i(t)$ is a closed volume moving with the fluid so that τ_i is a function of time. It is the volume maintaining mass conservation. And the fluid elements are of the Lagrangian type. It is also called material volume (Pope (2000)). In the other words,

$$\frac{d}{dt} \int_{\tau_i(t)} d\tau \rho = 0$$

The preceding definition implies that elements of FS is invariant under the Favre average on FEP. Recall the governing equation (2.3), (2.4), and (2.5), the resolved variable are \tilde{u}_j and $\tilde{\rho}$. i.e. These variables are all invariant on the Favre average.

Lemma 1 Favre space FS is an Abelian ring associated with algebraic addition, +, and multiplication, \times .

Proof. Let $\tau_i(t) \in FEP$, $\phi_1, \phi_2 \in FS$, and constant $a, b \in \mathbb{R}$, then,

$$\begin{aligned} a\phi_1 + b\phi_2 &= \frac{a}{\int_{\tau_i(t)} \rho(t) d\tau} \int_{\tau_i(t)} d\tau \rho(t) \phi_1 + \frac{b}{\int_{\tau_i(t)} \rho(t) d\tau} \int_{\tau_i(t)} d\tau \rho(t) \phi_2 \\ &= \frac{1}{\int_{\tau_i(t)} \rho(t) d\tau} \int_{\tau_i(t)} d\tau \rho(t) (a\phi_1 + b\phi_2) \end{aligned}$$

This implies that $a\phi_1 + b\phi_2 \in FS$. So Favre space is closed on addition, and the identity for addition is 0.

Since U is compact in \mathbb{R}^3 , and $\{\tau_i(t)\}$ is a partition of U , then there exists a H -projection-value measure $\tau_i(t) \rightarrow P_{\tau_i(t)}$. Without loss of generality, let $\phi_i, \phi_j \in FS$, and $\rho, \phi_j, \rho\phi_j \in L^1(U)$. Considering that

$$\begin{aligned} &\frac{1}{\int_{\tau_i(t)} \rho(t) d\tau} \int_{\tau_i(t)} d\tau_i \rho(a\phi_i b\phi_j) \\ &= \frac{1}{\int_{\tau_i(t)} \rho(t) d\tau} \int \rho(a\phi_i b\phi_j) dP_{\tau_i} \\ &= \frac{1}{\int_{\tau_i(t)} \rho(t) d\tau} \int \rho(a\phi_i b \int_{\tau_j(t)} \frac{\rho\phi_j dP_{\tau_j}}{\rho d\tau_j}) dP_{\tau_i} \end{aligned}$$

By the mass conservation, i.e. $\int_{\tau_j(t)} \rho d\tau_j = \text{const.}$

$$\begin{aligned} &= \frac{ab}{\int_{\tau_i(t)} \rho(t) d\tau \int_{\tau_j(t)} \rho d\tau_j} \int (\rho\phi_i \int \rho\phi_j dP_{\tau_j}) dP_{\tau_i} \\ &= \frac{ab}{\int_{\tau_i(t)} \rho(t) d\tau \int_{\tau_j(t)} \rho d\tau_j} \int (\rho\phi_i \chi_{\tau_i} \int \rho\phi_j \chi_{\tau_j} dP) dP \end{aligned}$$

Since P is an H -projection-valued measure,

$$\begin{aligned} &= \frac{ab}{\int_{\tau_i(t)} \rho(t) d\tau \int_{\tau_j(t)} \rho d\tau_j} \int (\rho\phi_i \chi_{\tau_i}) dp \int (\int (\rho\phi_j \chi_{\tau_j}) dP) dp \\ &= \frac{ab}{\int_{\tau_i(t)} \rho(t) d\tau \int_{\tau_j(t)} \rho d\tau_j} \int (\rho\phi_i \chi_{\tau_i}) dp \int (\rho\phi_j \chi_{\tau_j}) dP \\ &= \frac{ab}{\int_{\tau_i(t)} \rho d\tau_i \int_{\tau_j(t)} \rho d\tau_j} \int \rho\phi_i dP_{\tau_i(t)} \int \rho\phi_j dP_{\tau_j(t)} \\ &= a\phi_1 \times b\phi_2 \end{aligned}$$

Thus, Favre space is closed on multiplication, and the identity for addition is 1. It is easy to prove that the Favre space is commutative. Consequently, Favre space is an Abelian ring. \square

Theorem 2 Let $\tau_i(t) \in FEP$,

(1), if $\phi_i \in FS$, then the right inverse S of material derivative $\frac{D}{Dt}$ is

$$S = \frac{1}{\int_{\tau_i(t)} \rho(t) d\tau} \int_{t_0}^t dt' \int_{\tau_i(t')} d\tau \rho(t') \quad (2.41)$$

(2), if $\phi_i \in FS$ and $\phi_i(t_0) = 0$, then S is the inverse of material derivative.

(3), $\phi_i \in FS$, iff

$$\frac{D}{Dt} \circ S\phi_i = \phi_i \quad (2.42)$$

where $\frac{D}{Dt} = \frac{\partial}{\partial t} + u_i \frac{\partial}{\partial x_i}$,

Proof. (1), $\forall \phi_i \in FS$, let $\int_{\tau_i(t)} \rho d\tau = M(t)$.

$$\begin{aligned} \frac{D}{Dt} \circ S\phi_i &= \frac{d}{dt} \frac{1}{M(t)} \int_{t_0}^t dt' \int_{\tau_i(t')} d\tau \rho \phi_i \\ &= -\frac{\frac{dM(t)}{dt}}{M^2(t)} \int_{t_0}^t dt' \phi_i M(t) + \frac{1}{\int_{\tau_i(t)} \rho d\tau} \int_{\tau_i(t)} d\tau \rho \phi_i \end{aligned} \quad (2.43)$$

Due to the mass conservation, i.e. $\frac{dM(t)}{dt} = 0$, and $\phi_i \in FS$,

$$\frac{D}{Dt} \circ S\phi_i = \phi_i \quad (2.44)$$

Therefore, S is the right inverse of material derivative.

(2), According to Batchlor (1993) and Aris (1989), $\int_{\tau_i(t')} d\tau \rho(t') \frac{D\phi_i}{Dt'} = \frac{d}{dt'} \int_{\tau_i(t')} d\tau \rho \phi_i$.

This implies that

$$\begin{aligned} S \circ \frac{D}{Dt} \phi_i &= \frac{1}{\int_{\tau_i(t)} \rho d\tau} \int_{t_0}^t dt' \int_{\tau_i(t')} d\tau \rho(t') \frac{D\phi_i}{Dt'} \\ &= \frac{1}{\int_{\tau_i(t)} \rho d\tau} \int_{t_0}^t dt' \frac{d}{dt'} \int_{\tau_i(t')} d\tau \rho \phi_i \\ &= \frac{1}{\int_{\tau_i(t)} \rho d\tau} \left[\int_{\tau_i(t)} d\tau \rho \phi_i(t) - \int_{\tau_i(t_0)} d\tau \rho \phi_i(t_0) \right] \end{aligned}$$

Recall that ϕ_i is invariant on the Favre average in FEP, so

$$S \circ \frac{D}{Dt} \phi_i = \frac{1}{\int_{\tau_i(t)} \rho d\tau} \left[\phi_i(t) \int_{\tau_i(t)} \rho d\tau - \phi_i(t_0) \int_{\tau_i(t_0)} \rho d\tau \right] \quad (2.45)$$

by mass conservation, i.e. $\int_{\tau_i(t)} \rho d\tau = \int_{\tau_i(t_0)} \rho d\tau$

$$S \circ \frac{D}{Dt} \phi_i = \phi_i(t) - \phi_i(t_0) \quad (2.46)$$

Thus, S is the left inverse of $\frac{D}{Dt}$ if $\phi_i(t_0) = 0$. Combined with part (1), consequently, S is the inverse operator of material derivative if $\phi_i(t_0) = 0$.

(3), If $\phi_i \in FS$, by the proof above, we get (2.42) for free. Conversely, if (2.42) is held, by mass conservation and equation (2.43),

$$\begin{aligned} \frac{D}{Dt} \circ S\phi_i &= \frac{D}{Dt} \frac{1}{\int_{\tau_i(t)} \rho d\tau} \int_{t_0}^t dt' \int_{\tau_i(t')} \rho \phi_i d\tau \\ &= \frac{1}{\int_{\tau_i(t)} \rho d\tau} \frac{D}{Dt} \int_{t_0}^t dt' \int_{\tau_i(t')} \rho \phi_i d\tau \\ &= \frac{1}{\int_{\tau_i(t)} \rho d\tau} \int_{\tau_i(t)} \rho \phi_i d\tau \end{aligned}$$

thus, combine with equation 2.42,

$$\phi_i = \frac{1}{\int_{\tau_i(t)} \rho d\tau} \int_{\tau_i(t)} \rho \phi_i d\tau \quad (2.47)$$

This implies $\phi_i \in FS$. \square

The formulation of right inverse operator of material derivative will bring us benefits not only on the factorization of Jacobian matrix of equation (2.36) and (2.37), but also on the theoretical proof and numerical simulation. Theorem 2 provides an explicit formulation for the representation of the inverse operator of the material derivative.

Regardless of $\phi_i(t_0)$, if and only if $\phi_i \in FS$, equation (2.42) turns out:

$$S\phi_i = \left(\frac{D}{Dt}\right)^{-1} \phi_i \quad (2.48)$$

Thus, $\left(\frac{D}{Dt}\right)^{-1} \phi_i$ can be replaced by $S\phi_i$. Unlike operator $\left(\frac{D}{Dt}\right)^{-1}$, operator S can be calculated numerically.

Furthermore, it is clear that S is the unique representation of the inverse of $\frac{D}{Dt}$. Assume fail, then there exists a operator S_1 such that $\frac{D}{Dt} \circ S_1\phi_i = S_1 \circ \frac{D}{Dt}\phi_i = \phi_i$ for any $\phi_i \in FS$. And for $\phi_j \in FS$, $S_1\phi_j \neq S\phi_j$. But for any $\phi_i \in FS$

$$S\phi_i = S \circ \frac{D}{Dt} \circ S_1\phi_i = S_1\phi_i \quad (2.49)$$

This implies $S = S_1$ for any $\phi_i \in FS$. Thus S is the unique inverse of $\frac{D}{Dt}$ on FS .

Due to theorem 2, the substitution of $(\frac{D}{Dt})^{-1}$ with S only works when $\phi_i \in FS$. Clearly, the resolved variations δP , δu_i and δT are in FS , but the operator $eG \circ \delta P$ and $eG \circ \delta T$ which are represented by equation (2.37) may not be in the space FS .

In the manner of discretization, we substitute the gradient operator G with its discretization G' , where $G' := \sum_{j=1}^n a_j$ such that $\|G' \circ \phi_i - G \circ \phi_i\| \leq ch^n \|\phi_j^{(n)}\|$. G' is the n th order discretization of the gradient operator and h is the diameter of $\tau_i(t)$. Hence, equation (2.37) can be approached by

$$\begin{pmatrix} 1 & bD & 0 \\ 0 & C & 0 \\ 0 & B & E \end{pmatrix} \begin{pmatrix} a - bDC^{-1}eG' & 0 & 0 \\ C^{-1}eG' & I & 0 \\ -E^{-1}BC^{-1}eG' & 0 & I \end{pmatrix} \begin{pmatrix} \delta P \\ \delta u_i \\ \delta T \end{pmatrix} = \begin{pmatrix} -f_1 \\ -f_i \\ -f_5 \end{pmatrix}$$

Since FS is an Abelian ring, due to lemma 1, $eG' \delta P = \frac{\hat{T}R}{\hat{P}} \sum_{j=1}^n a_j \delta P \in FS$, where R and a_j are constant. By this fact and theorem 2, above equation reduces to

$$\begin{pmatrix} 1 & bD & 0 \\ 0 & C & 0 \\ 0 & B & E \end{pmatrix} \begin{pmatrix} a - bDS eG' & 0 & 0 \\ S eG' & I & 0 \\ -SBS eG' & 0 & I \end{pmatrix} \begin{pmatrix} \delta P \\ \delta u_i \\ \delta T \end{pmatrix} = \begin{pmatrix} -f_1 \\ -f_i \\ -f_5 \end{pmatrix} \quad (2.50)$$

If matrix

$$\begin{pmatrix} 1 & bD & 0 \\ 0 & C & 0 \\ 0 & B & E \end{pmatrix}$$

is invertible, then the error between equation (2.37) and equation (2.50) is

$$\begin{aligned} Err_{3 \times 3} &= \begin{pmatrix} 1 & bD & 0 \\ 0 & C & 0 \\ 0 & B & E \end{pmatrix} \begin{pmatrix} -bDC^{-1}e(G' - G) \circ \delta P & 0 & 0 \\ C^{-1}e(G' - G) \circ \delta P & 0 & 0 \\ -C^{-1}BC^{-1}e(G' - G) \circ \delta P & 0 & 0 \end{pmatrix} \\ &= \begin{pmatrix} 0 & 0 & 0 \\ e(G' - G) \circ \delta P & 0 & 0 \\ 0 & 0 & 0 \end{pmatrix} \end{aligned} \quad (2.51)$$

Theorem 3 if $e \in L^2$, $\delta P \in H^n(\tau_i)$ and matrix

$$\begin{pmatrix} 1 & bD & 0 \\ 0 & C & 0 \\ 0 & B & E \end{pmatrix}$$

is invertible then discretization error represented by equation (2.51) holds:

$$\|Err\|_{L^2} \leq c_1 h^n \|e\|_{L^2} \|\delta P\|_{H^n(\tau_i)}$$

Proof. For any $\delta P \in H^{n+2}$, by definition of G' ,

$$I := \|(G' - G) \circ \delta P\|_{L^2(\tau_i)} \leq c_1 h^n \|\delta P^{(n)}\|_{L^2(\tau_i)} \quad (2.52)$$

Equation (2.51) says:

$$\|Err\|_{L^2} = \|e(G' - G) \circ \delta P\|_{L^2} \quad (2.53)$$

by Hölder inequality,

$$\begin{aligned} \|Err\|_{L^2} &\leq \|e\|_{L^2} \|(G' - G) \circ \delta P\|_{L^2(\tau_i)} \\ &\leq c_1 h^n \|e\|_{L^2} \|\delta P\|_{H^n(\tau_i)} \end{aligned}$$

Now, we finish the proof. \square

In theorem 3, h represents the size of the $\tau_i(t)$. Providing that equation (2.37) has a uniform solution, in the other words, the eigenvalues of the matrix of the left hand side of the equation (2.37) are all nonzero, we can always find a small enough h such that $\|Err\|_{L^2}$ is small enough, which implies that by adjusting h the quasi-Newton methods can keep the descant direction during the iterative process.

By replacing the inverse of material derivative with operator S in equation (2.37), yields

$$\begin{pmatrix} 1 & bD & 0 \\ 0 & C & 0 \\ 0 & B & E \end{pmatrix} \begin{pmatrix} a - bDS_e G' & 0 & 0 \\ S_e G' & I & 0 \\ -SBS_e G' & 0 & I \end{pmatrix} \begin{pmatrix} \delta P \\ \delta u_i \\ \delta T \end{pmatrix} = \begin{pmatrix} -f_1 \\ -f_i \\ -f_5 \end{pmatrix} \quad (2.54)$$

The above equation can be solved by a fractional step method.

Since velocities, pressure, and temperature of flows satisfy the Navier-Stokes equations, this means the velocities, pressure, and temperature must be in $C^1(t_0, t; \tau_i)$. This feature enables us to deduct the relationship of Δt and operator S .

Lemma 4 *if $\phi(t, \tau_i(t)) \in FS \cap C^1(t_0, t; \tau_i)$, then there exists a constant c such that*

$$|S \circ \phi - \Delta t \phi(t_0, \tau_i(t_0))| \leq c(\Delta t)^2 \quad (2.55)$$

where $\Delta t = t - t_0$.

Proof. Since $\phi(t, \tau_i(t)) \in FS$,

$$\begin{aligned} S \circ \phi &= \frac{1}{\int_{\tau_i(t)} \rho(t) d\tau} \int_{t_0}^t dt' \int_{\tau_i(t')} d\tau \rho \phi \\ &= \frac{1}{\int_{\tau_i(t)} \rho(t) d\tau} \int_{t_0}^t \phi dt' \int_{\tau_i(t')} d\tau \rho \end{aligned}$$

by mass conservation, $\int_{\tau_i(t)} \rho(t) d\tau = \int_{\tau_i(t')} \rho(t') d\tau = \text{const.}$

$$S \circ \phi = \int_{t_0}^t \phi dt' \quad (2.56)$$

hence

$$|S \circ \phi - \phi(t_0, \tau_i(t_0))\Delta t| = \left| \int_{t_0}^t (\phi - \phi(t_0, \tau_i)) dt' \right|$$

Since $\phi(t, \tau_i) \in C^1(t_0, t_1; \tau_i)$, and τ_i is a function of t . Then there exists a positive constant c such that

$$\begin{aligned} &|\phi(t, \tau_i) - \phi(t_0, \tau_i(t_0))| \quad (2.57) \\ &= \left| \int_{t_0}^t \frac{d\phi}{dt} dt \right| \\ &\leq c \int_{t_0}^t dt \\ &= c\Delta t \end{aligned}$$

Hence

$$\begin{aligned} &|S \circ \phi - \phi(t_0, \tau_i(t_0))\Delta t| \\ &\leq c\Delta t \int_{t_0}^t dt' \\ &= c\Delta t^2 \end{aligned}$$

Thus, the proof is accomplished. \square

Lemma 4 shows that Δt is the second order approach of operator S . This verifies that Kim and Moin (1985)'s suggestion of replacing the advection-diffusion part of momentum equation with Δt actually is a second order approach. When a small enough Δt is chosen, the descent direction can be held. This increases the convergence rate. In the above, c is identified by the mesh, boundary condition and initial conditions. In the case $\Delta t = 0.4$, the error is less than $0.16c$. When a small enough Δt and a fine enough mesh are chosen, c can be small enough. Therefore, Choi and Moin (1994) can obtain fairly good results even with $\Delta t = 0.4$.

2.4.3 Numerical Procedure

The discretization of identity (2.37) follows

$$\begin{bmatrix} 1 & b_{\frac{\delta}{\delta x_1}} & b_{\frac{\delta}{\delta x_2}} & b_{\frac{\delta}{\delta x_3}} & 0 \\ 0 & G & 0 & 0 & 0 \\ 0 & 0 & G & 0 & 0 \\ 0 & 0 & 0 & G & 0 \\ 0 & c_{\frac{\delta}{\delta x_1}} & c_{\frac{\delta}{\delta x_1}} & c_{\frac{\delta}{\delta x_1}} & G \end{bmatrix} \begin{bmatrix} \frac{1}{R}G - b_{\frac{\delta}{\delta x_i}} \left(\frac{D}{Dt}\right)^{-1} e_{\frac{\delta}{\delta x_i}} & 0 & 0 & 0 & 0 \\ \left(\frac{D}{Dt}\right)^{-1} e_{\frac{\delta}{\delta x_1}} & 1 & 0 & 0 & 0 \\ \left(\frac{D}{Dt}\right)^{-1} e_{\frac{\delta}{\delta x_2}} & 0 & 1 & 0 & 0 \\ \left(\frac{D}{Dt}\right)^{-1} e_{\frac{\delta}{\delta x_3}} & 0 & 0 & 1 & 0 \\ -\left(\frac{D}{Dt}\right)^{-1} c_{\frac{\delta}{\delta x_i}} \left(\frac{D}{Dt}\right)^{-1} e_{\frac{\delta}{\delta x_i}} & 0 & 0 & 0 & 1 \end{bmatrix} \delta v = -P\vec{F} \quad (2.58)$$

where $\frac{\delta}{\delta x_i}$ corresponds to the discretization of $\frac{\partial}{\partial x_i}$ and the operator G corresponds to the discretization of the material derivative. According to the preceding section, $\left(\frac{D}{Dt}\right)^{-1} \circ \phi$ is equivalent to $S \circ \phi$. And $S \circ \phi$ can be approached by $\Delta t \phi$ with the second order accuracy. (See Lemma 8). As a result, the resolved equations suggested by this dissertation are given by:

$$\begin{bmatrix} 1 & b_{\frac{\delta}{\delta x_1}} & b_{\frac{\delta}{\delta x_2}} & b_{\frac{\delta}{\delta x_3}} & 0 \\ 0 & G & 0 & 0 & 0 \\ 0 & 0 & G & 0 & 0 \\ 0 & 0 & 0 & G & 0 \\ 0 & c_{\frac{\delta}{\delta x_1}} & c_{\frac{\delta}{\delta x_1}} & c_{\frac{\delta}{\delta x_1}} & G \end{bmatrix} \delta W_i = -P\vec{F} \quad (2.59)$$

and

$$\begin{bmatrix} \frac{1}{R}G - \Delta t b \frac{\delta}{\delta x_i} e \frac{\delta}{\delta x_i} & 0 & 0 & 0 & 0 \\ \Delta t e \frac{\delta}{\delta x_1} & 1 & 0 & 0 & 0 \\ \Delta t e \frac{\delta}{\delta x_2} & 0 & 1 & 0 & 0 \\ \Delta t e \frac{\delta}{\delta x_3} & 0 & 0 & 1 & 0 \\ -(\Delta t)^2 c \frac{\delta}{\delta x_i} e \frac{\delta}{\delta x_i} & 0 & 0 & 0 & 1 \end{bmatrix} \delta v = \delta W_i$$

Such a decomposition, essentially, is a fractional step procedure. The corresponding numerical procedure follows:

(New Fractional Step Method)

1: Solve equations

$$\vec{F}_1 = \frac{\delta \rho}{\delta t} + \frac{\delta(\rho u_j)}{\delta x_j} \quad (2.60)$$

$$\vec{F}_{i+1} = \frac{\delta(\rho u_i)}{\delta t} + \frac{\delta(\rho u_i u_j)}{\delta x_j} + \frac{\delta p}{\delta x_i} - \frac{\delta \sigma_{ij}}{\delta x_j} \quad (2.61)$$

$$\vec{F}_5 = \frac{\delta(\rho E)}{\delta t} + \frac{\delta[(\rho E + p)u_j]}{\delta x_j} - \frac{\delta(u_i \sigma_{ij})}{\delta x_j} + \frac{\delta q_j}{\delta x_j} \quad (2.62)$$

for the residual errors \vec{F} , where δ stands for the discretization of space and time. And then, calculate \vec{f} by $\vec{f} = P\vec{F}$. Decide to go to the next time step or not according to the modulus of \vec{f} .

2: Determine δW_2 , δW_3 and δW_4 by solving the equation

$$\begin{pmatrix} G & 0 & 0 \\ 0 & G & 0 \\ 0 & 0 & G \end{pmatrix} \begin{pmatrix} \delta W_2 \\ \delta W_3 \\ \delta W_4 \end{pmatrix} = \begin{pmatrix} -f_2 \\ -f_3 \\ -f_4 \end{pmatrix} \quad (2.63)$$

by using an iterative scheme, where G is the discretization of material derivative $\frac{D}{Dt}$.

3: Calculate δW_1 and δW_5 by

$$\delta W_1 = (-f_1 - b \frac{\delta}{\delta x_i} \delta W_i) \quad (2.64)$$

$$\delta W_5 = \Delta t (-f_5 - c \frac{\delta}{\delta x_i} \delta W_i) \quad (2.65)$$

4: Determine δP by solving the parabolic equation

$$\left(\frac{1}{R}G - b\Delta t \frac{\delta}{\delta x_i} e \frac{\delta}{\delta x_i}\right)\delta P = \delta W_1 \quad (2.66)$$

5: Calculate the velocity variance δu_i by

$$\delta u_i = \delta W_{i+1} - \Delta t e \frac{\delta}{\delta x_i} \delta P \quad (2.67)$$

6: Calculate the temperature variance δT by

$$\delta T = \delta W_5 + \Delta t^2 c \frac{\delta}{\delta x_i} e \frac{\delta}{\delta x_i} \delta P \quad (2.68)$$

7: Renew $u_i, p,$ and T with $u_i + \delta u_i, p + \delta P,$ and $T + \delta T$ respectively. And go back to step 1.

As a seven-step procedure, the resolution of step 2 and 4 requires some iterative procedures, but the rest can be solved by only one step. In step 2, since G is the material derivative, a small enough time step Δt can ensure diagonal dominance, which essentially guarantees the convergence of the iteration.

Considering that the determinant of the preconditioning matrix P is $\frac{R^4 T^5}{\bar{P}^4 C_v}$, which is bounded above and below for the turbulent boundary layer, the convergence of matrix $P\vec{F}$ is equivalent to the convergence of \vec{F} . In this sense, either \vec{F} or $P\vec{F}$ can be used to determine the stop of the iterative procedure in the step 1.

In the traditional fractional step method, the governing equation for the pressure correction is a Poisson equation as

$$\Delta \delta P = RHS \quad (2.69)$$

But in the compressible flow, shown by equation (2.66), it is a parabolic equation. Recall that $b = \frac{\hat{P}}{R} + \frac{\hat{P}}{C_v}$, $e = \frac{\hat{T}R}{\hat{P}}$ and $a = \frac{D}{RDt}$, equation (2.66) approximates:

$$\frac{D\delta P}{RDt} - \Delta t \left(\frac{\hat{P}}{R} + \frac{\hat{P}}{C_v}\right) \nabla \left(\frac{\hat{T}R}{\hat{P}} \nabla \delta P\right) = \delta P' \quad (2.70)$$

It can be reduced to

$$c_1 \frac{\partial \delta P}{\partial t} - \Delta \delta P - (\nabla \delta P) \cdot \left(\nabla \frac{\hat{T}R}{\hat{P}}\right) + c_1 (u \cdot \nabla) \delta P = c_2 \delta P' \quad (2.71)$$

where $c_1 = \frac{C_v}{\hat{P}(R+C_v)\Delta t}$ and $c_2 = \frac{RC_v}{\hat{P}(R+C_v)\Delta t}$.

2.5 Validation of Numerical Method

In order to demonstrate this numerical method, the LES simulations of compressible turbulent boundary layers with or without heat transfer were obtained at several Mach numbers. The calculated Reynolds number was from approximately 1800 to 2200 in terms of inlet displacement thickness. The Prandtl number was 0.71.

A second-order central difference finite volume scheme was applied. The second-order Euler backward scheme was utilized for the time difference. A fully implicit scheme was implemented. The numerical procedure included two loops: a inner loop and an outer loop.

A recycling and rescaling inlet condition proposed by Lund *et al.* (1998) and Kong *et al.* (2000) was utilized for the velocities and temperature. The inlet pressure was extrapolated from the interior. On the upper boundary, pressure and temperature were specified as free stream. The numerical domain was $72\delta_d \times 32\delta_d \times 16\delta_d$ in the streamwise, normal and spanwise directions, respectively, where δ_d was the inlet displacement thickness. A $240 \times 80 \times 100$ numerical mesh, which was uniform in the streamwise and spanwise directions, was applied, where $\Delta y_{\min}^+ = 0.56$, $\Delta y_{\max}^+ = 65$.

A random function was used to generate the initial fluctuations. The Blasius profile was used as the initial mean profile. The characteristic boundary conditions proposed in this paper were applied at the outlet.

2.5.1 Case1: Adiabatic Turbulent Boundary Layer

The first case is a flow at a Mach number of 0.06, a level at which a traditional compressible scheme would experience very poor convergence or even divergence.

The first and second order statistics at $Re_d = 2000$ are shown in Fig.2.1 - 2.4. The results were compared with the DNS results calculated by Spalart (1988) and the experimental data reported by DeGraaff and Eaton (2000). Fairly good agreement of our LES results with previous data is achieved.

Figures 2.5 - 2.6 show the downward view of streamwise velocity contours at $Y^+ = 23$ and $Y^+ = 200$, respectively. Those plots illustrate the different turbulent structures existing at

different distances from the wall. At $Y^+ = 23$, the length of the streaky structure was about $10 \sim 15\delta_d$, and experiments by Smith *et al.* (1983) reported that the streaky structure extends over a streamwise distance of $\Delta L_x^+ > 1000$. In this case, $\Delta L_x^+ > 10\delta_d$. $Y^+ = 200$ is located in the logarithmic layer. In this region, the eddies are extended in the spanwise direction.

2.5.2 Case2: Turbulent Boundary Layer with Heat Transfer

In this case, a turbulent boundary layer developing over a heated wall was simulated. The non-dimensional wall temperature, T_{wall} , was fixed at 1.3. The calculated Mach number was 0.4. Wall properties were used to normalize the quantities. A density-weighted transformation proposed by Huang *et al.* (1993) was utilized to compute a modified velocity, which was

$$U_c = \sqrt{B}[\sin^{-1}(\frac{A+u}{D}) - \sin^{-1}(\frac{A}{D})]$$

where

$$A = q_w/\tau_w, \quad B = \frac{2C_{p\infty}T_w}{Pr_t}, \quad D = \sqrt{A^2 + B}$$

subscript $_w$ stands for the wall property, and subscript $_\infty$ stands for the free stream property. Figure 2.7 shows the comparison of the modified velocity U_c and u^+ with experimental results from an incompressible turbulent boundary layer. This figure verifies that in the heated boundary layer the velocity profiles are deformed due to the change of the density across the boundary layer. Such a deformation causes the u^+ to depart from the law of the wall. But the modified velocity U_c maintains the law of the wall for the incompressible flow. These numerical results match the theoretical and experimental conclusions of Huang *et al.* (1993).

The calculated mean temperature profile for the turbulent boundary layer with $T_w/T_\infty = 1.3$ is presented by Fig. 2.7 also. The square symbols indicate the empirical mean temperature profile suggested by Kadar (1981), which followed:

$$\theta^+ = Pr y^+ \exp(-\Gamma) + \{2.12 \ln[(1 + y^+) \frac{2.5(2 - y/\delta)}{1 + 4(1 - y/\delta)^2}] + \beta(Pr)\} \exp(-\Gamma)$$

where $\theta^+ = \frac{T_w - T}{t_f}$, $t_f = \frac{q_w}{\rho_w C_p u_\tau}$, and,

$$\Gamma = \frac{0.01(Pr y^+)^4}{1 + 5 Pr^3 y^+}, \quad \beta(Pr) = (3.85(Pr)^{-1/3} - 1.3)^2 + 2.12 \ln Pr$$

The present result agrees with the formula given by Kadar (1981) in the viscous sublayer and logarithmic layer.

Since the density and temperature varied with the distance from the wall, in order to describe the influence of the temperature on the statistics of the turbulent fluctuations, we normalized the rms of the streamwise velocity fluctuations in three different ways. Figure 2.8 shows the comparison of the rms of the streamwise velocity fluctuations. The results shown by the dash-double-dotted line were normalized by the wall properties, where $U_{rms}^+ = \frac{U_{rms}}{U_{\tau,w}}$ and $Y^+ = Y \frac{U_{\tau,w}}{\nu_w}$. It matches with the experimental data of DeGraaff and Eaton (2000), which were obtained in an incompressible flow, in the viscous sublayer region, but deviates in the buffer zone and the outer part of the turbulent boundary layer. The dash-dotted line results were normalized by the global properties, where $U_{rms}^+ = \frac{U_{rms}}{U_{\tau,\infty}}$, and $Y^+ = Y \frac{U_{\tau,\infty}}{\nu_\infty}$. This curve is close to experimental results of DeGraaff and Eaton (2000) in both the viscous sublayer and the outer part of turbulent boundary layer, but deviates in the buffer zone and the logarithmic layer region. The solid line results were normalized by the local properties. More precisely, $U_{rms}^+ = \frac{U_{rms}}{U_{\tau,local}}$ and $Y^+ = Y \frac{U_{\tau,local}}{\nu_{local}}$. These results give the best match with the peak value of the experimental data. By using the local properties, the U_{rms}^+ of the heated turbulent boundary layer collapses to the U_{rms}^+ of incompressible turbulent boundary layers.

The same turbulent boundary layer flow ($T_w/T_\infty = 1.3$) was also calculated by the LUSGS method of Xu *et al.* (2005). Figure 2.9 shows the comparison of the average residual errors vs the iteration number of pseudo-time step loops (or inner loop) by these two different schemes. The magnitude of the average residual errors drops down 3 orders in just 9 steps by the present fractional step scheme. But during these 9 steps, the decay in the order of the magnitude using the LUSGS scheme is no more than 2. The convergence history shows the superior performance of the fractional step numerical scheme for the simulation of the subsonic flows. But for each pseudo-time step, the present method will take roughly 60 percent more CPU time than the LUSGS scheme because of the extra CPU time required for the pressure solver.

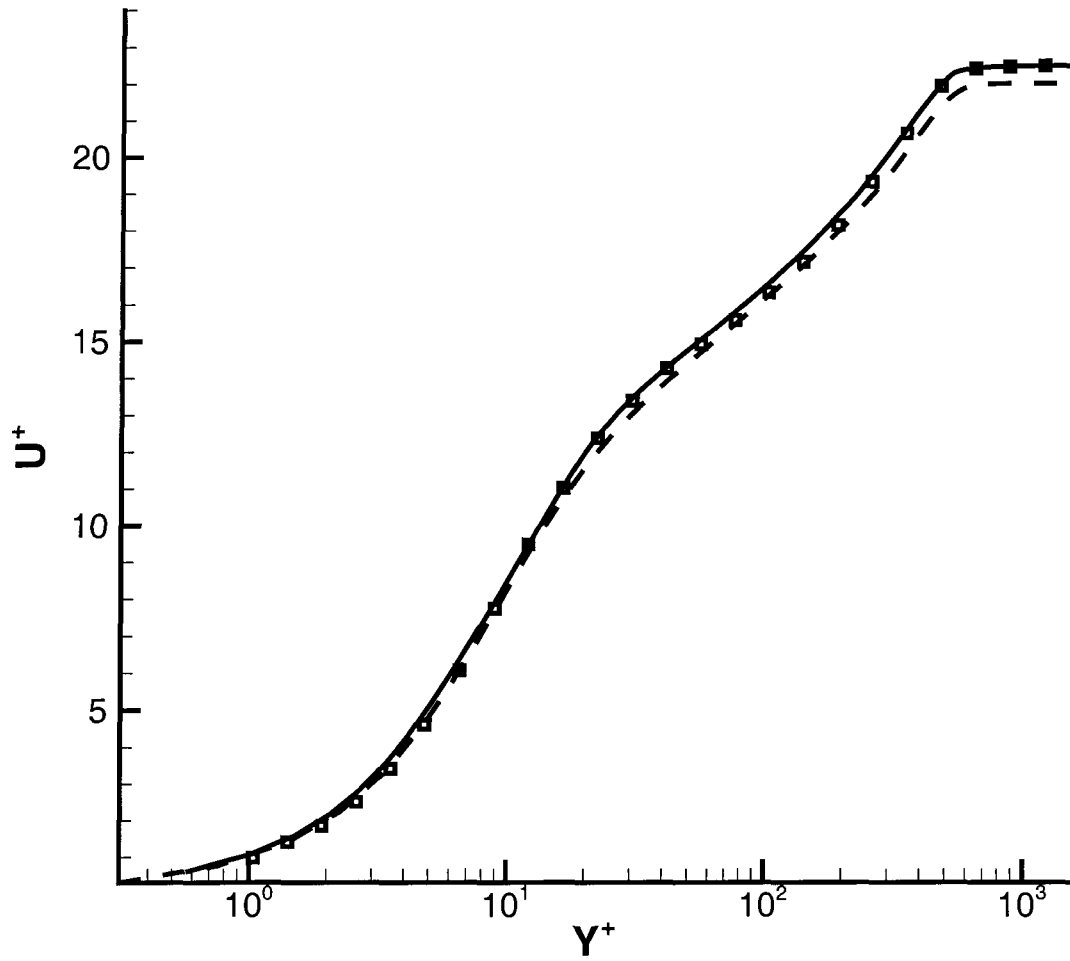


Figure 2.1 Comparison of mean velocity profile in a turbulent boundary layer $Re_{\delta_d} = 2000$ over an adiabatic wall : The solid line is LES results, the dashed line gives a DNS profile by Spalart (1988) and the square symbols are the experiment data by DeGraaff and Eaton (2000).

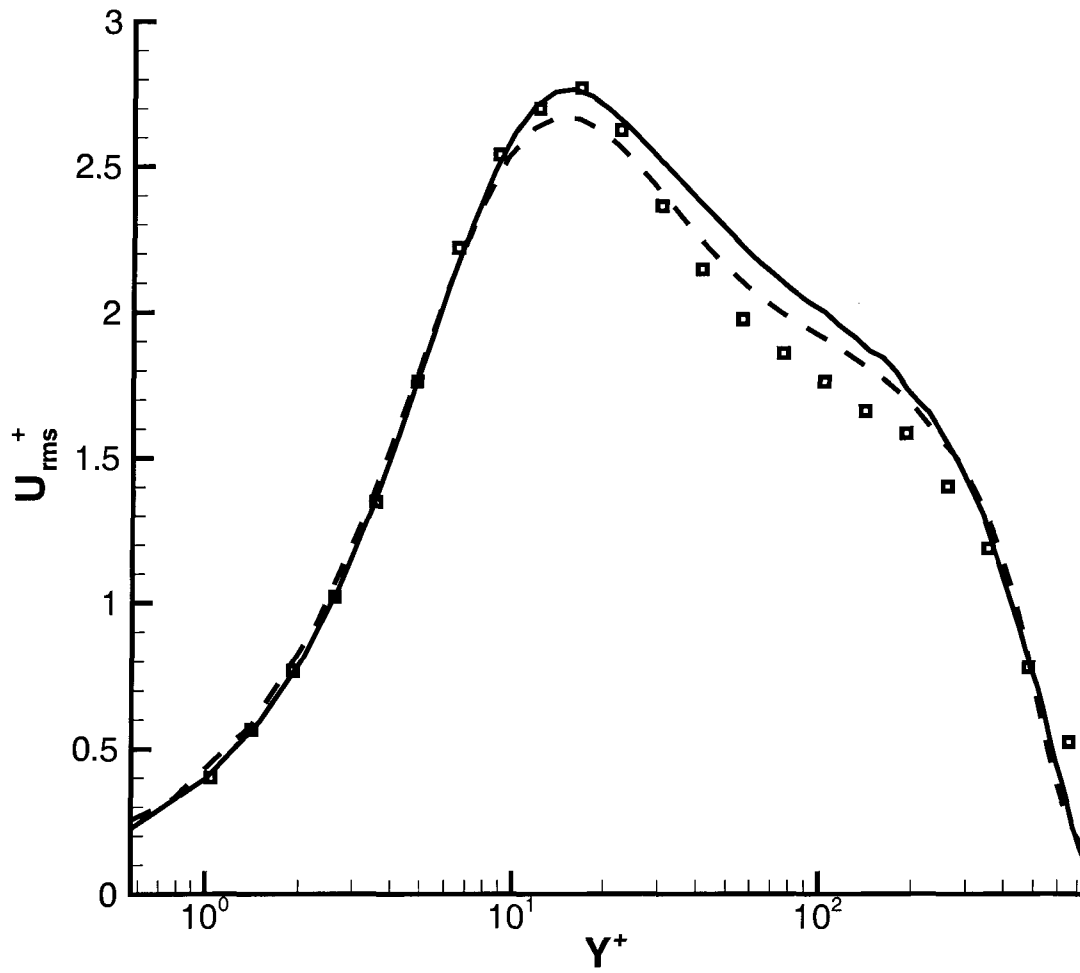


Figure 2.2 Comparison of rms of streamwise velocity profile in a turbulent boundary layer $Re_{\delta_d} = 2000$ over an adiabatic wall : The solid line is LES results, the dashed line gives a DNS profile by Spalart (1988), and the square symbols are the experimental data by DeGraaff and Eaton (2000).

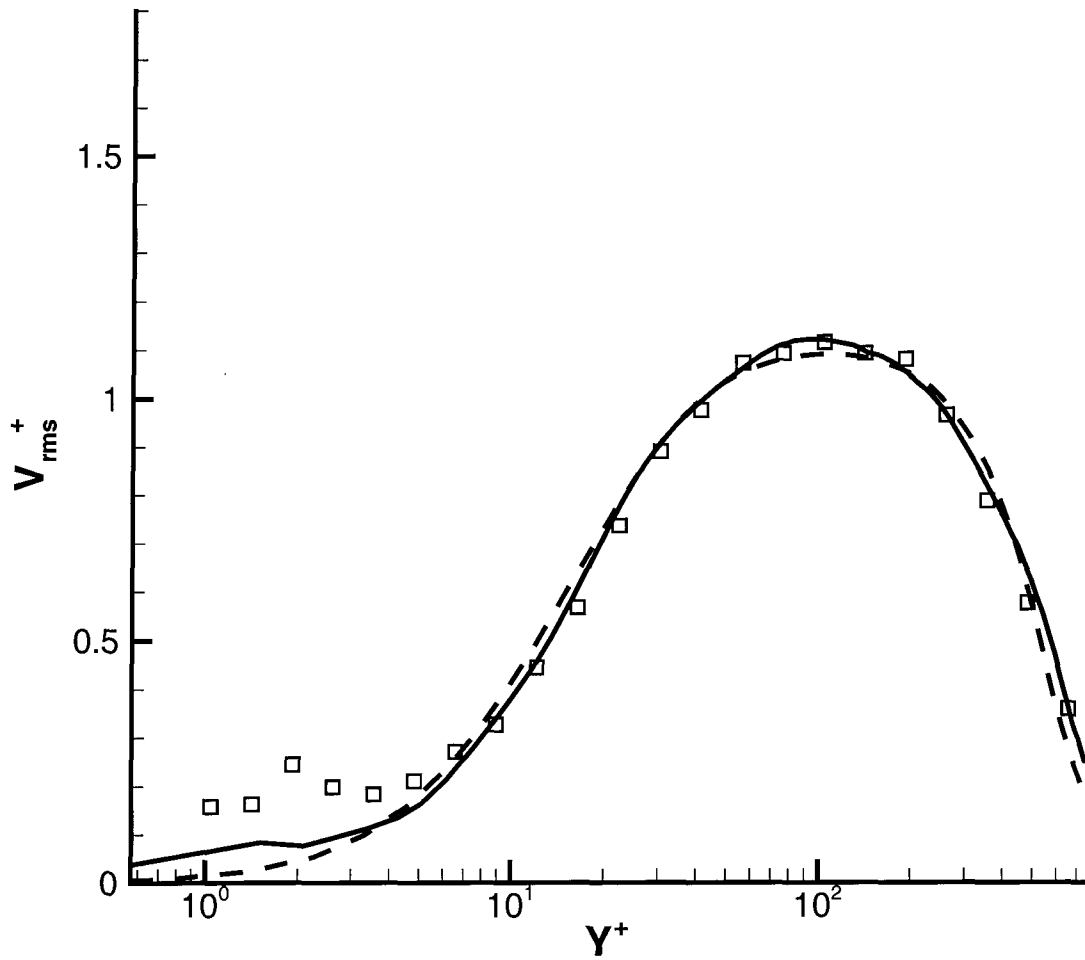


Figure 2.3 Comparison of rms of normal velocity profile in a turbulent boundary layer $Re_{\delta_d} = 2000$ over an adiabatic wall : The solid line is LES results, the dashed line gives a DNS profile by Spalart (1988), and the square symbols are the experimental data by DeGraaff and Eaton (2000).

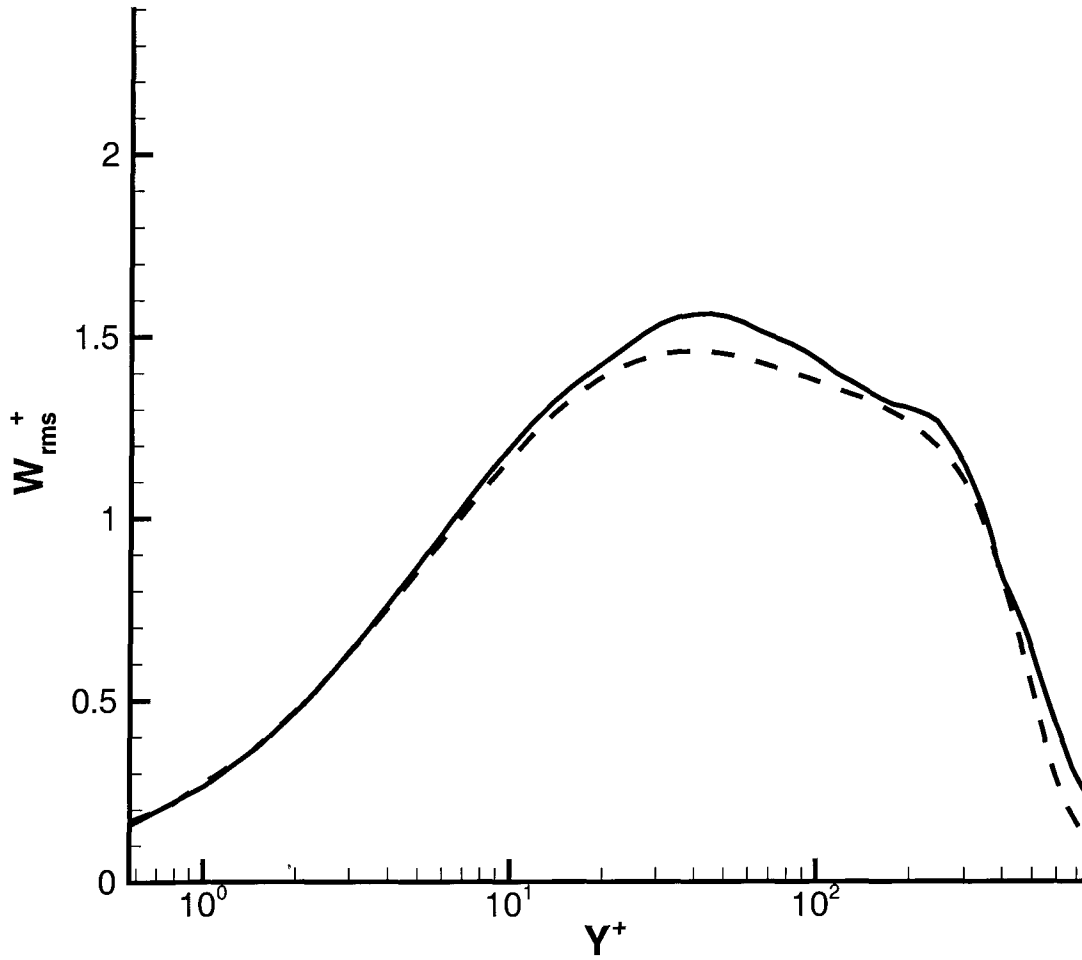


Figure 2.4 Comparison of rms of normal velocity profile in a turbulent boundary layer $Re_{\delta_d} = 2000$ over an adiabatic wall : The solid line is LES results, the dashed line gives a DNS profile by Spalart (1988).

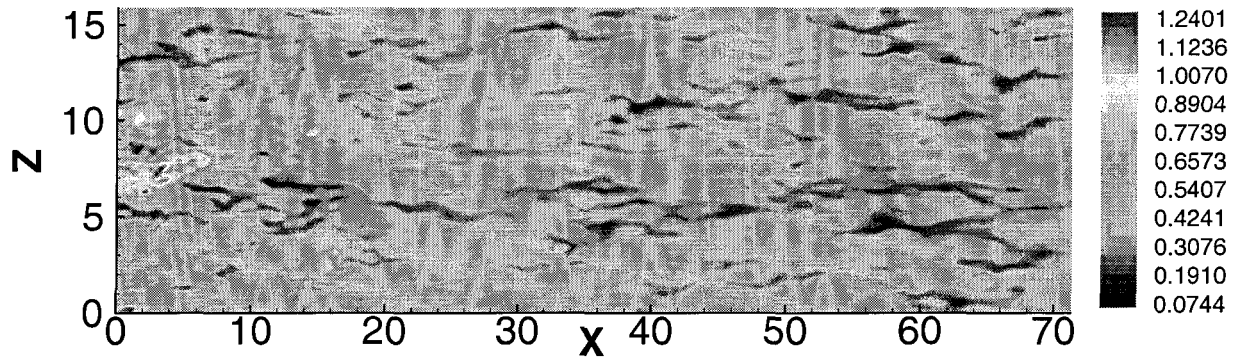


Figure 2.5 The downward view of streamwise velocity contours at $Y^+ = 23$.

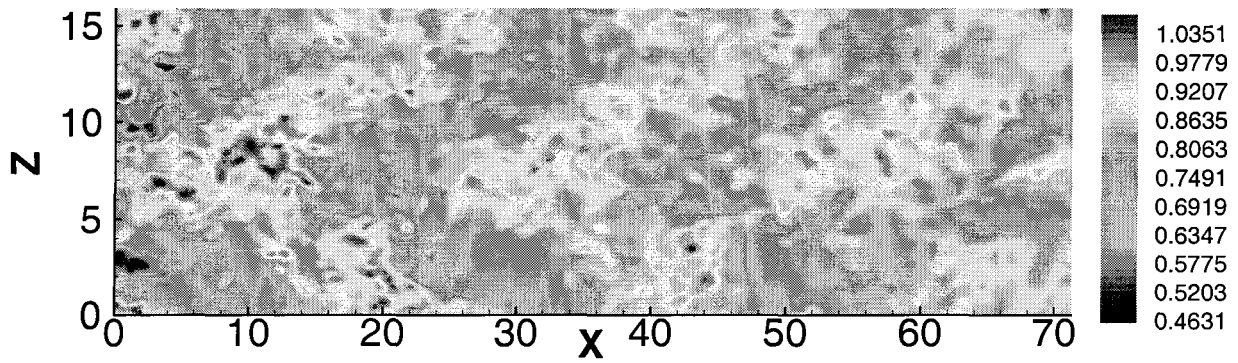


Figure 2.6 The downward view of streamwise velocity contours at $Y^+ = 200$.

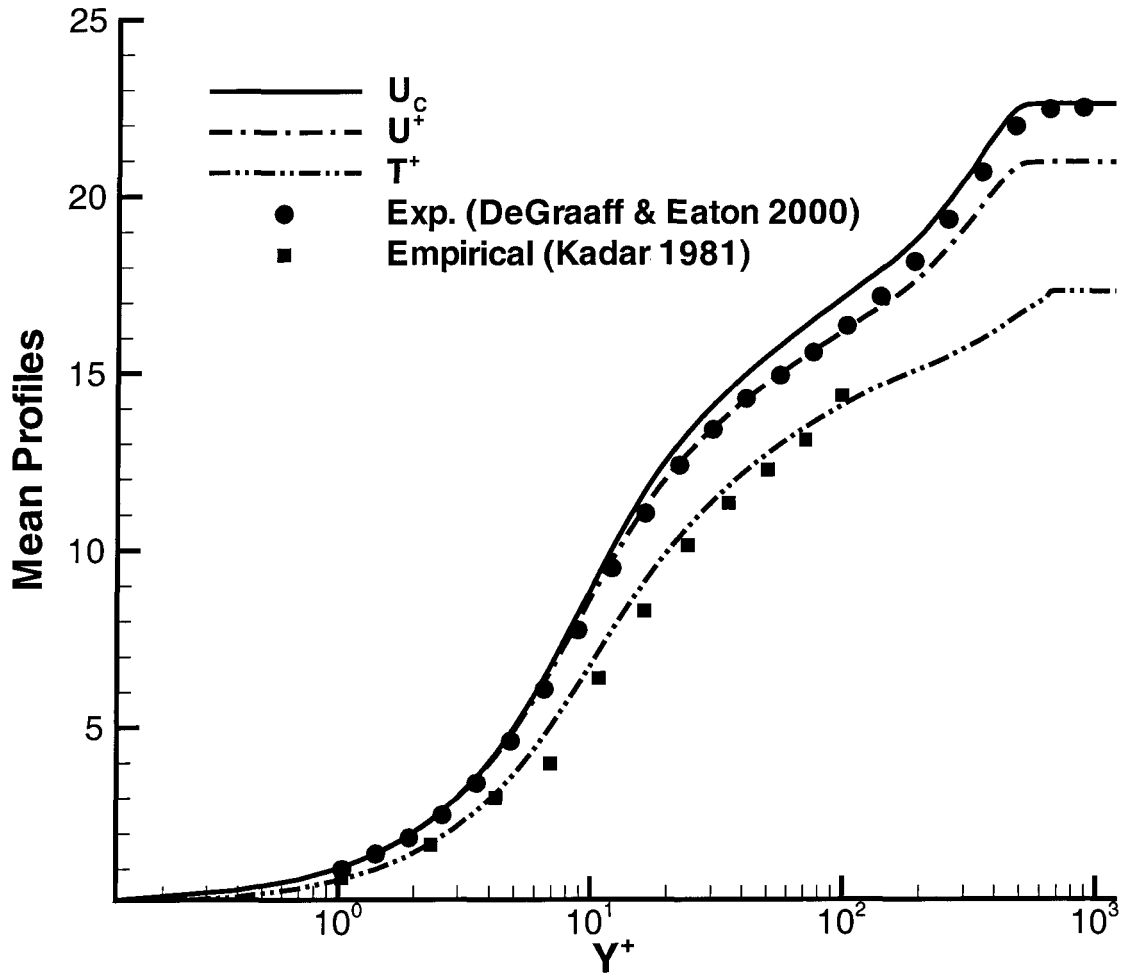


Figure 2.7 Mean velocity and temperature profiles in the heated turbulent boundary layer, $T_{wall} = 1.3$. The square symbols are the velocity profile of incompressible turbulent boundary layer by DeGraaff and Eaton (2000), and the circle symbols are the empirical temperature results suggested by Kadar (1981).

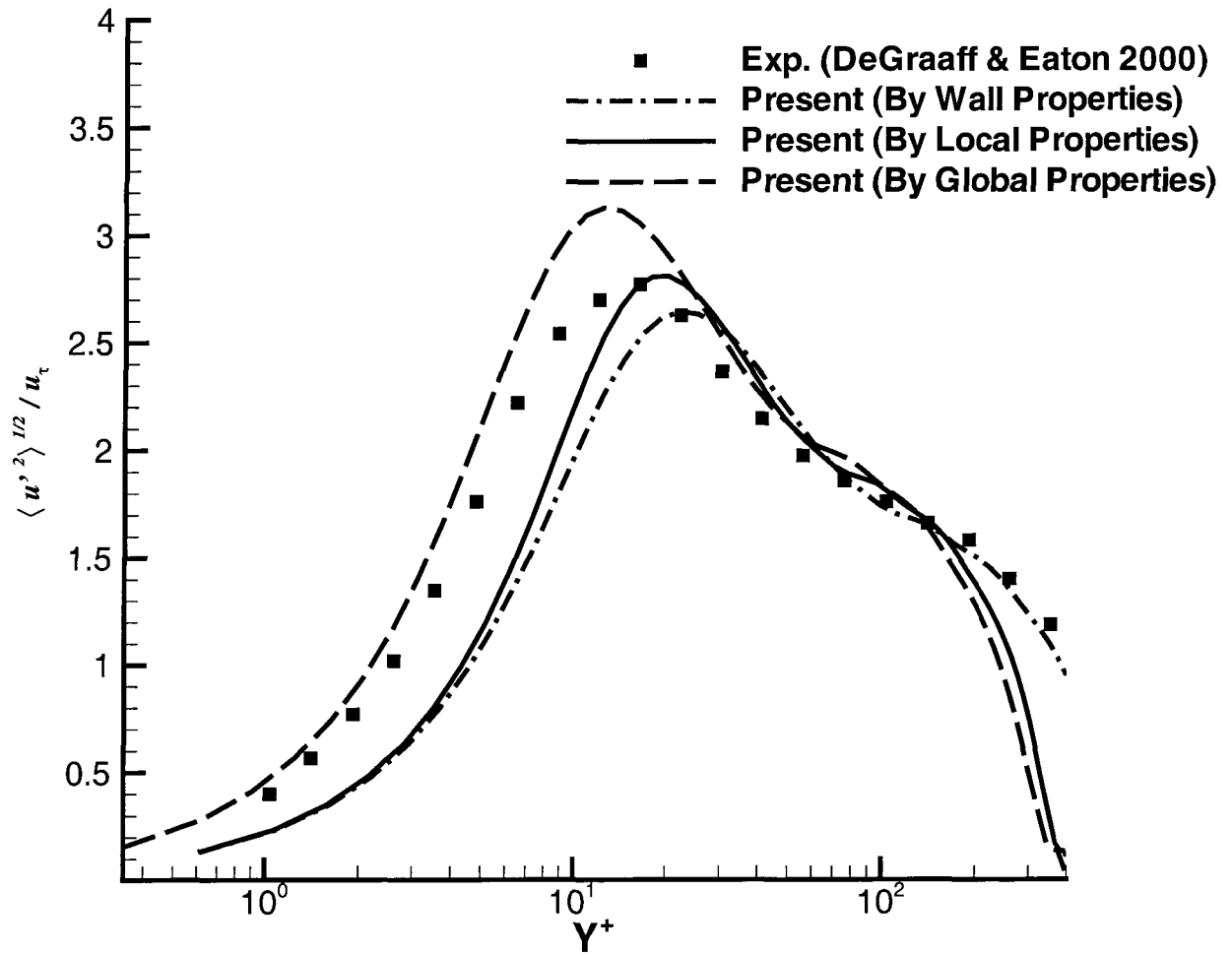


Figure 2.8 RMS fluctuation profiles of an heated turbulent boundary layer, $T_{wall} = 1.3$. The circle symbols are the experimental data of the incompressible turbulent boundary layer by DeGraaff and Eaton (2000).

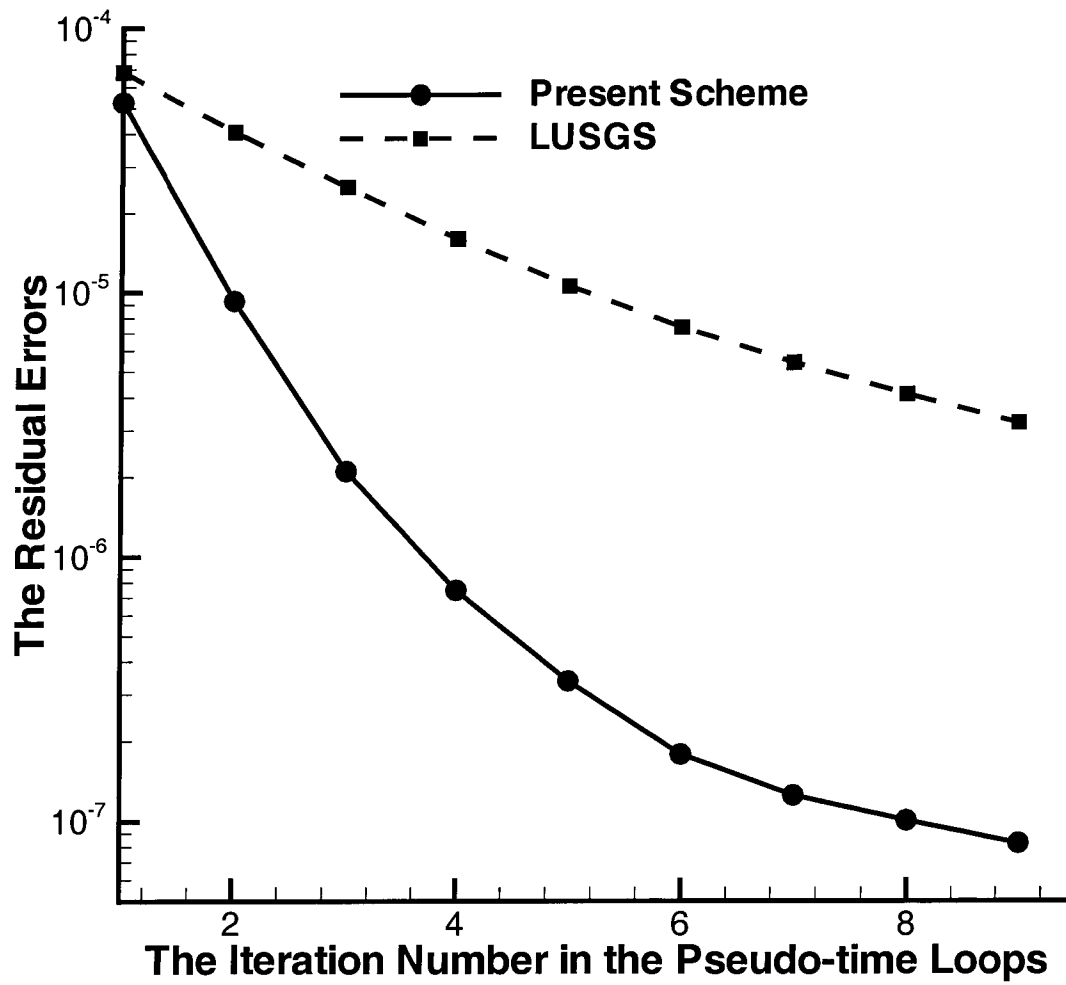


Figure 2.9 Convergence history of residual errors vs iteration steps in the pseudo-time loops. $T_{wall} = 1.3$, The solid line is the convergence history by the present scheme and dashed line is by the LUSGS scheme.

CHAPTER 3. BOUNDARY CONDITIONS

3.1 Introduction

The simulation of turbulent boundary layers require quite demanding inflow information since the resolved flow is unsteady and three-dimensional. Rather than simulating laminar and transitional regions arising near a leading edge, it is often more computational efficient to formulate a fully turbulent inflow condition. To date, three types of methods for creating appropriate inflow conditions have been suggested: the random fluctuation method (Rai and Moin (1993)), the matching database method (Schlüter *et al.* (2003)), and the recycling and rescaling method (Spalart (1988) and Lund *et al.* (1998)). The classification of those methods is based on their different treatment of the mean profile and fluctuations at inflow. Among those methods, the recycling method is the most efficient procedure to establish a turbulent shear flow with a fairly short inlet buffer zone and accurate downstream profiles.

The recycling method was introduced by Spalart (1988). Lund *et al.* (1998) further developed this concept, and introduced a rescaling idea. In their implementation, instantaneous profiles at a specific station were recycled to the inlet at each numerical step after rescaling. This rescaling was based on the similarity laws of the boundary layer: the law of the wall in the inner part and the defect law in the outer part of boundary layer.

However, for a simulation not starting from proper initial conditions, the rescaling treatment may lead to a decrease of skin friction (Spille-Kohoff and Kaltenbach (2001)) with increasing time. This results from the coupling of the initial and inflow conditions. To avoid this, Lund *et al.* (1998) suggested making a correction to the resolved velocities during the early part of simulation. Spille-Kohoff and Kaltenbach (2001) suggested adding a source term to the resolved equation based on the desired Reynolds stress.

This chapter proposes an advance to the method of Lund *et al.* (1998) for the simulation of turbulent boundary layers subjected to zero pressure gradient. In the present method, the recycle plane is dynamically selected according to the downstream instantaneous field. And Lund *et al.* (1998)'s rescaling method is modified according to the dissipation of the scheme and modeling. With this inlet generation technique, the first and second order statistics compare well with recent experimental and DNS results.

In order to control the numerical instability and the spurious wave reflections at the numerical boundaries, new characteristic boundary conditions consistent with this method are formulated.

3.2 A Dynamic Recycling Inflow Condition

The rescaling method has a weak point: initial and inflow conditions are coupled. That is, it is difficult to rapidly generate correct downstream turbulence to use for recycling if the initial inflow conditions are not accurate.

By the recycling, the downstream profiles are reloaded to the inlet; this procedure will couple the initial and inflow conditions in the early part of the simulation. If the initial condition is not well posed, the interior Reynolds stress may continuously decay. This tendency toward decay is hard to remedy by the above rescaling treatment. Moreover, if the initial condition is not proper, i.e. the correct large eddies have not been produced in interior flows at the right time, the mean profiles and velocity rms profiles may not be correct. Hence similarity laws cannot be applied. The method of Lund *et al.* (1998), which is based on an assumption that the recycling profile and the inflow profile data satisfy the similarity law, will then fail. In our numerical work, we found that the coupling of initial and inflow condition certainly results in the decay of skin friction. This decay is encountered at the early part of the simulation.

Thus, the rescaling method proposed by Lund *et al.* is a promising candidate, but needs to be modified in the early part of the simulation.

The convective speed of turbulent structures in the turbulent boundary layer with zero pressure gradient varies with the distance from the wall, and this speed is roughly proportional

to the streamwise velocity. Therefore, the fluid structures generated by inflow conditions will take some time to reach the recycling plane. Our numerical results show that the structures evolving from the initial condition tend to decay, but the structures produced by the rescaled inflow conditions keep the balance of turbulent production and dissipation quite well. Thereby, in order to efficiently and accurately establish the turbulent boundary layer, we suggest to dynamically select the recycling plane so that the recycling plane is kept within the turbulent region produced by inflow condition as early as possible. The proposed recycling plane is located by:

$$X_2 = X_1 + \min(X_{tag} - X_1, \alpha U_b \max(0, (t - t_0))) \quad (3.1)$$

where X_2 is the recycling location, X_{tag} is the desired recycling station when the numerical domain is occupied by the turbulent structures produced by the inlet conditions, X_1 is the starting location, t is non-dimensional time, U_b is the bulk velocity, which is an average velocity across the boundary layer, and t_0 is the time at which the leading edge of the convected flow generated at the inlet reaches station X_1 . Equation (3.1) indicates that the recycling plane stays at station X_1 from $t = 0$ up to $t = t_0$, at which time the structures generated by inlet conditions are supposed to pass through station X_1 except for the viscous sublayer, and then the recycling plane moves downstream with the speed αU_b until it reaches the desired recycling station X_{tag} . After that, the recycle plane will remain there for the rest of the calculation. The purpose of this is to keep the recycling plane inside the convective region generated by the inflow condition to achieve accurate first and second order statistics. In our simulation, $X_1 = 10\delta_d$, $\alpha = 0.5$, and, $t_0 = 10$.

Guarini *et al.* (2000)'s two-point correlation analysis shows that if the recycling station is far away from the inlet, the recycled profiles will be independent of the inlet profiles. This feature enables us to set up an inlet condition based on the recycling of downstream profiles without breaking up the fast moving or slow moving structures by keeping the recycling plane some distance from the inlet. Experiments conducted by Smith *et al.* (1983) observed that the streaky structure extends over a streamwise distance of $\Delta L_x^+ > 1000$, and Iritani *et al.* (1985) found that the thermal streaky structure extends over a streamwise distance of $\Delta L_x^+ > 1000$

also. Those studies implied that keeping a large enough distance is necessary when recycling. Thus, we start the recycling from the station X_1 , but not from the inlet.

3.2.1 The Inflow Conditions

The proposed inflow conditions follow:

$$U_{inlt}^{inner}(y_{inlt}^+) = \gamma U_{recy}(y_{inlt}^+) + \gamma_1 U'_{recy}(y_{inlt}^+, z, t) \quad (3.2)$$

$$T_{inlt}^{inner}(y_{inlt}^+) = \gamma T_{recy}(y_{inlt}^+) + \gamma_1 T'_{recy}(y_{inlt}^+, z, t) + T_{w,inlt} - \gamma T_{w,recy} \quad (3.3)$$

$$U_{inlt}^{outer}(\eta_{inlt}) = \gamma U_{recy}(\eta_{inlt}) + \gamma_1 U'_{recy}(\eta_{inlt}, z, t) + (1 - \gamma)U_{ref} \quad (3.4)$$

$$T_{inlt}^{outer}(\eta_{inlt}) = \gamma T_{recy}(\eta_{inlt}) + \gamma_1 T'_{recy}(\eta_{inlt}, z, t) + (1 - \gamma)T_{ref} \quad (3.5)$$

$$V_{inlt} = V_{recy} \quad W_{inlt} = W_{recy} \quad (3.6)$$

where $\gamma = \frac{U_{\tau,inlt}}{U_{\tau,recy}}$ and $\gamma_1 = 1$. Since Lund *et al.* (1998) applied a fixed recycling plane, γ is a function of distance between the recycling station and inlet, which is fixed. Thus, we suggest the following way to evaluate γ : when the recycling plane is moving, $U_{\tau,inlt}$ is calculated step by step, and $U_{\tau,recy}$ is assigned to be the desired inlet skin friction velocity. When the recycling plane reaches the desired station, Lund *et al.* (1998)'s γ is applied. Our numerical simulation shows that the recycling and rescaling over a long period of time may lead to incorrect levels of rms fluctuations. Since the dissipation in the numerical simulation contains three parts: viscous dissipation, the numerical dissipation and modeling dissipation, this feature may result from modeling, the numerical scheme or both. We find that a well-chosen γ_1 can work as a remedy. We tested different values of γ_1 , including $\gamma_1 = \gamma$. Our practices show that, when $\gamma_1 = 1$, the rms profiles match with DeGraaff and Eaton (2000)'s experiments better for the fully implicit LES scheme.

Since the law of the wall is only valid in the inner part of boundary layers and the defect law is only valid in the outer part, an improper weighting function may deform the profiles and cause the inflow rescaling to fail. Considering that the law of the wall and the defect law overlap in the logarithmic layer, we suggest the following weighting function:

$$W(y^+) = 1.0, \quad \text{when } y^+ < 50$$

$$W(y^+) = \frac{1}{2} [1.0 - \tanh(\frac{a(q-b)}{(1.0-2b)q+b}) / \tanh(a)], \quad \textit{otherwise}$$

$$W(y^+) = 0, \quad \textit{when } y^+ > 300$$

where $a = 0.5$, $b = 0.4$ and $q = (y^+ - 50)/(250)$. The above weighting function maintains the law of the wall or the defect law for $y^+ < 50$ or $y^+ > 300$, respectively. Only in the logarithmic region are the profiles composite.

3.3 Characteristic Boundary Conditions

An early chapter described a new fractional-step method for the simulation of the compressible Navier-Stokes equations. A corresponding boundary condition associated with this numerical method should be constructed. In the simulation of compressible flows, the characteristic boundary condition proposed by Poinso and Lele (1992) has been widely utilized. It has been shown to be remarkably effective in the control of numerical instability and the spurious wave reflections at the computational boundary. But the traditional characteristic boundary condition needs to be improved as long as preconditioning is applied because the preconditioning matrix changes the eigenvalues and eigenvectors. In the present section, we propose a new characteristic boundary condition for the present numerical method.

Now, let us consider a boundary located at $x_1 = L$. Multiplying the governing equations (2.3)-(2.5) by the preconditioning matrix (2.32), yields

$$\frac{\partial W}{\partial t} + A \frac{\partial W}{\partial x_1} + B \frac{\partial W}{\partial x_2} + C \frac{\partial W}{\partial x_3} - Vis. = 0$$

where $Vis.$ is the viscous term, $W = [\bar{P}, \tilde{u}_1, \tilde{u}_2, \tilde{u}_3, \tilde{T}]^{-1}$,

$$A = \begin{pmatrix} \frac{\tilde{u}_1}{\bar{R}} & \frac{\bar{P}}{\bar{R}} + \frac{\bar{P}}{C_v} & 0 & 0 & 0 \\ \frac{\tilde{T}\bar{R}}{\bar{P}} & \tilde{u}_1 & 0 & 0 & 0 \\ 0 & 0 & \tilde{u}_1 & 0 & 0 \\ 0 & 0 & 0 & \tilde{u}_1 & 0 \\ 0 & \frac{\tilde{T}\bar{R}}{C_v} & 0 & 0 & \tilde{u}_1 \end{pmatrix}$$

and

$$B = \begin{pmatrix} \frac{\tilde{u}_2}{R} & 0 & \frac{\bar{P}}{R} + \frac{\bar{P}}{C_v} & 0 & 0 \\ 0 & \tilde{u}_2 & 0 & 0 & 0 \\ \frac{\tilde{T}R}{\bar{P}} & 0 & \tilde{u}_2 & 0 & 0 \\ 0 & 0 & 0 & \tilde{u}_2 & 0 \\ 0 & 0 & \frac{\tilde{T}R}{C_v} & 0 & \tilde{u}_2 \end{pmatrix}, \quad C = \begin{pmatrix} \frac{\tilde{u}_3}{R} & 0 & 0 & \frac{\bar{P}}{R} + \frac{\bar{P}}{C_v} & 0 \\ 0 & \tilde{u}_3 & 0 & 0 & 0 \\ 0 & 0 & \tilde{u}_3 & 0 & 0 \\ \frac{\tilde{T}R}{\bar{P}} & 0 & 0 & \tilde{u}_3 & 0 \\ 0 & 0 & 0 & \frac{\tilde{T}R}{C_v} & \tilde{u}_3 \end{pmatrix}$$

Referring to appendix A, the eigenvalues of A follows:

$$\lambda_1 = [\tilde{u}_1(1+R) - \sqrt{\tilde{u}_1^2(R-1)^2 + 4R^2\tilde{T}(1 + \frac{R}{C_v})}]/(2R)$$

$$\lambda_2 = [\tilde{u}_1(1+R) + \sqrt{\tilde{u}_1^2(R-1)^2 + 4R^2\tilde{T}(1 + \frac{R}{C_v})}]/(2R)$$

$\lambda_3 = \tilde{u}_1$, $\lambda_4 = \tilde{u}_1$, and $\lambda_5 = \tilde{u}_1$. Define a 5×5 diagonal matrix Λ by

$$\Lambda = \text{diag}[\lambda_1, \lambda_2, \lambda_3, \lambda_4, \lambda_5]$$

Thereby, A can be split as

$$A = Q\Lambda P$$

where

$$Q = \begin{pmatrix} q_{11} & q_{12} & 0 & 0 & 0 \\ q_{21} & q_{22} & 0 & 0 & 0 \\ 0 & 0 & 1 & 0 & 0 \\ 0 & 0 & 0 & 1 & 0 \\ 1 & 1 & 0 & 0 & 1 \end{pmatrix}, \quad P := Q^{-1} = \begin{pmatrix} p_{11} & p_{12} & 0 & 0 & 0 \\ p_{21} & p_{22} & 0 & 0 & 0 \\ 0 & 0 & 1 & 0 & 0 \\ 0 & 0 & 0 & 1 & 0 \\ p_{51} & p_{52} & 0 & 0 & 1 \end{pmatrix}$$

The definitions of the entries are given by appendix A.

If we denote $\Lambda P \frac{\partial W}{\partial x_1}$ by L_i , it yields

$$L_1 = \lambda_1(p_{11} \frac{\partial \bar{P}}{\partial x_1} + p_{12} \frac{\partial \tilde{u}_1}{\partial x_1}) \quad (3.7)$$

$$L_2 = \lambda_2(p_{21} \frac{\partial \bar{P}}{\partial x_1} + p_{22} \frac{\partial \tilde{u}_1}{\partial x_1}) \quad (3.8)$$

$$L_3 = \lambda_3 \frac{\partial \tilde{u}_2}{\partial x_1} \quad (3.9)$$

$$L_4 = \lambda_4 \frac{\partial \tilde{u}_3}{\partial x_1} \quad (3.10)$$

$$L_5 = \lambda_5 \left(p_{51} \frac{\partial \bar{P}}{\partial x_1} + p_{52} \frac{\partial \tilde{u}_1}{\partial x_1} + \frac{\partial \tilde{T}}{\partial x_1} \right) \quad (3.11)$$

where L_i are the amplitude of the characteristic waves associated with each characteristic velocity λ_i . Unlike the traditional characteristic system, the propagation waves corresponding to L_1 and L_2 are not the acoustic waves any more. By using these L_i ,

$$A \frac{\partial W}{\partial x_1} = \begin{bmatrix} q_{11}L_1 + q_{12}L_2 \\ q_{21}L_1 + q_{22}L_2 \\ L_3 \\ L_4 \\ L_3 + L_4 + L_5 \end{bmatrix}$$

It is known that the upstream-propagating waves are associated with the negative eigenvalues, and the downstream-propagating waves are associated to the positive eigenvalues. In order to control the spurious wave reflection and achieve numerical stability, the forward scheme is recommended for the downstream-propagating waves and the backward scheme is recommended for the upstream-propagating waves. Without loss of generality, assume $\lambda_1 \leq 0$ and $\lambda_2 \geq 0$. Thus,

$$L_1 = \lambda_1 \left(p_{11} \frac{\bar{P}_{I+1,j,k} - \bar{P}_{I,j,k}}{\Delta x_1} + p_{12} \frac{\tilde{u}_{1I+1,j,k} - \tilde{u}_{1I,j,k}}{\Delta x_1} \right)$$

and

$$L_2 = \lambda_2 \left(p_{21} \frac{\bar{P}_{I,j,k} - \bar{P}_{I-1,j,k}}{\Delta x_1} + p_{22} \frac{\tilde{u}_{1I,j,k} - \tilde{u}_{1I-1,j,k}}{\Delta x_1} \right)$$

Since the numerical boundary condition must be given in order to calculate L_i , Poinso and Lele (1992) suggested a series of methods to evaluate those L_i . But those need to be modified since the preconditioning is applied.

3.3.1 Outlet Characteristic Boundary Conditions For Subsonic Flows

We discuss the outlet boundary condition for the subsonic flows here. Clearly, λ_2 , λ_3 , λ_4 , and, λ_5 are positive. Hence, L_2 , L_3 , L_4 , and, L_5 are calculated by a backward difference. But

L_1 must be specified. Poinso and Lele (1992) suggested applying

$$L_1 = \sigma(1 - M^2)(P - P_\infty)c/L$$

where M is the maximum Mach number in the flow, c is the acoustic speed, L is the characteristic size of the domain, and σ is a constant. Clearly, the transfer of numerical information in the system with preconditioning is not carried by the acoustic waves, but by a upstream-propagating wave with an eigenvalue λ_1 satisfying $|\lambda_1| < |\tilde{u}_1 - c|$. Hence, directly using the L_1 proposed by Poinso and Lele (1992) in this system will overestimate the speed of upstream-propagating waves. Certainly, it is not an optimum choice for the compressible system with preconditioning. For the subsonic flow, $R = \frac{\gamma}{M_\infty^2} > 1$,

$$\begin{aligned} \lambda_1 &= [\tilde{u}_1(1+R) - \sqrt{\tilde{u}_1^2(R-1)^2 + 4R^2\tilde{T}(1 + \frac{R}{C_v})}]/(2R) \\ &= \frac{\frac{\tilde{u}_1^2}{R} - \tilde{T}(1 + \frac{R}{C_v})}{\tilde{u}_1(\frac{1+R}{2R}) + \sqrt{\tilde{u}_1^2(\frac{R-1}{2R})^2 + \tilde{T}(1 + \frac{R}{C_v})}} \\ &= -\frac{\tilde{T}(1 + \frac{R}{C_v})}{\tilde{u}_1(\frac{1+R}{2R})} \left[\frac{1 - \frac{\tilde{u}_1^2 C_v}{\tilde{T}R(C_v+R)}}{1 + \sqrt{1 + \tilde{T}(1 + \frac{R}{C_v})/[\tilde{u}_1^2(\frac{R-1}{2R})^2]}} \right] \\ &= -2\alpha \frac{\tilde{T}(C_v+R)R}{\tilde{u}_1(1+R)C_v} \end{aligned}$$

where $\alpha \in (0, 1)$. We therefore suggest that

$$L_1 = \frac{\sigma(1 - M^2)(P - P_\infty) \tilde{T}^\infty(C_v+R)R}{L \tilde{u}_1^\infty(1+R)C_v}$$

where \tilde{u}_1^∞ is the free-stream nondimensional velocity and \tilde{T}^∞ is the free stream temperature. σ is suggested to be 0.25.

3.4 Results And Conclusions

A second-order central difference finite volume scheme was utilized. The time difference was represented by a second-order Euler backward scheme. A fully implicit scheme was implemented. The numerical procedure included two loops: inner loop and outer loop, (or pseudo time step and physical time step). Newton iteration was applied in the inner loop. We use

random fluctuations as our initial fluctuation field and the Blasius profile as our initial mean profile. The dynamic recycling method was utilized as the inflow condition. The characteristic boundary condition proposed in this chapter was applied at the outflow boundary. A dynamic subgrid-scale model proposed for compressible turbulence by Moin *et al.* (1991) and recommended by Lilly (1992) was implemented.

For evaluating this inflow procedure, turbulent boundary layers ranging from $Re_d = 1850$ up to $Re_d = 2250$ were calculated, where Re_d is the Reynolds number based on displacement thickness. The numerical mesh was $280 \times 80 \times 120$ in the streamwise, normal and spanwise directions, respectively. The computational domain was $84 \times 30 \times 19.2$ in length normalized by the inlet displacement thicknesses. The Mach number was 0.06. The numerical time step was $0.2 \frac{\delta_d}{U_\infty}$. An adiabatic wall temperature condition was applied.

Figure 3.1 compares the LES rms results with DNS profiles obtained by Spalart (1988), and experimental profiles by DeGraaff and Eaton (2000). Figure 3.2 shows a comparison of the mean streamwise velocity profile with the same DNS data and experimental data. The agreement is generally good.

The comparison of skin friction is shown in Fig. 3.3. In this figure, the solid line was obtained by the method proposed in this dissertation, and the dashed line shows the results using the same rescaling treatment but with the fixed recycling station at the downstream $X = X_{tag}$, which is $40\delta_d$, and the empirical curve is the Ludwig-Tillmann correlation. Both the solid line and the dashed line are the average from $T = 100 \frac{\delta_d}{U_\infty}$ to $T = 300 \frac{\delta_d}{U_\infty}$. For the fully implicit scheme, the starting transient method proposed by Lund *et al.* (1998) does not work until $T = 500 \frac{\delta_d}{U_\infty}$. Fig. 3.4 shows that even when $T < 10 \frac{\delta_d}{U_\infty}$ the accurate skin friction was established at the region near to inlet. And it shows the evolution of skin friction by the present inflow methods at different times.

In conclusion, this proposed dynamic recycling procedure is able to establish the correct skin friction, and it is very efficient at reducing the starting transient. Furthermore, a change was made to Lund *et al.* (1998)'s inflow condition regarding the treatment of inflow fluctuations.

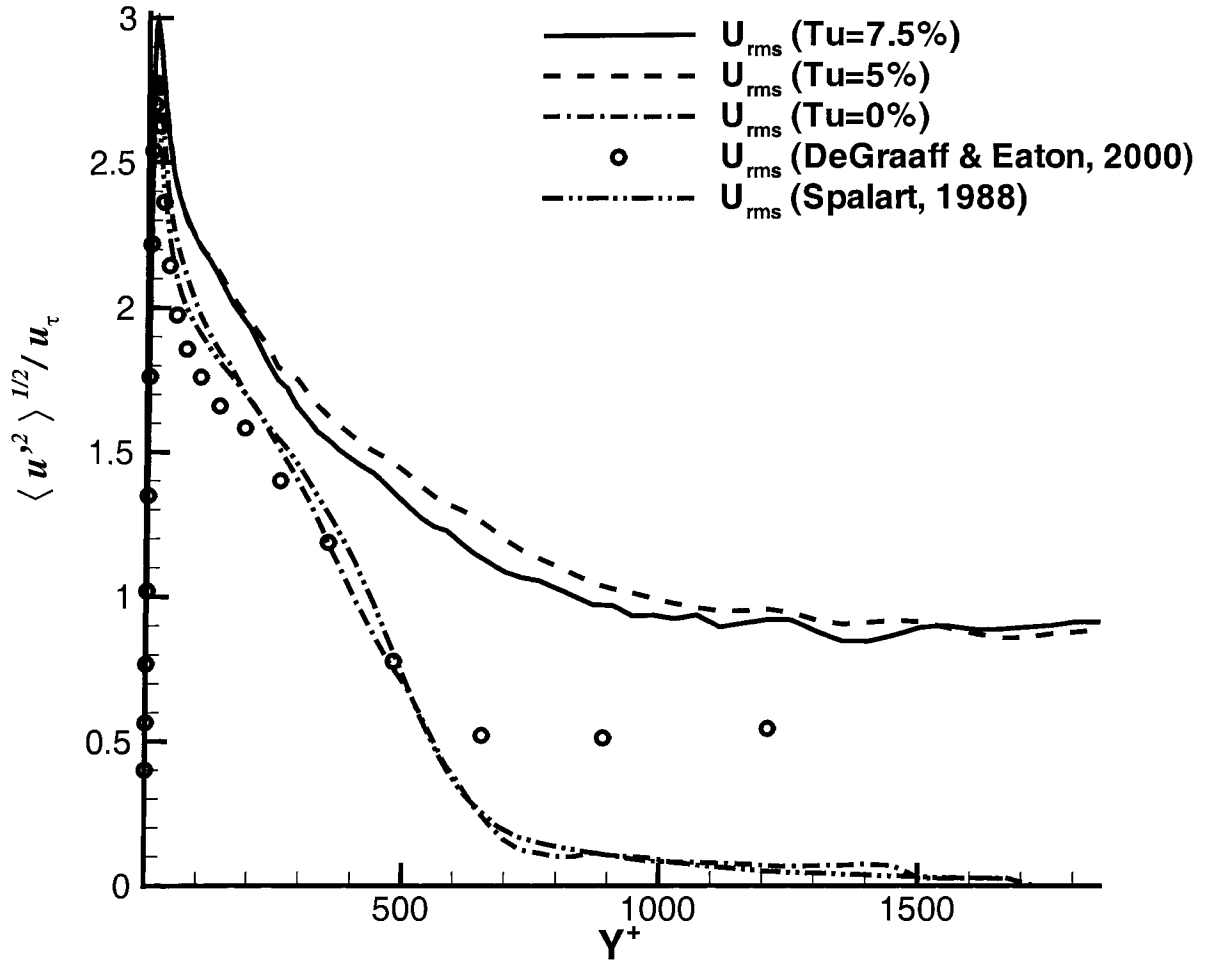


Figure 3.1 Comparison of rms profiles by present method in a turbulent boundary layer $Re_{\delta_d} = 2000$ and $T_w = T_{ref}$ with the DNS data reported by Spalart (1988) and the experimental data reported by DeGraaff and Eaton (2000).

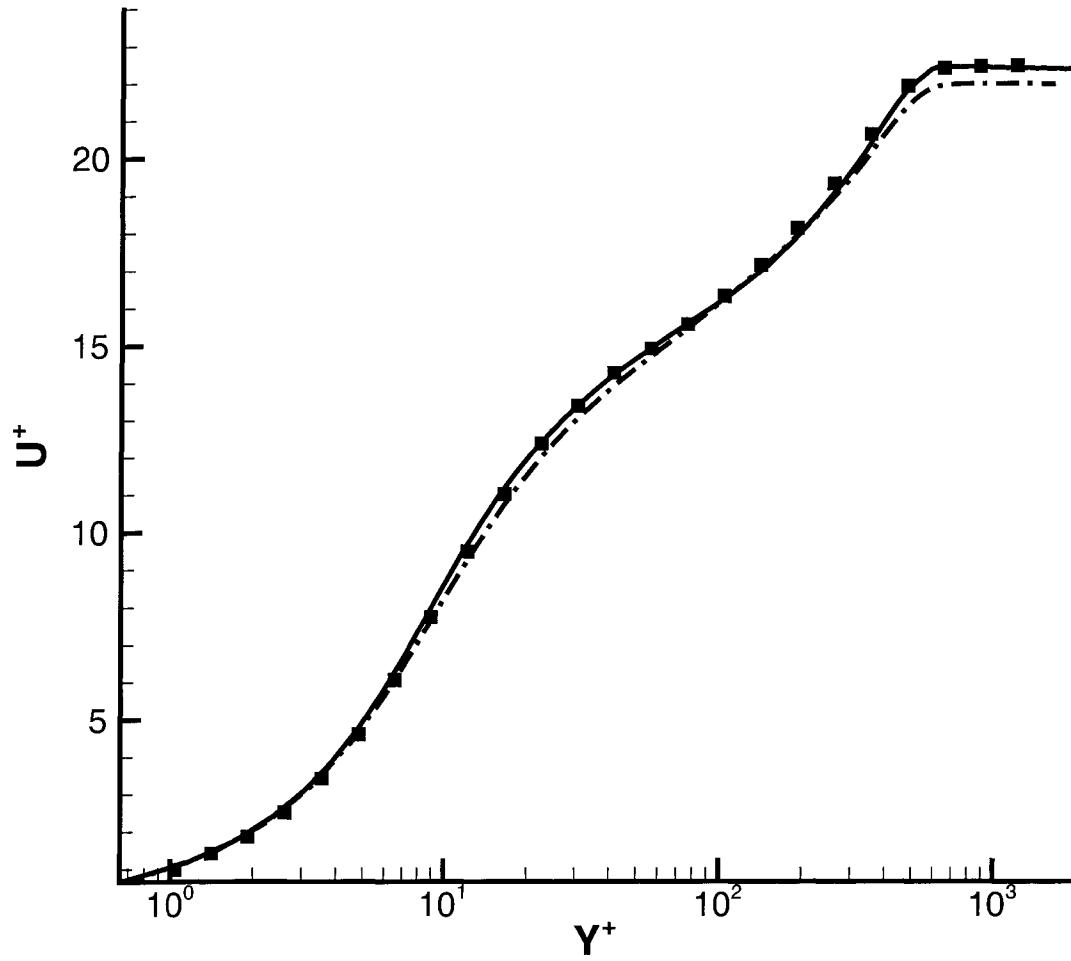


Figure 3.2 Comparison of mean streamwise velocity profiles in a turbulent boundary layer $Re_{\delta_d} = 2000$, $T_w = T_{ref}$: The solid line is LES results, the dashed line gives a DNS profile by Spalart (1988), and the square symbols are experimental data by DeGraaff and Eaton (2000).

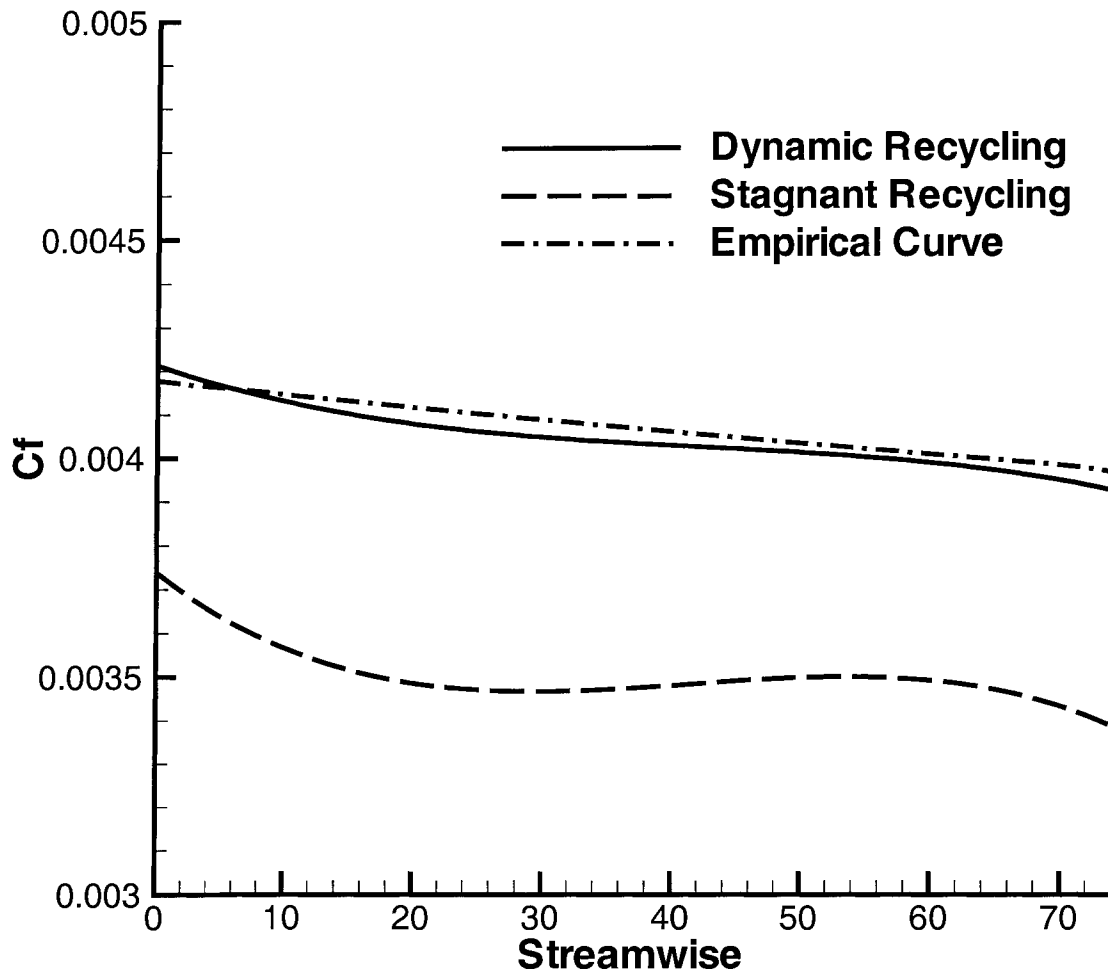


Figure 3.3 Evolution of skin friction: —, Recycling plane was dynamically chosen by equation (3.1), - - -, Recycling plane was fixed. — · —, Empirical curve is the Ludwig-Tillmann correlation.

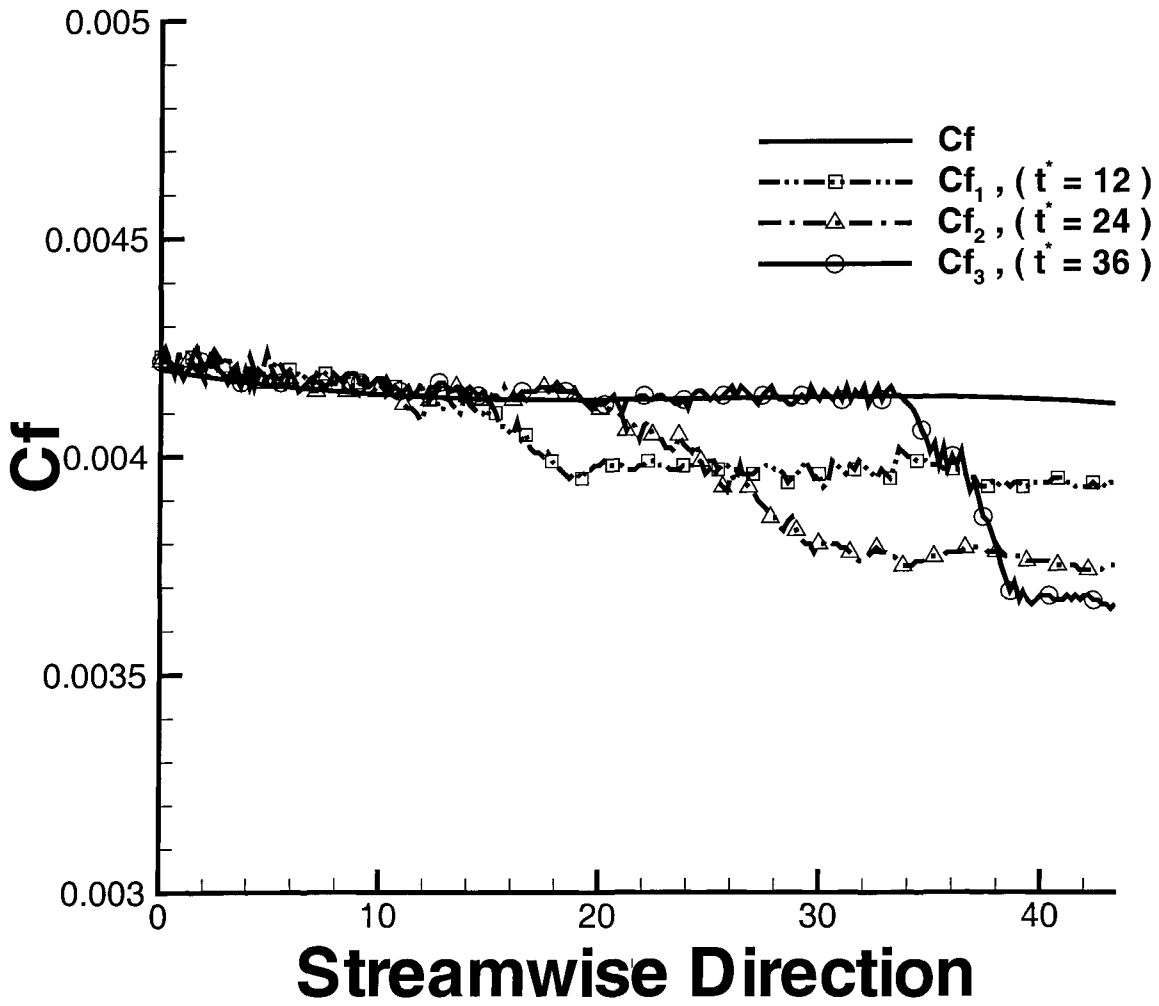


Figure 3.4 Evolution of skin friction: Solid line is mean profile of skin friction from $t = 100 \frac{\delta_d}{U_\infty}$ to $t = 600 \frac{\delta_d}{U_\infty}$, the square symbol is the spanwise average skin friction at $t = 12 \frac{\delta_d}{U_\infty}$, the delta symbol is the spanwise average skin friction at $t = 24 \frac{\delta_d}{U_\infty}$, and the circle symbol is the spanwise average skin friction at $t = 36 \frac{\delta_d}{U_\infty}$.

CHAPTER 4. AN ANISOTROPIC TURBULENCE: A TURBULENT BOUNDARY LAYER

The purpose of this study is to conduct theoretical and numerical studies to explore the concept of local homogeneity, the influence of the strong anisotropy on the global homogeneity, and the two-point correlations and mechanism of anisotropy for the strong anisotropy and non-homogeneous turbulence. We show that the strong fully developed anisotropic turbulence cannot be global homogeneous without external forcing. We prove that the small scale structures obey the incremental homogeneity. This answers Frisch *et al.* (2005)'s paradox about the concept of local homogeneity. In order to investigate the strong anisotropic effects on the structure functions, we calculated a two-dimensional fully developed turbulent boundary layer with a Reynolds number 2000 based on the displacement thickness using direct numerical simulation. The three dimensional two-point correlations and the one-point turbulent structure tensors are formulated. The results indicate the Reynolds stress and the hairpin vortices cause the rotation and asymmetry of the two-point correlations of R_{ww} , but such a rotation has not been found for R_{vv} . The rotation angle of R_{ww} is a function of normal distance from the wall. And the tails of the two-point correlations decay faster than the power functions. The anisotropy of the turbulent boundary layer has been studied. Results show that the turbulent production makes the major contribution to the anisotropy of the anisotropic tensor b_{ij} compared with turbulent dissipation and transport.

4.1 Introduction

Based on the level of homogeneity and isotropy, turbulence can be categorized into 16 parts, which are displayed in the Table 4.2. The concepts of local homogeneity and local

isotropy were discussed firstly by Kolmogorov (1941) and then described in detail by Monin and Yaglom (1975) and Frisch (1995). These classic concepts are fundamental to the K41 theory (see Kolmogorov (1941)) and the theory of return-to-isotropy (see Lumley and Newman (1977)). Moreover, considering the influence of the strong anisotropy on the homogeneity of turbulence, which will be deduced in the section 4.2.1, the anisotropic turbulence should be decomposed into two parts: strong anisotropy and weak anisotropy. The definition of the strong anisotropy follows:

Definition 3 *A field $u_i(x_j; t)$ is called a strong anisotropy if there does not exist a group of constant $a_{i,j}$ and b_i such that*

$$\sum_j a_{i,j} \frac{\partial u_i(x_j; t)}{\partial x_j} = b_i$$

is obeyed for any x and t in the domain.

Recently, a $SO(3)$ theory (see Arad *et al.* (1999), Biferale and Toschi (2001), Biferale *et al.* (2004), and Jacob *et al.* (2004)) has been developed for the study of the turbulence. $SO(3)$ theory discovered a hierarchy law of the structure functions and the self-similarity of the scaling exponents in the weak non-homogeneous turbulence. It is believed that this hierarchy law and self-similarity will be modified or even fail when the non-homogeneity becomes strong; for instance, strong mixing turbulence, and turbulent jets, etc. In this sense, the non-homogeneity should be decomposed into weak non-homogeneity and strong non-homogeneity.

Table 4.1 The categories of the turbulence in terms of the level of anisotropy and non-homogeneity

| | Global homogeneity | Local homogeneity | Weak nonhomogeneity | Strong nonhomogeneity |
|-----------------|-----------------------|----------------------|------------------------|--------------------------|
| Isotropy | region 1 (K41) | region 2 (K41) | region 5 (?) | region 6 (?) |
| Local isotropy | region 3 (K41) | region 4 (K41) | region 7 (\times) | region 8 (\times) |
| Weak isotropy | region 10 (SO(3)) | region 14 (EEM) | region 12 (SO(3)) | region 15 |
| Strong isotropy | region 9 (?) | region 13 (EEM) | region 11 (SO(3)) | region 16 |

4.1.1 A Brief Summary of Previous Turbulence Theories

The previous turbulence theories are summarized here. Indeed, there are four different types of turbulence theories: isotropic homogeneous turbulence theory, K41 theory, $SO(3)$ theory of turbulence, and the EEM (exact equation method). Some of them have been developed quite well, and the rest still keep developing. We classify them according to the turbulent regions with which they deal. The theory of turbulence contains various aspects. In this summary, we only focus on the anisotropy, length scale, and structure functions. The purpose of this summary is to determine the questions for the current and future research.

The region 1 of Table 4.1 is the isotropic homogeneous turbulence. The classic theory of isotropic homogeneous turbulence, namely TB in this dissertation, has been developed by G.I. Taylor and G.K. Batchelor (see Batchelor (1953)) and plays a fundamental role in the analysis of the one point and two-point statistical behavior of isotropic homogeneous turbulence. The theory is a powerful archetype offering a way to estimate the length scale and the structure functions of microscale structures.

Almost at the same time, Kolmogorov (1941) developed a completely different theory called K41 theory, which was based on the assumptions: (i) at the high Reynolds number, the local structures are homogeneous and isotropic, (ii) the local scale is dominated by the dissipation. K41 theory applied to the regions 1, 2, 3, and 4 introduced the concept of local isotropy and local homogeneity, and anticipated that the anisotropic effect associated with the large scales will continuously decay during the process of energy transfer toward the small scales. Also, the anisotropic structure will not be produced by the random forcing associated with the small scales for the high Reynolds flows (Frisch (1995) and Monin and Yaglom (1975)). The K41 theory together with the theory of isotropic homogeneous turbulence provides us a promising way to deal with the closure of the turbulent modeling and the analysis of the energy cascade. To date, two important issues are relevant to the K41 theory: the return of isotropy and the concept of local homogeneity. The returning of homogeneous turbulence to isotropy has been studied theoretically and experimentally (Lumley and Newman (1977), Choi and Lumley (2001)). For anisotropic flows with negative third invariant of the anisotropy tensor b_{ij} , the

restoring of the isotropy is efficient, although the turbulence trajectory may not be linear. But, the rate of the homogeneous turbulence returning to isotropy is lower when the third invariant of the anisotropy tensor is positive (Lumley and Newman (1977)). The concept of local isotropy was described by §21.2 of Monin and Yaglom (1975). The definition immediately follows that the local isotropy implies the local homogeneity or global homogeneity. In this sense, without the external forcing, there is no turbulence in region 7 and 8. However, the strict proof of this assertion does not exist. Recently, the concept of the local homogeneity was questioned by Frisch *et al.* (2005); their results revealed that the one-dimensional Burgers equation does not obey the assumption of the local homogeneity in which the incremental homogeneity should be independent of u_0 . Thereby, to understand the fundamental properties of the turbulence, it is worthwhile to argue the consistency of local homogeneity and local isotropy again.

In the past decade, an anisotropic turbulence theory, namely $SO(3)$ theory of turbulence, has been developed for the anisotropic homogeneous or weak non-homogeneous turbulence, which deals with regions 10, 11, and 12. The first representation of this theory using the $SO(3)$ decomposition was traced back to Arad *et al.* (1999). By using the $SO(3)$ decomposition, a hierarchy law of the structure functions and the self-similarity of the scaling exponents were discovered (Arad *et al.* (1999), Grossmann *et al.* (2001), Biferale and Toschi (2001), Biferale *et al.* (2004), and Jacob *et al.* (2004)). Nevertheless, the advance of the $SO(3)$ theory of turbulence is to generalize it. When the data were analyzed by using $SO(3)$ decomposition, a hierarchy law of the scaling exponents was observed. And such a hierarchy law exists universally among a number of flows including random Kolmogorov flow and the inertial region of the high Reynolds turbulent boundary layers (Biferale and Vergassola (2001), Biferale and Toschi (2001), Jacob *et al.* (2004), and Kurien and Sreenivasan (2000)).

Region 10 was studied numerically (Pumir (1996)) and experimentally (Jacob *et al.* (2004)). The hierarchy law of the scaling exponents was satisfied in this region. Results matched with the anticipation of the $SO(3)$ formalism of anisotropic turbulence. Also Jacob *et al.* (2004) and Kurien and Sreenivasan (2000)'s experiments in the inertial region of the high Reynolds number turbulent boundary layers indicated that the $SO(3)$ theory works for region 11 since

the turbulent fluctuations in the log layer of high Reynolds number turbulent boundary layers are strong anisotropic but weakly homogeneous (because the rms of turbulent fluctuations change slightly in the streamwise, spanwise, and normal directions (see DeGraaff and Eaton (2000))). Therefore, it is natural to conclude that the $SO(3)$ theory works for region 12.

Recently, the exact equations method (Yakhot (2001) and Hill (2001)), namely EEM, has been addressed in order to analyze local homogeneous turbulence including the anisotropic or locally anisotropic turbulence. The exact equations method provides a way to formulate the structure functions. A standard case in regions 13 and 14 is the high Reynolds number turbulent boundary layer. When the Reynolds number is high, the small scale structures may tend to be homogeneous. This will be discussed in section 4.2.2.

The turbulence corresponding to the regions 15 and 16 is of strong homogeneity. The previous research in these regions focused more on the closure and the modeling of anisotropy tensors including the velocity-pressure-gradient correlation, the dissipation rate tensor, the turbulent production tensor or the triple correlation (Antonia *et al.* (1994), Oberlack (1997) and Speziale (1991) etc.). The detailed information on the nonlinear evolution of two-point correlations and the integral length scale due to the strong non-homogeneity and strong anisotropy is lacking. Similarly, very little is known about the formulation of structure functions. In order to observe the behavior of the structure functions due to the strong anisotropic effects, we calculated a two-dimensional turbulent boundary layer with Reynolds numbers from 1800 to 2300 based on the inlet displacement thickness.

4.1.2 Motivation for This Study

Based on the discussion above, this chapter contains two parts: a theoretical part and a numerical part. In the theoretical part, the influence of the strong anisotropy on the homogeneity will be deduced. We will show that without the external force, there is no fully developed turbulence in region 9: the strong anisotropy but global homogeneity. Secondly, the concept of local homogeneity will be discussed. We will show that the small structures of the turbulence must be incrementally homogeneous. This answers Frish's paradox to K41 theory (see Frisch

et al. (2005)) about the local homogeneity. In the numerical part, the anisotropy effects and the structure functions of a low Reynolds number turbulent boundary layer which corresponds to region 16 has been studied. The purpose of this numerical study was try to add more information to the understanding of the fluid physics in this region. The three-dimensional structure of the two-point correlations will be evaluated.

The rest of this chapter is organized as follows: In section 4.2.1, we will prove that there does not exist any realistic fully developed turbulence in region 9 without external forcing. In section 4.2.2, we discuss the local homogeneity. In section 4.3, the numerical algorithm will be described, and the validation of the numerical simulations are addressed and analyzed. In the last section, we exhibit the results about the simulation of turbulent boundary layers subjected to zero pressure gradient.

4.2 Theoretical Analysis and Problem Formulation

4.2.1 The strong fully developed anisotropic flows cannot be globally homogeneous without forcing

In this section, we will show that without the external forcing, the strong anisotropic flows cannot be globally homogeneous. Assume that it fails. In other words, there exists a strong anisotropic flow with the homogeneous distributed structure functions. The turbulent kinetic energy equation follows

$$\frac{\partial k}{\partial t} + \frac{\partial U_j k}{\partial x_j} = -\frac{1}{\rho} \frac{\partial \langle u_j p \rangle}{\partial x_j} - \nu \left\langle \frac{\partial u_j}{\partial x_i} \frac{\partial u_j}{\partial x_i} \right\rangle - \frac{1}{2} \frac{\partial \langle u_j u_i u_i \rangle}{\partial x_j} - \langle u_j u_i \rangle \frac{\partial U_i}{\partial x_j} - \nu \nabla^2 k. \quad (4.1)$$

where $k = \frac{\langle u_i u_i \rangle}{2}$. Note that the fully developed turbulence is statistically stagnant, i.e. $\frac{\partial k}{\partial t} = 0$. Suppose that the flow is global homogeneous, then the space derivative of the statistical quantities are all zero. Thus, equation 4.1 can be reduced to

$$-\nu \left\langle \frac{\partial u_j}{\partial x_i} \frac{\partial u_j}{\partial x_i} \right\rangle - \langle u_j u_i \rangle \frac{\partial U_i}{\partial x_j} = 0 \quad (4.2)$$

Clearly, $\left\langle \frac{\partial u_j}{\partial x_i} \frac{\partial u_j}{\partial x_i} \right\rangle$ and $\langle u_j u_i \rangle$ are constant owing to the assumptions of the global homogeneity and fully developed flows. Together with (equ13), it turns out that $\frac{\partial U_i}{\partial x_j}$ is a constant. This

contradicts to the fact of the strong anisotropy in which $\frac{\partial U_i}{\partial x_j}$ is not a constant (see the definition 3).

Indeed, by adding the random force, Benzi *et al.* (1996) and Biferale *et al.* (2002) obtained some strong anisotropic homogeneous flows. Such flows are called a random Kolmogorov flow.

4.2.2 Local Homogeneity

Frisch *et al.* (2005) found that the second-order structure function $\langle [u(x+r) - u(x)]^2 \rangle$ cannot lose its dependence on the reference point x for the Burgers system, which is equivalent to the Navier-Stokes equation of isotropic flows. This implies that incremental homogeneity is not equivalent to the local homogeneity, which is fundamental to the K41 theory. We notice that such a dependence of the structure functions on the reference point x reported by Frisch *et al.* (2005) is produced by the large scale structures. Actually, the K41 theory only requires that the small structures satisfy the incremental homogeneity. We can prove that small scale structures in the realistic turbulence always obey the incremental homogeneity if the flows satisfy the following two assumptions:

(A1) the flow has a smallest microscale not only for velocity $u(x)$ but also for $\frac{1}{\rho} \frac{\partial p}{\partial x_j}$.

(A2) the spectrum of $\frac{\partial}{\partial x} [u(x+r) - u(x)]^m$ is Lipschitz continuous and bounded, where $x, r \in \mathbb{R}^N$.

The existence of smallest microscale of isotropic homogeneous turbulence, Kolmogorov scale, has been proved (See Tennekes and Lumley (1972) and Frisch (1995)). The nonlinear effects of the convective term will continuously generate the structures with a scale smaller than the Kolmogorov scale. Such structures are not steady and very easily broken and dissipated because viscous effects are dominant at these scales. Assumption (A2) relates to the regularity issue of the solution of the Navier-Stokes equation. It is an open and challenging question for this century. But, physically, it is believed that most of the solutions should be smooth. This is the basis of the assumption (A2).

We will show that under the assumptions (A1) and (A2), there exists a scale $\eta_{l,\max}$ and R

so that, for any m and $\varepsilon \geq 0$, when $\zeta_l > \eta_{l,\max}$ and $0 \leq r \leq R$,

$$\left| \left\langle \frac{\partial}{\partial x} [u(x+r) - u(x)]^m, e^{i\zeta_l x_l} \right\rangle \right| \leq \varepsilon \quad (4.3)$$

where $\langle \cdot, \cdot \rangle$ stands for the inner product, $i = \sqrt{-1}$, m is a positive integer, and ζ_l is the wavenumber. Clearly, the inequality (4.3) implies the incremental homogeneity of the small scale.

Let operator F be the Fourier transformation. According to the Plancherel theorem

$$\begin{aligned} \left| \left\langle \frac{\partial}{\partial x} [u(x+r) - u(x)]^m, e^{i\zeta_l x_l} \right\rangle \right| &= \left| \left\langle F\left(\frac{\partial}{\partial x} [u(x+r) - u(x)]^m\right), F(e^{i\zeta_l x_l}) \right\rangle \right| \\ &= \left| \left\langle F\left(\frac{\partial}{\partial x} [u(x+r) - u(x)]^m\right), \delta(\zeta_l - \xi_l) \right\rangle \right| \\ &= \left| \left\langle \underbrace{i\xi_l F(\Delta u) \otimes F(\Delta u) \otimes \cdots \otimes F(\Delta u)}_m, \delta(\zeta_l - \xi_l) \right\rangle \right|. \end{aligned} \quad (4.4)$$

Here, δ is the delta "function", $\Delta u = u(x+r) - u(x)$, and \otimes is the convolution.

Owing to the condition (A1), we assume that Fu_j is nonzero only in an interval $[0, \zeta_{l,\max}]$. This implies that, for any $\zeta_l > \zeta_{l,\max}$, $\langle Fu_j, \delta(\zeta_l - \eta_l) \rangle = 0$. Hence,

$$\langle i\kappa_k Fu_j \otimes Fu_k, \delta(\zeta_l - \xi_l) \rangle = 0 \quad (4.5)$$

for any $\zeta_l > 2\zeta_{l,\max}$.

Due to the condition (A2), we can find a scale $\eta_{l,\max}$ so that, for any $\varepsilon \geq 0$, when $\zeta_l > \eta_{l,\max}$,

$$|\langle i\kappa_k Fu_j \otimes Fu_k, \delta(\zeta_l - \xi_l) \rangle| \leq \varepsilon/5 \quad (4.6)$$

In the same way for the inequality (4.4), we have

$$\left| \left\langle \frac{\partial}{\partial x} [u_j u_k], e^{i\zeta_l x_l} \right\rangle \right| \leq \varepsilon/5$$

It is known that $\overline{u_j(x+r)u_k(x)} - \overline{u_j}\overline{u_k}$ is nothing but the turbulent energy spectrum, which has the smallest microscale. Thus,

$$\left| \left\langle \frac{\partial}{\partial x} [u_j(x+r)u_k(x)], e^{i\zeta_l x_l} \right\rangle \right| \leq \varepsilon/5$$

for some small enough ζ_l . Again, the condition (A2) tells us that there exists an R so that when $0 \leq r \leq R$,

$$\left| \left\langle \frac{\partial}{\partial x} [u_j(x+r)u_k(x+r)] - \frac{\partial}{\partial x} [u_j(x)u_k(x)], e^{i\zeta_l x_l} \right\rangle \right| \leq \varepsilon/5 \quad (4.7)$$

Considering that

$$\begin{aligned} \left| \left\langle \frac{\partial}{\partial x} [u(x+r) - u(x)]^2, e^{i\zeta_l x_l} \right\rangle \right| &\leq \left| \left\langle \frac{\partial}{\partial x} u(x+r)^2, e^{i\zeta_l x_l} \right\rangle \right| + \left| \left\langle \frac{\partial}{\partial x} u(x)^2, e^{i\zeta_l x_l} \right\rangle \right| \\ &\quad + 2 \left| \left\langle \frac{\partial}{\partial x} u(x+r)u(x), e^{i\zeta_l x_l} \right\rangle \right| \\ &\leq \left| \left\langle \frac{\partial}{\partial x} [u_j(x+r)u_k(x+r)] - \frac{\partial}{\partial x} [u_j(x)u_k(x)], e^{i\zeta_l x_l} \right\rangle \right| + \\ &\quad + 2 \left| \left\langle \frac{\partial}{\partial x} u(x)^2, e^{i\zeta_l x_l} \right\rangle \right| + 2 \left| \left\langle \frac{\partial}{\partial x} u(x+r)u(x), e^{i\zeta_l x_l} \right\rangle \right| \end{aligned}$$

we obtains

$$\left| \left\langle \frac{\partial}{\partial x} [u(x+r) - u(x)]^2, e^{i\zeta_l x_l} \right\rangle \right| \leq \varepsilon$$

This proves the incremental homogeneity of the small scale in the sector 2. By using the same computation, we can prove the incremental homogeneity of the small scale for any m th order order structure functions.

We address here the difference of local homogeneity and weak non-homogeneity. The weak non-homogeneous is in a global sense, which means the structure functions change slightly on the space. But the local homogeneity discussed here is in a local sense, which emphasizes the smoothness of the high frequency part of structure functions. It is possible that the local homogeneous flow is weakly non-homogeneous. But they are not equal.

4.3 The Validation of the Numerical Method

To investigate anisotropic effects on the structure functions and the three dimensional structures of two-point correlations, a two-dimensional incompressible turbulent boundary layer was calculated by a direct numerical simulation. The calculated Reynolds number ranged from 1800 up to 2300 based on the displacement thickness δ_d . The detailed information of the current simulation are addressed in this section. The parameters utilized here are compared with the

simulation of Spalart (1988) and the experiment of DeGraaff and Eaton (2000), which are described in the table 4.2:

Table 4.2 Comparison of parameters used in the incompressible simulation of Spalart (1988), DeGraaff and Eaton (2000), and the present simulations.

| Sim. | Case 1 | Case 2 | S1 | DE |
|---------------------|--------|--------|------|------|
| N_x | 350 | 350 | 432 | - |
| N_y | 90 | 90 | 80 | - |
| N_z | 192 | 192 | 320 | - |
| Re_d | 2000 | 2000 | 2000 | 2000 |
| M | 0.02 | 0.02 | 0.0 | 0.02 |
| Δx^+ | 20.0 | 16.0 | 20.0 | - |
| Δz^+ | 6.7 | 4.7 | 6.7 | - |
| Δy_{\min}^+ | 0.3 | 0.2 | 0.3 | - |

The length scale for the Reynolds number in Table 4.2 is the displacement thickness, and the unit of $(\cdot)^+$ components is the wall unit, for instance, $y^+ = yu_\tau/\nu_w$. The numerical mesh was uniform in the streamwise and spanwise directions, but was stretched in the normal direction. The non-traditional time step $\Delta t^+ = 0.2\delta_d/U_\infty$ where δ_d is the inlet displacement thickness. The comparison of the first two cases is to investigate the grid resolution. We obtained the same statistical results.

4.3.1 Numerical Method

The fractional step method proposed by this dissertation was employed. The governing equations are presented by Chapter 3. We solved the compressible Navier-Stokes equations. Since the evaluated Mach number is low, 0.02, the calculated turbulent boundary layer is nearly incompressible. A periodic boundary condition was utilized in the spanwise direction. A characteristic boundary condition proposed in chapter 4 was applied at the outlet and a dynamic recycling inlet method proposed in chapter 4 was employed to generate the fully developed turbulent boundary layer.

4.3.2 Validation of the Numerical Simulations of the First and Second Order Statistics.

To validate the numerical simulations, the following points need to be established: (1) a grid resolution study is carried out such that the grid-converged results had been achieved. (2) the first, second, and higher order statistical results are accurately obtained.

For examining the grid resolution, we calculated the cases 1 and 2, where the case 2 was computed with a fine mesh. The results indicated that the first and second-order statistics of both cases overlapped. This indicates that the numerical mesh utilized by the case 1 was adequate. The comparison of the mean velocity with the DNS profiles reported by Spalart (1988) and the experimental results reported by DeGraaff and Eaton (2000) was shown in the Figure 5.1. Figure 5.2 shows a comparison of the rms of fluctuations with Spalart (1988)'s DNS data and experimental data (DeGraaff and Eaton (2000)). The compared DNS and experimental results are all with the Reynolds number 2000 based on the inlet displacement thickness. The agreement is generally good.

The simulation of turbulent boundary layers requires quite detailed inflow information since the resolved flow is unsteady and three-dimensional. Currently, there are three different methods to generate the inflow conditions of turbulent boundary layer: the random fluctuation method Lee *et al.* (1992), the matching database method Schlüter *et al.* (2003), and the recycling and rescaling method (See Spalart (1988), Lund *et al.* (1998)). A common point to those three methods is the existence of the inlet buffer zone because the inflow condition is not the solution of Navier-Stokes equation, but a guess. It must have some errors. Such errors can be reduced, but are unavoidable. Owing to the errors in the inflow conditions, the numerical domain will take a distance to adjust the fluid structures such that the correct turbulent structure can be generated downstream. The recycling and rescaling method provides a promising way to reduce the inlet buffer zone. The inflow condition utilized in this study (Liu and Pletcher (2006)) is a modification of Lund *et al.* (1998)'s method.

4.3.3 Reynolds Stress Budget

The governing equation for the Reynolds stress is given by

$$\frac{\partial \langle u_i u_j \rangle}{\partial t} + U_k \frac{\partial \langle u_i u_j \rangle}{x_k} = P_{ij} + T_{ij} + D_{ij} + \Pi_{ij} - \varepsilon_{ij} \quad (4.8)$$

where P_{ij} is the turbulent production tensor, T_{ij} is the turbulent transport tensor, D_{ij} is the viscous dissipation tensor, Π_{ij} is the velocity pressure gradient tensor, and ε_{ij} is the turbulent dissipation tensor. The representation of those terms are given by,

$$\begin{aligned} P_{ij} &= -\langle u_i u_k \rangle \frac{\partial U_j}{\partial x_k} - \langle u_j u_k \rangle \frac{\partial U_i}{\partial x_k} \\ \varepsilon_{ij} &= 2\nu \left\langle \frac{\partial u_i}{\partial x_k} \frac{\partial u_j}{\partial x_k} \right\rangle \\ T_{ij} &= -\left\langle \frac{\partial u_i u_j u_k}{\partial x_k} \right\rangle \\ \Pi_{ij} &= -\frac{1}{\rho} \left\langle u_i \frac{\partial p}{\partial x_j} + u_j \frac{\partial p}{\partial x_i} \right\rangle \\ D_{ij} &= \nu \Delta \langle u_i u_j \rangle \end{aligned}$$

The trace of the equation (4.8) is the turbulent kinetic energy equation, which follows

$$\frac{\partial k}{\partial t} + U_k \frac{\partial k}{x_k} = P_{ii} + T_{ii} + D_{ii} + \Pi_{ii} - \varepsilon_{ii} \quad (4.9)$$

where $k = \frac{\langle u_i u_i \rangle}{2}$. The Reynolds stress budget reveals the detailed information and mechanism of the turbulent behavior. The turbulent transport and dissipation terms including the viscous dissipation and the turbulent dissipation are symmetric, while the turbulent production and velocity-pressure gradient are asymmetric. In the inertial region, the turbulent production is balanced with the dissipation. As the local Reynolds number is increased, the dissipation becomes dominant. In this circumstance, the local structure returns to isotropy. But the nonlinear effects of the velocity-pressure gradient usually obscure this returning procedure. Experimental results showed that when the velocity-pressure gradient is not too weak, the turbulence tends to stay in the anisotropic state rather than returning to isotropy (Choi and Lumley (2001)). Unfortunately, our knowledge of the velocity-pressure gradient still remains limited. In order to model the velocity-pressure gradient, recently, Oberlack (1997) deduced the pressure-stain tensor by using a Green's function method. Although the symmetry does not

always tend to isotropy or local isotropy, it is reasonable to assume that when the turbulence returns to isotropy, the Reynolds stress tensor will increase the order of invariant frame. In the other words, the sector should decrease. If it is true, then the asymmetric tensor like velocity-pressure gradient and the turbulent production should decay faster than the symmetric tensor. This phenomena has been observed in the high Reynolds number but weak homogeneous flows (Jacob *et al.* (2004) and Kurien and Sreenivasan (2000)). In order to outline the evolution of the Reynolds stress tensor in terms of the Reynolds number, it is worthwhile to observe the behavior of the turbulence production, dissipation, transport and velocity-pressure gradient tensor in the low Reynolds number turbulent boundary layer.

For this purpose, we calculated the Reynolds stress tensor at the Reynolds number 2000. Fig. 4.3-4.6 gives the Reynolds stress budget of $\langle u^2 \rangle$, $\langle v^2 \rangle$, $\langle w^2 \rangle$ and $\langle uv \rangle$ with the corresponding components reported by Spalart (1988). The agreement is fairly good. Without making confusion, the exhibited results starting from this section to the rest of this chapter are all from case 1.

4.4 Results and Discussion

4.4.1 Anisotropic Tensors

As we described above, return-to-isotropy is fundamental to the K41 theory. In order to understand the mechanism relevant to the return-to-isotropy, we need to figure out the cause of anisotropy firstly because there is no return-to-isotropy without the anisotropy. We are interested in finding out the major cause of the anisotropy in the turbulent boundary layer, and its evolution with respect to the Reynolds number. The anisotropy of turbulence is described by the Reynolds stress anisotropic tensor b_{ij} defined by $b_{ij} = \frac{\langle u_i u_j \rangle}{2K} - \frac{\delta_{ij}}{3}$, where K is the turbulent kinetic energy given by $K = \frac{\langle u_i u_i \rangle}{2}$. By using the Reynolds stress equation (4.8) and the turbulent kinetic energy equation (4.9), we have the equation of b_{ij} , which is described by

$$\frac{\partial b_{ij}}{\partial t} + U_k \frac{\partial b_{ij}}{\partial x_k} = P_{ij} + T_{ij} + D_{ij} + \Pi_{ij} - \varepsilon_{ij}.$$

Let

$$\begin{aligned}\overline{P_{ij}} &= P_{ij} - \frac{\delta_{ij}}{3}P_{ss} \quad , & \overline{T_{ij}} &= T_{ij} - \frac{\delta_{ij}}{3}T_{ss} \quad , & \overline{D_{ij}} &= D_{ij} - \frac{\delta_{ij}}{3}D_{ss}, \\ \overline{\Pi_{ij}} &= \Pi_{ij} - \frac{\delta_{ij}}{3}\Pi_{ss} \quad , & & & \overline{\varepsilon_{ij}} &= \varepsilon_{ij} - \frac{\delta_{ij}}{3}\varepsilon_{ss}.\end{aligned}$$

It yields

$$\frac{\partial b_{ij}}{\partial t} + U_k \frac{\partial b_{ij}}{\partial x_k} = \frac{1}{2K} [(\overline{P_{ij}} + \overline{T_{ij}} + \overline{D_{ij}} + \overline{\Pi_{ij}} - \overline{\varepsilon_{ij}}) - (2b_{ij} + \frac{\delta_{ij}}{3})(P_{ss} + T_{ss} + D_{ss} + \Pi_{ss} - \varepsilon_{ss})]. \quad (4.10)$$

Here, $\overline{P_{ij}}$, $\overline{T_{ij}}$, $\overline{\varepsilon_{ij}}$, $\overline{\Pi_{ij}}$, and $\overline{D_{ij}}$ are the anisotropic tensors corresponding to the turbulent production, transport, dissipation, velocity-pressure gradient, and viscous dissipation, respectively. The detailed deduction of the identity (4.10) is addressed by appendix A. Clearly, b_{ij} , $\overline{T_{ij}}$, $\overline{D_{ij}}$, and $\overline{\varepsilon_{ij}}$ are symmetric, while $\overline{P_{ij}}$ and $\overline{\Pi_{ij}}$ are asymmetric. Since any 3×3 symmetric matrix is six dimensional, by the Cayley-Hamilton theorem, three invariants of the matrix can be used to identify the three eigenvalues of the matrix. The value of the eigenvalues reveals the deviation of the matrix from the isotropy because, for the isotropic flows, all of the eigenvalues are equal. The dynamic behavior of the second and third invariants of the tensor b_{ij} had been anticipated by Lumley and Newman (1977) in the study about the return-to-isotropy. The purpose of this study is to find out the major contribution of the anisotropy of b_{ij} in terms of the second and third invariants. Note that the first invariant of b_{ij} is zero.

After rearranging the equation (4.10), we obtain that

$$b_{ij} = \frac{(\overline{P_{ij}} + \overline{T_{ij}} + \overline{D_{ij}} + \overline{\Pi_{ij}} - \overline{\varepsilon_{ij}})}{2(P_{ll} + T_{ll} + D_{ll} + \Pi_{ll} - \varepsilon_{ll})} - \frac{K(\frac{\partial b_{ij}}{\partial t} + U_k \frac{\partial b_{ij}}{\partial x_k})}{(P_{ll} + T_{ll} + D_{ll} + \Pi_{ll} - \varepsilon_{ll})} - \frac{\delta_{ij}}{6} \quad (4.11)$$

For the fully developed two-dimensional turbulent boundary layer, $\frac{\partial b_{ij}}{\partial t} + U_k \frac{\partial b_{ij}}{\partial x_k} \sim V \frac{\partial b_{ij}}{\partial x_2}$, where x_2 and V are normal distance and normal velocity. Thus, the identity (4.11) implies that the dynamic evolution of b_{ij} in the normal direction depends on the anisotropy of $\overline{P_{ij}}$, $\overline{T_{ij}}$, $\overline{D_{ij}}$, $\overline{\Pi_{ij}}$, and $\overline{\varepsilon_{ij}}$. Antonia *et al.* (1994) observed the correlations between the b_{ij} and $\overline{\varepsilon_{ij}}/\varepsilon_{ss}$. It is known that for the wall shear flow, ε_{ss} is a function of the normal distance from the wall. Normalizing $\overline{\varepsilon_{ij}}$ by using ε_{ss} would enable us to recognize the link between b_{ij} and $\overline{\varepsilon_{ij}}$, but it is not enough to identify the major cause of the anisotropy of b_{ij} . Here, we give a comparison study of $\overline{P_{ij}}$, $\overline{T_{ij}}$, $\overline{\varepsilon_{ij}}$ and b_{ij} .

Figures 4.7 and 4.8 show the second and third invariants of the matrix. II_b and III_b stand for the second and third invariant of matrix b_{ij} , i.e. $II_b = -\frac{1}{2}b_{ij}b_{ji}$ and $III_b = \frac{1}{3}b_{ij}b_{jk}b_{ki}$. And II_p and III_p stand for the second and third invariant of matrix $\overline{P_{ij}}$, i.e. $II_p = -\frac{1}{2}\overline{P_{ij}P_{ji}}$ and $III_p = \frac{1}{3}\overline{P_{ij}P_{jk}P_{ki}}$. And so on. Fig. 4.7 and 4.8 show that comparing with the dissipation and transport terms, turbulence production plays a more important role to the anisotropy of the Reynolds stress anisotropic tensor. Although the third invariant of the dissipation matrix is very tiny across the boundary layer, the results represented by Fig. 4.3-4.5 show that ε_{11} , ε_{22} , and ε_{33} are entirely different. Thus, we conclude that the turbulent production makes the major contribution to the anisotropy of b_{ij} . Generally, turbulent production keeps decreasing as the wavenumber increases once the wavenumber is larger than that of the energy containing structures. This feature is associated with the process of the return-to-isotropy.

4.4.2 Two-point Correlations of Velocities

It is known that the strong shear force near the wall will deform the vortices and develop some stretched coherent structures such as streaks and hairpin packages, which eventually cause the anisotropy of wall shear flows. The behavior of the hairpin packages in wall shear flows like channel and boundary layers has been investigated for a long time (See Moin and Kim (1985), Smith *et al.* (1991), Zhou *et al.* (1999), and Ganapathisubramani *et al.* (2005)). Moin and Kim (1985) found the 45° lifting of the head of the hairpin vortices in a channel flow. Zhou *et al.* (1999) reported a 15° lifting of the leg of the hairpin vortices. Note that the legs of the hairpin vortices are in the inner part of the wall shear flows, while their heads are in the outer part of the wall shear flows. Recently, Ganapathisubramani *et al.* (2005) investigated the lifting of R_{uu} in an experimental study of the turbulent boundary layer. This study is intended to investigate the influence of shear force on the two-point correlations by using a numerical simulation. We focus on the two-point correlations of velocities and the lifting effect of R_{vv} and R_{ww} , where u , v , and w correspond to streamwise, normal, and spanwise velocities, respectively.

For a flow that is fully developed, which is statistical stagnant, the ensemble average is

equivalent to the average on time. The two-dimensional turbulent boundary layer is homogeneous in the spanwise direction and the statistical qualities change only slightly in the streamwise direction. Therefore, the two-point correlation

$$R_{u_i u_j}(x, y, z; x_1, y_1, z_1) = \langle u_i(x_1, y_1, z_1; t) u_j(x, y, z; t) \rangle$$

can be reduced to

$$R_{u_i u_j}(x, y, z; x_1, y_1, z_1) \sim R_{u_i u_j}(r_x, r_y, r_z; y_1)$$

where (x_1, y_1, z_1) is the location of the first point, the (x, y, z) is the location of the second point, and $r_x = x - x_1$, $r_y = y - y_1$, and $r_z = z - z_1$.

4.4.2.1 The Formulation of R_{vv}

Figures 4.9-4.11 give the statistics of the two-point correlation R_{vv} , and illustrate the three dimensional structure of $R_{vv}(r_x, r_y, r_z; y_1)$, which is symmetric by means of r_x and r_z . Three different first points are analyzed. For those three, the x_1 and z_1 locations stay the same, where $x_1 = 31.6$ and $z_1 = 6$. But the normal distance is different, they are $y_1^+ = 56$, $y_1^+ = 178$, and $y_1^+ = 378$. Also the second point is taken arbitrarily in the numerical domain.

Figure 4.9 is the log plot of the $R_{vv}(0, 0, r_z; y_1)$ at the three different y_1 locations. The results show that $R_{vv}(0, 0, r_z; y_1)$ is symmetric in the spanwise direction. As y_1 increases, the length scale increases. $R_{vv}(0, 0, r_z; y_1)$ can be approximated by

$$R_{vv}(0, 0, 0; y_1) \exp(-(r_z/L_{vv,z}(y_1))^2),$$

where $L_{vv,z}(y_1)$ is the length scale which is function of y_1 . More precisely,

$$\frac{R_{vv}(0, 0, r_z; y_1)}{R_{vv}(0, 0, 0; y_1)} = \exp(-(\frac{r_z}{L_{vv,z}(y_1)})^2) \quad (4.12)$$

when r_z is small, identity (4.12) can be approximated by

$$\frac{R_{vv}(0, 0, r_z; y_1)}{R_{vv}(0, 0, 0; y_1)} \simeq 1 - (\frac{r_z}{L_{vv,z}(y_1)})^2$$

The above formulas match with the facts that $R_{vv}(0, 0, r_z; y_1)$ is even and symmetric. As r_z increases, the tail of $R_{vv}(0, 0, r_z; y_1)$ decays faster than the power function. We notice that the

exponential function describes the global behavior of $R_{vv}(0, 0, r_z; y_1)$ more accurately than the power function.

Fig. 4.10 shows the plot of the $R_{vv}(r_x, 0, 0; y_1)$ in terms of r_x and y_1 . The negative r_x implies upstream of the first point, and the positive r_x is the downstream of the first point. Three different first points are plotted by Fig. 4.10. From this figure, $R_{vv}(r_x, 0, 0; y_1)$ is roughly symmetric if y_1 is in the inner part of the turbulent boundary layer. But as y_1 increases, the symmetry is lost. This is relevant to the increase of the intermittency. Indeed, $R_{vv}(r_x, 0, 0; y_1)$ can be roughly represented by

$$\frac{R_{vv}(r_x, 0, 0; y_1)}{R_{vv}(0, 0, 0; y_1)} = \exp\left(-\left(\frac{r_x}{L_{vv,x}(y_1)}\right)^2\right)$$

where $L_{vv,x}(y_1)$ is the length scale corresponding to the station y_1 . Likewise, Fig. 4.11 shows $R_{vv}(0, r_y, 0; y_1)$ in terms of y . The structure of $R_{vv}(0, r_y, 0; y_1)$ has been stretched due to the lifting effects of the turbulent boundary layer. Convective effects relevant to the normal velocity is not the only or direct cause of such a lifting phenomena. Indeed, the vortex plays an important role on the lifting of the turbulent structures. Unlike the previous two figures, as y_1 increases, $R_{vv}(0, r_y, 0; y_1)$ becomes more and more regular. In other words, $R_{vv}(0, r_y, 0; y_1)$ has a tendency to be symmetric. By selecting a proper length scale $L_{vv,y}(y_1)$, $R_{vv}(0, r_y, 0; y_1)$ can be approximated by the following formula

$$\frac{R_{vv}(0, r_y, 0; y_1)}{R_{vv}(0, 0, 0; y_1)} = \exp\left(-\left(\frac{r_y^+}{L_{vv,y}(y_1)}\right)^2\right)$$

where $r_y^+ = r_y u_{\tau_{local}} / u_{\infty}$ and $u_{\tau_{local}}$ is the local wall friction velocity. As a result,

$$R_{vv}(r_x, r_y, r_z; y_1) = R_{vv}(0, 0, 0; y_1) \exp\left(-\left(\frac{r_x}{L_{vv,x}(y_1)}\right)^2 - \left(\frac{r_y^+}{L_{vv,y}(y_1)}\right)^2 - \left(\frac{r_z}{L_{vv,z}(y_1)}\right)^2\right)$$

4.4.2.2 The Formulation of R_{ww}

The side view of $R_{ww}(r_x, r_y, 0; y_1)$ is presented by Figs. 4.12 and 4.13. Those figures capture the lifting effects of the turbulent boundary layer, which cause the rotation of R_{ww} . Such a rotation angle θ is an increasing function of y_1 . When y_1^+ is less than 100 and larger than 15 (Fig. 4.12), the rotation angle θ is roughly 15° . Recall that, at the inner part of

turbulent boundary layer, the mean streamwise velocity U is at least 10 times larger than the mean normal velocity V . Thus, convection is not the major or directly reason for the rotation of R_{ww} . We notice that, in a turbulent boundary layer experiment reported by Zhou *et al.* (1999), the vortex structures have a 15° lifting angle. The other interesting phenomena is the appearance of the anticorrelated kernels. Shown in Figs. 4.12 and 4.13, there exists at least one anticorrelated region, region B, at the right downward side of region A. In region B, the spanwise velocity w usually has a different sign than the spanwise velocity in the region A. This phenomena is believed to be produced by the hairpin vortices. Since the hairpin vortices exist in pairs, one rotates on the clockwise direction, and the other must rotate in the counterclockwise direction. Hence, it is reasonable to assume that the lifting phenomena of the two-point correlation R_{ww} is relevant to the hairpin vortices.

Figure 4.14 is the plot of $R_{ww}(0, 0, r_z; y_1)$ at three different y_1 locations. Since spanwise is the homogeneous direction, $R_{ww}(0, 0, r_z; y_1)$ is symmetric in this direction. The length scale $L_{ww,z}(y_1)$ of $R_{ww}(0, 0, r_z; y_1)$ keeps increasing with increasing y_1 . And $R_{ww}(0, 0, r_z; y_1)$ can be approximated by

$$\frac{R_{ww}(0, 0, r_z; y_1)}{R_{ww}(0, 0, 0; y_1)} = \exp\left(-\left(\frac{r_z}{L_{ww,z}(y_1)}\right)^2\right)$$

$L_{ww,z}(y_1)$ is a nonlinear function of y_1 . Due to Figs. 4.12 and 4.13, we make a frame transformation such that

$$\begin{bmatrix} x^* \\ y^* \\ r_z \end{bmatrix} = \begin{bmatrix} \cos \theta & \sin \theta & 0 \\ -\sin \theta & \cos \theta & 0 \\ 0 & 0 & 1 \end{bmatrix} \begin{bmatrix} r_x \\ r_y \\ r_z \end{bmatrix} =: \Lambda_\theta \begin{bmatrix} r_x \\ r_y \\ r_z \end{bmatrix}$$

where Λ_θ is the rotation matrix. Fig. 4.15 plots $R_{ww}(x^*, 0, 0; y_1)$ in terms of x^* and y_1 . $R_{ww}(x^*, 0, 0; y_1)$ can be roughly represented by

$$\frac{R_{ww}(x^*, 0, 0; y_1)}{R_{ww}(0, 0, 0; y_1)} = \exp\left(-\left(\frac{x^*}{L_{ww,x}(y_1)}\right)^2\right)$$

where $L_{ww,x}(y_1)$ is the length scale at the station y_1 . Likewise, Fig. 4.16 plots $R_{ww}(0, y^*, 0; y_1)$ in terms of y . And $R_{ww}(0, r_y, 0; y_1)$ can be approximated by

$$\frac{R_{ww}(0, y^*, 0; y_1)}{R_{ww}(0, 0, 0; y_1)} = \exp\left(-\left(\frac{y^*}{L_{ww,y}(y_1)}\right)^2\right)$$

As a result,

$$\begin{aligned}
& R_{ww}(r_x, r_y, r_z; y_1) \\
&= R_{ww}(0, 0, 0; y_1) \exp\left(-\left(\frac{x^*}{L_{ww,x}(y_1)}\right)^2 - \left(\frac{y^*}{L_{ww,y}(y_1)}\right)^2 - \left(\frac{r_z}{L_{ww,z}(y_1)}\right)^2\right) \\
&= R_{ww}(0, 0, 0; y_1) / \exp\left(\begin{bmatrix} \frac{x^*}{L_{ww,x}(y_1)} & \frac{y^*}{L_{ww,y}(y_1)} & \frac{r_z}{L_{ww,z}(y_1)} \end{bmatrix} \begin{bmatrix} x^*/L_{ww,x}(y_1) \\ y^*/L_{ww,y}(y_1) \\ r_z/L_{ww,z}(y_1) \end{bmatrix}\right)
\end{aligned}$$

Let \mathbf{r}^T be the variable vector, $\mathbf{r}^T = [r_x, r_y, r_z]$, D is the dilation matrix obeying

$$D = \begin{bmatrix} \frac{1}{L_{ww,x}(y_1)} & 0 & 0 \\ 0 & \frac{1}{L_{ww,y}(y_1)} & 0 \\ 0 & 0 & \frac{1}{L_{ww,z}(y_1)} \end{bmatrix}$$

and Λ_θ is the rotation matrix. The representation of $R_{ww}(r_x, r_y, r_z; y_1)$ can be reduced to

$$R_{ww}(r_x, r_y, r_z; y_1) = R_{ww}(0, 0, 0; y_1) / \exp(\mathbf{r}^T \Lambda_\theta^T D^T D \Lambda_\theta \mathbf{r})$$

where $(\cdot)^T$ is the transpose of the matrix (\cdot) .

We plot in Fig. 4.17 the downward view of the two-point correlations of R_{ww} and R_{vv} , where X is the streamwise direction and Z is the spanwise direction. For the first and the third images in Fig. 4.17, the first point of the two-point correlations is located on the $Y^+ = 378$. And the first point of the two-point correlations locates on the $Y^+ = 178$ for the other two images of Fig. 4.17. These results are in qualitative agreement with the PIV measurements of Ganapathisubramani *et al.* (2005). Note that R_{vv} is the two-point correlation of spanwise velocities by Ganapathisubramani *et al.* (2005), but, in this dissertation, w is defined to be the spanwise velocity and v is defined to be the normal velocity. From the Fig. 4.17, we find that the X-Z contour of the R_{ww} develops a square-like structure as the distance increases from the center. But that of the R_{vv} keeps the elliptic-like shape.

4.5 Conclusions

Based on the level of the homogeneity and isotropy, turbulence can be categorized into 16 parts, which are presented in Table 4.1. Some regions are understood very well, but the rest

still remain elusive. It is possible that each of these regions requires a unique theory. The major goal of this chapter was to conduct some theoretical and numerical studies to explore three fundamental problems about the fluid physics of turbulence. This chapter included two parts: theoretical part and numerical part. In the theoretical part, we dealt with regions 2, 3, and 9 of Table 4.1. We proved that without external forcing, the strong fully developed anisotropic flows cannot be globally homogeneous. Under the assumption (A1)-(A2), this chapter indicated that small scale structures in realistic turbulence always obey the incremental homogeneity. This answers Frish's paradox to K41 theory (see Frisch *et al.* (2005)) about the local homogeneity. In the numerical part, the one point Eulerian statistics and the two-point Eulerian correlations of velocity over a two-dimensional flat-plate turbulent boundary layer subjected to the zero pressure gradient have been calculated by the direct numerical simulation. The anisotropic effects and the structure functions of a low Reynolds number turbulent boundary layer which corresponds to region 16 has been studied. The major goal of this study was to investigate the anisotropic effect of the strong non-homogeneous flows and observe the similarity laws for the two-point correlations of velocity in the anisotropic flows. The scaling exponents of the two-point correlations of strong anisotropic non-homogeneous flow were formulated.

Results were presented for a region having a Mach number of $M = 0.02$ and a Reynolds number 2000, based on displacement thickness. The results indicate that the two-point correlations are homogeneous in the spanwise direction and have a slight variation in the streamwise direction. But, they change greatly in the normal direction. The influence of Reynolds stress and the hairpin vortices causes the rotation and asymmetry of the two-point correlations R_{ww} , and the rotation angle is a function of normal distance from the wall. The length scales and the formulations of the two-point correlations were addressed here. The two-point correlation of spanwise velocities or normal velocities, namely R_{ww} or R_{vv} , are formulated as

$$R_{ww}(r_x, r_y, r_z; y_1) = R_{ww}(0, 0, 0; y_1) / \exp(\mathbf{r}^T \Lambda_\theta^T D^T D \Lambda_\theta \mathbf{r})$$

or

$$R_{vv}(r_x, r_y, r_z; y_1) = R_{vv}(0, 0, 0; y_1) \exp\left(-\left(\frac{r_x}{L_{vv,x}(y_1)}\right)^2 - \left(\frac{r_y^+}{L_{vv,y}(y_1)}\right)^2 - \left(\frac{r_z}{L_{vv,z}(y_1)}\right)^2\right),$$

where y is the normal distance, and, r_x , r_y , and r_z are the distance of two points in the streamwise, normal, and spanwise directions respectively. This implies that R_{ww} and R_{vv} are self-similar.

The rotation angle θ in the Fig.4.13, where $y_1^+ = 178$, is roughly 25° .

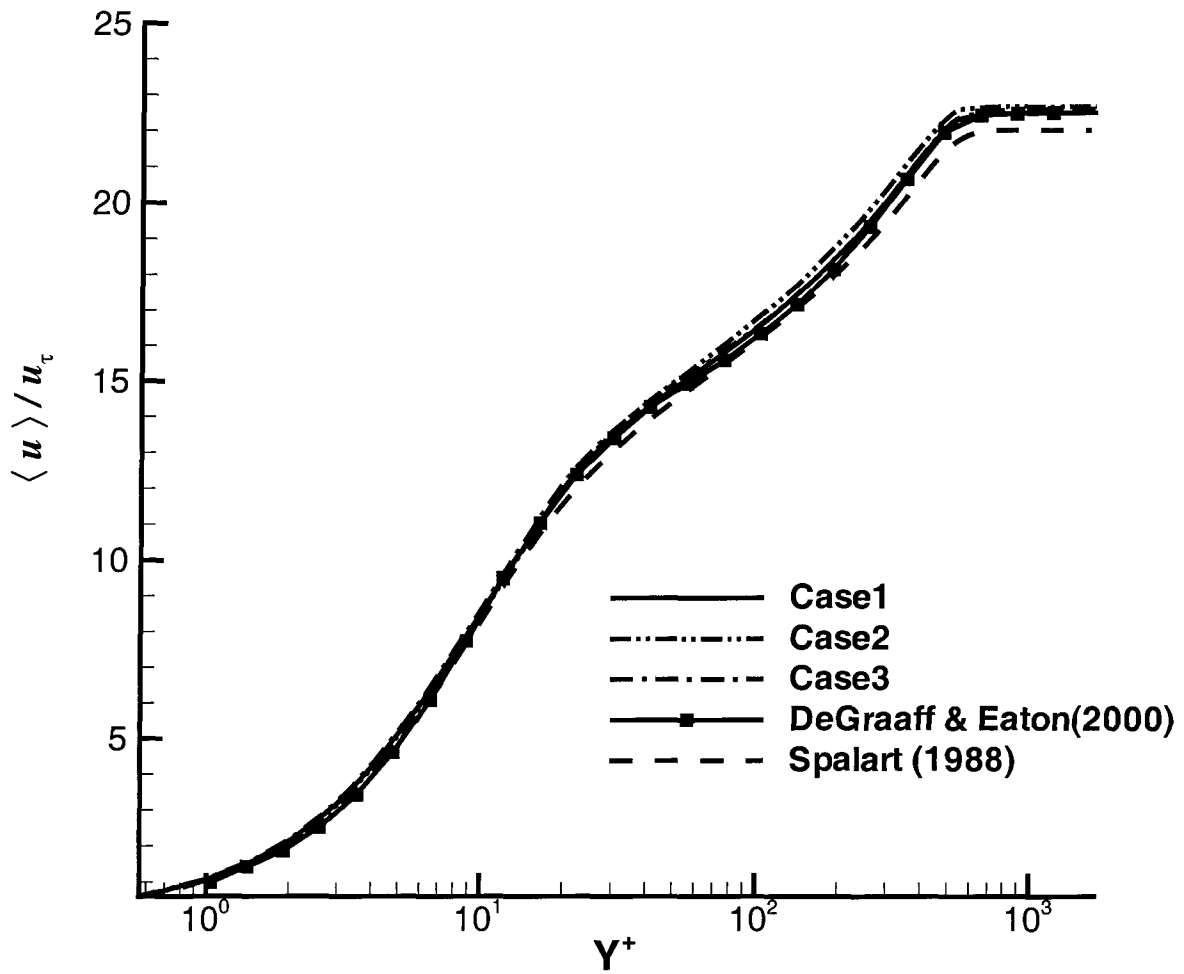


Figure 4.1 The comparison of the present mean streamwise velocity profile with the DNS results reported by Spalart (1988) and experimental data reported by DeGraaff and Eaton (2000).

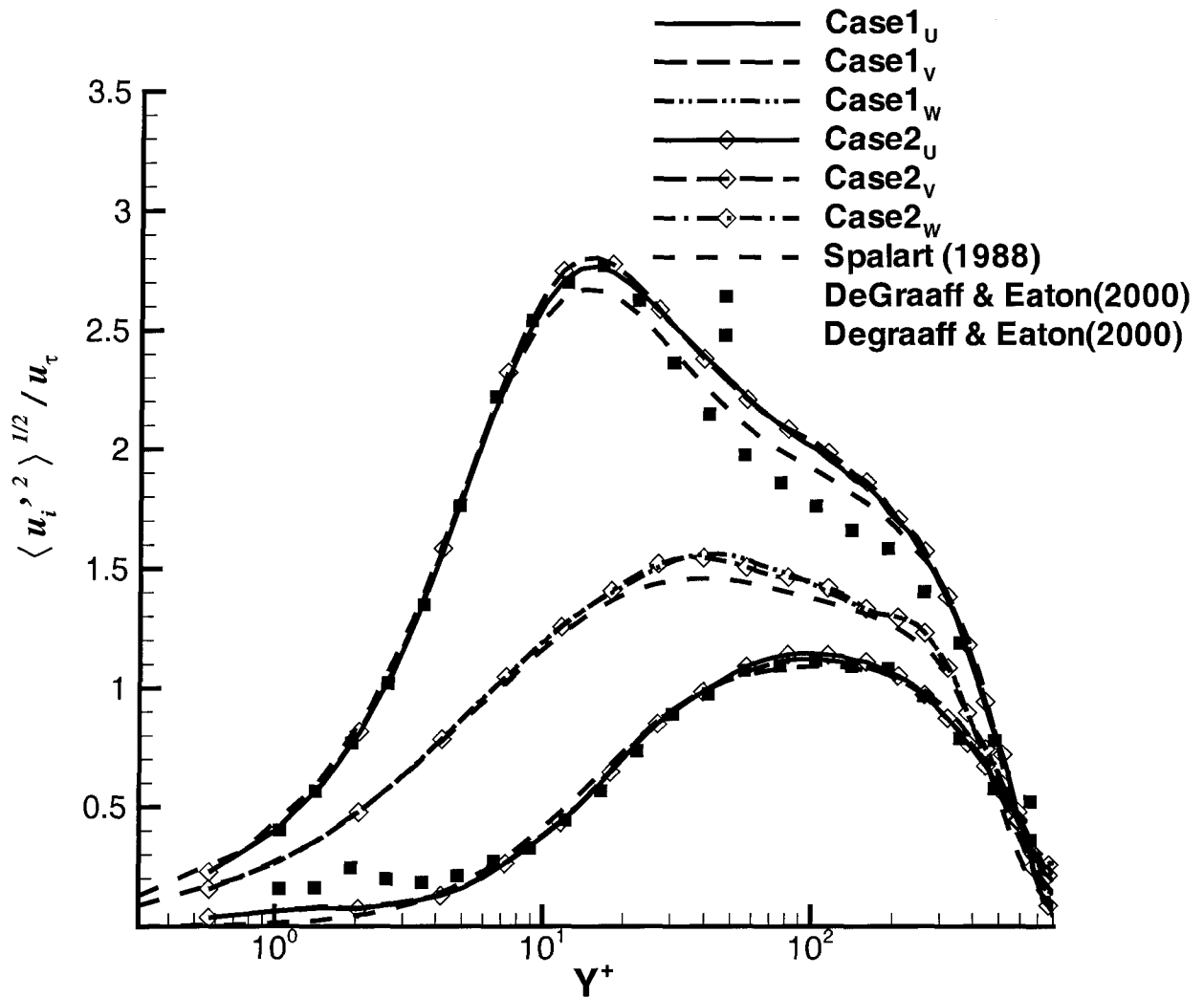


Figure 4.2 Comparison of the present rms profiles of the turbulence fluctuations with the DNS results reported by Spalart (1988) and experimental data reported by DeGraaff and Eaton (2000).

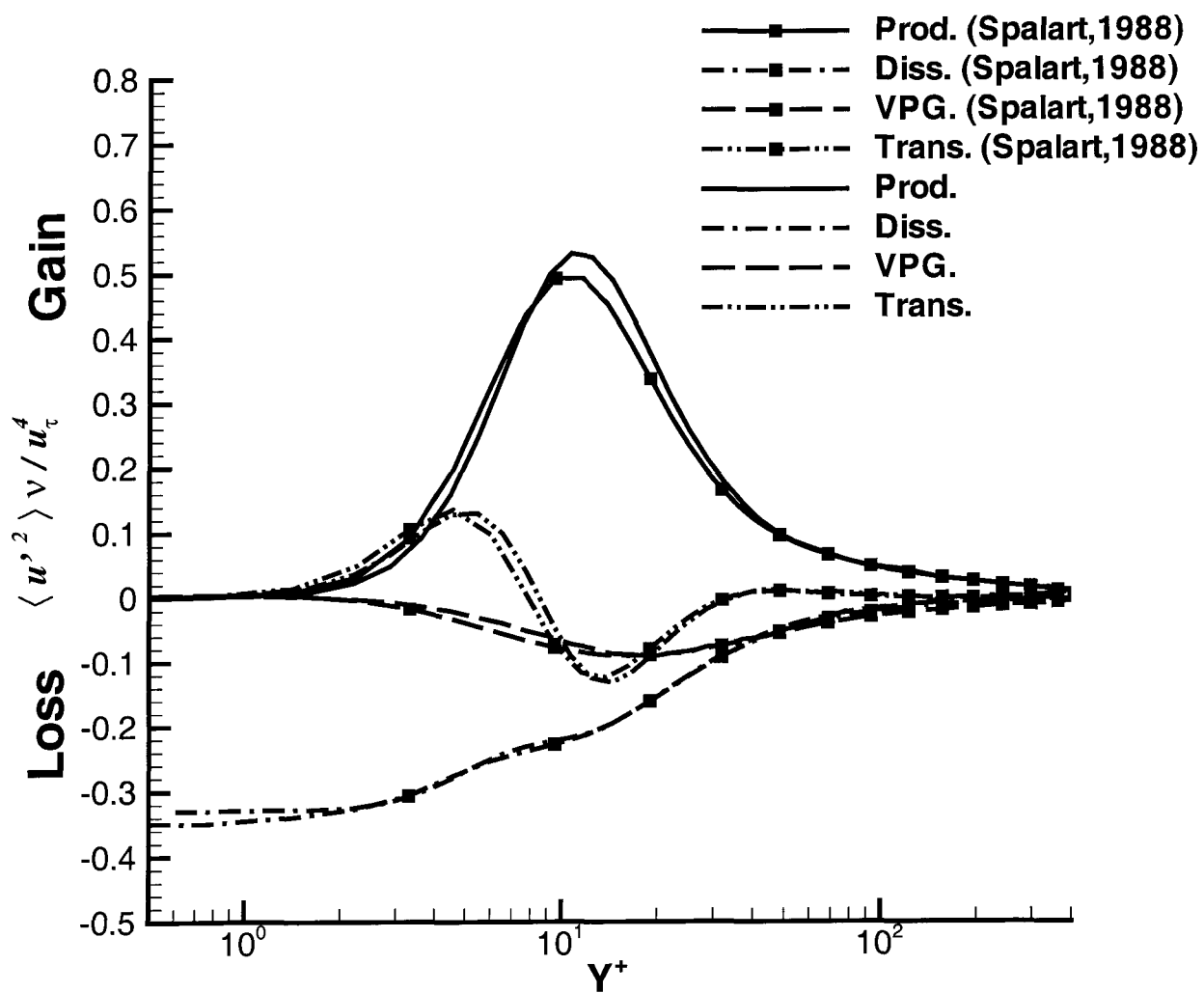


Figure 4.3 Reynolds stress budget of u^2 normalized by u_τ^4/ν .

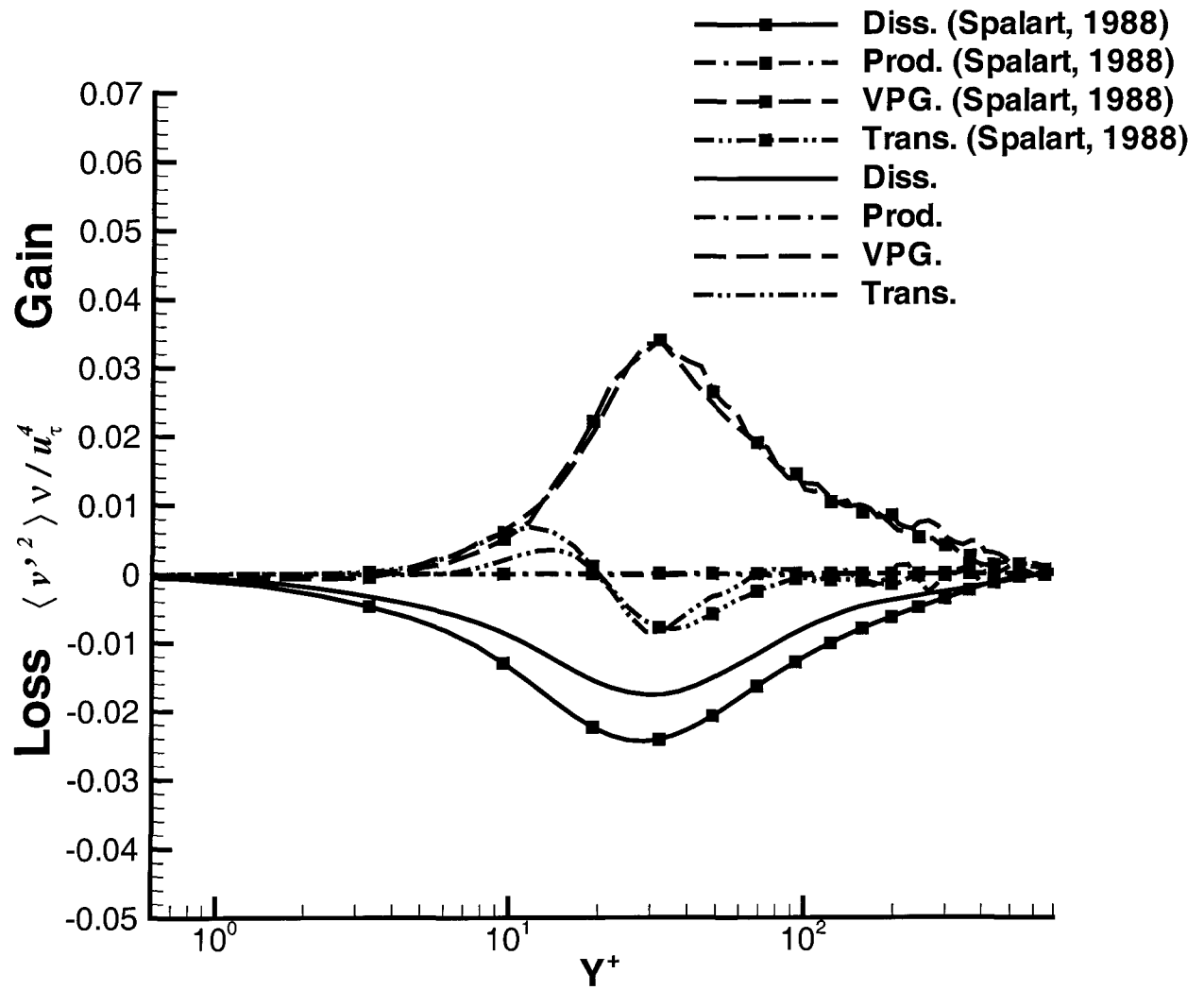


Figure 4.4 Reynolds stress budget of v^2 normalized by u_τ^4/ν .

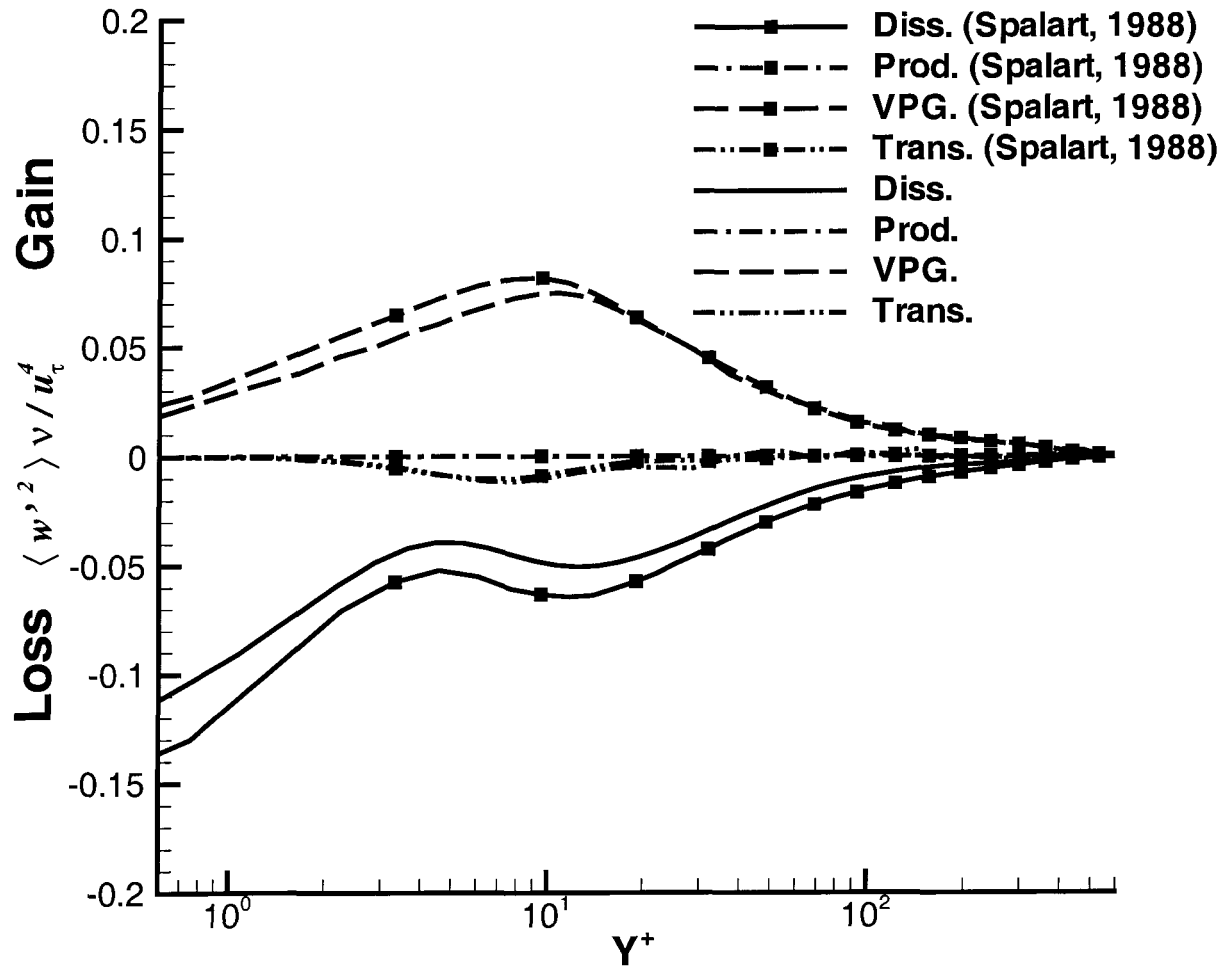


Figure 4.5 Reynolds stress budget of w^2 normalized by u_τ^4/ν .

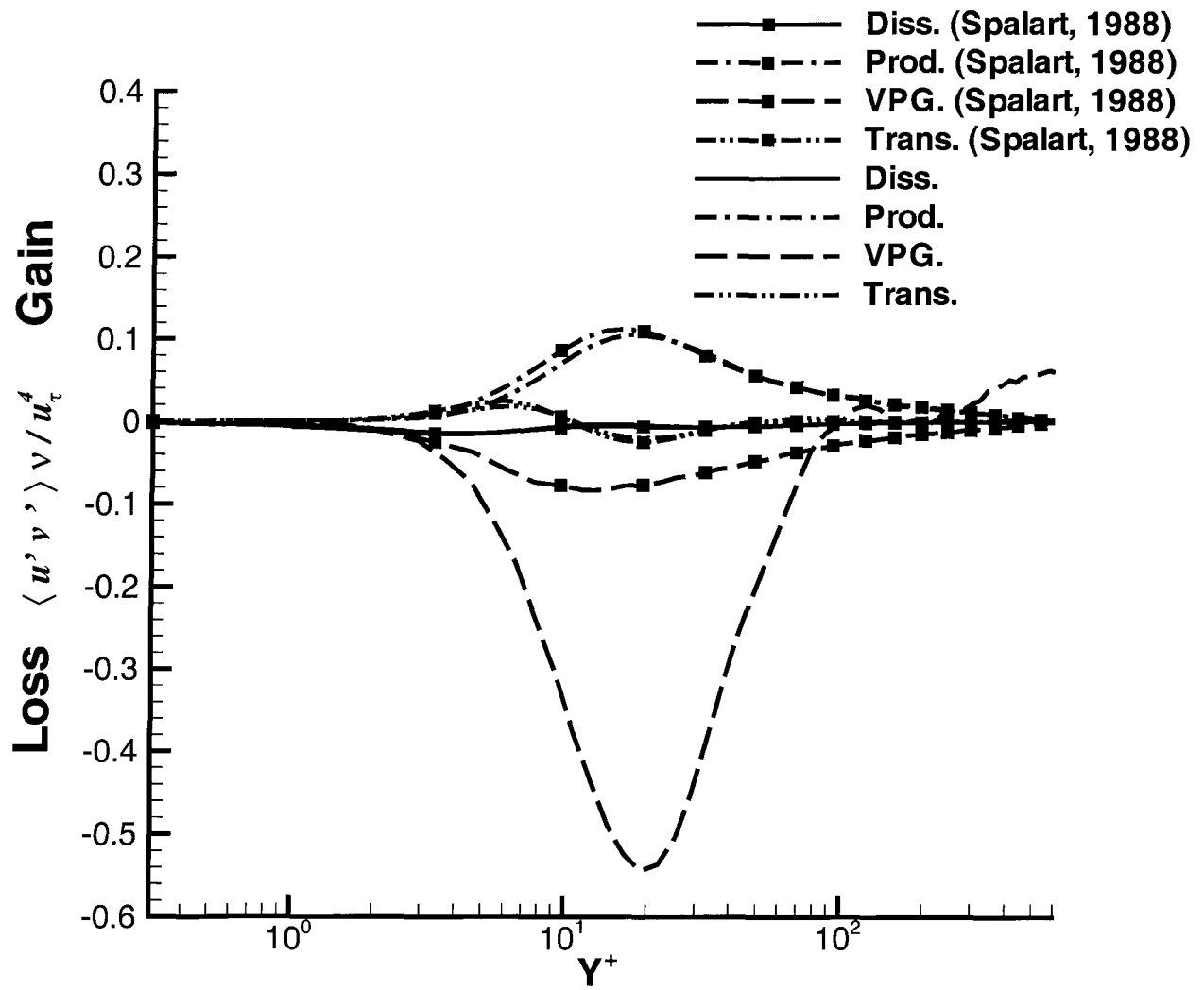


Figure 4.6 Reynolds stress budget of $-uv$ normalized by u_τ^4/ν .

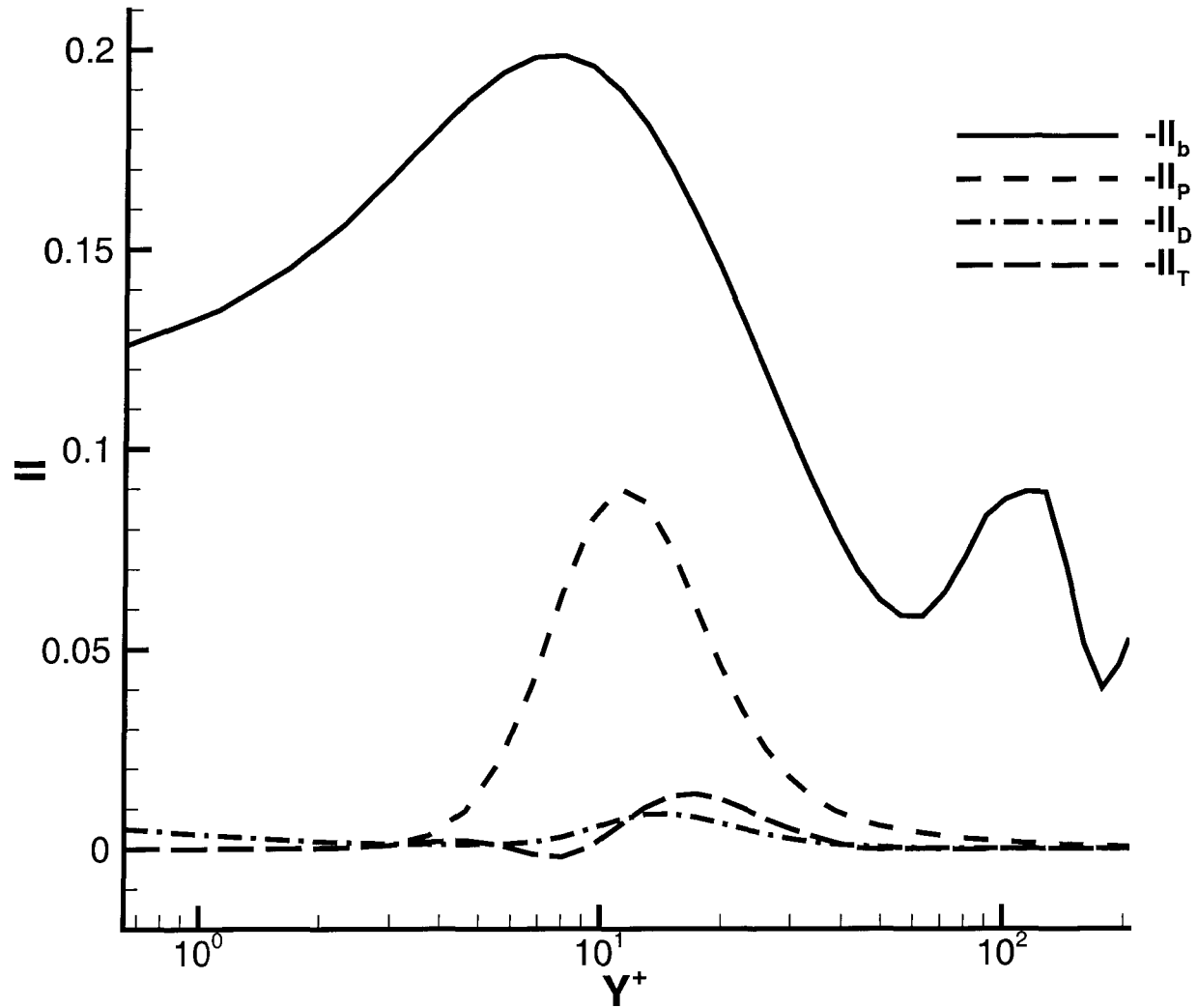


Figure 4.7 Comparison of the second invariance of the Reynolds stress anisotropic tensor b_{ij} ($-II_b$), the turbulent production anisotropic tensor \overline{P}_{ij} ($-II_P$), the turbulent dissipation anisotropic tensor $\overline{\varepsilon}_{ij}$ ($-II_D$), and the the turbulent transport anisotropic tensor \overline{T}_{ij} ($-II_T$).

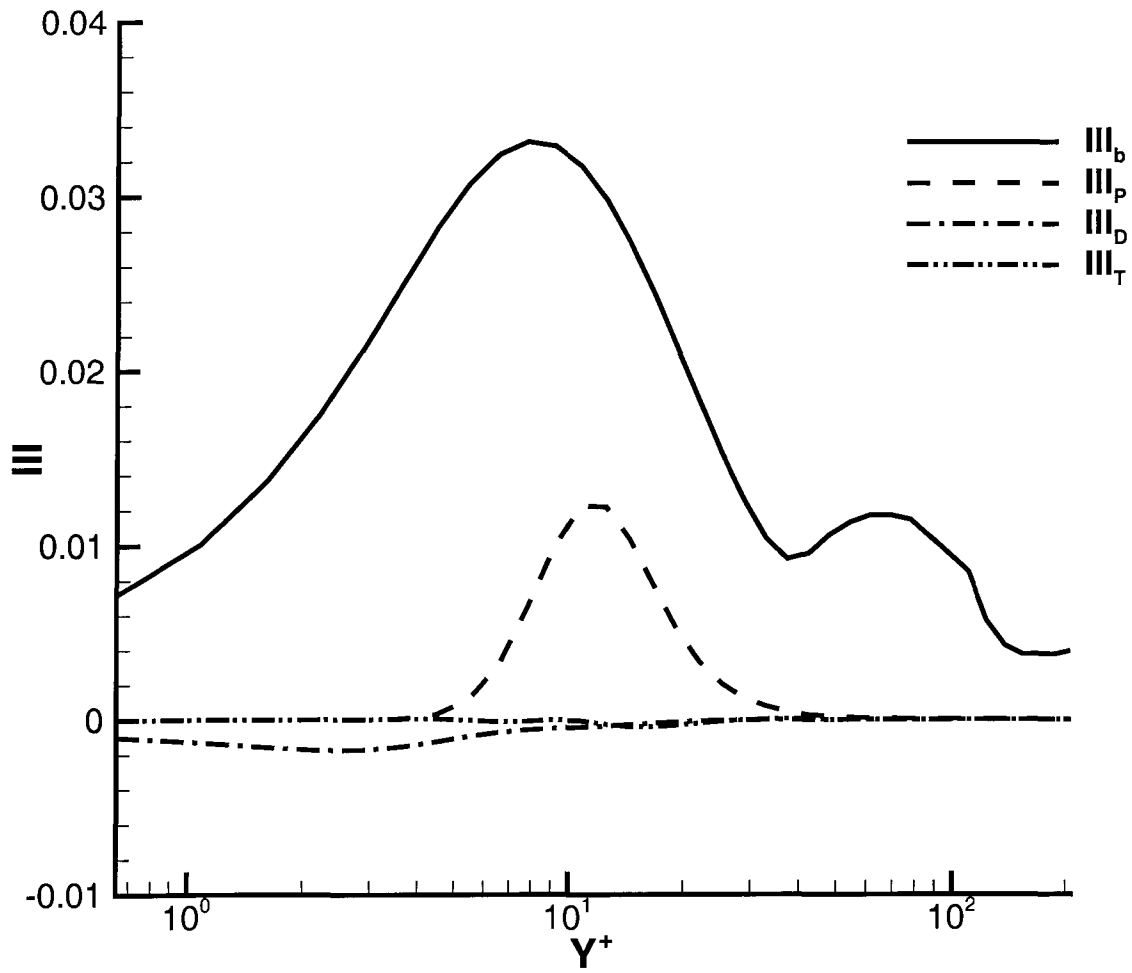


Figure 4.8 Comparison of the third invariance of the Reynolds stress anisotropic tensor b_{ij} (III_b), the turbulent production anisotropic tensor \overline{P}_{ij} (III_P), the turbulent dissipation anisotropic tensor $\overline{\varepsilon}_{ij}$ (III_D), and the the turbulent transport anisotropic tensor \overline{T}_{ij} (III_T).

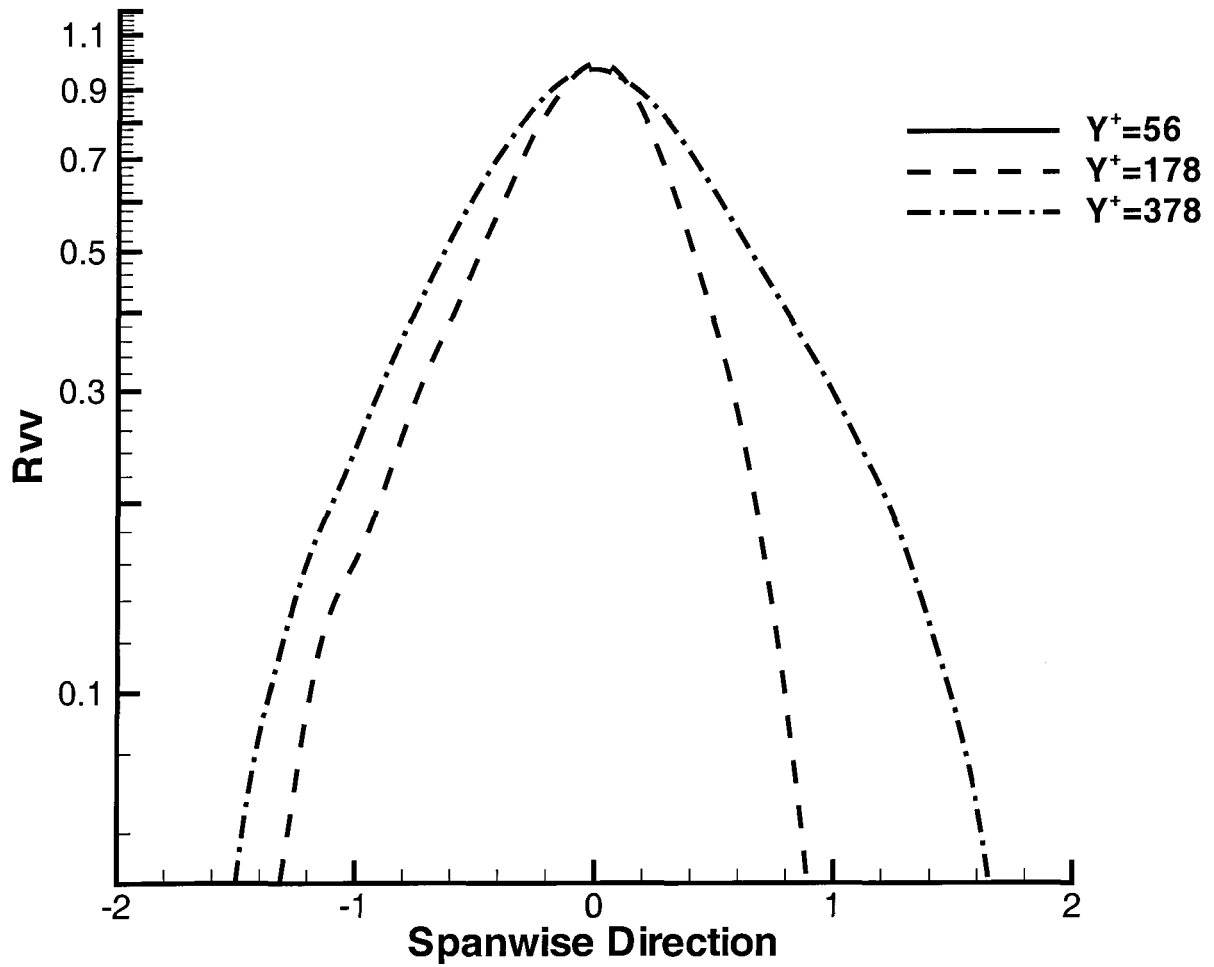


Figure 4.9 The log plot of the $R_{vv}(0,0,r_z;y_1)$, normalized by $R_{vv}(0,0,0;y_1)$, at the three different y_1 locations.

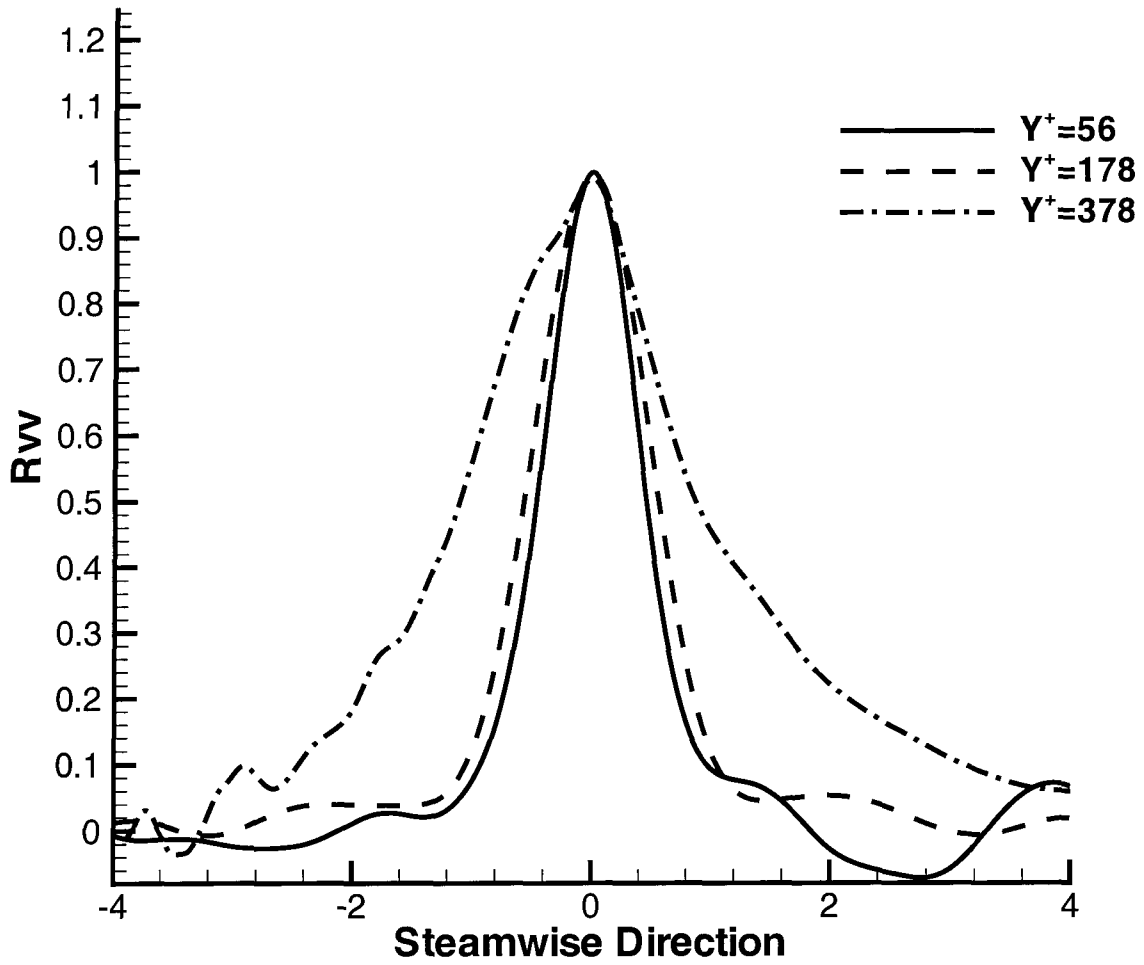


Figure 4.10 Plot of the $R_{vv}(r_x, 0, 0; y_1)$, normalized by $R_{vv}(0, 0, 0; y_1)$, at the three different y_1 locations.

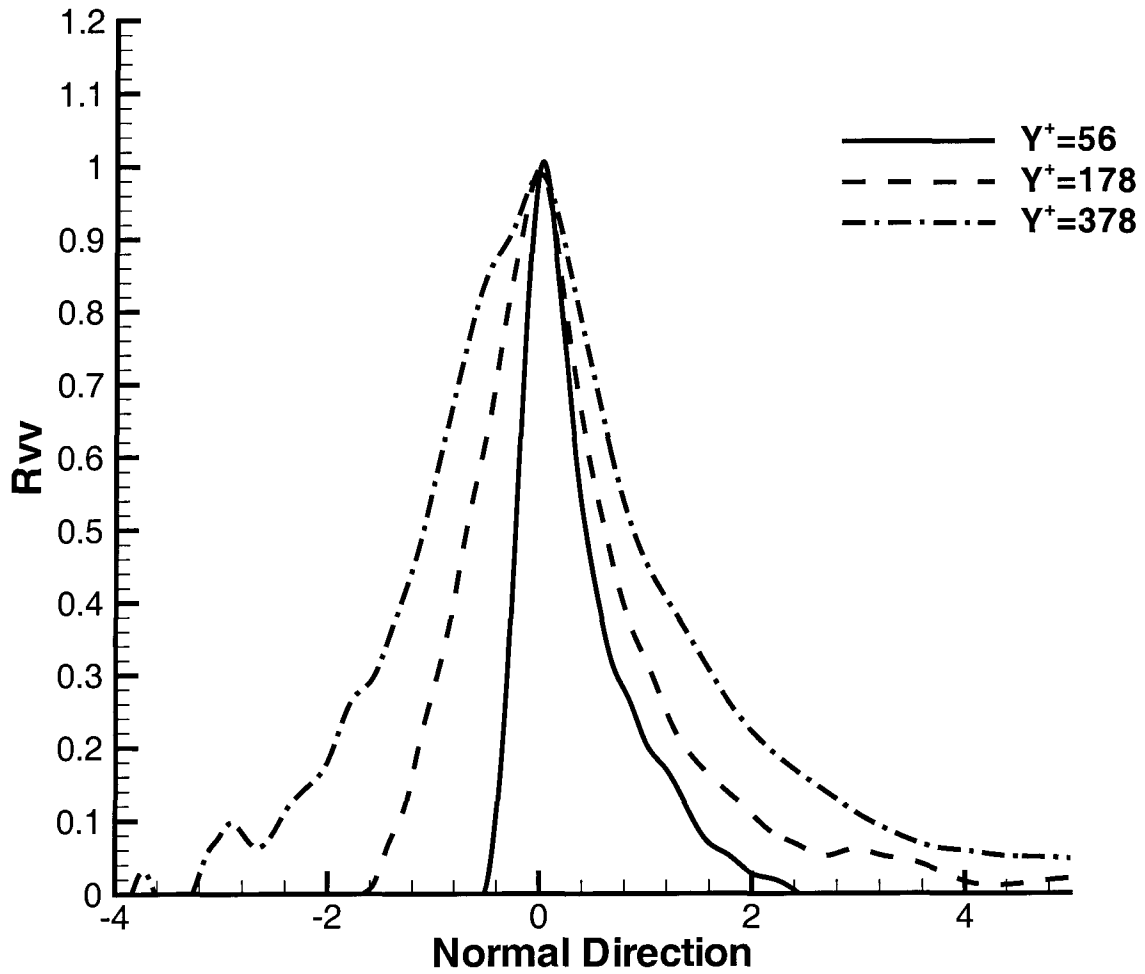


Figure 4.11 Plot of $R_{vv}(0, r_y, 0; y_1)$, normalized by $R_{vv}(0, 0, 0; y_1)$, at the three different y_1 locations.

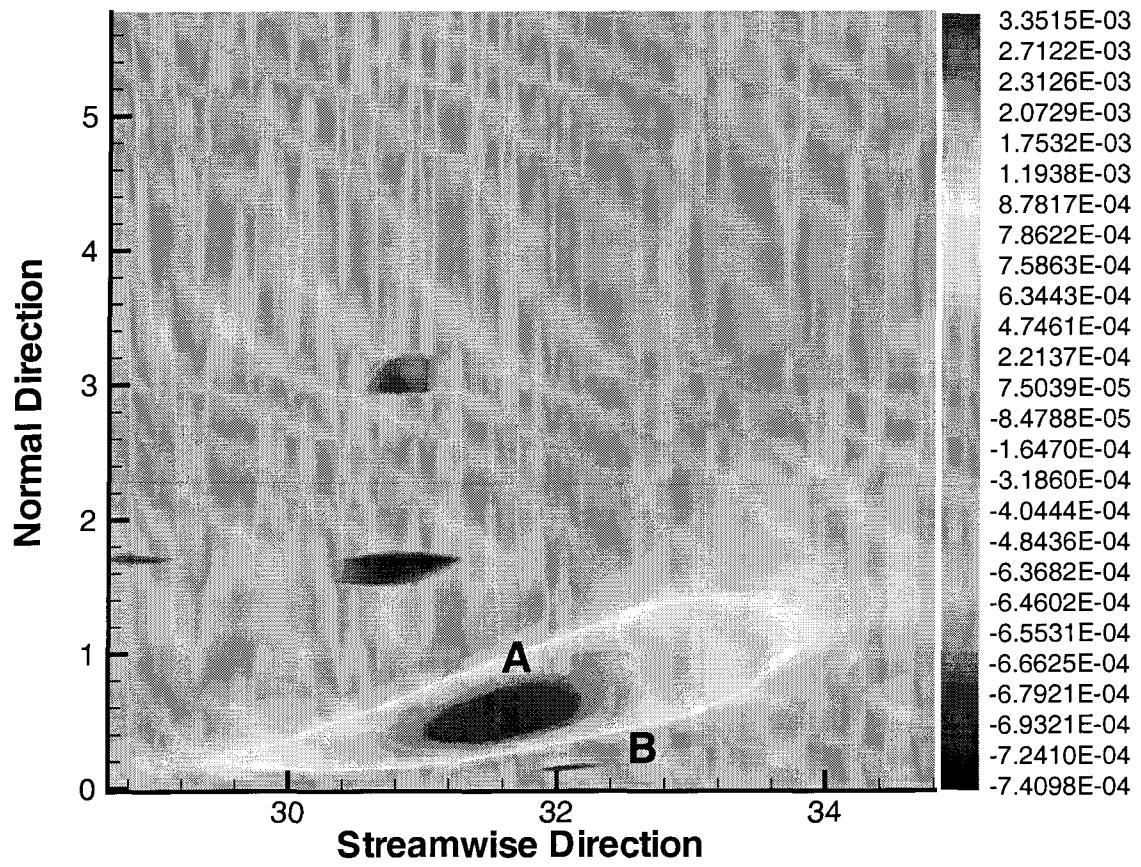


Figure 4.12 Plot of $R_{ww}(r_x, r_y, 0; y_1)$ normalized by $R_{ww}(0, 0, 0; y_1)$ where $y_1^+ = 56$.

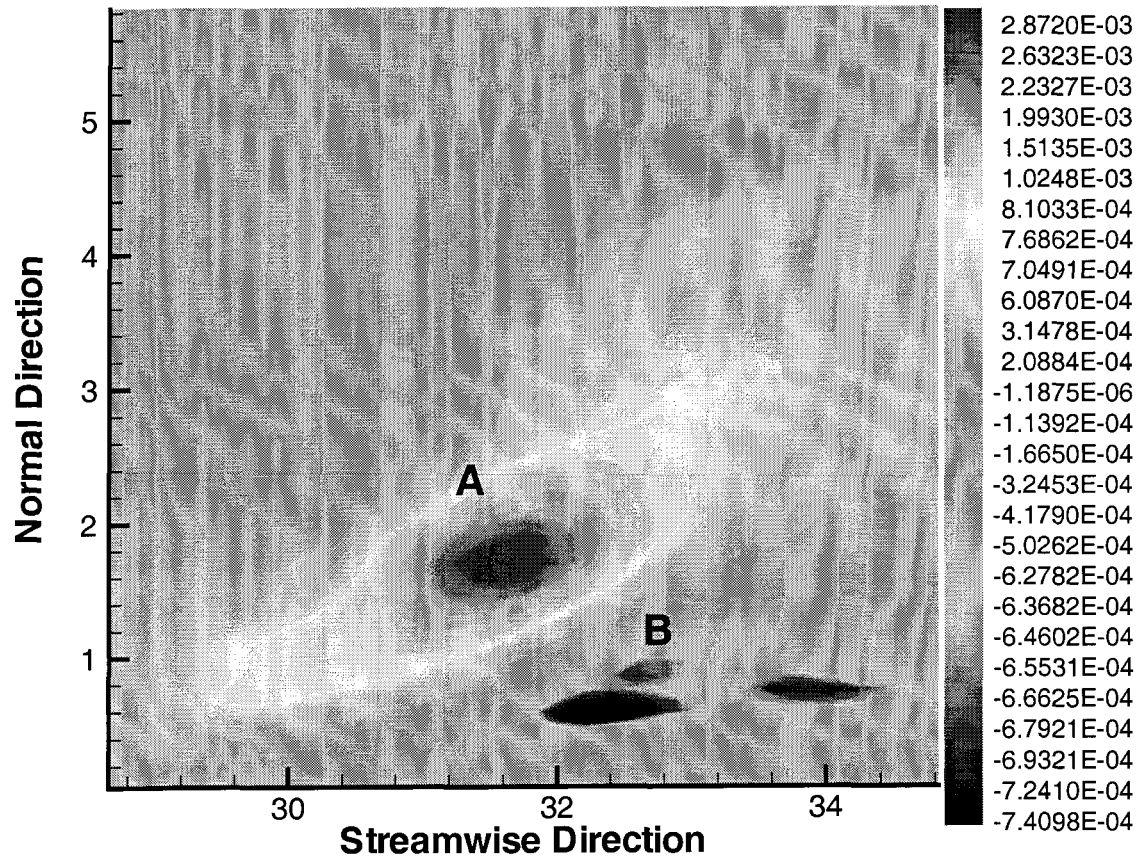


Figure 4.13 Plot of $R_{ww}(r_x, r_y, 0; y_1)$ normalized by $R_{ww}(0, 0, 0; y_1)$ where $y_1^+ = 178$.

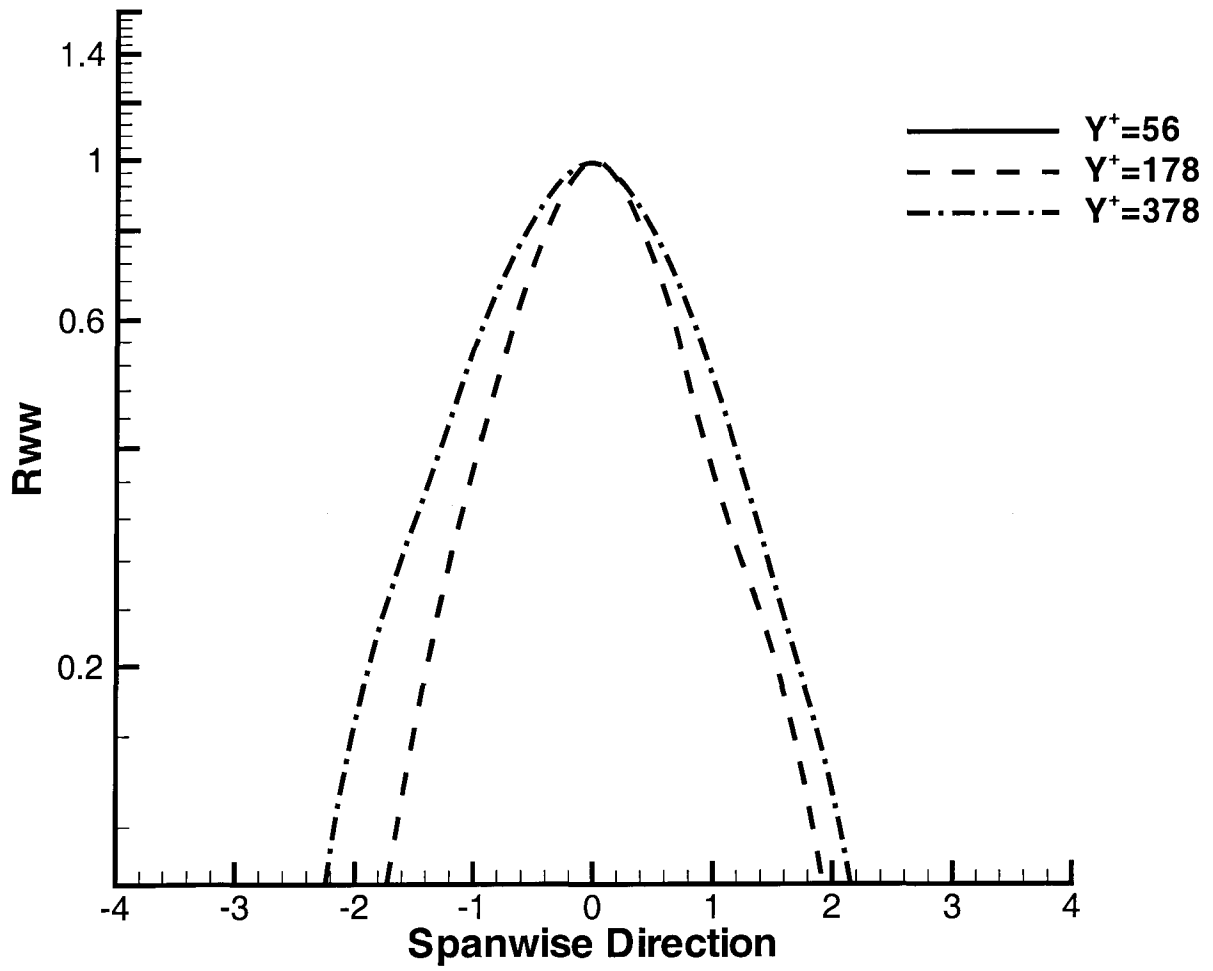


Figure 4.14 Plot of $R_{ww}(0, 0, r_z; y_1)$, normalized by $R_{ww}(0, 0, 0; y_1)$, at the three different y_1 locations.

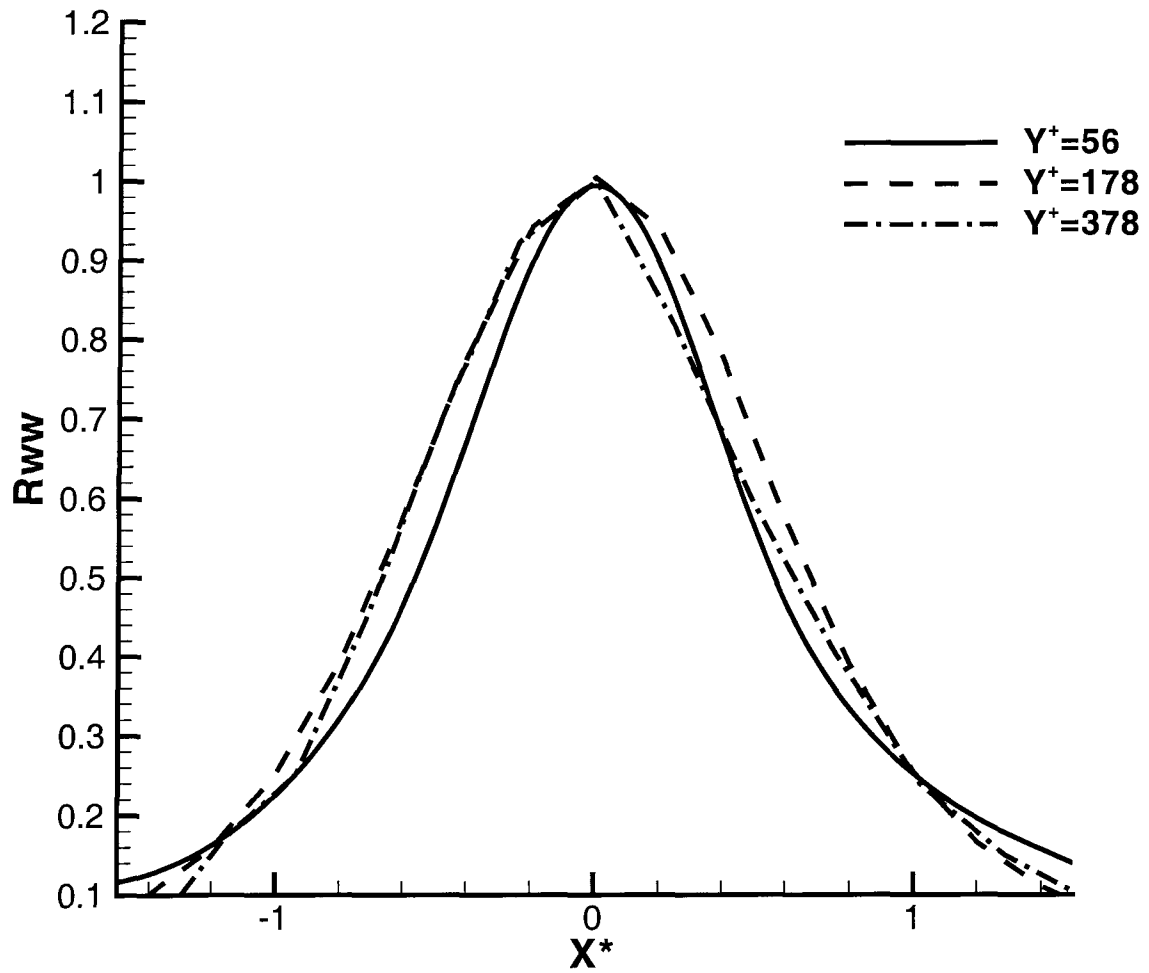


Figure 4.15 Plot of $R_{ww}(r_x, 0, 0; y_1)$, normalized by $R_{ww}(0, 0, 0; y_1)$, at the three different y_1 locations.

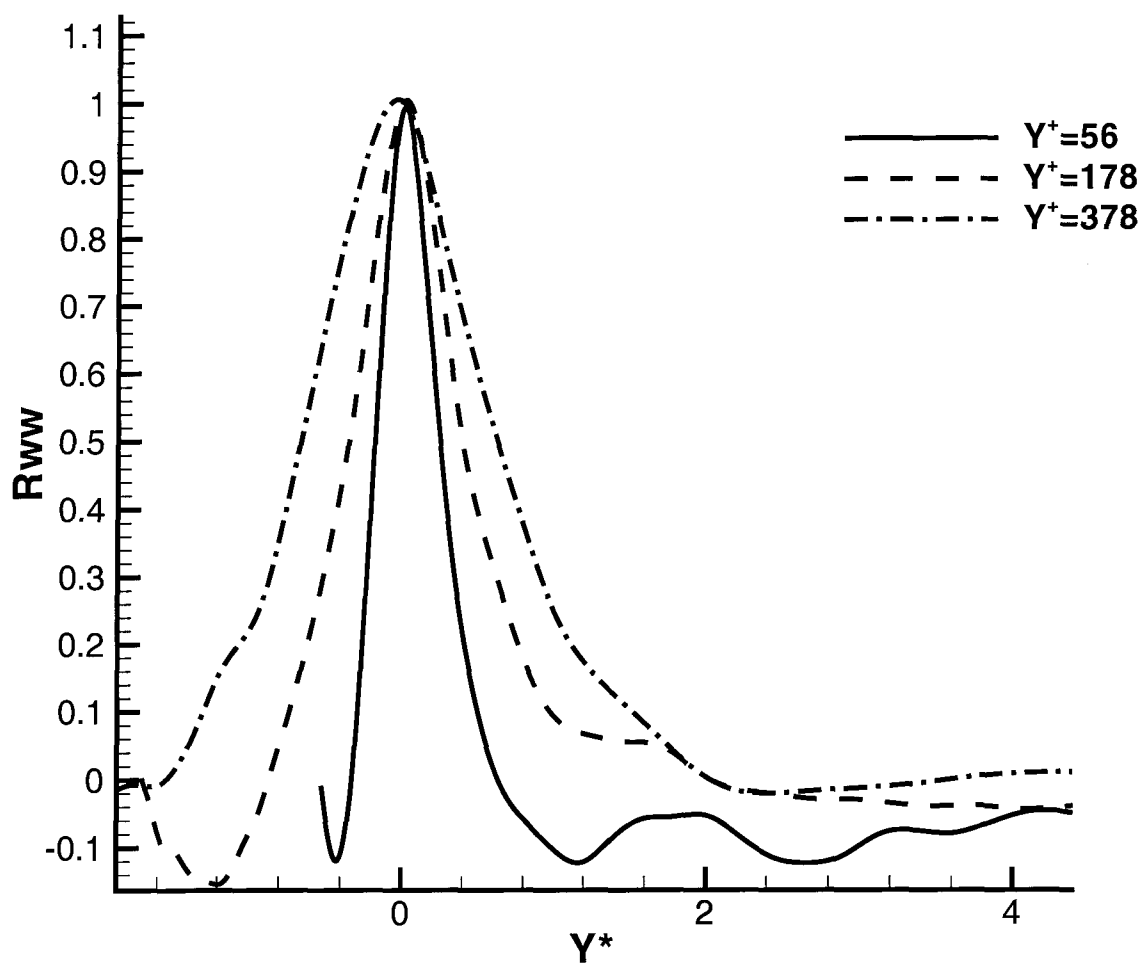


Figure 4.16 Plot of $R_{ww}(0, r_y, 0; y_1)$, normalized by $R_{ww}(0, 0, 0; y_1)$, at the three different y_1 locations.

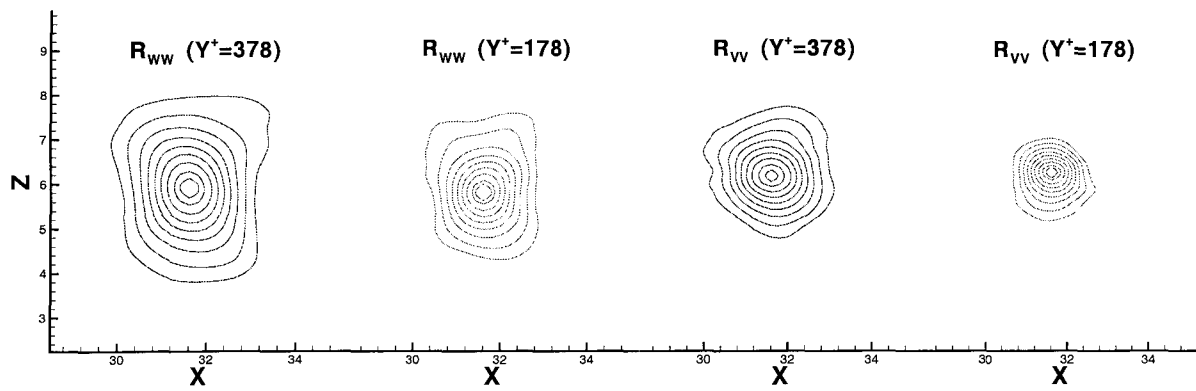


Figure 4.17 R_{ww} and R_{vv} correlations at $Y^+ = 378$ and $Y^+ = 178$. The contour levels range from 0.1 to 0.9 with increments of 0.1.

CHAPTER 5. COMPRESSIBILITY EFFECTS AND VARIABLE DENSITY EFFECTS OF TURBULENT BOUNDARY LAYERS

Two compressible turbulent boundary layers have been calculated by using direct numerical simulation. One case is a subsonic turbulent boundary layer with constant wall temperature $T_w = 1.58T_e$ for which the flow is incompressible, and the other is a supersonic adiabatic turbulent boundary layer subjected to a supersonic free-stream with a Mach number 1.8. The purpose of this study is to test the strong Reynolds analogy, the Van Driest transformation, and the applicability of Morkovin's hypothesis. For the first case, the influence of the variable density effects will be addressed. For the second case, the role of the density fluctuations, the turbulent Mach number, and dilatation on the compressibility will be investigated. The results show that the Van Driest transformation and the strong Reynolds analogy are satisfied for both of the flows. Use of local properties enable the statistical curves to collapse the corresponding incompressible curves. These facts reveal that both of the compressibility and variable density effects satisfy the similarity laws. A study about the differences between the compressibility effects and the variable density effects associated with heat transfer are performed. In addition, the difference between the Favre average and Reynolds average are measured, and the SGS terms of the Favre-filtered Navier-Stokes equations are calculated and analyzed.

5.1 Introduction

The compressibility of flows is a measure of the volume change or density change of fluids as a response to a pressure change, $\beta = -\frac{1}{V} \frac{\partial V}{\partial P}$ or $\beta = \frac{1}{\rho} \frac{\partial \rho}{\partial P}$, under the circumstance that the substantial derivative of the density is nontrivial or the velocity is not divergence-free. In this manner, if the pressure gradient or pressure variation is large enough to effect a substantial

change in the density of the flow, such a flow is compressible. The effects associated with the volume change of the fluid elements in response to the pressure change are regarded as compressibility effects (Lele (1994)). For gases, the density is a function of pressure and temperature. Thus, for the flows with heat transfer, the major contribution of the density change may be from the temperature change rather than the pressure change. Such flows are nearly incompressible but the substantial change in the density is nonzero. Otherwise, the system will be inconsistent because assuming the zero substantial derivative of density will add one more equation to the Navier-Stokes equations while the number of the variables does not increase. In order to distinguish such density changes from the compressibility effects, we call the effects associated with the density change in response to the temperature changes rather than the changes in the pressure the variable density effects. Clearly, for both situations, the governing equations are the compressible Navier-Stokes equations. This will be discussed in detail in section 5.2.1.

In low Mach number flows, the influence of density fluctuations on the turbulent boundary layer is negligible as long as the mean density remains constant across the boundary layers (Bradshaw (1977)). Such flows usually are treated as incompressible flows. However, the density varies with the distance from the wall once heat transfer is involved. The density changes that occur with heat transfer can greatly deform the turbulent structures. As a result, the mean velocity profiles will eventually be deformed even though the Mach number is small (Nicoud and Bradshaw (2000)). The nonzero gradient of the mean density will cause a nontrivial distribution of the substantial derivative of density. Thus, flows will be incompressible but have large density variations because of the temperature fluctuations. For instance, owing to the equation of state, $\frac{d\rho}{\rho} = \frac{dP}{P} - \frac{dT}{T}$. The magnitude of the pressure is significantly larger than that of the density and temperature for the low Mach number flows. Thus, $\frac{dP}{P}$ is negligible compared with $\frac{d\rho}{\rho}$ and $\frac{dT}{T}$. This implies that flows are incompressible.

Huang *et al.* (1993) and Nicoud and Bradshaw (2000) suggested using density-weighted transformations, which are similar to the Van Driest transformation, to modify the velocity profiles. In this manner the similarity laws for incompressible flows can be applied to com-

compressible turbulent boundary layers or incompressible turbulent boundary layers with a heated wall. Note that Huang *et al.* (1993) dealt with compressible flows but Nicoud and Bradshaw (2000) dealt with incompressible flows with strong heat transfer. Therefore, it is worthwhile to compare the influence of the compressibility effects and variable density effects on the validation of the Van Driest transformation. Also, based on the assumption that $\overline{u'v'}$ profile is not modified by the heating, Meignen and Berthoud (1998) formulated the law of the wall and the defect law for strongly heated subsonic turbulent boundary layers. In this chapter, we will check this assumption and test the Van Driest transformations by using the direct numerical simulations.

When the adiabatic turbulent boundary layer is supersonic, the compressibility effects will have a dramatic influence on the flows. Conversely, for a heated subsonic turbulent boundary layer, the variable density effects will have a significant influence on the flows. More specifically, compressibility effects and variable density effects will deform the first and second order statistics of velocities and pressure, change the turbulent kinetic energy budget, adjust the anisotropy tensor b_{ij} , and amend the energy transport between the different turbulent components. The compressibility or variable density effects on the turbulent flows are represented by following components: density fluctuations, gradient of the mean density, pressure dilatation, and temperature fluctuations, etc. To sketch the differences between both effects, the density fluctuations and gradient of the mean density are calculated.

The magnitude of the density fluctuations may be independent of the Mach number. The earlier experiments found that the density fluctuations can be neglected if the free-stream pressure gradient is small (Bradshaw (1977)) for a compressible turbulent boundary layer with a Mach number less than 5, especially in the outer part of the turbulent boundary layer, which is fundamental to Morkovin's hypothesis. However, the very recent DNS results for a supersonic turbulent boundary layer with heat transfer at a Mach number of 2.5 (Guarini *et al.* (2000)) and a thermal turbulent channel flow at the Mach number 1.5 (Morinishi *et al.* (2004)) show that $\rho_{rms}/\bar{\rho}$ is approximately 0.05 in the near wall region. LES results for a turbulent channel flow at the Mach number 0.01 with the significant heat transfer show that

$\rho_{rms}/\bar{\rho}$ is approximately 0.08 in the near wall region Wang and Pletcher (1996). Indeed, even 0.05 is not a negligible number for turbulent wall shear flows. (For instance, v_{rms}/u_τ is of this level in a large Reynolds number range from $Re_\theta = 1000$ to $Re_\theta = 3000$, where v_{rms} is the rms of the normal component of velocity and Re_θ is the Reynolds number based on the momentum thickness). In this sense, the contribution of the density fluctuations to the compressibility effects or variable density effects in the inner part of the wall shear flow is underestimated for the wall shear flows that have a Mach number less than 5. To check the value of $\rho_{rms}/\bar{\rho}$, we calculate an adiabatic supersonic turbulent boundary layer with the Mach number 1.8. Moreover, we consider the effect of heat transfer on density fluctuations for the low Mach number flows.

In addition to the influence of density fluctuations, the large gradient of the mean density profiles $\partial\bar{\rho}/\partial y$ has a significant influence on the mass and heat transfer of flows. It causes the lifting of the turbulent coherent structures in the boundary layers, which further deform the large eddies even when $M_e < 5$ (Bradshaw (1977)). Eventually, the statistical profiles and the heat and mass transfer in the boundary layer are modified. Such lifting behavior relates to the mean density gradient. Usually, this lifting process is a part of the variable density effects which change the convection of the boundary layers.

One influence of the compressibility on the flow is the energy transfer from kinetic energy to internal energy. This process is not reversible. The extra dissipation resulting from the compressibility relates to the turbulent Mach number $M_t = q/c$ (q is a velocity scale characteristic of the turbulence and c is a representative speed of sound), the density variance $\rho_{rms}/\bar{\rho}$, the mean of the density, and the pressure dilatation (Lele (1994)). Note that, by the continuity equation, the mean of density is associated with the mean of the dilatation $\theta = \frac{\partial u_i}{\partial x_i}$ and the density fluctuation is associated with the dilatation fluctuation θ' because $\frac{D\rho}{Dt} + \theta = 0$. For an adiabatic compressible supersonic turbulent boundary layer (ACSTBL), the order of the magnitude of density fluctuation, turbulent Mach number M_t , and the pressure dilatation depends on the temperature difference across the flow. Thus, its energy transfer from the kinetic energy to the internal energy is driven by the gradient of the mean density, and the molecular

viscosity and the solenoidal part of turbulent viscosity, which are dominated by dissipation and largely independent of compressibility effects. The increasing M_t is usually associated with the increasing density fluctuations $\rho_{rms}/\bar{\rho}$ (Lele (1994)). When M_t is in excess of 0.2-0.3, the compressibility effects become significant (Bradshaw (1974)). DNS results reported by Guarini *et al.* (2000) show that the local M_t exceeds 0.2 in most of the inner part of the supersonic turbulent boundary layer at Mach number 2.5. This implies that the compressibility dramatically deforms the near wall turbulent structures even though the M_t is less than 5. Thus, the local distribution of M_t must be argued in order to investigate the compressibility effects. Unlike the isotropic turbulence, the pressure dilatation $\Pi_d := \overline{p'\theta'}$ makes a significant contribution to the transformation of the turbulent kinetic energy (Lele (1994)). Rapid distortion theory (Durbin and Zeman (1992)) anticipates the dependence of pressure dilatation on the compressibility. These features correspond to the acoustic waves and are distinct from the subsonic wall shear flows. To distinguish the compressibility effects from the variable density effects, the turbulent Mach number M_t , the density fluctuations $\rho_{rms}/\bar{\rho}$, and the dilatation fluctuation θ' are calculated for both compressible and incompressible flows.

An important issue associated with the compressibility and variable density effects is the Favre average (Favre (1983)). To account for the compressibility and variable density effects, a mass-weighted averaging, Favre-filtering, was suggested. This idea is similar to the Van Driest transformation. Without the compressibility and variable density, the Favre average is equivalent to the Reynolds average. Therefore, the influence of the compressible and variable density effects on the deviation of the Favre average from the Reynolds average should be discussed.

By using the Favre average, the Navier-Stokes equations are modified. Several additional terms are produced. These terms need to be modeled for LES schemes. However, information about the influence of Mach number and heat transfer on these additional terms in the Favre-filtered Navier-Stokes equations is lacking. To provide further information for the LES modeling, we calculate both the compressible and incompressible flows by using DNS and then evaluate these Favre-filtered terms.

In summary, this chapter will focus on testing the strong Reynolds analogy, calculating the density fluctuations for both of the cases, determining the difference between Favre average and Reynolds average for velocities, and illustrating the influence of Mach number and heat transfer on additional terms in the Favre-filtered Navier-Stokes equations.

5.1.1 Numerical Configurations

The fractional step method proposed in this dissertation was utilized for the calculation of the turbulent boundary layers. A periodic boundary condition was utilized in the spanwise direction. A characteristic boundary condition (Liu and Pletcher (2006)) was applied at the outlet and a dynamic recycling inlet method (Liu and Pletcher (2006)) was employed to generate the fully developed turbulent boundary layer. Two cases were calculated by DNS: The first case was a turbulent boundary layer with Reynolds number 2000 based on the displacement thickness at the Mach number $M_e = 0.06$ with a constant temperature heated wall, $T_w = 1.58T_e$. Case 2 was an adiabatic supersonic turbulent boundary layer at Mach number 1.8, where the Reynolds number is 2000 based on the displacement thickness. Although case 2 was adiabatic, the wall temperature of the turbulent boundary layer was $1.58T_e$ because of the viscous heating effects.

The numerical mesh for all of three cases were the same, which was uniform in the streamwise and spanwise directions, but was stretched in the normal direction, and $\Delta y_{\min}^+ = 0.38$, $\Delta y_{\max}^+ = 65$, $\Delta x^+ = 18.4$, and $\Delta z^+ = 5$. The nondimensional time step $\Delta t^+ = 0.2\delta_d/U_\infty$. The numerical mesh was $240 \times 90 \times 192$ corresponding to streamwise, normal, and spanwise directions, respectively.

5.2 Results and Discussion

5.2.1 Compressibility and Variable Density Effects

To check the validation of the numerical simulations, we plot the first and second order statistics of both cases.

For purpose of comparison, a density-weighted transformation proposed by Huang *et al.* (1993) was utilized to modify the velocity,

$$U^c = \sqrt{B}[\sin^{-1}(\frac{A+u}{D}) - \sin^{-1}(\frac{A}{D})]$$

where

$$A = q_w/\tau_w, \quad B = \frac{2C_{pe}T_w}{Pr_t}, \quad D = \sqrt{A^2 + B}$$

The subscript $_w$ stands for a wall property, and subscript $_e$ stands for the free stream property. Figure 5.1 shows the comparison of modified velocity U^c and u^+ with experimental results of an incompressible turbulent boundary layer. This figure indicates that the velocity profiles are deformed due to the change of the density across the boundary layer. Such a deformation causes u^+ to depart from the law of the wall. However, the modified velocity U^c conforms to the law of the wall. These numerical results match the theoretical and experimental conclusions proposed by Huang *et al.* (1993). The results confirm that the similarity laws can be approximately satisfied if the density-weighted transformation is applied.

Although the wall temperature was the same for both cases, $u_{\tau_{wall}}$ were different. Considering that the maximum value of U^+ is $1.0/u_{\tau_{wall}}$, through Fig. 5.1, we see that both the heat transfer and high Mach number will increase $u_{\tau_{wall}}$, but such a change contributed by heat transfer is larger.

Fig.5.2 displays the rms profiles of velocities, which were normalized by the local properties as $U_{rms}^+ = \frac{U_{rms}}{U_{\tau,local}}$ and $Y^+ = Y \frac{U_{\tau,local}}{\nu_{local}}$, where $U_{\tau,local}$ uses the wall shear stress but local density. More precisely, $U_{\tau,local} = \sqrt{\frac{\rho}{\rho_{wall}}} U_{\tau,wall}$. The magnitude and location of maximum U_{rms}^+ agree with Spalart (1988)'s DNS results. By using the local properties, the U_{rms}^+ of the turbulent boundary layer on a heated wall nearly coincides with the distribution for an isothermal incompressible turbulent boundary layer. The DNS and experimental results are both for a Reynolds number of 2000 based on the inlet displacement thickness. The agreement is generally good.

Fig.5.3 shows $-\overline{u'v'}/U_{\tau,local}$ plotted against $Y^+ = Y \frac{U_{\tau,local}}{\nu_{local}}$. The distributions agree well with the corresponding incompressible curve, particularly in the inner part of the boundary

layer. This does not agree the assumption made by Meignen and Berthoud (1998) for their mixing length formula, which said that $\overline{u'v'}$ does not change with the heat transfer.

Fig.5.4 shows the mean and RMS of density for both cases. The results show that the wall density is the same for both cases because the wall temperature is the same. But, over most of the boundary layer, the subsonic flow with strong heat transfer has a larger density compared with the supersonic flow. Since the mean pressure gradient is very small for both cases, the larger density implies a lower temperature and internal energy. Although the wall temperature is the same for both cases, the internal energy is larger for Case 2. For both flows, the maximum value of the RMS of density is approximately equal. In the near wall region, the RMS of density of Case 1 is larger than that of Case 2. Conversely, Case 2 has a larger value of the RMS of density compared with Case 1 in the outer part of boundary layer. For both cases, the amplitude of density fluctuations is over 5% of the free stream density. Morinishi *et al.* (2004) found the density fluctuation of the compressible turbulent channel flows at Mach number 1.5 is of the same level. Wang and Pletcher (1996) reported that the amplitude of the density fluctuation can even be 9% of the free stream density for the turbulent channel flows if the heat transfer is strong enough. These results show the influence of variable density effects on the density fluctuations.

As we described above, there are five quantities associated with the compressibility of flows, which are Mach number M , turbulent Mach number M_t , the mean of the dilatation θ , turbulent dilatation $\overline{\theta'^2}$, and the pressure dilatation $\overline{p'\theta'}$. To check the compressibility of the turbulence, we calculated the mean and the rms of dilatation θ . Fig.5.5 shows the mean of the dilatation, $\overline{\theta}\delta_d/u_\tau$, and the rms of the dilatation, $\sqrt{\overline{\theta'^2}}\delta_d/u_\tau$, where δ_d is the inlet displacement thickness, $\overline{\theta} = \frac{\partial \overline{u_i}}{\partial x_i}$ and $\overline{\theta'^2} = \overline{(\frac{\partial u'_i}{\partial x_i})^2}$. The results show that the value of $\overline{\theta}$ is nontrivial and reaches a peak value in the buffer zone for both the subsonic and supersonic turbulent boundary layers. Moreover, the heat transfer will lead to a nontrivial distribution of θ' even when the Mach number is a factor 16 smaller than the sound speed. Again from Fig.5.5, we notice that variable density effects make a larger contribution to the density changes in terms of $\overline{\theta}$ compared with compressibility effects even though the flows have the same wall

same wall temperature. However, compressibility effects make a larger contribution to the turbulent dilatation. For the subsonic flows, although the heat transfer will cause the variable density effects, the fluctuations of θ or density are still very weak. They achieve the maximum values in the buffer zone. For the supersonic flow, much of the kinetic energy is transferred to internal energy in the near wall region. This feature leads to the strong density fluctuations. Although Case 1 is incompressible, its governing equation should be the compressible Navier-Stokes equations because $\bar{\theta}$ and $\overline{\theta'^2}$ are all nontrivial.

Morkvin (1962) suggested that the turbulence is weakly affected by compressibility provided the RMS fluctuations of the Mach number $M' \leq 0.2$. Guarini *et al.* (2000) reported that when the Mach number is 2.5, the peak values of M' and the turbulent Mach number M_t , $M_t = \frac{\overline{u'_i u'_i}}{\alpha}$, of an adiabatic turbulent boundary layer are approximately 0.3. To illustrate the compressibility of the cases 1 and 2, M_t is plotted in Fig.5.6. The results show that the subsonic flow at a Mach number of 0.06 has a very small M_t , although its density and temperature vary as functions of time and space because of the heat transfer. The supersonic adiabatic turbulent boundary layer at Mach number 1.8 still exhibits a fairly strong compressibility in the inner part of the turbulent boundary layer.

The strong Reynolds analogy was proposed by Morkvin (1962), which suggested that

$$-\frac{T'}{C_p \overline{u'_1 u'_1}} \approx 1 \quad (5.1)$$

and

$$\text{Pr}_t = \frac{\overline{u_1 u_2} (\partial \overline{T} / \partial y)}{\overline{T u_2} (\partial \overline{u_1} / \partial y)} \approx 1 \quad (5.2)$$

Fig.5.7 shows the value of Pr_t and $-\frac{\overline{T'}}{C_p \overline{u'_1 u'_1}}$ as functions of Y^+ . The results show that the strong Reynolds analogy was satisfied for Case 2, but was violated in Case 1. $-\frac{\overline{T'}}{C_p \overline{u'_1 u'_1}}$ was close to zero at all of the boundary layer region for Case 1, while the formula (5.1) was obeyed at most parts of the boundary layer region for case 2. In addition, the turbulent Prandtl number Pr_t was approximately 0.88 in the inner part of the boundary layer, which is close to 1.0. However, the lower Mach number subsonic turbulent boundary layer, case 1, does not satisfy the strong Reynolds analogy even though the turbulent heat transfer is involved. The

turbulent Prandtl number Pr_t is around 0.9 in the inner part of the boundary layer for Case 1. However, case 1 violates the formula (5.1), which is based on the assumption that the total temperature fluctuations are negligible compared to the static temperature fluctuations.

5.2.2 Favre Average

As we described above, the compressible Navier-Stokes equations should be solved if strong heat transfer is involved in wall shear flows even though the Mach number of flows is low. To account for property changes, a mass-weighted averaging is recommended. Favre-filtering (Favre (1983)) are usually utilized for this purpose. Here, we use DNS to evaluate various subgrid scale quantities that appear in the filtered equations used in LES, some of these terms are usually modeled in LES but some are often neglected. The Favre-filtered compressible Navier-Stokes equations are

$$\frac{\partial \bar{\rho}}{\partial t} + \frac{\partial(\bar{\rho}\tilde{u}_j)}{\partial x_j} = 0 \quad (5.3)$$

$$\frac{\partial(\bar{\rho}\tilde{u}_i)}{\partial t} + \frac{\partial(\bar{\rho}\tilde{u}_i\tilde{u}_j)}{\partial x_j} = -\frac{\partial \bar{p}}{\partial x_i} + \frac{\partial \bar{\sigma}_{ij}}{\partial x_j} - \frac{\partial \tau_{ij}}{\partial x_j} \quad (5.4)$$

$$\frac{\partial(\bar{\rho}\hat{E})}{\partial t} + \frac{\partial[(\bar{\rho}\hat{E} + \bar{p})\tilde{u}_j]}{\partial x_j} = \frac{\partial(\tilde{u}_i\bar{\sigma}_{ij})}{\partial x_j} - \frac{\partial \bar{q}_j}{\partial x_j} - \frac{\partial Q_j}{\partial x_j} - \gamma - \pi - \varepsilon \quad (5.5)$$

The effects of the small-scale motions are present in the above equations through the subgrid-scale (SGS) stress tensor, τ_{ij} , in the momentum equation as

$$\tau_{ij} = \bar{\rho}(\widetilde{u_i u_j} - \tilde{u}_i \tilde{u}_j)$$

and the SGS terms that are the last four terms on the right hand side of Eq. 5.5 as:

$$Q_j = \bar{\rho}c_v(\widetilde{T u_j} - \tilde{T} \tilde{u}_j),$$

$\gamma = \tilde{u}_i \frac{\partial \tau_{ij}}{\partial x_j}$, $\pi = \overline{p \frac{\partial u_j}{\partial x_j}} - \bar{p} \frac{\partial \tilde{u}_j}{\partial x_j}$ and $\varepsilon = \overline{\sigma_{ij} \frac{\partial u_i}{\partial x_j}} - \hat{\sigma}_{ij} \frac{\partial \tilde{u}_j}{\partial x_j}$ where Q_j is the SGS heat flux vector.

The overtilde and overline, $\widetilde{(\bullet)}$ and $\overline{(\bullet)}$, stands for the Favre average and Reynolds average, respectively. More precisely, $\tilde{\phi} = \frac{\overline{\rho \phi}}{\bar{\rho}}$. A dynamic model proposed by Moin *et al.* (1991) and recommended by Lilly (1992) provides a solution for the SGS stress tensor τ_{ij} and heat flux vector \bar{q}_j in the Favre-filtered equations. The terms γ , π , and ε can be neglected for the low

Mach number flows (Vreman *et al.* (1995)). However, for flows with moderate Mach numbers, the influence of γ , π , and ε on the heat transfer may be significant. Thus, the changes in γ , π , and ε due to the Mach number and heat transfer should be addressed not only for the modeling of the Favre-filtered equations but also for the understanding of turbulent heat and mass transfer. In this section, we are going to illustrate the effect of Mach number and heat transfer on the Favre average, τ_{ij} , γ , and π .

Considering that

$$\tilde{u} - \bar{u} = \frac{\overline{\rho u}}{\bar{\rho}} - \bar{u} = \frac{\overline{\rho' u'}}{\bar{\rho}},$$

to present the difference between the Favre average and Reynolds average, we plot Fig. 5.8. More precisely, $(\tilde{u}_1 - \bar{u}_1)/u_\tau$. The maximum value in Fig. 5.8 is a factor of 20 smaller than that of Fig. 5.2 for both of the cases. This implies that the difference between the Favre average and Reynolds average exists but is small. And such a difference can be neglected under the circumstance that 5% errors are acceptable for turbulence modeling.

The subgrid-scale (SGS) stress tensor can be decomposed as

$$\begin{aligned} \tau_{ij} &= \overline{\rho(\tilde{u}_i \tilde{u}_j - \tilde{u}_i \tilde{u}_j)} = \overline{\rho u'_i u'_j} + \overline{\rho' u'_i u'_j} - \overline{\rho' u'_j \rho' u'_i} / \bar{\rho} \\ &= \tau_{ij_t} + \tau_{ij_c} + \tau_{ij_F} \end{aligned}$$

the first term $\tau_{ij_t} = \overline{\rho u'_i u'_j}$ is associated with the mean density $\bar{\rho}$ and the Reynolds SGS stress tensor $\overline{u'_i u'_j}$, where $\overline{u'_i u'_j} = \overline{u_i u_j} - \bar{u}_i \bar{u}_j$, the second term $\tau_{ij_c} = \overline{\rho' u'_i u'_j}$ relates to the compressible part of τ_{ij} , and the last term $\tau_{ij_F} = \overline{\rho' u'_j \rho' u'_i} / \bar{\rho}$ describes the contribution of the difference between Favre and Reynolds average. Fig. 5.9 gives a comparison of those components. The results show that the major contribution of τ_{11} and τ_{22} is from $\overline{\rho u'_1 u'_1}$ and $\overline{\rho u'_2 u'_2}$ respectively. The compressibility and the variable density effects do not have a significant effect on τ_{11} and τ_{22} .

Fig.5.10 plots γ and π for both cases, where $\gamma = \tilde{u}_i \frac{\partial \tau_{ij}}{\partial x_j}$ and $\pi = \overline{p \frac{\partial u_j}{\partial x_j}} - \bar{p} \frac{\partial \bar{u}_j}{\partial x_j}$. By Fig. 5.10, we found that both of γ and π take on larger values for case 1 compared with that of the case 2. This implies that heat transfer has a larger influence on γ and π compared with the compressibility effects if both flows have the same wall temperature. Clearly, π contains the

pressure dilatation $\overline{p' \frac{\partial u'_j}{\partial x_j}}$, which is the pressure dilatation relative to the compressibility. The magnitude of γ and π is of an order -3, which is much smaller than the amplitude of the heat flux. Thus, γ and π can be neglected even though the Mach number of flow is 1.8 and wall is $T_w = 1.58T_e$.

5.3 Conclusion

Two turbulent flows with a Reynolds number 2000 based on the displacement thickness was calculated by using DNS: Case 1 was an subsonic turbulent boundary layer at Mach number 0.06 over a heated wall and $T_w = 1.58T_e$ and Case 2 was an adiabatic supersonic turbulent boundary layer at a Mach number of 1.8. The heat transfer driven by the heated wall will cause the variable density effects of the turbulent boundary layer even when the Mach number of flows is as small as 0.06. The results show that the Van Driest transformation can help to collapse the mean profiles of velocity to the corresponding incompressible curves. By using the local properties, the RMS of velocities for both of the flows can approach the incompressible curves. These facts reveal that both of the compressibility and variable density effects satisfy the similarity laws. The compressibility effects have a different contribution to the fluctuations of the dilatation compared with the variable density effects. The turbulent dilatation of supersonic flows is stronger than that of the lower Mach flows if the wall temperature is the same. The calculation of M_t indicates that the Mach number 1.8 is large enough to produce the compressibility in the inner part of the turbulent boundary layer. The strong Reynolds analogy proposed by Morkvin (1962) was tested. The results indicate that the Morkvin's hypothesis is obeyed by the adiabatic supersonic turbulent boundary layer at Mach number 1.8. The variable density effect has a large influence on the density fluctuations.

In addition, the Favre average is examined by this chapter. The difference between the Favre average and the Reynolds average was measured. The results show that such a difference is small compared with the rms of velocities for both cases. The SGS stress tensor τ_{ij} was evaluated; we found that τ_{ij} can be approximated by $\overline{\bar{\rho} u'_i u'_j}$. Furthermore, the calculation shows that γ and π are negligible even when the Mach number is 1.8 or for a low speed case

with a heated wall, $T_w = 1.58T_e$. These features help to simplify the turbulence modeling of compressible flows.

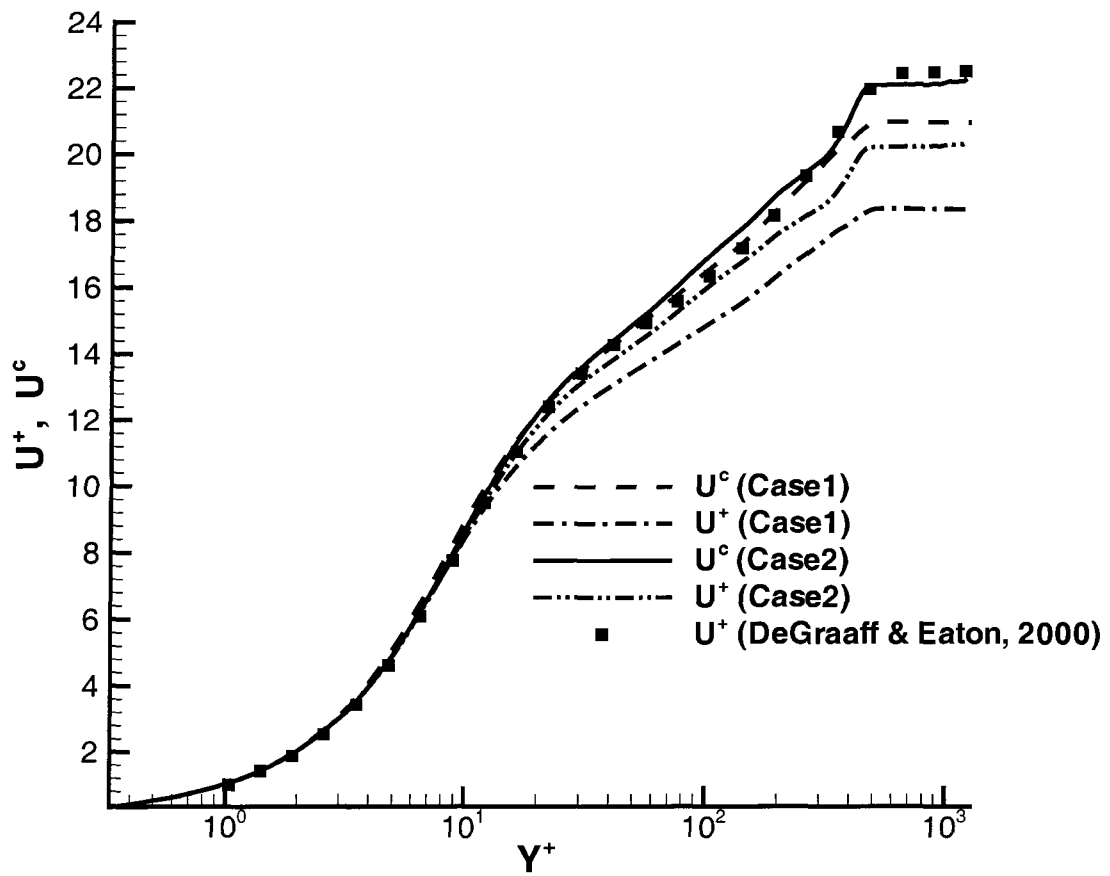


Figure 5.1 Comparison of mean streamwise velocity with experimental results reported by DeGraaff and Eaton (2000).

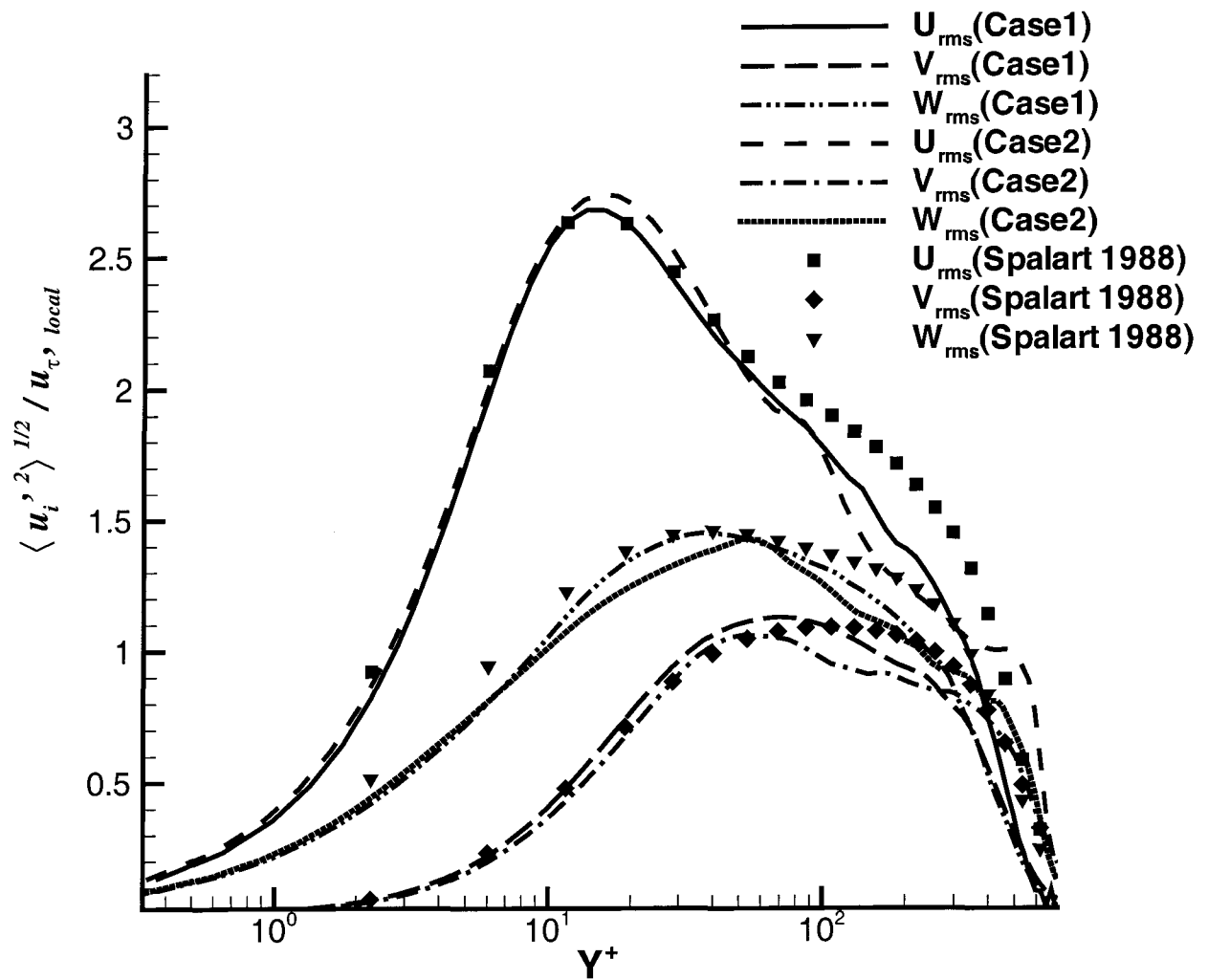


Figure 5.2 Comparison of rms profiles of velocity with the DNS results reported by Spalart (1988).

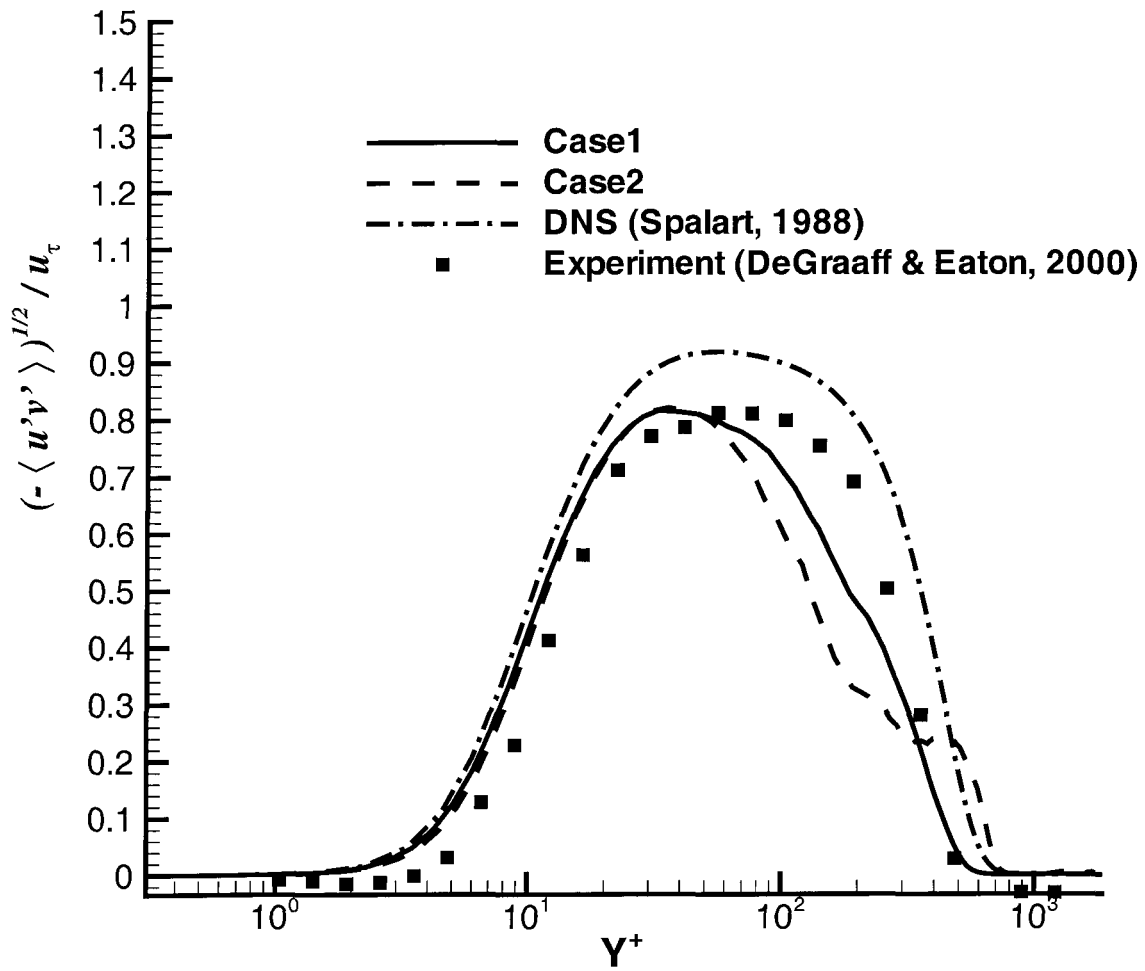


Figure 5.3 The plots of $\sqrt{-\overline{u'v'}} / U_{\tau,local}$ vs. Y^+ .

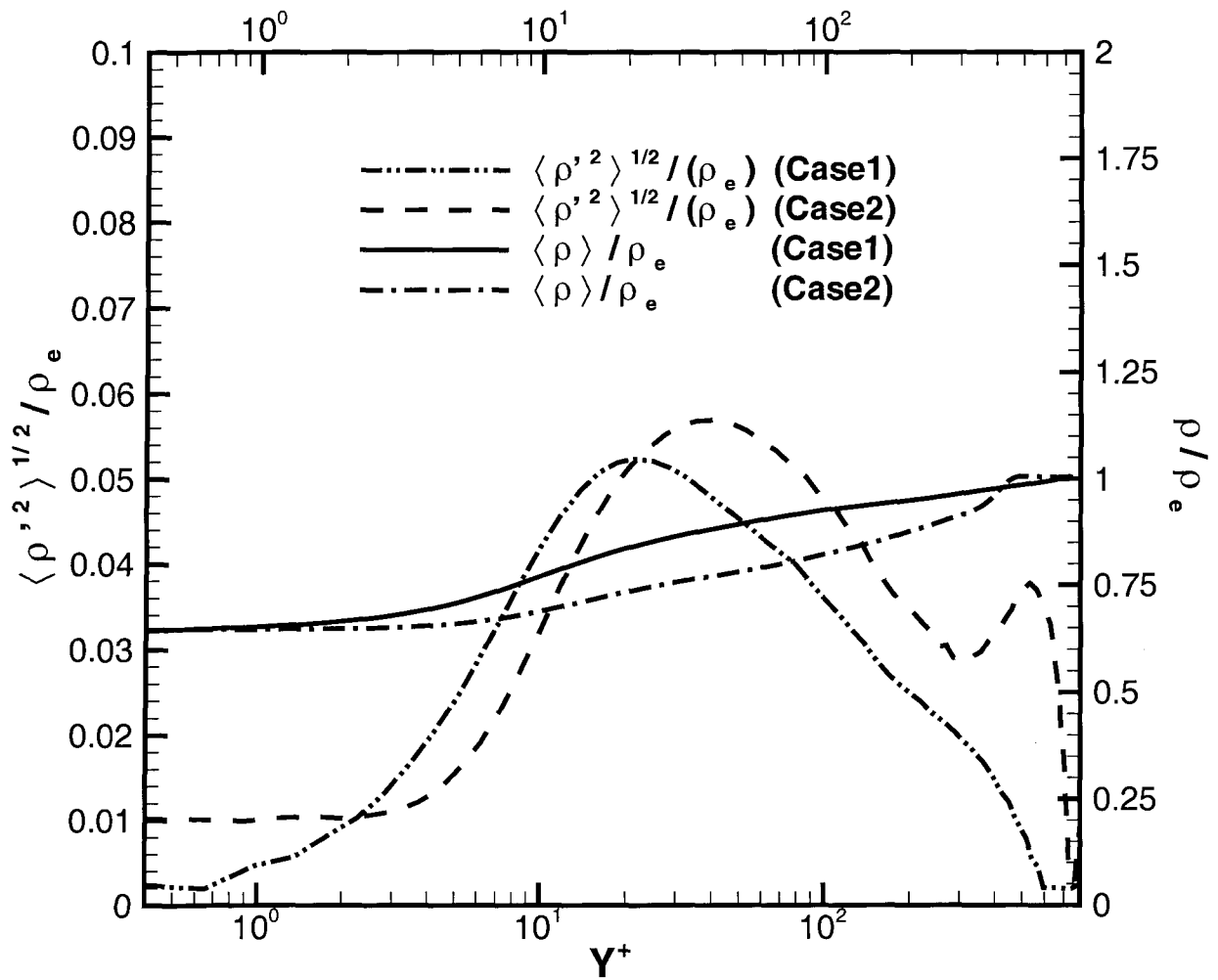


Figure 5.4 Plot of the mean density, $\bar{\rho}/\rho_e$, and the RMS of density, $(\overline{\rho'^2})^{1/2}/\rho_e$ as functions of Y^+ .

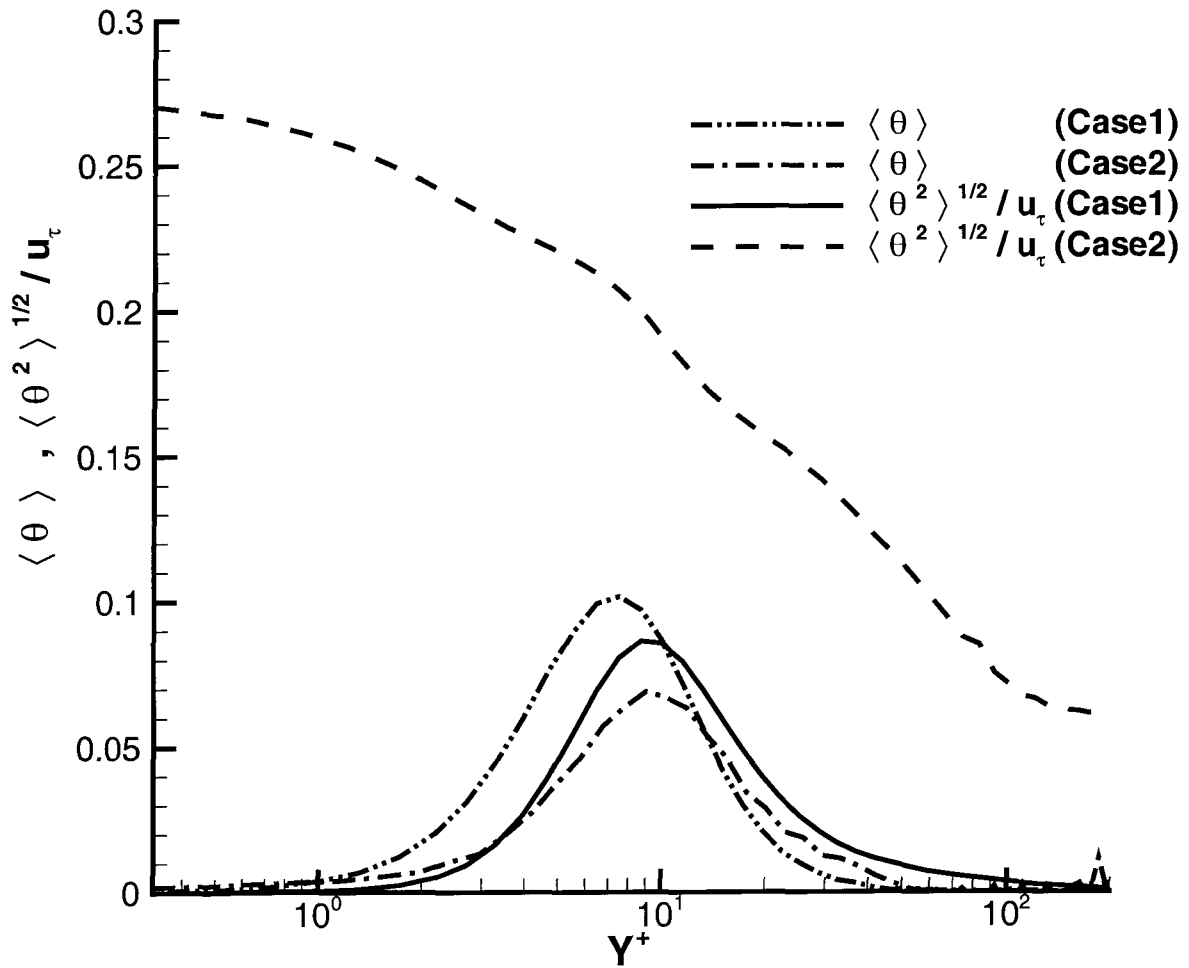


Figure 5.5 The mean and RMS of dilatation of velocities vs. Y^+ , i.e. $\bar{\theta}$ and $\sqrt{\theta'^2}/u_\tau$.

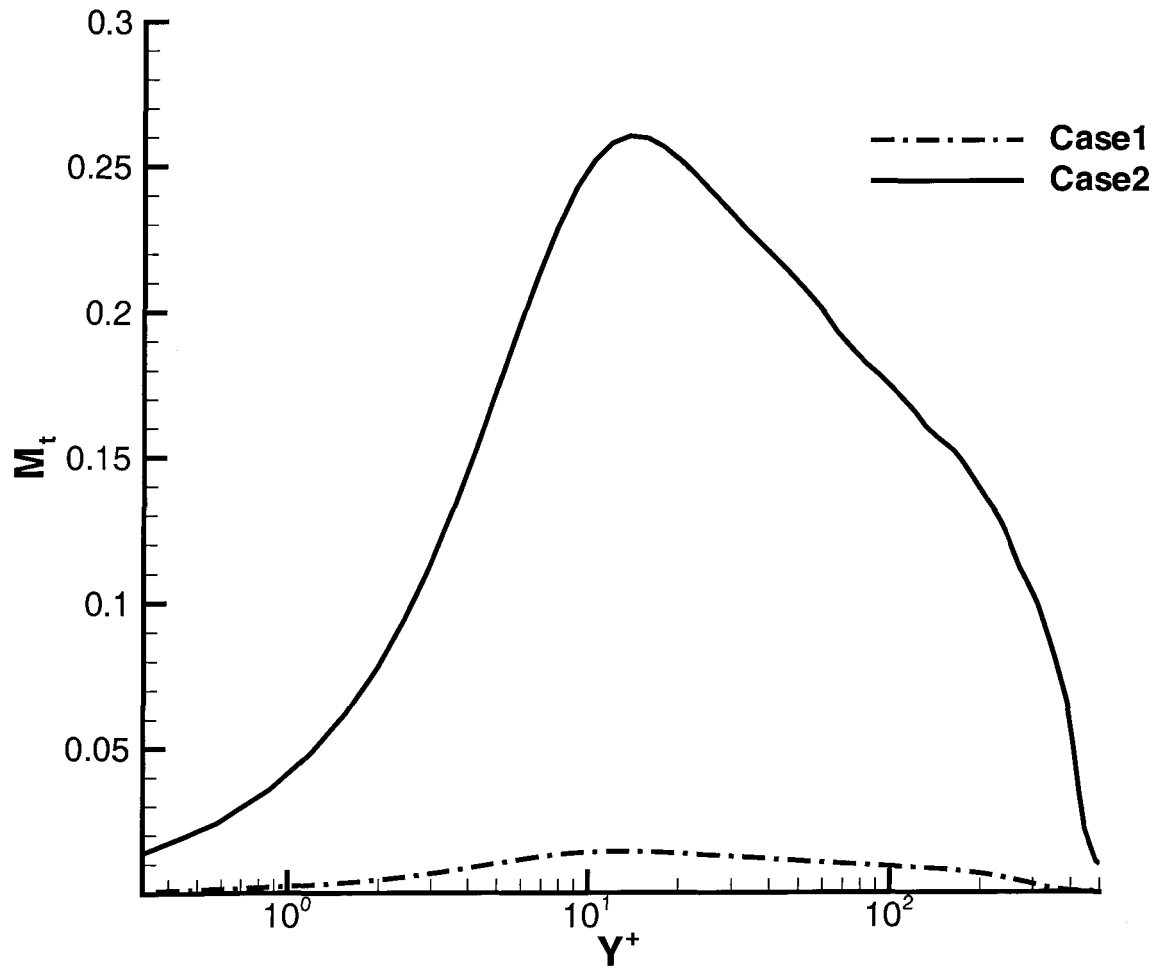


Figure 5.6 Turbulent Mach number, M_t , as functions of y^+ .

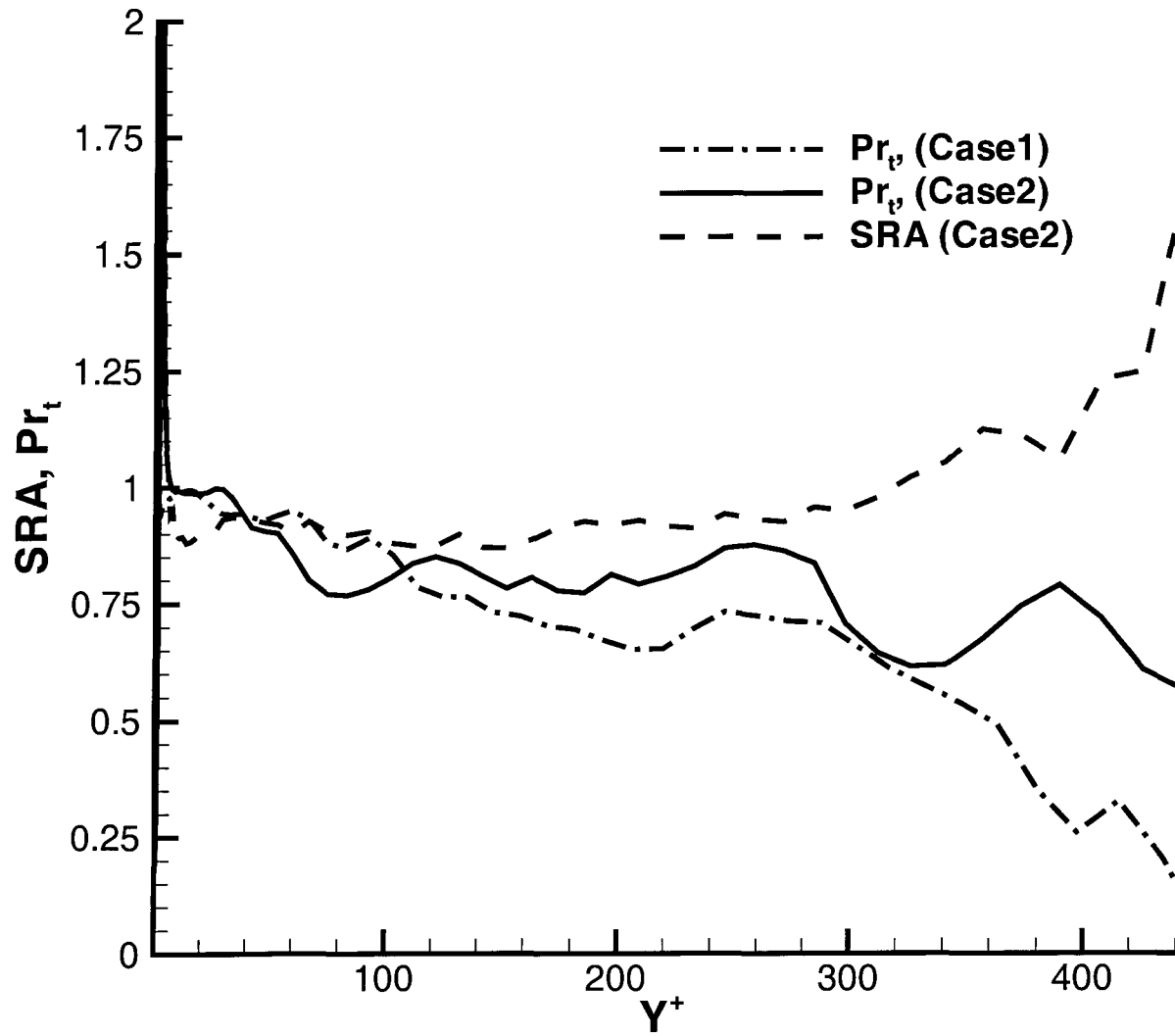


Figure 5.7 Turbulent Prandtl number Pr_t as functions of Y^+ , and the test of strong Reynolds analogy as expressed by 5.1.

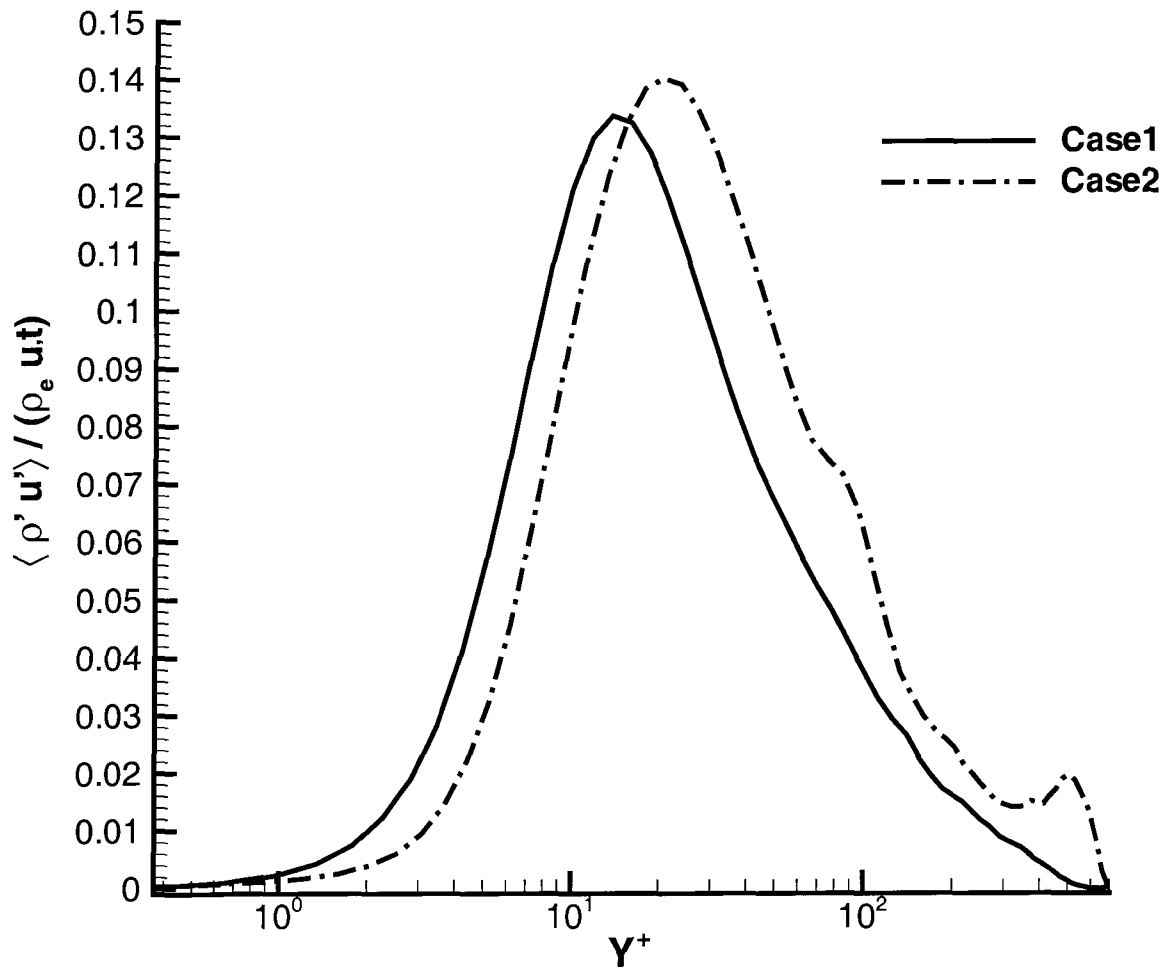


Figure 5.8 Comparison of $(\widetilde{u}_1 - \overline{u}_1)/u_\tau$.

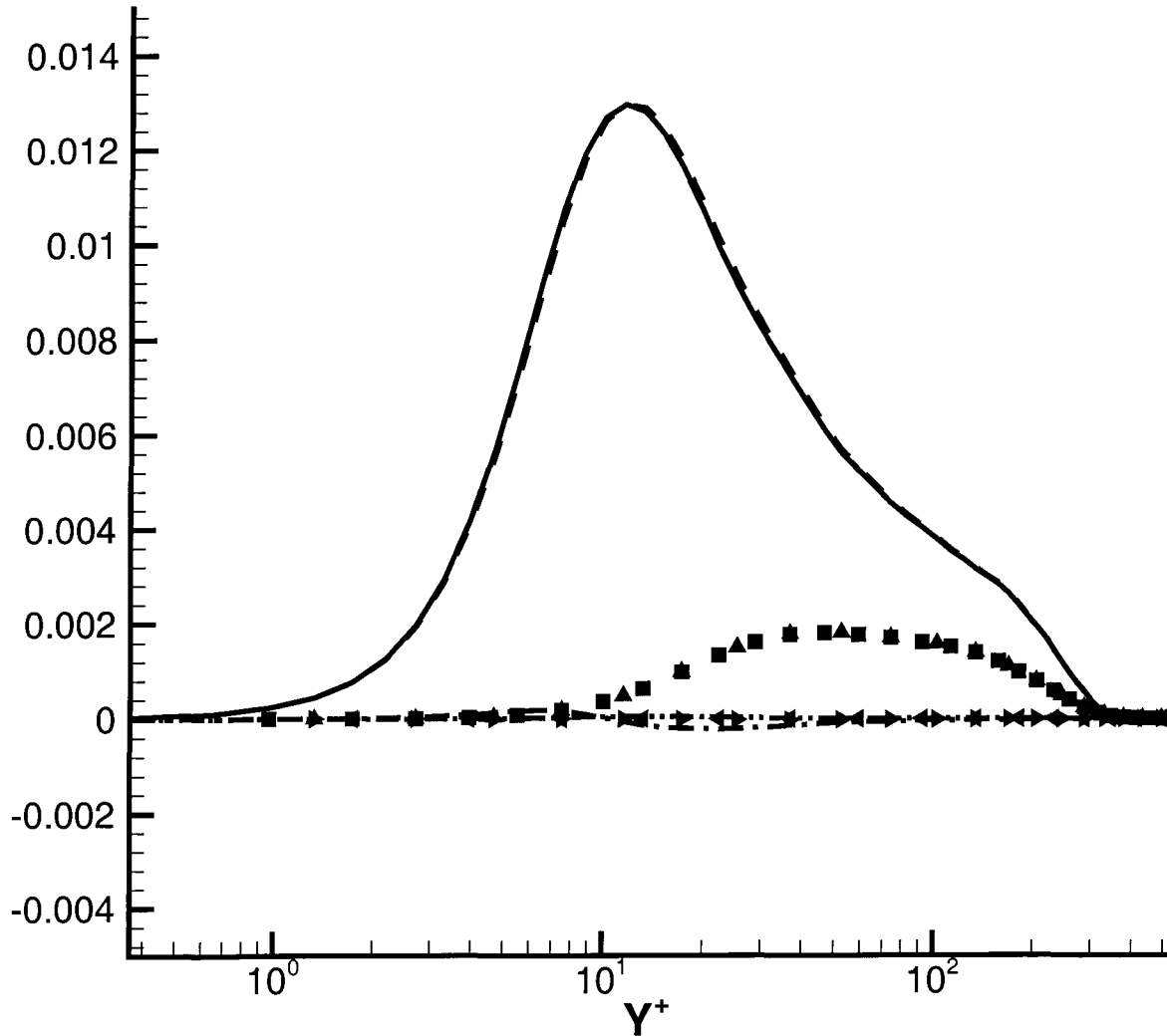


Figure 5.9 The components of τ_{11} . The solid line is τ_{11} , the dashed line is the τ_{11_t} , the dash-dotted line is τ_{11_e} , and the dash-double-dotted line is τ_{11_F} . The square samples are τ_{22} , The delta samples are τ_{22_t} , the right triangular samples are τ_{22_e} , and the left triangular samples are τ_{22_F} .

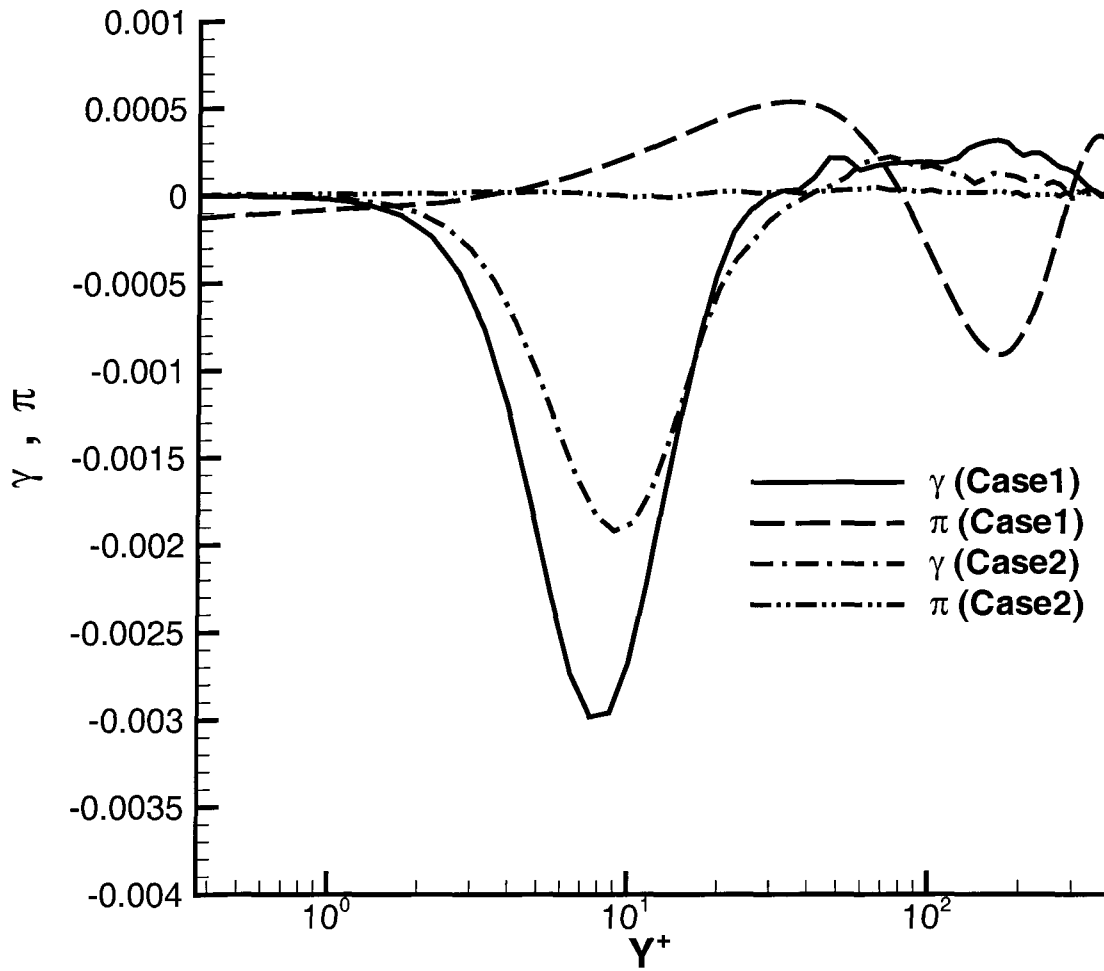


Figure 5.10 Comparison of γ and π vs. Y^+ , where the solid line is γ for the case 1, the dash-dotted line is γ for the case 2, the dashed line is π for the case 1, the dash-double-dotted line if π for the case 2.

CHAPTER 6. PROBABILITY DENSITY FUNCTION OF VELOCITY FLUCTUATIONS IN A TURBULENT BOUNDARY LAYER

The probability density function (PDF) of velocities is central to the one point statistics of complicated fluid phenomena such as hydraulic turbulence (Croteau and Ronis (2002), Serio (1998), Falkovich and Lebedev (1997), and Jayesh and Warhaft (1991)), granular flows (Kudrolli and Henry (2000)), cosmological flows (Tatekawa (2005)), magnetohydrodynamic turbulence (Sorriso-Valvo *et al.* (1999), Sorriso-Valvo *et al.* (2000)), and the movement of the global ocean (Gille and Smith (2000)). A number of PDFs of velocity or passive scalars have been reported. However, the influence of large scale structures on PDFs and the corresponding mechanism to produce such PDFs has not been documented. It is believed that the strong shear force in the turbulent boundary layer will deform the PDFs of velocities and produce the non-Gaussian distribution. It is worthwhile to conduct a numerical study to reveal the mechanism controlling the production of the non-Gaussian PDFs of velocities. This chapter reports the numerical results about the PDF of velocities.

6.1 Introduction

Boltzmann's pioneer study about the molecule-ordered distribution, namely the Boltzmann distribution (Boltzmann (L.)), has proven pivotal to the development of classical statistical mechanics. However, the Boltzmann distribution, which relates to a Gaussian distribution, is valid only for sufficiently short range circumstances. A number of nonequilibrium fluid phenomena (Croteau and Ronis (2002), Serio (1998), Kudrolli and Henry (2000), Tatekawa (2005), Sorriso-Valvo *et al.* (2000), and Gille and Smith (2000)) have been reported to have non-Gaussian distributions. Such a deviation of PDFs from the Gaussian distribution is a

nonlinear process. These flows present a multiscale behavior. And the PDFs of velocity vary over different scales (Sorriso-Valvo *et al.* (1999), Gille and Smith (2000)). However, detailed information on the influence of multiscale structures on the PDFs, including the stochastic process and the intrinsic physical mechanism relevant to such PDFs, is lacking. Similarly, very little is known about how the multiscales affect the stochastic process and the deviation of PDFs from the Gaussian distribution. It is not possible to rigorously assess the role of scales in the nonlinear natural phenomena. Therefore, it is worthwhile to discuss the dynamic evolving of PDFs in the complex flows.

Moreover, the evolution of PDF of velocity and velocity acceleration in turbulent flows and the corresponding Lagrangian statistic are of fundamental importance to the understanding of the physical mechanism of turbulence. In the recent two decades, the PDF methods developed by Pope and other researchers (Pope (2000), Sawford and Yeung (2001)) have enjoyed dramatic success in the study of turbulence. In order to close the governing equation, Pope developed the simplified Langevin model and the generalized Langevin model (Pope (2000), Pope (1994a)). The comparisons showed the success of these PDF methods in homogeneous turbulence and uniform shear turbulence (Pope (2002a), Pope (2002b), Sawford and Yeung (2000), Sawford and Yeung (2001)). However, for the complicated flows including wall shear flows, the deficiency in the experimental and DNS data causes difficulty in the modeling of the stochastic process and the PDFs. This obscures the way to close these governing equations.

6.2 Results and Discussion

In order to investigate the influence of large scales on the PDFs of velocity of turbulence and provide information to understand the corresponding physical mechanism, a two-dimensional turbulent boundary layer was calculated by a direct numerical simulation. The PDFs of velocity fluctuations in the normal, streamwise, and spanwise directions were analyzed. The calculated Reynolds number ranged from 1800 up to 2300 based on the displacement thickness δ_d . And the Mach number was low, 0.02, hence, the flow was effectively incompressible. The numerical method proposed by Liu and Pletcher (2006) was employed. The numerical mesh was uniform

in the streamwise and spanwise directions, but was stretched in the normal direction. It was $350 \times 88 \times 192$ in the streamwise, normal, and spanwise directions, respectively. In this study, $\Delta x^+ = 18$, $\Delta z^+ = 5$, $\Delta y_{\min}^+ = 0.23$, and $\Delta y_{\max}^+ = 50.0$ based on the wall units. And $\Delta t^+ = 0.2$ in the units of $\frac{\delta_d}{U_\infty}$. A periodic boundary condition was unitized in the spanwise direction. A characteristic boundary condition (Liu and Pletcher (2006) or Chapter 3) was applied at the outlet and a dynamic recycling inlet method (Liu and Pletcher (2006) or Chapter 3) was employed to generate the fully developed turbulent boundary layer. Due to the effect of the viscous terms, the numerical value of instantaneous velocity varies only over a finite domain. This enables us to account for the PDFs numerically. An estimated velocity domain was separated into 100 parts equally. The amount t_i was defined by the times that the instantaneous velocity was in the velocity range of the part i . The function ρ_i was defined by $\rho_i = \frac{t_i}{ndv}$, where n is the total number of the samples and dv is the velocity range of each part, more precisely,

$$dv = \frac{\text{maximum estimated velocity} - \text{minimum estimated velocity}}{100}$$

20,000 samples were accounted for in the statistics of the PDFs.

It is known that the turbulent production, dissipation, transport, and the mean flow convection are all the functions of the normal distance from the wall. To investigate the evolution of the PDFs of velocity fluctuations in the normal direction, these PDFs were collected on the six different normal stations described by Table 6.1.

Table 6.1 Table of the corresponding y^+ value of the statistical locations

| Station | Y_1 | Y_2 | Y_3 | Y_4 | Y_5 | Y_6 |
|---------|-------|-------|-------|-------|-------|-------|
| y^+ | 2.5 | 13.8 | 49.9 | 164.0 | 345.8 | 570.0 |

Clearly, Y_1 was in the viscous sublayer where the dissipation is dominant, Y_2 was in the buffer zone where the turbulent production is stronger than the dissipation, Y_3 was in the log layer in which the turbulent production balances the turbulent dissipation, Y_4 was at the upper bound of the log layer, and Y_5 and Y_6 were located in the outer part of turbulent boundary

layer.

Numerical results presented by Fig.6.1 indicate that the PDFs of spanwise velocity are Gaussian in the most of the boundary layer. Since the two-dimensional turbulent boundary layer is homogeneous in the spanwise direction and the mean spanwise velocity is zero, the stochastic process is non-biased in the spanwise direction and the Reynolds stress corresponding to the w momentum equation is near zero. These features evidently lead to the Gaussian distribution of spanwise velocity even though the flow is anisotropic.

The numerical results presented by Fig.6.2 describe the PDFs of the normal velocity fluctuations, which are approximately a Gaussian distribution. We found that the evolution of the PDFs of the normal velocity fluctuations is related to the skewness of the normal velocity fluctuations, namely γ_{1_v} . Shown by Fig.6.2, γ_{1_v} is roughly an increasing function of the distance from the wall except in the vicinity of wall. As γ_{1_v} increases, the PDFs of the normal velocity persevere in the shape of the tail, but with a twisted head which tends to turn left. When γ_{1_v} becomes larger, the PDF is evidently approximately a beta distribution, just like the image F in Fig.6.2. The evolution of the PDFs of the normal velocity fluctuations with respect to the distance from the wall show us how the PDFs of the velocity fluctuations deviate from the Gaussian distribution.

Figure 6.3 shows the PDF of streamwise velocity fluctuations in the different normal direction. The PDFs of the normal velocity fluctuations is approximately a beta distribution. Due to the viscous effect, the velocities only vary over a finite interval, i.e., $\rho(u^*)$ is nonzero only in a finite interval $[u_{\min}, u_{\max}]$. By using the linear transformation $u^* = \frac{u - u_{\min}}{u_{\max} - u_{\min}}$, the $\rho(u^*)$ evidently collapses the beta distribution. More precisely,

$$\rho(u^*) = \frac{u^{*\alpha-1}[1 - u^*]^{\beta-1}}{B(\alpha, \beta)}$$

Indeed, the beta distribution of the single composition has been reported by a number of experiments (Rhodes (1975)).

We found that the coefficients α and β were relevant to the skewness of streamwise vorticity γ_{1_u} . When γ_{1_u} is positive, the PDFs are the backward beta distribution roughly, i.e., $\alpha < \beta$. Otherwise, the PDFs are the forward beta distribution roughly, i.e., $\alpha > \beta$. Clearly, when

$\alpha < \beta$, the mean of the beta function is less than the mode of the PDF. This implies that the velocity fluctuation has a higher probability to move backward. We outline the α, β value of Fig. 6.3 in the Table 6.2.

Table 6.2 Table of the α, β values of the beta distribution shown by Fig. 6.3

| | Y_1 | Y_2 | Y_3 | Y_4 | Y_5 | Y_6 |
|----------|-------|-------|-------|-------|-------|-------|
| α | 6.11 | 6.95 | 17.9 | 17.8 | 15.7 | 57.3 |
| β | 11.9 | 8.36 | 13.9 | 15.7 | 11.5 | 54.4 |

In order to explain the relationship between the PDF and the skewness, we compute

$$\gamma_{1_u} = \frac{\langle (u - \langle u \rangle) \cdot \rho_\sigma(u - \langle u \rangle) \rangle}{\sqrt{\langle (u - \langle u \rangle)^2 \rangle}} = \frac{\langle (u - \langle u \rangle) \cdot \rho_\sigma^+(u - \langle u \rangle) \rangle}{\sqrt{\langle (u - \langle u \rangle)^2 \rangle}} + \frac{\langle (u - \langle u \rangle) \cdot \rho_\sigma^-(u - \langle u \rangle) \rangle}{\sqrt{\langle (u - \langle u \rangle)^2 \rangle}}$$

where $\rho_\sigma(u - \langle u \rangle) = \frac{(u - \langle u \rangle)^2}{\langle (u - \langle u \rangle)^2 \rangle}$ is the distribution of the energy of the fluctuations, $\rho_\sigma^+(u - \langle u \rangle)$ given by

$$\rho_\sigma^+(u - \langle u \rangle) = \begin{cases} \frac{(u - \langle u \rangle)^2}{\langle (u - \langle u \rangle)^2 \rangle} & \text{If } u - \langle u \rangle > 0 \\ 0 & \text{Otherwise} \end{cases}$$

is the distribution of the energy of the fluctuations moving forward, and $\rho_\sigma^-(u - \langle u \rangle)$ given by

$$\rho_\sigma^-(u - \langle u \rangle) = \begin{cases} \frac{(u - \langle u \rangle)^2}{\langle (u - \langle u \rangle)^2 \rangle} & \text{If } u - \langle u \rangle < 0 \\ 0 & \text{Otherwise} \end{cases}$$

is the distribution of the energy of the fluctuations moving backward. Thus, $\gamma_{1_u} \sqrt{\langle (u - \langle u \rangle)^2 \rangle}$ represents the dominant direction of the turbulent structures. More precisely, when $\gamma_{1_u} > 0$, the forward moving turbulent structures contain more energy. Otherwise, the backward moving turbulent structures contain more energy. Therefore, the skewness shows us that how far the PDF deviates from a Gaussian distribution. In this sense, the skewness of velocity is the quantity associated with the non-Gaussian distribution. However, it is just an outcome, not a cause of non-Gaussian PDFs. We are interested in finding out the mechanism causing non-Gaussian PDFs.

According to Fig. 6.4, the skewness of the vortex takes the same sign with the skewness of velocity in most of the boundary layer except the viscous sublayer in which the dissipation

is dominant. More precisely, the skewness of the vortex is positive in the buffer zone region, while negative at the other regions. Shown by Fig. 6.4, the one third power of the skewness of the normal vorticity is roughly proportional to the one third power of the skewness of the streamwise velocity which correlates to the PDF of velocity. As we know, the positive skewness of the vortex implies the dominance of counterclockwise vortices. Otherwise, the clockwise vortices are dominant. Hence, the counterclockwise vortices accumulate in the buffer zone, and clockwise vortices occupy the other regions. Fig. 6.4 evidently verifies that the direction and the strength of vortices have a significant influence on the PDF of the velocity. We have not found out the direct correlation between the Reynolds stress and the skewness of the velocities. Results suggest that the vortices may be one of the causes of non-Gaussian distributions.

In order to examine the effects of the distribution of initial data, two different initial conditions were utilized: one case followed

$$u_i(0; \Omega) = h(x, y, z) = B_i(x, y) + 0.2r, \quad p(0; \Omega) = P_\infty$$

where $B_i(x, y)$ was the Blasius boundary layer profile and r was a random function, and the other case was given by

$$u_i(0; \Omega) = B_i(x, y) + 0.2 \sin(2.0x) \sin(4.0y) \sin(4.0z), \quad p(0; \Omega) = P_\infty$$

Results show that both cases generate the same PDFs as shown in Fig. 6.1, 6.2, and 6.3. And the influence of the initial condition on the final results is negligible.

To explain this phenomena, an exact implicit solution of the incompressible Navier-Stokes equation:

$$\frac{\partial \rho u_i}{\partial t} - \mu \frac{\partial^2 u_i}{\partial x_j \partial x_j} = - \frac{\partial \rho u_j u_i}{\partial x_j} - \frac{\partial p}{\partial x_i} \quad (6.1)$$

$$\nabla \bullet u_i = 0 \quad (6.2)$$

$$u_i(t, \partial\Omega) = f_i(t, \partial\Omega), \quad u_i(0, \Omega) = h_i(\Omega), \quad p(t, \partial\Omega) = g(t, \partial\Omega)$$

is formulated by using an integral method. At the above, $f_i(t, \partial\Omega)$ and $g(t, \partial\Omega)$ are boundary conditions and $h_i(\Omega)$ is the initial condition. It is known that the pressure obeys

$$\Delta p = - \frac{\partial \rho u_j u_i}{\partial x_j} \quad (6.3)$$

which is called the pressure Poisson equation. By using the Green's function (Stakgold (2000)), the solution of the pressure Poisson equation is given by

$$p(y) = \int_{\Omega} G(y|z) \left[\frac{\partial}{\partial z_i} \left(-\frac{\partial \rho u_j u_i}{\partial z_j} \right) \right] dz - \int_{\partial\Omega} g \frac{\partial G(y|z)}{\partial n_z} dS_z \quad (6.4)$$

where $G(x|y)$ is the Green's function subjected to the Dirichlet boundary condition. Likewise, by using the general solution of the heat equation (Stakgold (2000)), the Eq.(6.1) can be represented as

$$\begin{aligned} \rho u_i(t; x) = & \int_0^t \int_{\Omega} \psi(t; x|\tau; y) \left[-\frac{\partial \rho u_j u_i}{\partial y_j} - \frac{\partial p(y)}{\partial y_i} \right] dy d\tau + \int_{\Omega} \frac{g}{RT} h_i(y) \psi(t; x|0; y) dy \\ & - \int_0^t \int_{\partial\Omega} \frac{g}{RT} f_i(\tau; y) \frac{\partial \psi(t; x|\tau; y)}{\partial n_y} ds d\tau \end{aligned} \quad (6.5)$$

where T is temperature and

$$\psi(t; x|t_1; x_1) := \frac{H(t - t_1)}{[4\pi(t - t_1)]^{3/2}} \exp\left(\frac{-|x - x_1|^2}{4\nu(t - t_1)}\right) \quad (6.6)$$

is the fundamental solution of causal Green's function holding

$$\left(\frac{\partial}{\partial t} - \mu \nabla^2 \right) \psi(t; x|t_1; x_1) = \delta(x - x_1) \delta(t - t_1) \quad (6.7)$$

and $H(t - t_1)$ is the Heaviside function. Consequently, the identities (6.4) and (6.5) form the exact implicit solution of the incompressible Navier-Stokes equation subjected to the Dirichlet boundary condition. Obviously, the influence of initial condition on the solution is described by the second term of the right hand side of Eq. (6.5), which decays in time because of $\psi(t; x|0; y)$.

Consequently, the above theoretical analysis together with the numerical simulation suggests that the initial conditions do not have a conspicuous influence on the PDF of velocity and velocity fluctuations when the turbulent boundary layer is fully developed. In this study, the outlet condition was a characteristic boundary condition by which the outlet data were identified by the interior data and free stream pressure. And the inlet condition was generated by a recycling and rescaling method, which recycles an interior station to the inlet and rescales it due to the similarity laws: the law of the wall and the defect law. As a result, the boundary conditions did not specify the PDFs. Thus, the PDFs of velocities should be identified by an intrinsic mechanism of the turbulent boundary layer. By comparing the PDFs of velocities

and the skewness of vortices, we propose that the sign and the strength of the vortices have a significant influence on the distribution of velocity, and determine the deviation of the PDFs from the Gaussian distribution.

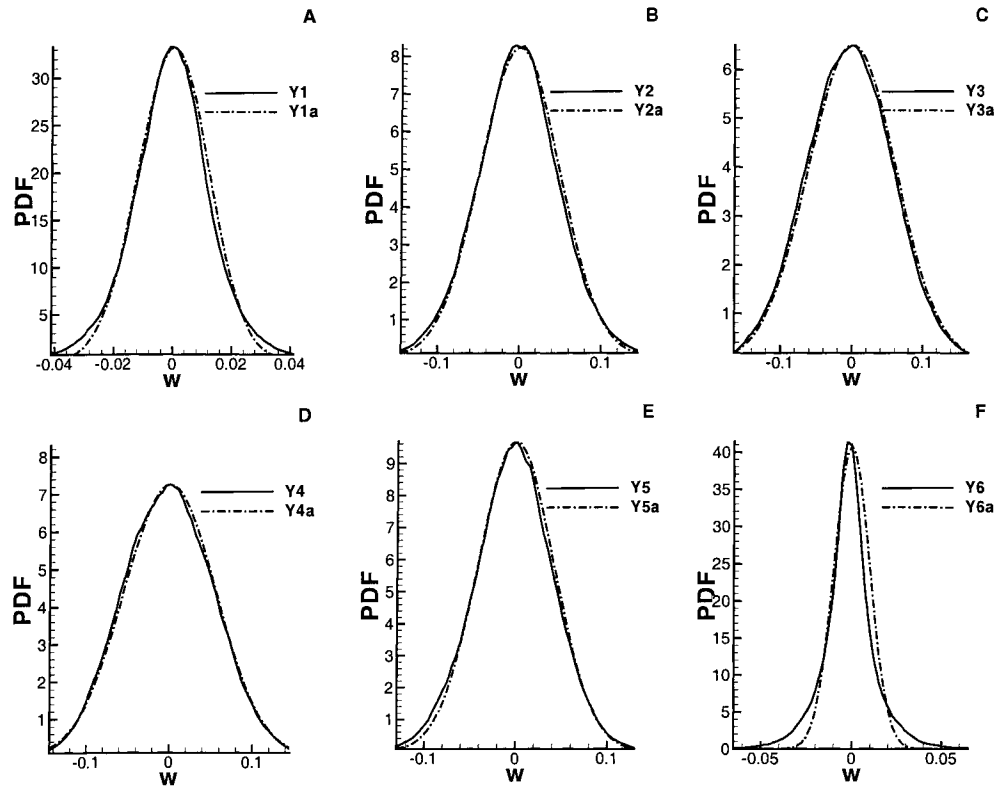


Figure 6.1 The PDFs of spanwise velocities. The solid curves are the numerical results, and the dash-dotted curves are the Gaussian distributions having the same mean and variance with the corresponding solid curves.

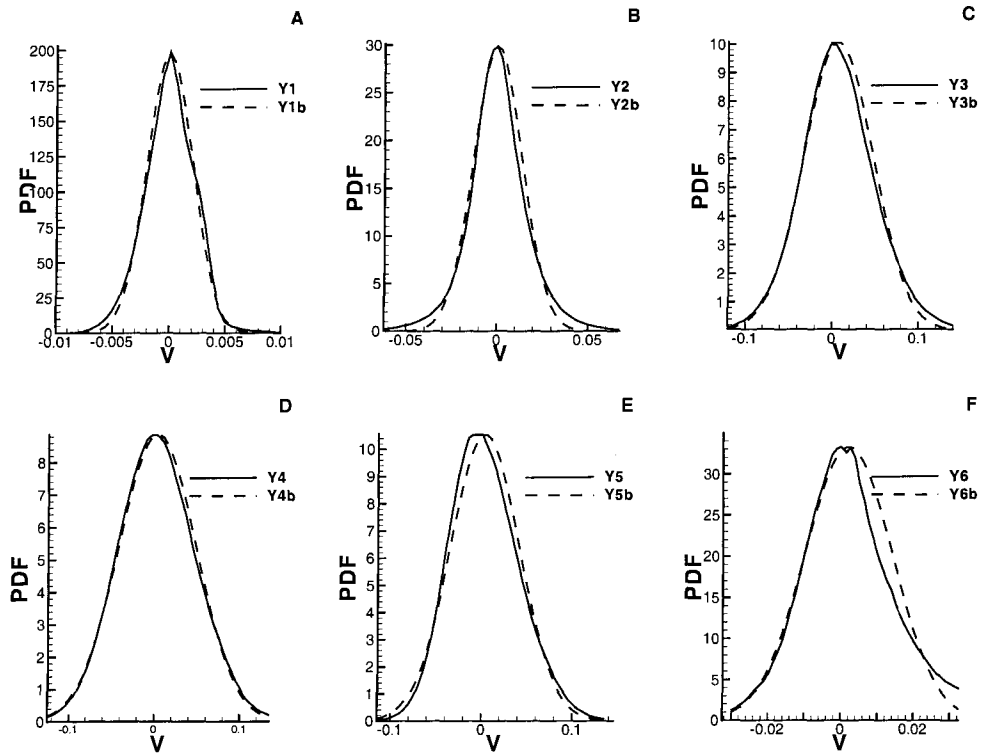


Figure 6.2 The PDFs of normal velocity fluctuations. The solid curves are the numerical results, and the dashed curves are the Gaussian distributions having the same mean and variance with the corresponding solid curves.

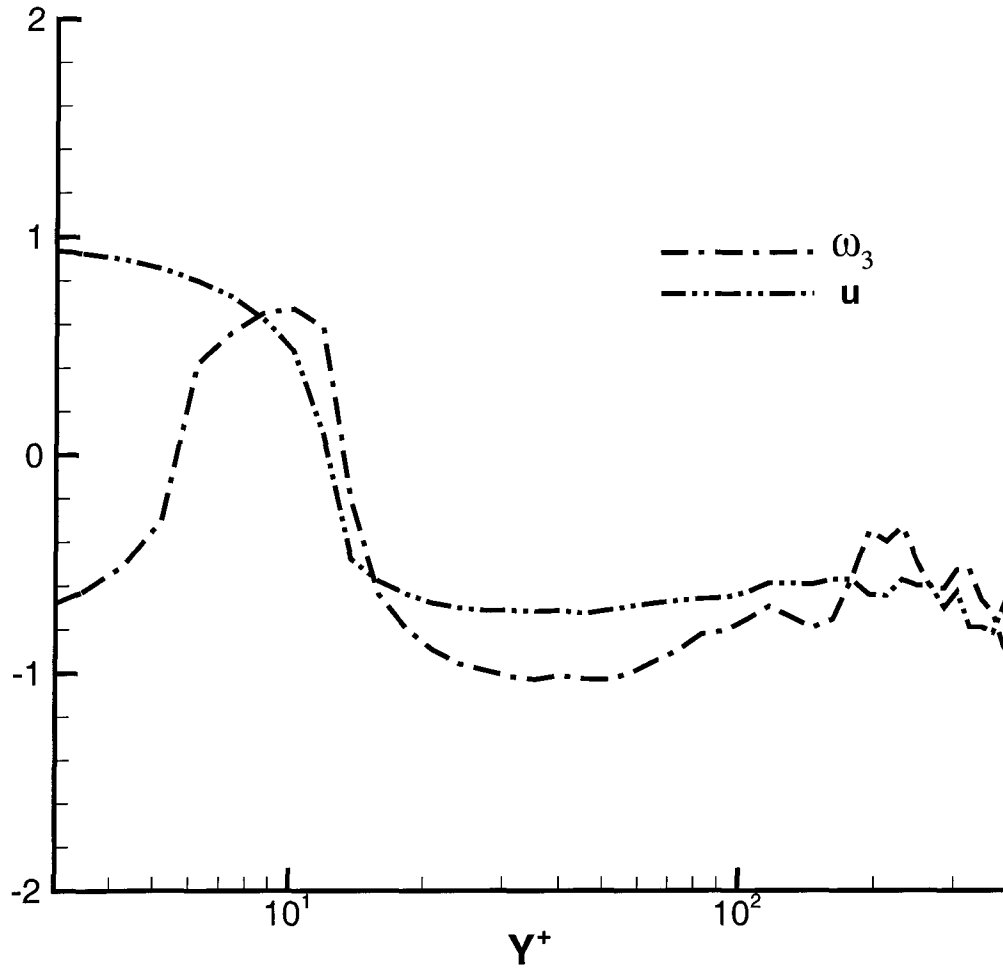


Figure 6.3 The plot of skewnesses and the Reynolds stress with respect to the normal distance from the wall. The solid and the dashed curves are the one third power of the streamwise velocity and normal vorticity, respectively. i.e. $\gamma_{1\omega_3}^{1/3} = \left(\frac{\langle (\omega_3 - \langle \omega_3 \rangle)^3 \rangle}{\langle (\omega_3 - \langle \omega_3 \rangle)^2 \rangle^{3/2}} \right)^{1/3}$ and $\gamma_{1u}^{1/3} = \left(\frac{\langle (u - \langle u \rangle)^3 \rangle}{\langle (u - \langle u \rangle)^2 \rangle^{3/2}} \right)^{1/3}$.

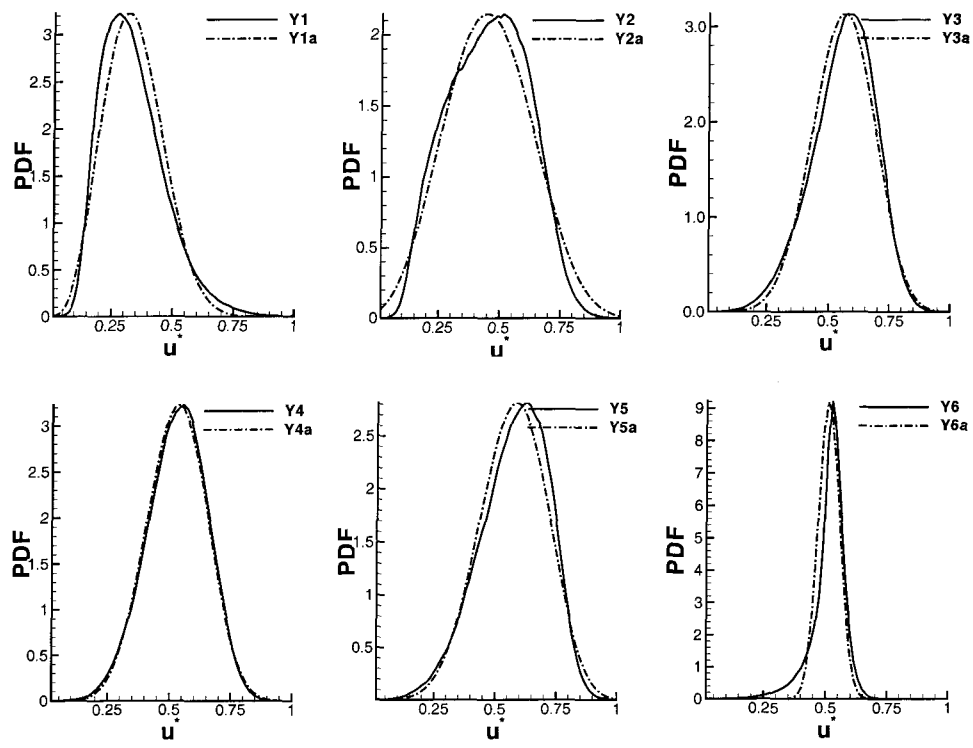


Figure 6.4 The PDF of streamwise velocity fluctuations. The solid curves are the numerical results, and the dash-dotted lines are the beta distributions having the same variance, skewness, mode and maximum value with the corresponding solid curves.

CHAPTER 7. LARGE EDDY SIMULATION OF TURBULENT BOUNDARY LAYERS SUBJECTED TO FREE-STREAM TURBULENCE

A numerical method is presented to simulate turbulent boundary layers subjected to free-stream turbulence. The fact that free-stream turbulence can have a dramatic effect on the properties of a turbulent boundary layer has been known for quite some time. However, even now it remains a major challenge to capture this effect adequately in a numerical simulation. A scheme is presented whereby the flow domain is considered to be composed of three main components: an inner near wall part, an outer part, and the free stream part. Turbulent boundary layers developing under the influence of a free-stream turbulence levels of 0%, 5%, and 7.5% are considered. The influence of free-stream turbulence length scale and intensity on the skin friction, mean velocity, and rms profiles are investigated.

7.1 Introduction

The turbulent boundary layer subjected to free stream turbulence is encountered daily not only in a variety of engineering applications involving the design of aircraft, ships, automobiles, and propulsion systems, but also in research about the fundamental mechanisms of turbulence. The interaction between the turbulent boundary layer and the free stream and the effect of free stream turbulence on the turbulent boundary layer have been of interest for quite a long time. Developing appropriate algorithms to compute turbulent boundary layers with free stream turbulence that capture such an interaction process continues to be challenge.

We consider that the external turbulent boundary layer involves three different regions: an inner part, an outer part, and free-stream part. The inner part includes the viscous sublayer,

buffer layer, and part of logarithmic layer. The outer part includes the rest of logarithmic layer and the wake of the turbulent boundary layer.

In the turbulent boundary layer without free stream turbulence, most of the turbulence is generated in the inner part because of the strong shear there. In the outer part, the dissipation of turbulence will exceed its production. So the turbulence production will decrease with increasing normal direction from the wall. In a statistical sense, the transport direction of turbulent energy is from inner part to outer part.

But with free-stream turbulence, there exists the possibility of energy transport from the free stream to the boundary layer. The skin friction will be increased due to the effect of free stream turbulence (Blair (1983), Hancock and Bradshaw (1983), Simonich and Bradshaw (1978)). The increasing skin friction implies the increasing of turbulence production. This phenomenon was investigated in several experiments, but what is interesting is that when the free-stream turbulence level is less than 12.5%, the effect of free stream turbulence on the turbulent production in the inner part is not very obvious, but when the free-stream turbulent level is beyond 12.5%, the turbulent production in the inner part suddenly increases (Barrett and Hollingsworth (2003), Thole and Bogard (1996)). On the other hand, a smaller turbulent free stream length scale makes a larger contribution to the skin friction compared with a larger turbulent free stream length scale (Blair (1983), Hancock and Bradshaw (1983), Barrett and Hollingsworth (2003)). Recall that the larger eddies correspond to larger integral length scales. This fact, essentially, verifies that the smaller eddies or higher frequency structures more easily penetrate into the boundary layer.

Moreover, the effect of free stream turbulence on the mean profiles in the wake region is more dramatic than on the inner part (Blair (1983), Hoffmann and Mohammadi (1991), Freire *et al.* (1995)). Since shear is not large in the free stream, there is not much turbulent production there; therefore, the main feature in the free stream is dissipation. Length scale is a parameter to measure the decay rate of the intensity of fluctuations. Usually, grid turbulence has a length scale range from $10\delta_d$ to $50\delta_d$ (Barrett and Hollingsworth (2001), Barrett and Hollingsworth (2003)). In this range, the dissipation of free stream turbulence is very strong. Therefore,

the mean profile in the wake region of turbulent boundary changes rapidly in the downstream direction compared to the case without free stream turbulence. In the other words, the defect law does not apply with free stream turbulence.

Those features are extremely interesting, but very difficult to capture in numerical simulations. The difficult point is to correctly represent the correlation between free-stream turbulence and the turbulent boundary layer in numerical simulations. The goal of this chapter is to evaluate a numerical technique to account for free stream turbulence effects on the turbulent boundary layer.

7.2 Model

There is no shear force in the free stream, so the turbulent production is extremely weak. And dissipation dominates the free stream turbulence. Therefore, it is essential to produce inflow conditions so that an appropriate turbulence level and length scale can be achieved in the free stream. In order to accomplish this, we propose advances to the inflow generator concepts from the work of Spalart (1988) and Lund *et al.* (1998).

Spalart (1988) introduced a periodic boundary condition method to produce the inlet profile of spatially evolving turbulent boundary layers. Lund *et al.* (1998) further developed this concept. In their implementation, instantaneous profiles at a specific station were recycled to the inlet at each numerical step after rescaling. This rescaling was based on the similarity laws of the boundary layer: the law of the wall in the inner part and defect law in the outer part of boundary layer. Kong *et al.* (2000) applied Lund *et al.*'s idea to temperature, and formulated an inlet generator for turbulent thermal boundary layers. Their simulation results showed that this treatment also works well for the energy equation, when fluid properties can be assumed to be constant.

Spalart (1988) decomposed the velocity into two parts, the mean profiles and fluctuations,

$$U = \bar{U} + A(x, \eta)u_p(x, \eta, z, t) \quad (7.1)$$

where \bar{U} is the mean profile $A(x, \eta)$ is the rms profiles, both are coming from experiment or empirical correlations, and $u_p(x, \eta, z, t)$ is the normalized signal which was loaded by the

corresponding data from a downstream plane. When the mean profile and rms profiles are both known, this is a robust treatment. But for some flows like turbulent boundary layers subjected to free stream turbulence, the existing database for the mean and rms profiles is limited, even unknown. For evaluating such cases, Lund *et al.* (1998)'s treatment is more efficient. They suggested to decompose the velocity into

$$U_{inlt}^{inner}(y_{inlt}^+) = \gamma(U_{recy}(y_{inlt}^+) + U'_{recy}(y_{inlt}^+, z, t)) \quad (7.2)$$

$$U_{inlt}^{outer}(\eta_{inlt}) = \gamma(U_{recy}(\eta_{inlt}) + U'_{recy}(\eta_{inlt}, z, t)) + (1 - \gamma)U_{ref} \quad (7.3)$$

where *inner* stands for the value at the inner part, *outer* stands for the value at the outer part, *inlt* stands for the value at the inlet plane, *recy* stands for the value at the recycle plane, $\gamma = \frac{U_{\tau_{inlt}}}{U_{\tau_{recy}}}$, which is deduced from the law of the wall, and $\eta = \frac{y}{\delta}$, which is the nondimensional variable for the defect law. The advantage of this method is that the exact mean and rms profiles are not required, but sometimes, the desired skin friction may not be approached correctly and efficiently. But, unfortunately, in the turbulent boundary layer subjected to free-stream turbulence, the defect law does not work. Therefore, Lund *et al.*'s method must be improved for the calculation of the turbulent boundary layer subjected to free stream turbulence.

The revised inflow condition for such flows suggested by present researchers is given by

$$U_{inlt}^{inner}(y_{inlt}^+) = \bar{U} + A(x, \eta)u_p(x, \eta, z, t) \quad (7.4)$$

$$U_{inlt}^{outer}(\alpha_{inlt}) = (\gamma_1 U_{recy}(\alpha_{inlt}) + \gamma_2 U'_{recy}(\alpha_{inlt}, z, t)) + (1 - \gamma_1)U_{ref} \quad (7.5)$$

$$U_{inlt}^{free}(\alpha_{inlt}) = \gamma_3 \left(\sum_{0 \leq i \leq m} Weight_i U'_{recy_i} \right) + U_{ref} \quad (7.6)$$

where the inner part ranges from 0 to 200 in the y^+ sense.

Since the skin friction of turbulent boundary layers subjected to free stream turbulence will be influenced by the turbulence level and the turbulence length scale, in order to accurately

capture the shift of the skin friction, a flexible inflow condition should be proposed. The increasing of the skin friction depends on the free stream turbulent length scale (Blair (1983), Hancock and Bradshaw (1983), Simonich and Bradshaw (1978)), but such a length scale cannot be known until the numerical simulation is accomplished. The inflow condition proposed by Lund *et al.* (1998) offers a way to adjust the inlet skin friction in the case the length scale is unknown. But this recycling and rescaled method is based on two assumptions:

- 1) The influence of the turbulent length scale on skin friction varies only slightly in the streamwise direction.
- 2) The flow between the inlet and recycling station satisfies the law of the wall.

The integral length scale utilized in this chapter was defined by Hancock and Bradshaw (1983), which is

$$L = -\frac{\overline{w'^2}_e}{U} / \frac{d(\overline{w'^2}_e)}{dx} \quad (7.7)$$

where $\overline{w'^2}_e$ is the kinetic energy of fluctuations averaged in the spanwise and free stream part of the normal direction, which decreases monotonically in the streamwise direction. U is the mean velocity of the free stream.

Technically, the second assumption cannot always be maintained because of the inevitable errors in the initial conditions. Since the recycling procedure couples the initial conditions and inflow conditions, considering that the initial condition may not satisfy the law of the wall, this coupling behavior may cause a lower skin friction. Liu and Pletcher (2006) suggested a dynamic recycling procedure to reduce the effect of this coupling. This idea works for turbulent boundary layers without free stream turbulence, but needs adjustments to achieve an appropriate length scale.

In this chapter, we suggest a two step method to solve this problem. Firstly, Spalart (1988)'s inflow condition has been applied for the inner part of the turbulent boundary layer up to $t = 160 \frac{\delta_d}{U_{ref}}$ where $\frac{\delta_d}{U_{ref}}$ is the nondimensional time. This idea works because the correlation of free stream turbulence and skin friction was successfully formulated by experiments. Experimental results (Cebeci and Bradshaw (1977)) showed that the mean velocity profile works in the inner part. If the free stream turbulence level is less than 12.5%, rms profiles without free stream

turbulence can be applied. Therefore, Spalart (1988)'s inflow condition can be utilized as long as the free stream turbulence level is lower than 12.5%. When the numerical time is larger than $t = 160 \frac{\delta_d}{U_{ref}}$, the inner part of turbulent boundary layer already contains the turbulent structures produced by inflow conditions (Liu and Pletcher (2004)). The similarity law can be satisfied in the inner part. It is hard to obtain the desired skin friction by Spalart (1988)'s inflow condition above, because the appropriate turbulent length scale is unknown. In our simulation, we initialized the length scale with $6\delta_d$, but this was not maintained in the two cases calculated. This will be discussed in detail in a later section. The main purpose of this step is to build up a turbulent boundary layer satisfying the law of the wall. Skin friction will be adjusted by the second step. In this step, the inflow method of Lund *et al.* (1998) is used. The advantage of this method is to adjust the skin friction dynamically provided the downstream and inlet satisfy the law of the wall.

The profiles at the outer part of boundary layer are more complex compared with the inner part. In Eq. (7.3), γ is identified with the defect law, and η is denotes $\frac{y}{\delta}$. Currently, the experimental database for the turbulent boundary layer subjected to free stream turbulence is not complete enough to formulate a reasonable inflow mean profile for the purpose of LES or DNS. Taking advantage of a recycling procedure, we do not need to know the details of the targeted mean profile; it will be dynamically adjusted by the fluid itself. We kept Lund *et al.* (1998)'s outer part treatment, but changed the coefficients. In Eq. (7.5):

$$\alpha_{inlt} = \frac{\delta_{inlt}}{\delta_{99}} y_{recy} \quad (7.8)$$

where δ_{inlt} is the desired inlet boundary layer thickness, and δ_{99} is the boundary layer thickness located at the recycle plane. This formula shows the geometric map between the recycle plane and inlet plane. Since the defect law does not work here, γ_1 was chosen such that the inner part and outer part are continuous in the mean velocity, i.e.

$$\gamma_1 = \frac{1.0 - \bar{U}(y^+ = 30)}{1.0 - U_{recy}(y^+ = 30)} \quad (7.9)$$

γ_2 was chosen such that rms velocity profile was continuous at the edge of boundary layer, i.e.

$$\gamma_2 = \frac{TU}{U_{rms}(y = \delta)} \quad (7.10)$$

where TU is free stream turbulence level.

Equation (7.6) represents our treatment of free stream turbulence. We need to maintain the free stream turbulence level and turbulent length scale. Since the free stream does not contain turbulent production, small eddies decay faster than the larger eddies. Thus, at the different downstream stations, the ratios of energy contained by small eddies and the energy contained by large eddies are different. Actually, this ratio decreases with distance. When the scaled periodic boundary condition is utilized, we cannot obtain a perfect inlet profile by only recycling a single downstream plane because that ratio is variable, which results from the fact that small eddies decay faster than larger eddies. So we recycle several planes, and use those planes to produce our inlet free stream profile. In Eq. (7.6), $weight_i$ are weight functions, which monotonically decrease in the order of increasing downstream distance,

$$\sum_{0 \leq i \leq m} Weight_i = 1 \quad (7.11)$$

and γ_3 is a coefficient such that the TU is maintained in the inlet profile. This we call a multi-level recycling method. The weighting function used in this chapter is listed in Table 7.1:

Table 7.1 Table of chosen weighting functions

| Station | Location | weighting |
|---------|-----------------|-----------|
| 1 | $x = 0.8\delta$ | 1.0/1.75 |
| 2 | $x = 1.6\delta$ | 0.5/1.75 |
| 3 | $x = 8.0\delta$ | 0.25/1.75 |

Three stations were utilized in our simulations. Such a weighting was chosen so that the targeted length scale would be approached. In our simulation, a fully implicit scheme was applied (Liu and Pletcher (2006)). A Newton method was utilized in the pseudo-time step.

For accelerating the convergence, the preconditioning technique proposed by Pletcher and Chen (1993) was applied. The equations governing the resolved flows were formulated with the dynamic SGS modeling by Germano *et al.* (1991). An convective boundary condition was employed at out flow.

7.3 Results

Turbulent boundary layers ranging from $Re_d = 1800$ up to $Re_d = 2150$ were calculated by a Newton iteration (Liu and Pletcher (2006)). The simulated free stream turbulence levels were 0%, 5%, and 7.5%. Figure 7.1 shows the comparison of mean velocity profile in a turbulent boundary layer at $Re_{\delta_d} = 2000$ and the DNS profile calculated by Spalart (1988) and an experimental profile by DeGraaff and Eaton (2000). Those DNS and the experimental data are all at $Re_{\delta_d} = 2000$, but without free-stream turbulence. The LES results in the Fig. 7.1 exhibit almost the same mean velocity curve in the inner part of boundary layers as the DNS and experimental data whose free stream is laminar, but exhibit a larger difference in the wake part. Moreover, this figure verifies that the higher free stream turbulence corresponds to the smaller wake in the mean profiles. These phenomena match with the experimental observations by Blair (1983), Barrett and Hollingsworth (2003), and Hancock and Bradshaw (1983).

In order to examine the reliability of this inflow generator, we calculated a turbulent boundary layer without free stream turbulence, because in such a case, there are a lot of reliable DNS or experimental results, such as Spalart's DNS results (Spalart (1988)) and DeGraaff and Eaton's experimental results (DeGraaff and Eaton (2000)), for comparison. Figure 7.2 shows the comparison of the rms of fluctuations in this case with Spalart's DNS (Spalart (1988)) and DeGraaff and Eaton's experimental data (DeGraaff and Eaton (2000)). Fairly good agreement is noted.

To investigate the distribution of first order statistics in the streamwise direction, we plot the curve of U_τ vs x in Fig. 7.3, and the Reynolds number, Re_d , based on displacement thickness vs x in Fig. 7.4. Re_d was calculated by:

$$Re_d = \int_0^{y_1} (1 - \bar{\rho}\tilde{U}) dy \quad (7.12)$$

where y_1 is the upper bound of the numerical domain, the over-line, $\overline{\langle \bullet \rangle}$, stands for the Favre-filtering and $\overline{\langle \bullet \rangle}$ stands for the ensemble average in time and the spanwise direction.

The comparison of skin friction is exhibited in Fig. 7.4. The dashed line is the Ludwig-Tillman empirical curve (Hinz (1975)), where 1.38 is chosen for H . Figure 7.4 suggested that the higher free stream turbulence level would produce a larger shift in the skin friction of turbulent boundary layer. In our simulation, the skin friction coefficient $Cf = 0.00438$ ($U_\tau = 0.0469$) and the length scale was $41.9\delta_d$ or 4.7δ when free stream turbulence level $Tu = 7.5\%$ at the station $Re_{\delta_d} = 2000$. And the skin friction coefficient $Cf = 0.004232$ ($U_\tau = 0.046$) and the length scale was $29.2\delta_d$ or 3.6δ when free stream turbulence level $Tu = 5\%$ at the station $Re_{\delta_d} = 2000$.

Hancock and Bradshaw (1983) formulated the correlation between $\frac{\Delta Cf}{Cf_0}$ and $\frac{Tu}{2.0+L/\delta}$, which is

$$\frac{\Delta Cf}{Cf_0} = \beta \frac{TU \times 100}{2 + L/\delta} \quad (7.13)$$

where L is the integral length scale, and β is about 0.1. Since the skin friction calculated by Spalart (1988) in the case of no free stream turbulence was $Cf = 0.004159$ or $U_{\tau_{au}} = 0.0456$, hence, the contribution of free stream turbulence to the increase of skin friction is

$$\beta = \frac{\Delta Cf}{Cf_0} / \frac{TU \times 100}{2 + L/\delta} \quad (7.14)$$

$$\beta = \frac{0.0046 - 0.004159}{0.004159} / \frac{5}{2 + 3.6} = 0.118 \quad (7.15)$$

when $Tu = 5\%$. Likewise, if $Tu = 7.5\%$,

$$\beta = \frac{\Delta Cf}{Cf_0} / \frac{TU \times 100}{2 + L/\delta} \quad (7.16)$$

$$\beta = \frac{0.00469 - 0.004159}{0.004159} / \frac{7.5}{2 + 4.7} = 0.114 \quad (7.17)$$

Therefore, our numerical results match well with Hancock and Bradshaw (1983)'s experiment.

Figure 7.5 examines the effect of free stream turbulence on the rms fluctuations in the outer part of boundary layer. And Fig. 7.6 shows the effect of free stream turbulence on the rms of fluctuations in the inner region. Those figures verify that free stream turbulence at the level

$Tu = 5\%$ or $Tu = 7.5\%$ can deform the rms profiles of the outer part of the boundary layers, but has only a slight effect on the inner part of the boundary layer.

Figure 7.7 presents the effect of free stream turbulence on the V_{rms} . In the case $Tu = 7.5\%$, a peak appeared about $Y^+ = 900$. This peak is due to the interaction between turbulent boundary layer and free stream turbulence. But in the case $Tu = 5\%$, the location of the peak is in the inner part of boundary layer. This implies that the larger the turbulence level, the higher the peak station in terms of Y^+ . Figure 7.8 shows the effect of free stream turbulence on the W_{rms} .

Figures 7.9 - 7.12 present the downward view of streamwise instantaneous velocity contours at $Y^+ = 23$, $Y^+ = 200$, $Y^+ = 440$ and $Y^+ = 1400$, respectively. Those plots show the different turbulent structures at the different normal distances from the wall. At the station $Y^+ = 23$, the length of the streaky structure is about $10\delta_d \sim 15\delta_d$ or $909 \sim 1364$ in terms of Y^+ . Experiments by Smith *et al.* (1983) indicated that the streaky structure extends over a streamwise distance in wall units of $\Delta L_x^+ > 1000$. In the case of $Re_d = 2000$, $\Delta L_x^+ > 10\delta_d$. $Y^+ = 200$ is located in the logarithmic layer. In this region, the eddies extend more in the spanwise direction, but contract streamwise. $Y^+ = 400$ is located in the outer part of boundary layer. Figure 7.12 shows typical turbulent intermittency phenomena. $Y^+ = 1400$ is in the free stream part.

7.4 Conclusions

Turbulent boundary layers subjected to 0%, 5%, and 7.5% free stream turbulence were calculated by LES. A method to generate inflows with free stream turbulence was discussed in this chapter.

Our numerical results verified that as the free stream turbulence level increased, the extent of the logarithmic region increased and the size of the wake component decreased, a trend reported by Blair (1983), Barrett and Hollingsworth (2003), and Hancock and Bradshaw (1983). And the maximum U_{rms} values increased with increasing turbulence level, but the location of the peak remained fixed between $Y^+ = 10 - 15$. Likewise, the maximum levels of V_{rms}

and W_{rms} increased with increasing free stream turbulence levels. At the 5% and 7.5% free stream turbulence levels, V_{rms} and W_{rms} tended to remain at elevated levels in a narrow range throughout the wake region of the turbulent boundary layer. The increase in Cf with an increase in free stream turbulence agreed fairly well with the experimentally based correlation of Hancock and Bradshaw (1983).

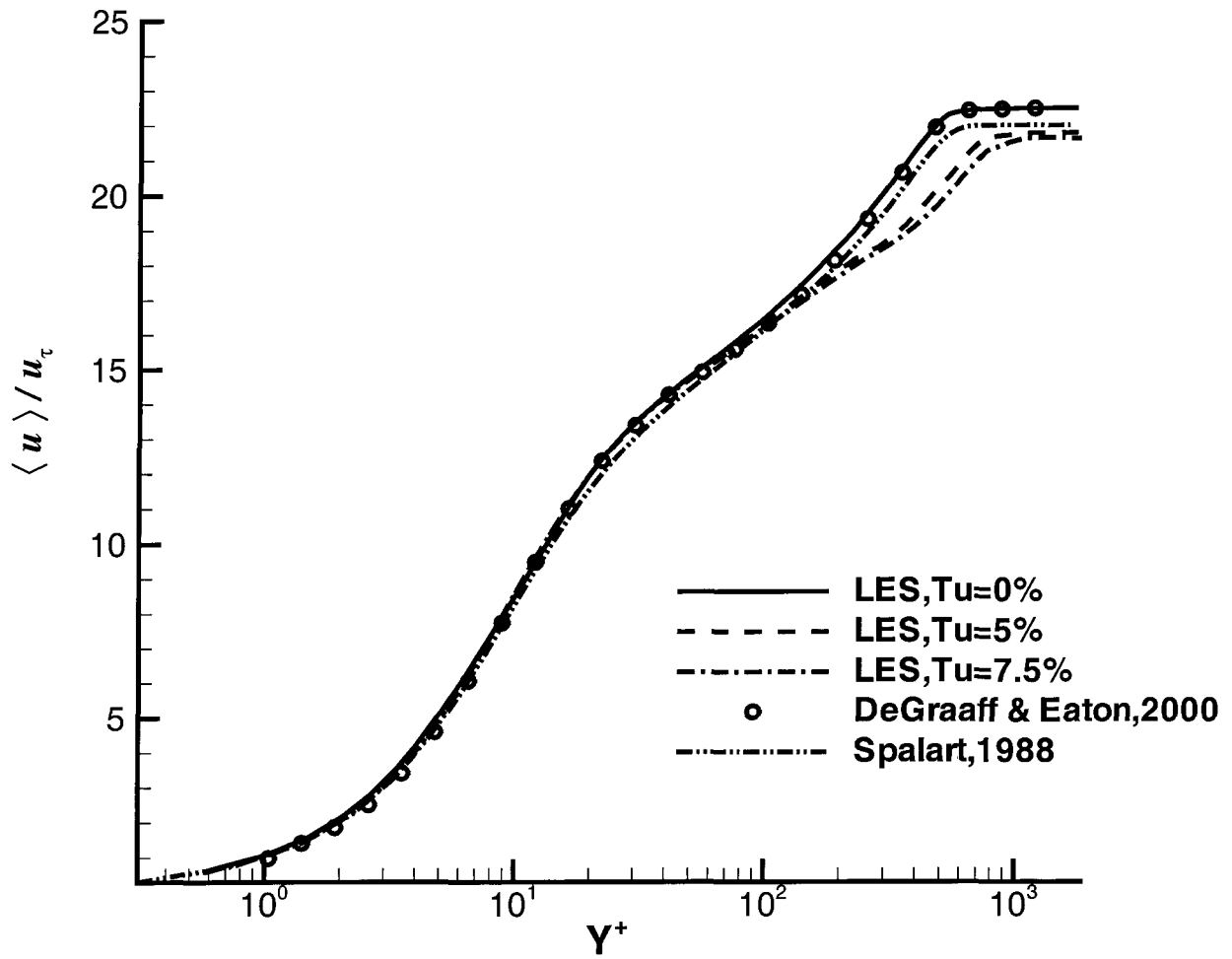


Figure 7.1 Comparison of mean velocity profiles in a turbulent boundary layer $Re_{\delta_d} = 2000$: The solid, dash dot, and long dash line are LES results, the dashed dot dot line gives a DNS profile by Spalart (1988) and the circle symbols are experimental data by DeGraaff and Eaton (2000).

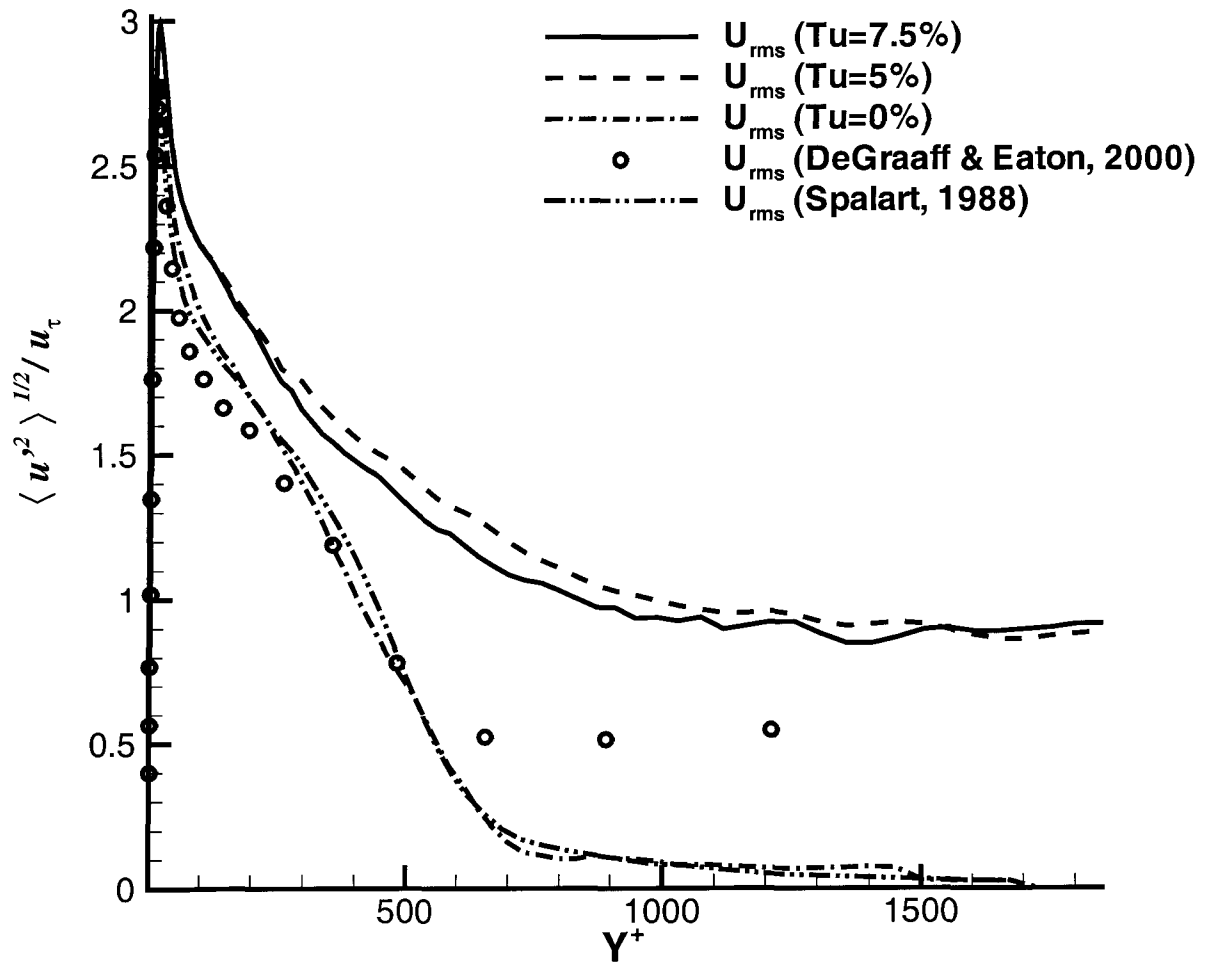


Figure 7.2 Comparison of rms of fluctuations in a turbulent boundary layer $Re_{\delta_a} = 2000$, $TU = 0\%$ and $T_w = T_{ref}$ with DNS profile by Spalart (1988), and the experimental data by DeGraaff and Eaton (2000).

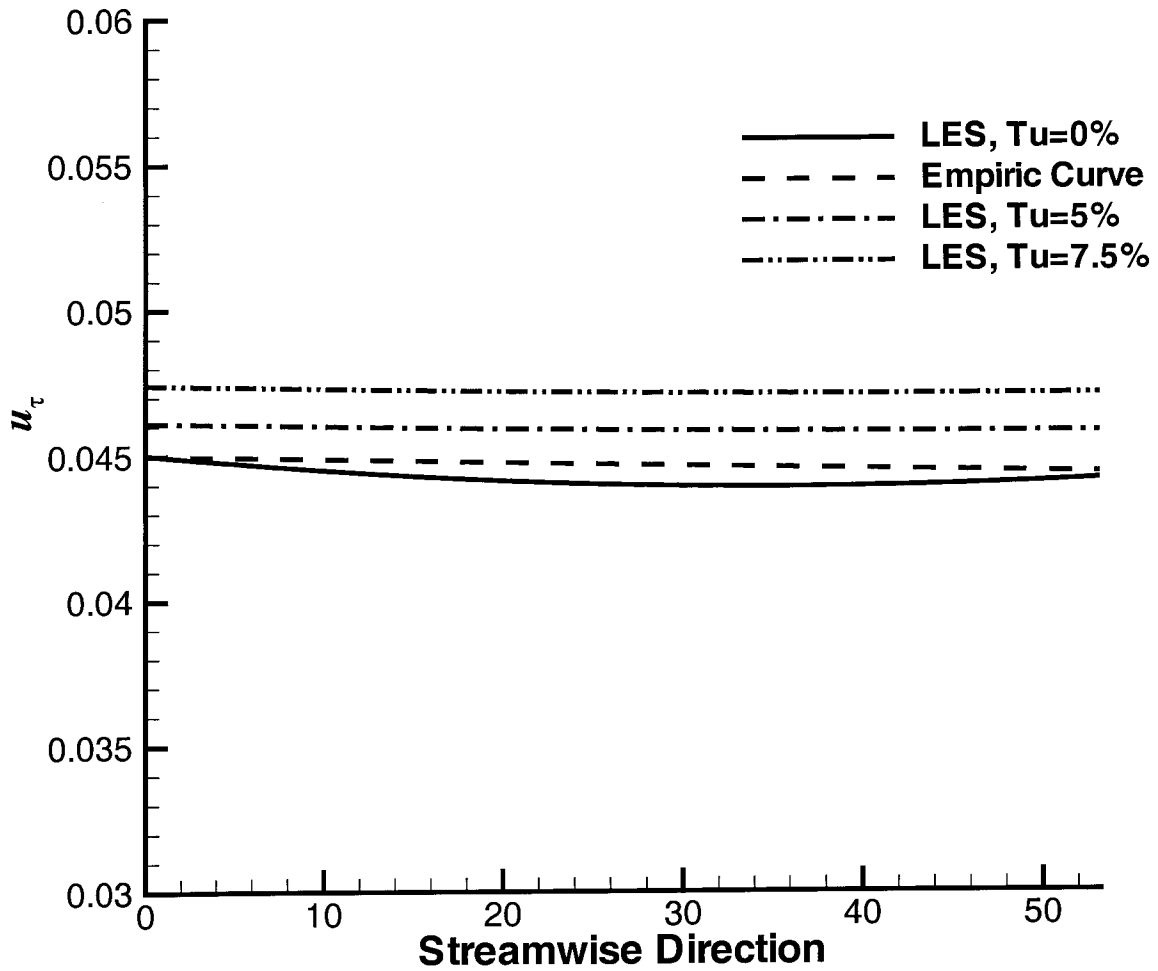


Figure 7.3 The plot of nondimensional U_τ vs streamwise direction in a region from $Re_{\delta_d} = 1760$ up to $Re_{\delta_d} = 2100$.

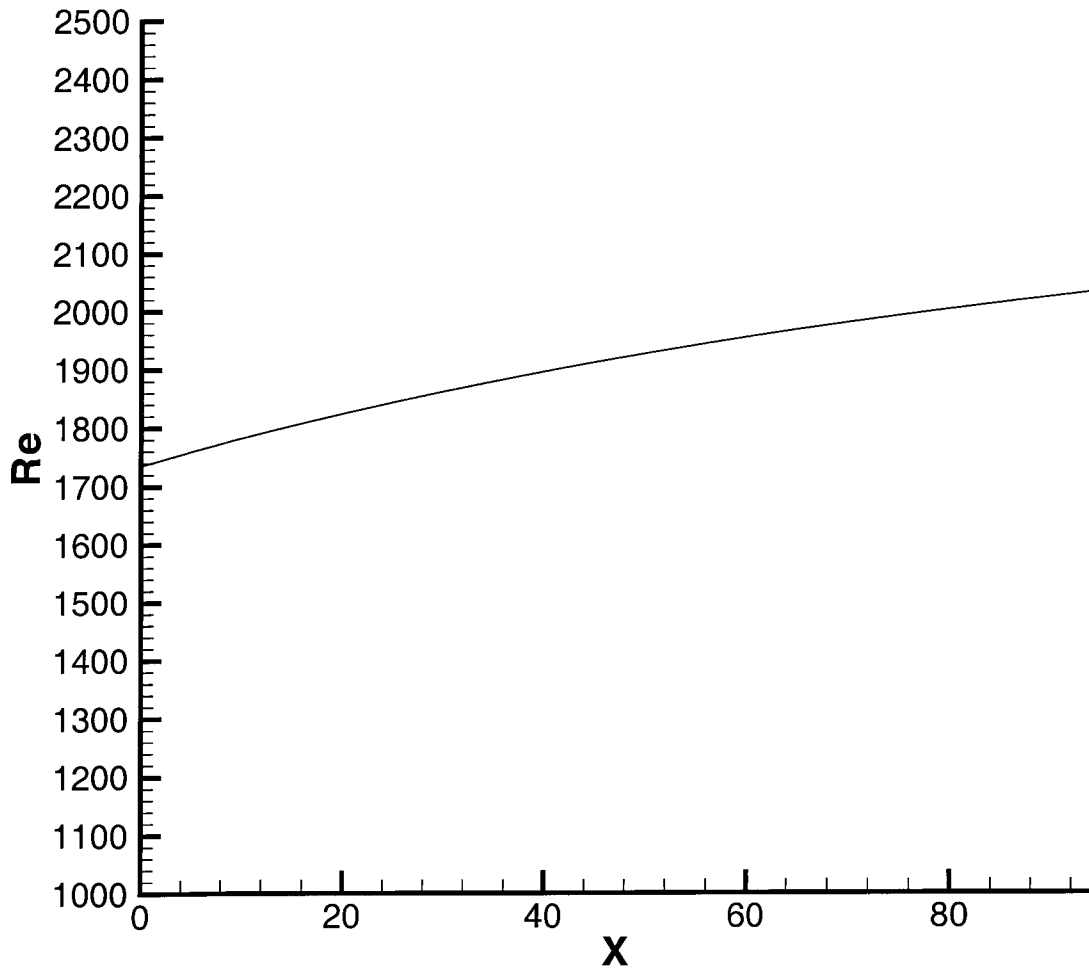


Figure 7.4 Plot of Reynolds number based on displacement thickness vs streamwise distance.

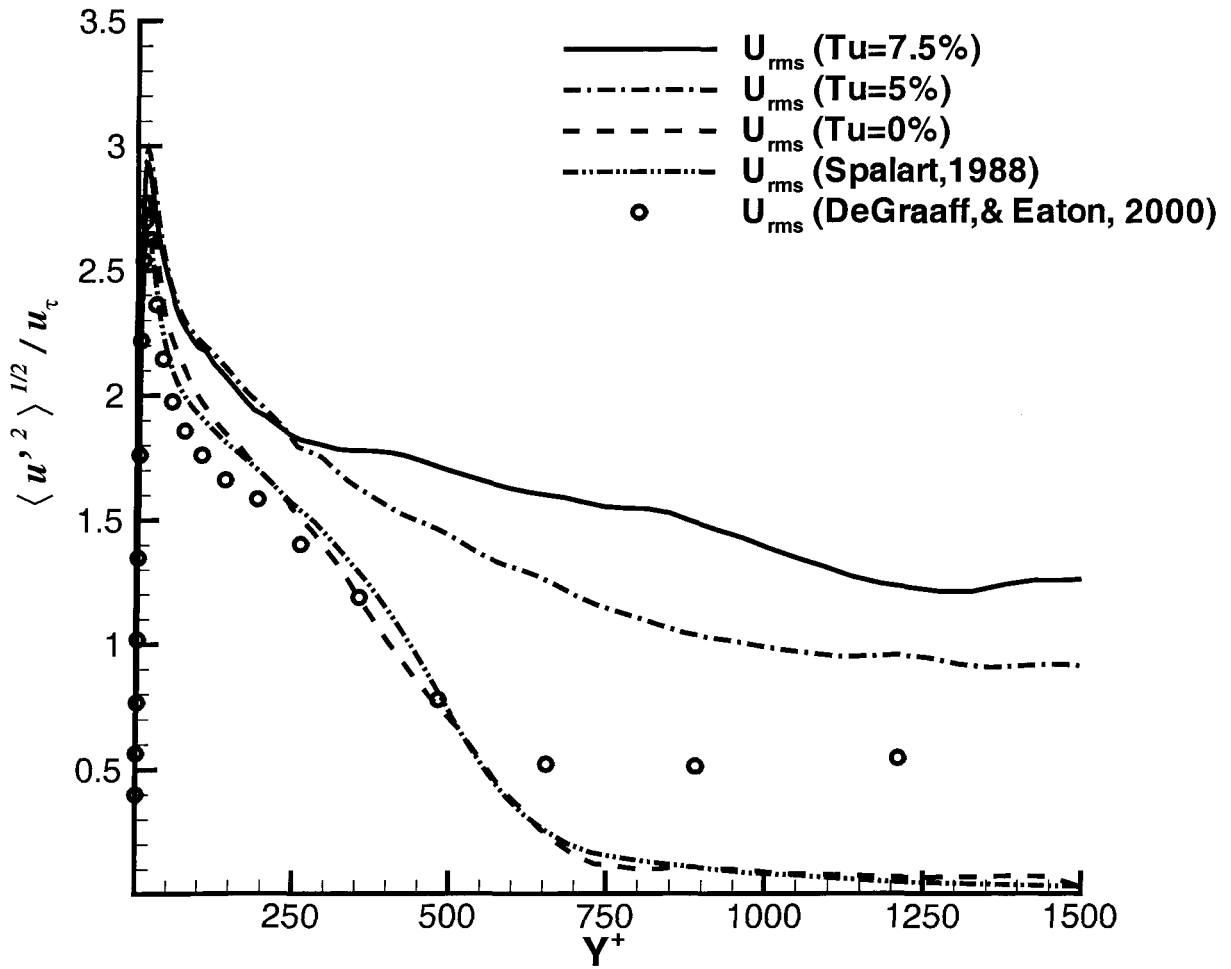


Figure 7.5 Plot of U_{rms} vs normal distance at $Re_{\delta_d} = 2000$ and $T_w = T_{ref}$.

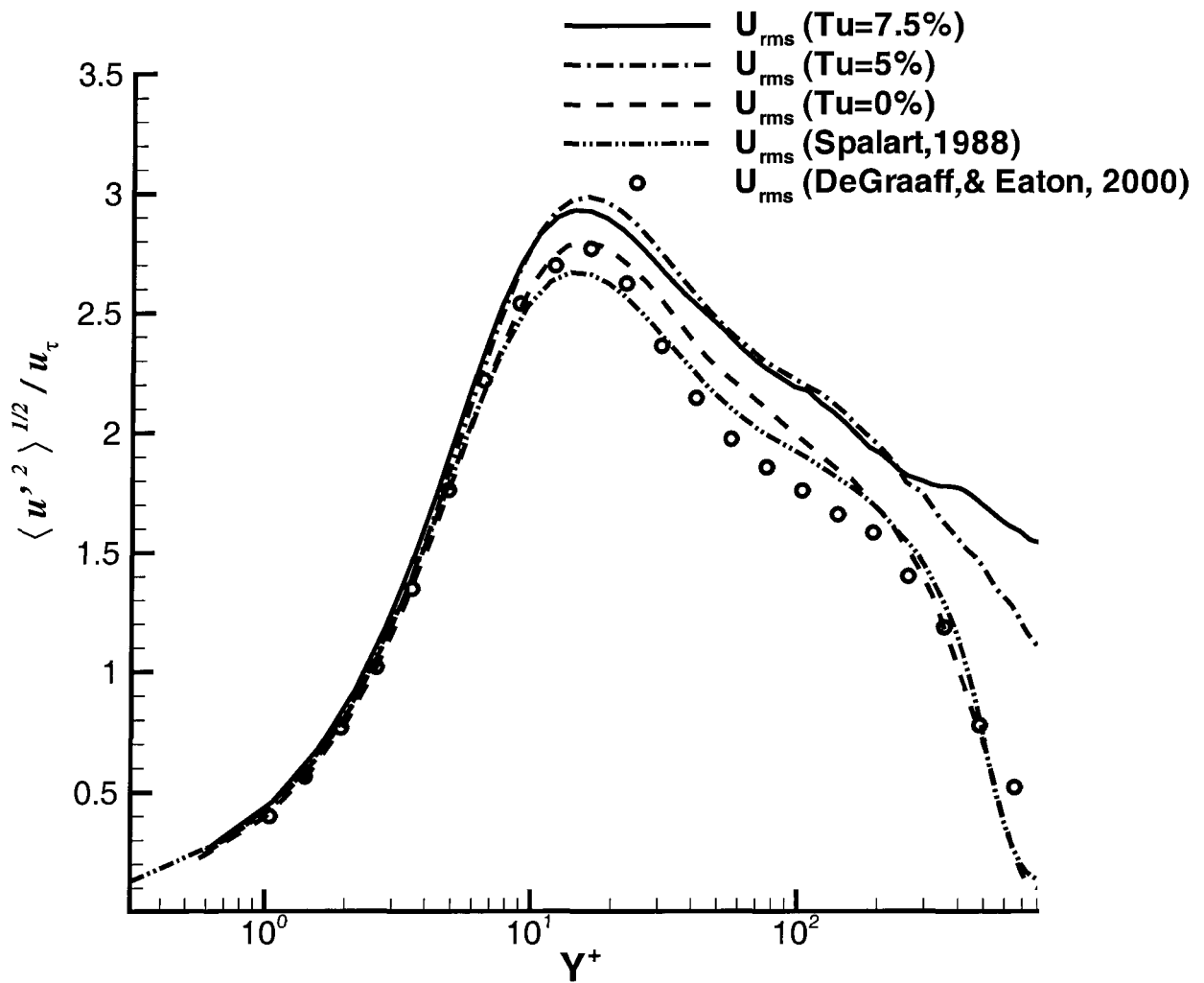


Figure 7.6 The log plot of U_{rms} vs normal distance at $Re_{\delta_d} = 2000$ and $T_w = T_{ref}$.

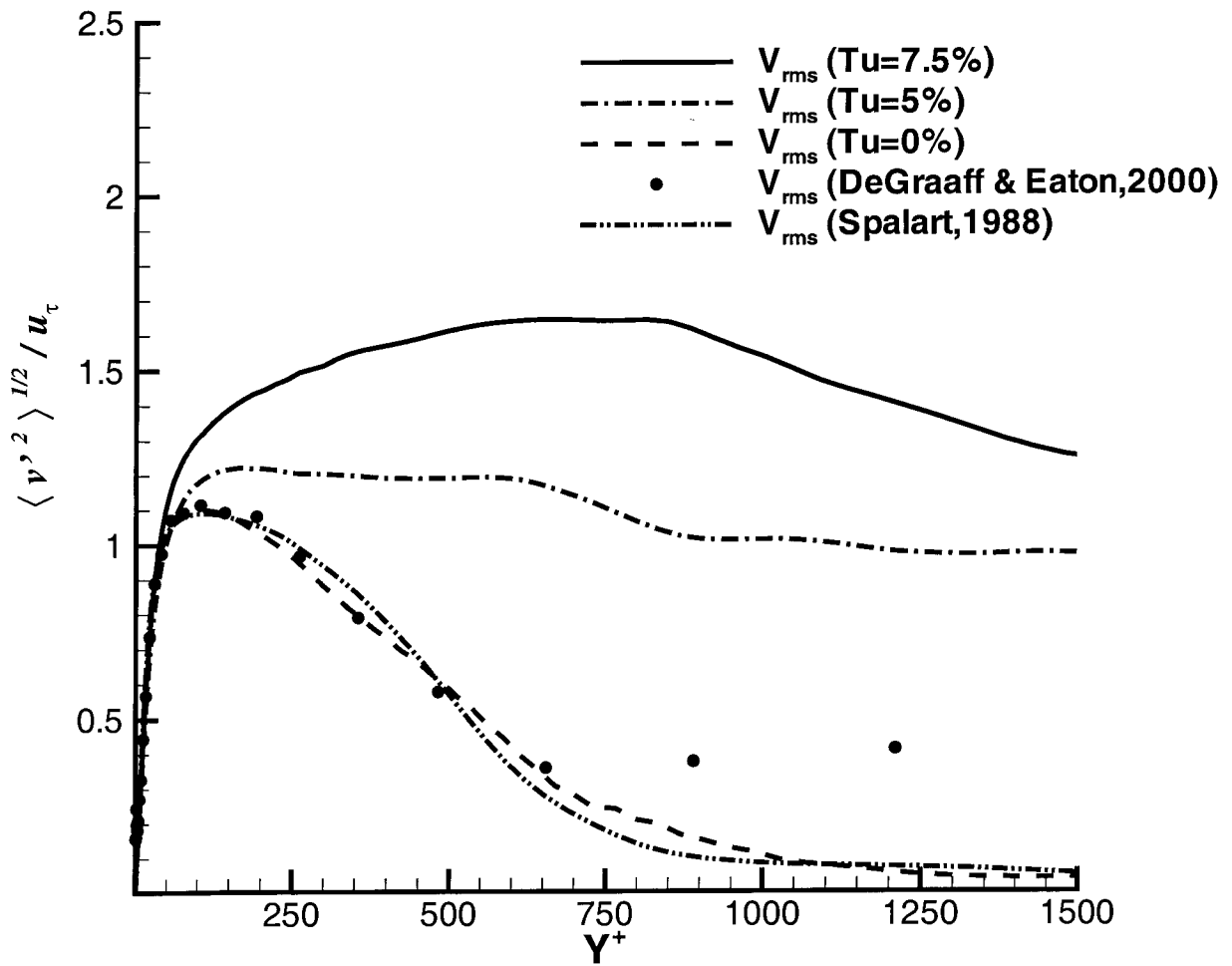


Figure 7.7 Plot of V_{rms} vs normal distance at $Re_{\delta_d} = 2000$ and $T_w = T_{ref}$.

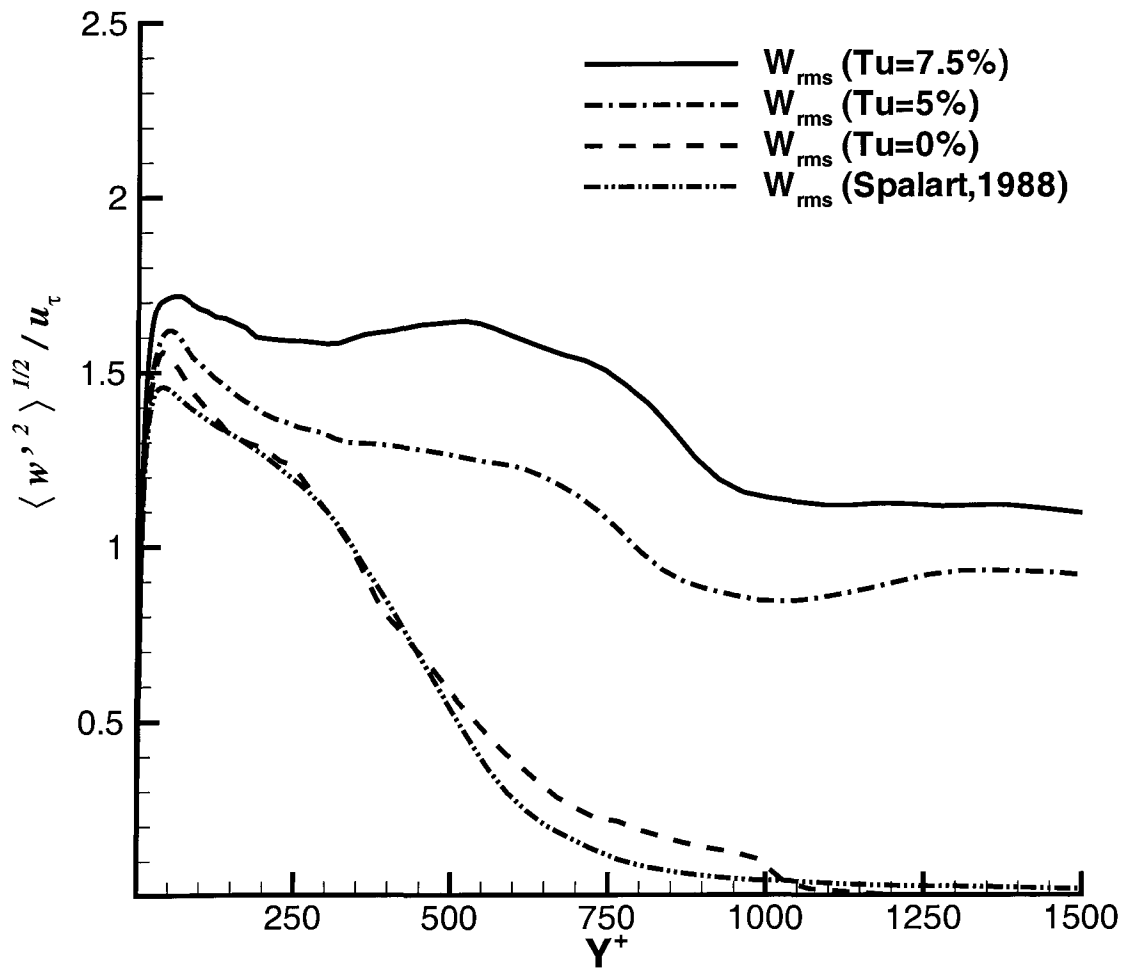


Figure 7.8 Plot of W_{rms} vs normal distance at $Re_{\delta_d} = 2000$ and $T_w = T_{ref}$.

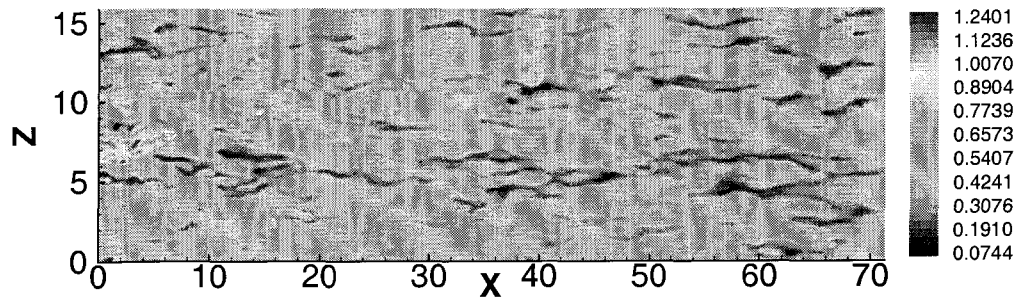


Figure 7.9 The downward view of streamwise velocity contours at $Y^+ = 23$ and $TU = 5\%$.

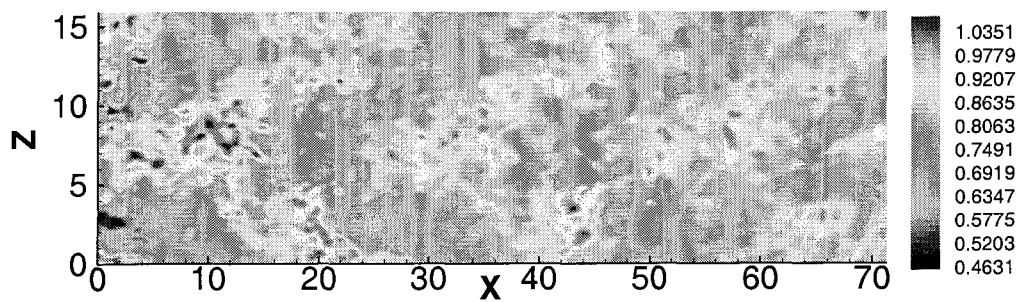


Figure 7.10 The downward view of streamwise velocity contours at $Y^+ = 200$ and $TU = 5\%$.

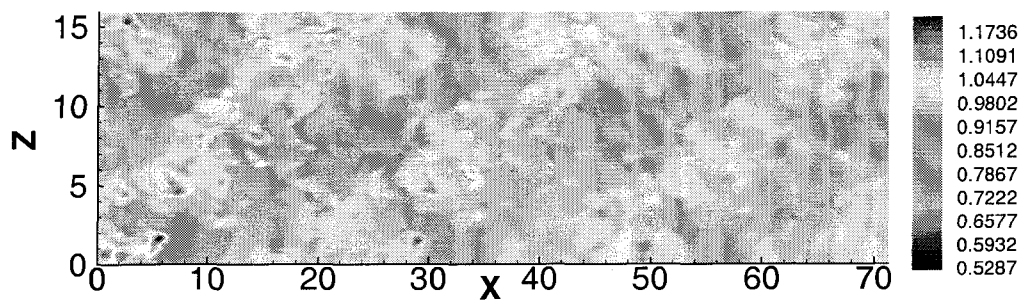


Figure 7.11 The downward view of streamwise velocity contours at $Y^+ = 440$ and $TU = 5\%$.

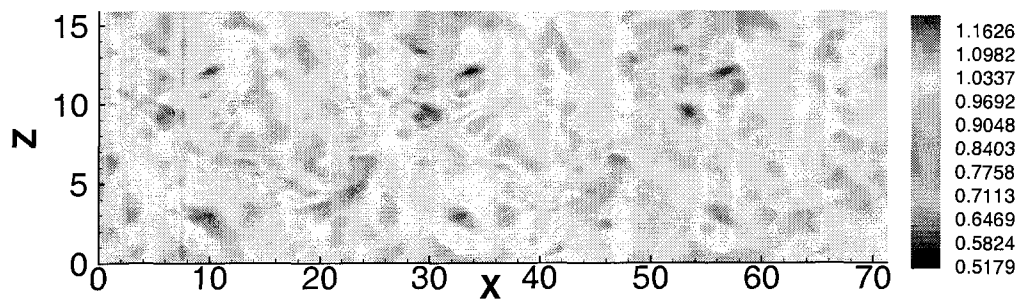


Figure 7.12 The downward view of streamwise velocity contours at $Y^+ = 1400$ and $TU = 5\%$.

CHAPTER 8. LARGE EDDY SIMULATION OF DISCRETE-HOLE FILM COOLING IN FLAT PLATE TURBULENT BOUNDARY LAYERS

Large eddy simulation has been applied to an example discrete hole film cooling configuration. The computational domain included the coolant supply tube as well as the main mixing region. A tube L/D of 8 and an injection angle of 35 degrees was employed for a simulation with a blowing ratio of 0.5 and a density ratio of 2 to demonstrate that realistic cooling conditions can be simulated. Comparisons with experimental data are presented in this chapter.

8.1 Introduction

The advance of turbine engine technology has led to higher turbine inlet temperatures, which requires active cooling in order to maintain blades of the turbine engine at a safe temperature, since extremely high temperatures will reduce the life of blades and even cause the failure of those blades. Film cooling is a widely used technique to achieve this goal. A number of experiments (Ligrani *et al.* (1994a), Ligrani *et al.* (1994b), Sen *et al.* (1996), and Schmidt *et al.* (1996)) have been reported that examine the performance of film cooling.

The effect of the length of the coolant supply tube has received considerable attention in the literature. The tube L/D influences the tube discharge conditions and the resulting downstream structures. A large L/D will produce fully-developed turbulence inside of the pipe. This suggests that a long pipe would provide different counter-rotating vortex structures and local jetting effect compared with the flow promoted by a short pipe. Goldstein *et al.* (1974) found on appreciable difference in effectiveness between an $L/D = 5.2$ and long injection lengths. As the L/D increases, the discharge velocity profiles become more uniform. For a long tube, say $L/D > 6$, the discharge condition becomes nearly independent of tube entrance

conditions.

Burd *et al.* (1996) compared the film cooling effectiveness of an $L/D = 7.0$ configuration with one having $L/D = 2.3$. Their experiments showed that the short-tube injection flow penetrated farther from the wall and influenced a greater extent of the region downstream from the hole under low free stream turbulence, but no significant differences in normalized mean velocities were noted with high free stream turbulence.

Ligrani *et al.* (1994b)'s experimental results examined the film cooling effectiveness of a single row of film-cooling holes with or without compound angle orientations. Regardless of the discharge angle, downstream of the hole at a distance $X/D = 9.9$, fluid properties were periodic in the spanwise direction and remain so up to $X/D = 86$.

The experimental data are limited due to the difficulty of obtaining the measurements, especially with a large temperature difference. In order to provide details for the optimization of blade cooling, it is important to develop accurate numerical simulation methods. The purpose of this chapter is to report progress toward the use of LES to simulate realistic film cooling configurations.

8.2 Numerical Configurations

The Favre-filtered compressible Navier-Stokes equations were employed for the simulation of film cooling. For accelerating convergence, a preconditioning technique suggested by Pletcher and Chen (1993) was applied. A second order central difference finite volume scheme was utilized. The time difference was represented by a second order Euler backward scheme. A fully implicit scheme was implemented. The numerical procedure included two loops: inner loop and outer loop, (or pseudo time step and physical time step). Thus, components were represented as $\langle \bullet \rangle^{m,n}$, where the superscript m stands for the pseudo time step, and the superscript n stands for the physical time step. Newton iteration was applied in the inner loop.

A long-tube configuration with $L/D = 8$ was selected for a LES film cooling simulation. The blowing ratio was 0.5 and the density ratio 2.0. The wall was adiabatic. The arrangement

of the computational domain is shown in Fig. 8.1.

The ratio of the diameter of the pipe to the width of boundary layer namely D/Z was $1/5$. The ratio of the diameter of pipe to the boundary layer thickness namely D/δ was 0.44 . The calculated Reynolds number of the boundary layer range from 1800 up to 2700 based on displacement thickness. The distance from inlet to the center of the hole was $56.5\delta_d$, where δ_d is the inlet displacement thickness. And the distance from the hole center to the outlet was $72.5\delta_d$, which corresponds to $22.656D$. The Reynolds number of the boundary layer at the discharge hole center was $Re_{\delta_d} = 2000$. The Reynolds number for the pipe was 9357.1 . And the injection angle was 35° .

The grid was non-orthogonal in the tube and near the injection hole. Conservation was maintained by employing control volume concepts similar to those employed with unstructured meshes. Figure 8.2 gives a downward view of the numerical mesh employed for the external boundary layer near the injection hole. Figure 8.3 shows the mesh in more detail.

Sixteen processors were used to calculate this case. The LU-SGS scheme and dynamic SGS model were utilized. The numerical grid for the external turbulent boundary layer was $591 \times 85 \times 101$ corresponding to the streamwise, normal and spanwise directions, respectively. And the numerical domain was $126 \times 22 \times 16$ in the units of the inlet displacement thickness. In the internal pipe domain, the numerical grid was $241 \times 41 \times 101$ corresponding to the streamwise, normal and circumferential directions, respectively. The total number of control volumes used in the simulation exceeded 6 million. In units of the external boundary layer initial displacement thickness, the pipe radius was 1.6 and the length was 25.6 .

Since a long pipe was used, the flow at the entrance of the pipe could be treated as a fully developed flow. In order to generate the fully developed flow, an isolated code was executed synchronously. In this subdomain, periodic boundary conditions were utilized in the streamwise direction. A velocity profile in the middle station of this subdomain was reloaded to the entrance of the pipe. The isothermal and no-slip wall condition was used in the pipe.

A recycling and rescaling technique (Liu and Pletcher (2006)) was applied to generate the inflow condition for the external turbulent boundary layer. Considering the effect of the hole

on the upstream flow, the recycling station was kept at least $6D$ from the hole. The adiabatic wall condition was utilized at the wall.

8.3 Numerical Results

Figure 8.4 shows the evolution of the coolant in the buffer zone of the turbulent boundary layer. Due to the strong turbulence in this region, the coolant mixes with the external flow very rapidly. Appearance of turbulence in such a region enlarges the convective heat and mass transfer, which accelerates the mixing of coolant and main flows.

Figure 8.5 shows a side view of the instantaneous temperature contours. This figure clearly shows the evolution of the coolant downstream. Although not discernible in the temperature field, the flow reverses immediately downstream of the hole. Such a reversed flow can be visualized as a vortex. The coolant reattaches to the wall just behind this vortex. The reattachment accelerated the mixing.

Figure 8.6 shows the distribution of adiabatic effectiveness, on the flat plate, which is defined as

$$\eta = \frac{T_{a,w} - T_{r,\infty}}{T_{r,c} - T_{r,\infty}}$$

In this case, the Reynolds number of the external turbulent boundary layer ranges from 1800 to 2700 based on displacement thickness, the density ratio was 2.0, and the blowing ratio was 0.5. The free stream turbulence level was zero in this case. This figure verifies that the distribution of adiabatic effectiveness on the wall is nearly symmetric about the center line of the hole. The magnitude decays in the streamwise direction as the cooled area increases in width.

Figure 8.7 shows the distribution of adiabatic effectiveness on the wall at the station $X/D = 8.75$ downstream of the hole. This plot presents a symmetric like shape, which matches with experimental results (Ligrani *et al.* (1994a), Ligrani *et al.* (1994b), and Burd *et al.* (1996)). Figure 8.8 shows the corresponding contours of the instantaneous temperature field at this station. Denote ξ as the expansion angle,

$$\xi = \tan^{-1}(z(x)/x)$$

where x is the distance from the center of the hole in the streamwise direction, and $z(x)$ is the minimum distance of the point with zero effectiveness to the center line at this specific x station, i.e. $z(x) = \min_z(|z_1(x, z) - z_0(x, z)|)$, where $z_0(x)$ is the center line in the terms of spanwise, and $z_1(x)$ is the point with zero effectiveness. Clearly, ξ represents the expansion of effectiveness in the spanwise direction. Our numerical results show that $\xi \leq 18^\circ$ when $4D < x < 10D$. This implies that the spacing of discrete holes should not be too large.

Figure 8.9 is the plot of adiabatic effectiveness along the center line downstream of the hole. Very near the hole, the adiabatic effectiveness decreases due to a region of reversed flow. The local minimum was located at $X/D = 0.9$ from the center of the hole. The peak value occurred at $X/D = 3.2$ from the center of the hole. The increase in adiabatic effectiveness results from the reattachment of the flow, which increases the heat transfer at the wall. The peak value of the adiabatic effectiveness for this case with a density ratio of 2.0 and a velocity ratio of 0.5 was 0.78.

Figure 8.10 presents the comparison of central line effectiveness with Schmidt *et al.* (1996)'s experimental results. Except very near the injection hole, the numerical results match well with the experimental results. The reason for the discrepancy very near the point of injection is believed to be the difference in the length of the supply tube and Reynolds number of external boundary layer. The experiments used a very short tube, $L/D = 4$, and the Reynolds number of external boundary layer on the location of hole was 1,628 in the units of inlet displacement thickness. But in our current numerical simulation, the Reynolds number of the external boundary layer was 2,000 based on the inlet displacement thickness. And the jet was a fully developed turbulent flow. Thus, the separation and reattachment of the numerical results are different than in the experimental results. What is interesting is that the downstream center line effectiveness seems depend more on the mass fluid ratio than density ratio. This feature was reported by Schmidt *et al.* (See Fig. 4 in Schmidt *et al.* (1996)), and also described by Figure 8.10.

8.4 Conclusions

Film cooling predictions based on the Reynolds-averaged Navier-Stokes equations using a turbulence model generally fail to accurately predict important features of film cooling flows. The present work demonstrates the potential for LES where the modeling issue is kept to a minimum. Comparisons with experiments have been initiated but more needs to be done. We are optimistic the important features of this complex flow can be accurately captured by the present LES procedure.

The numerical results demonstrate the ability of LES to reveal the significant features of film cooling flows. The LES results indicate the effect of reverse flows on the adiabatic effectiveness, which is expected, but is not revealed in experiments. Moreover, the expansion angle of adiabatic effectiveness was measured numerically, which could provide guidance for design purposes. The numerical results provide a measure of the cooling performance of a configuration with an injection angle of 35° , blowing ratio of 0.5 and densities ratio of 2 .

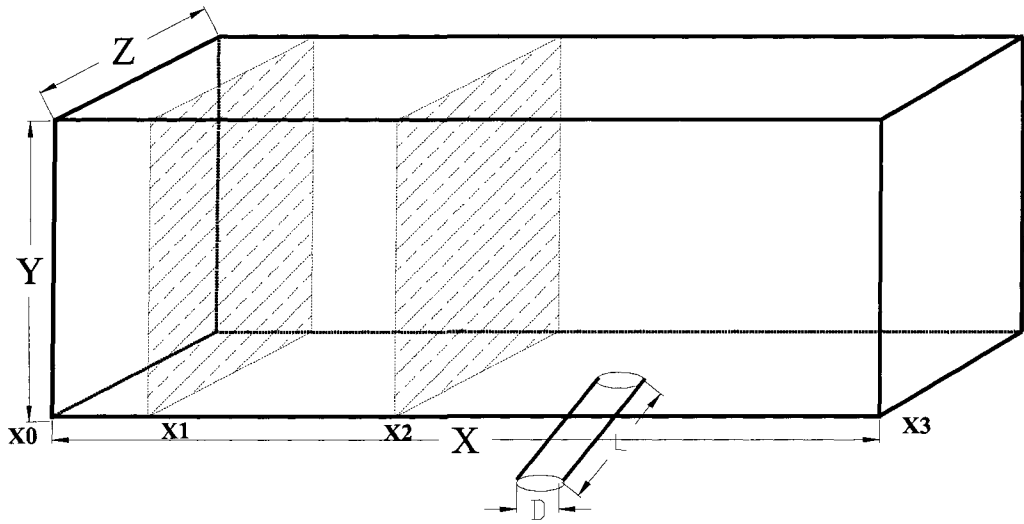


Figure 8.1 The numerical configuration for film cooling.

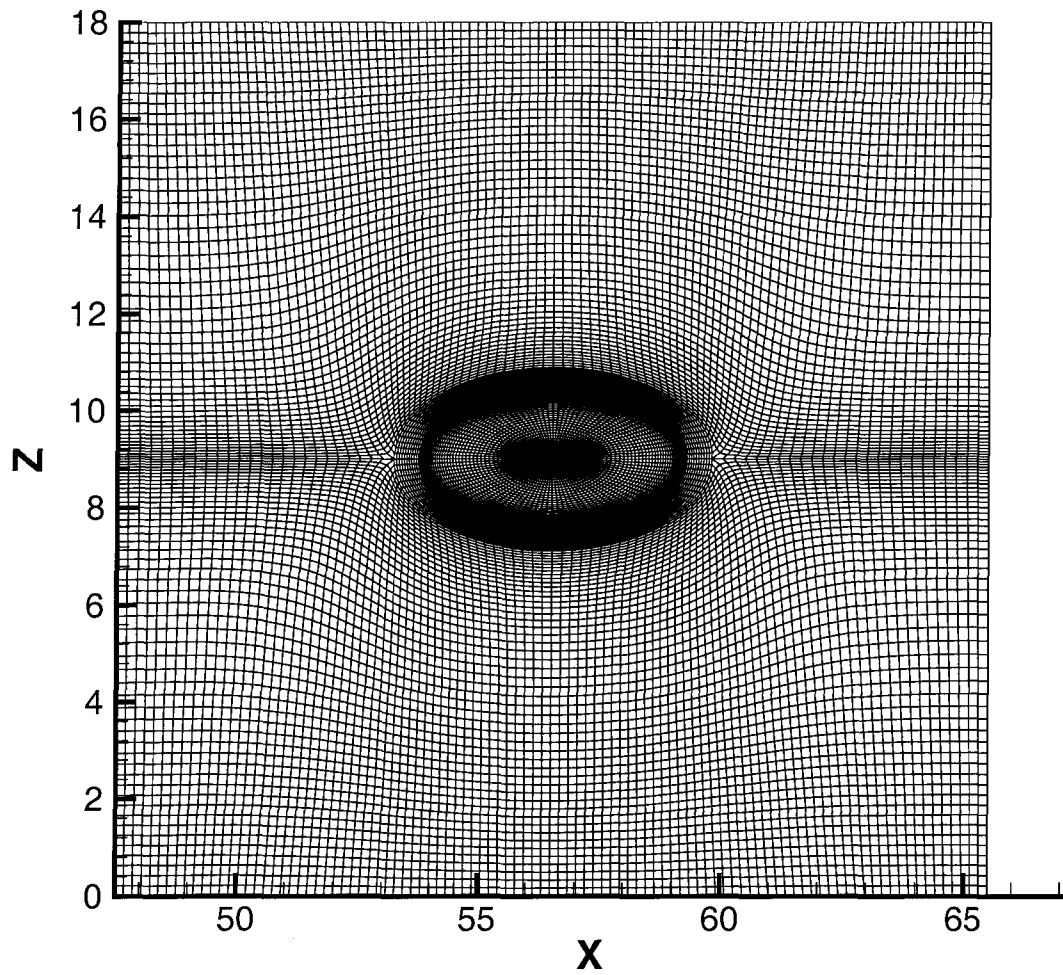


Figure 8.2 The downward view of numerical mesh in the near hole region.

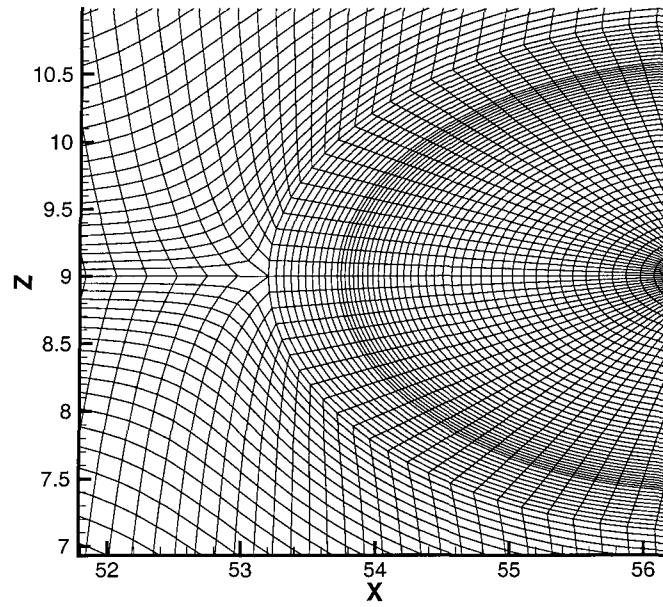


Figure 8.3 The downward view of numerical mesh in the near hole region.

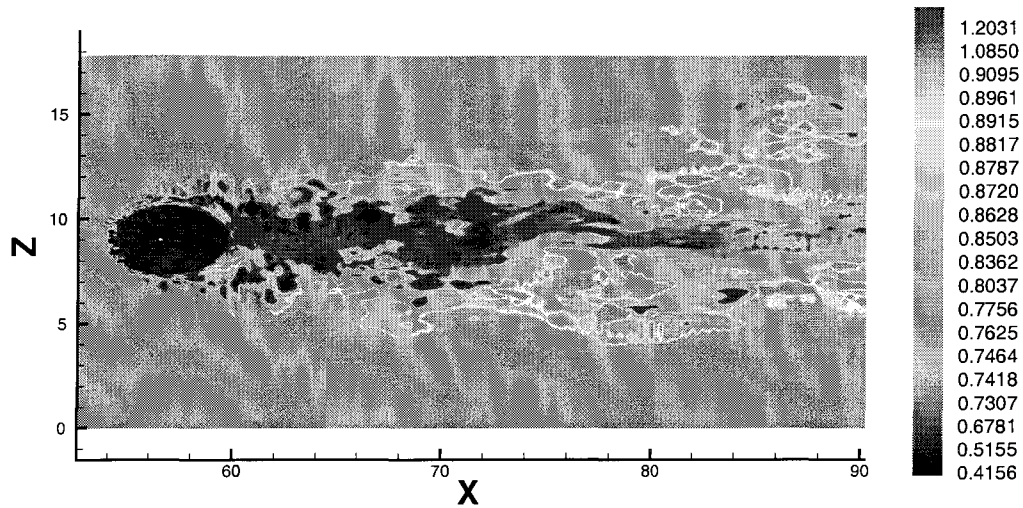


Figure 8.4 The downward of temperature contours at the station $y^+ = 14$, the units of axis are displacement thickness, and the center of the hole is located at $x = 56.5$.

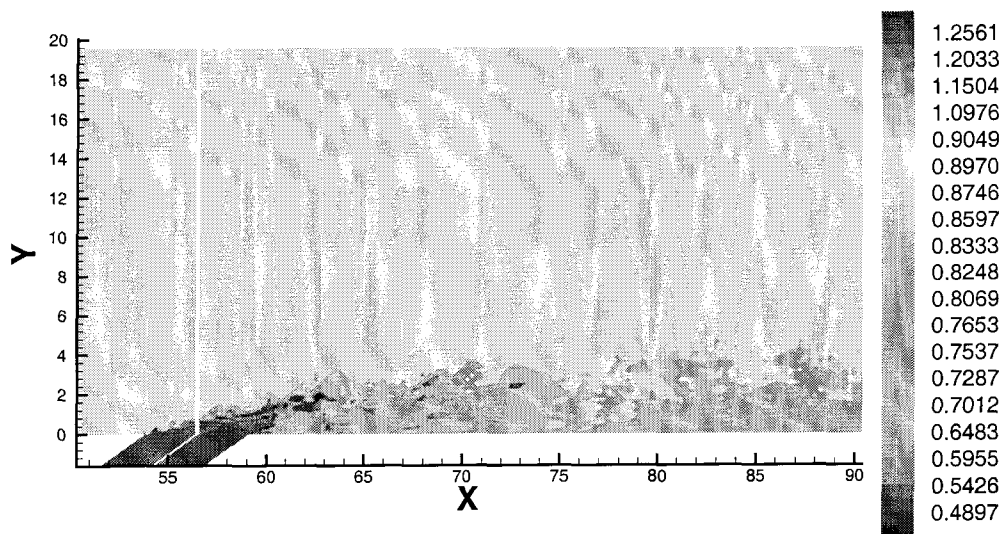


Figure 8.5 The sideview of temperature contours at the centerline of numerical domain. The unit of axis is displacement thickness, and the center of the hole is located at $x = 56.5$.

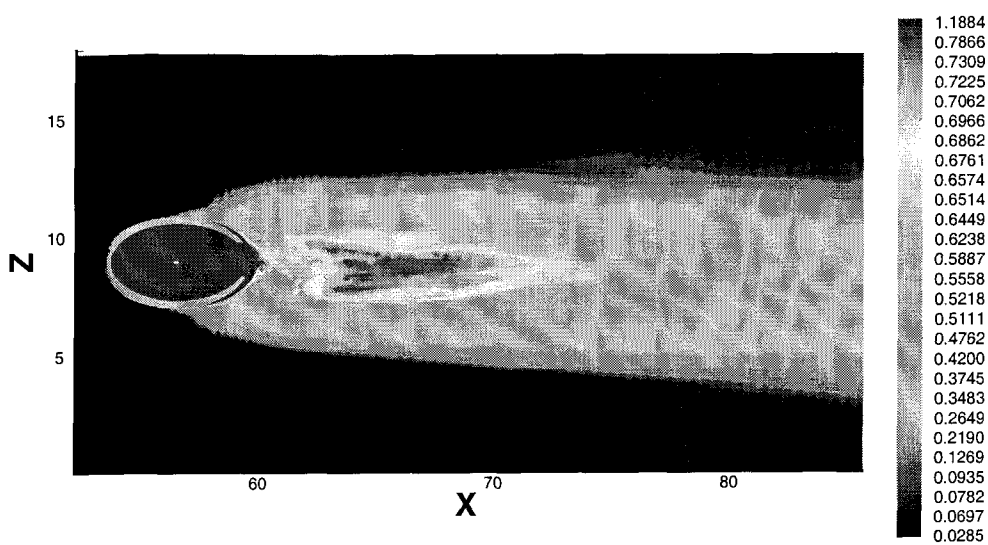


Figure 8.6 The distribution of adiabatic effectiveness on the flat plate in the the case density ratio $DR = 2.0$, blowing ratio $BR = 0.5$, free stream turbulence level $Tu = 0.0$. X is the streamwise direction and Z is the spanwise direction.

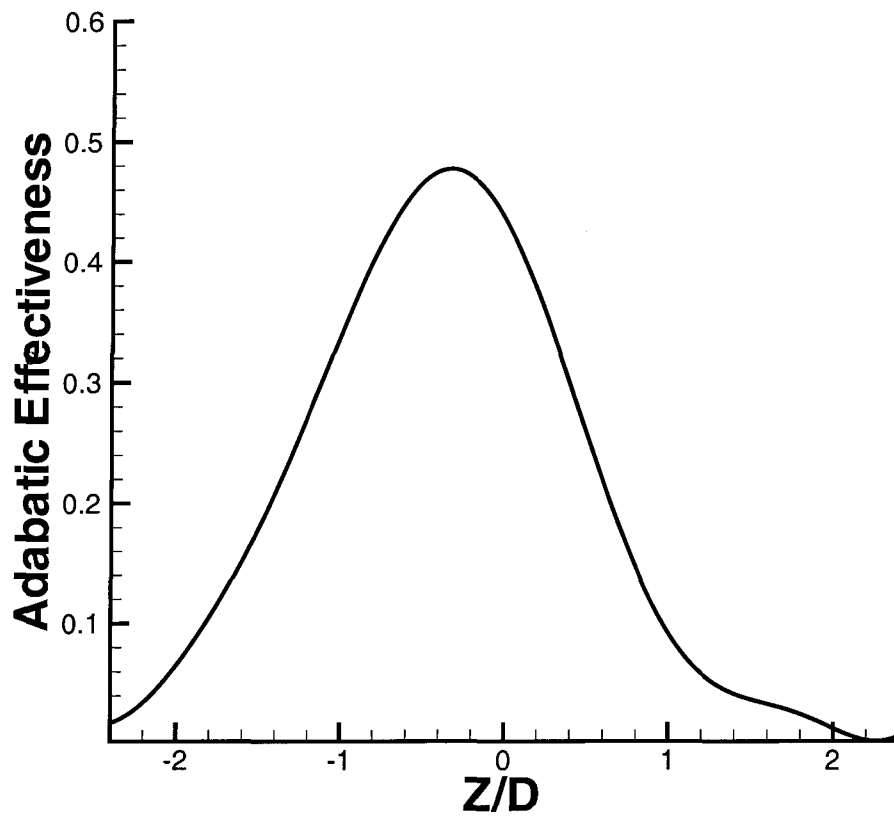


Figure 8.7 The plot of adiabatic effectiveness at the downstream $X/D = 8.75$, where density ratio $DR = 2.0$, blowing ratio $BR = 0.5$ and free stream turbulence level $Tu = 0.0$.

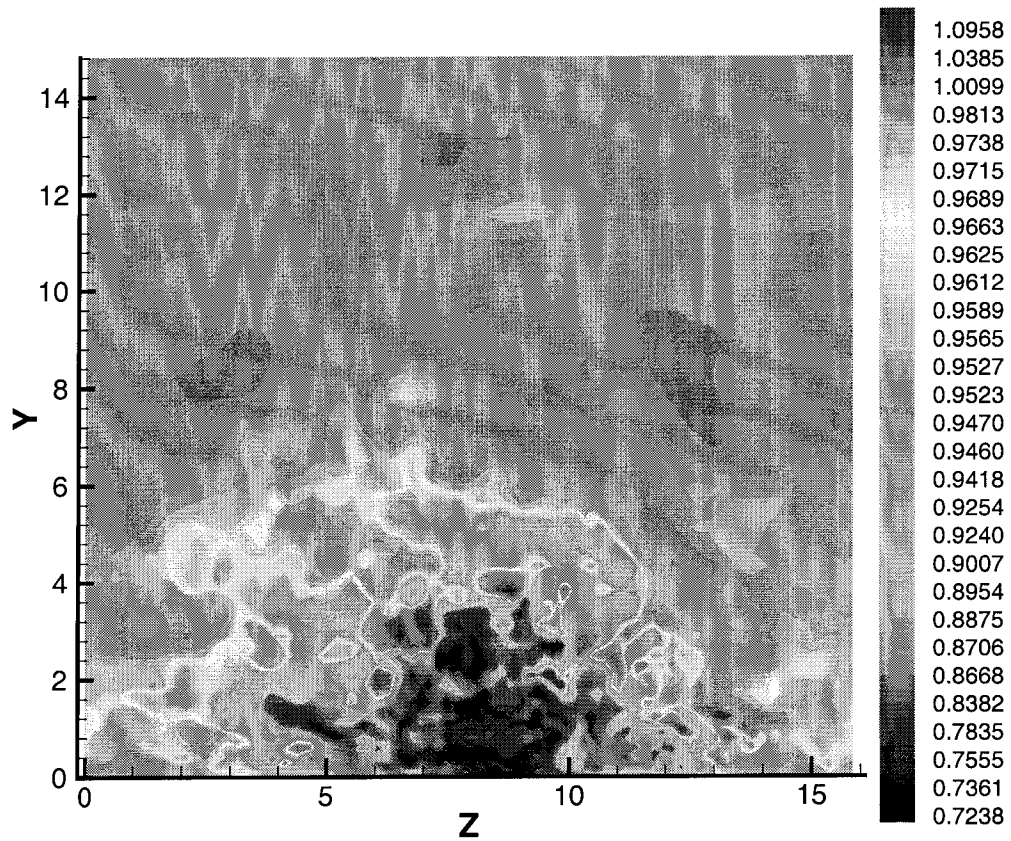


Figure 8.8 The upstream view of temperature contours at $X = 84$; the unit of axis is displacement thickness, and the center of the hole located at $X/D = 8.75$.

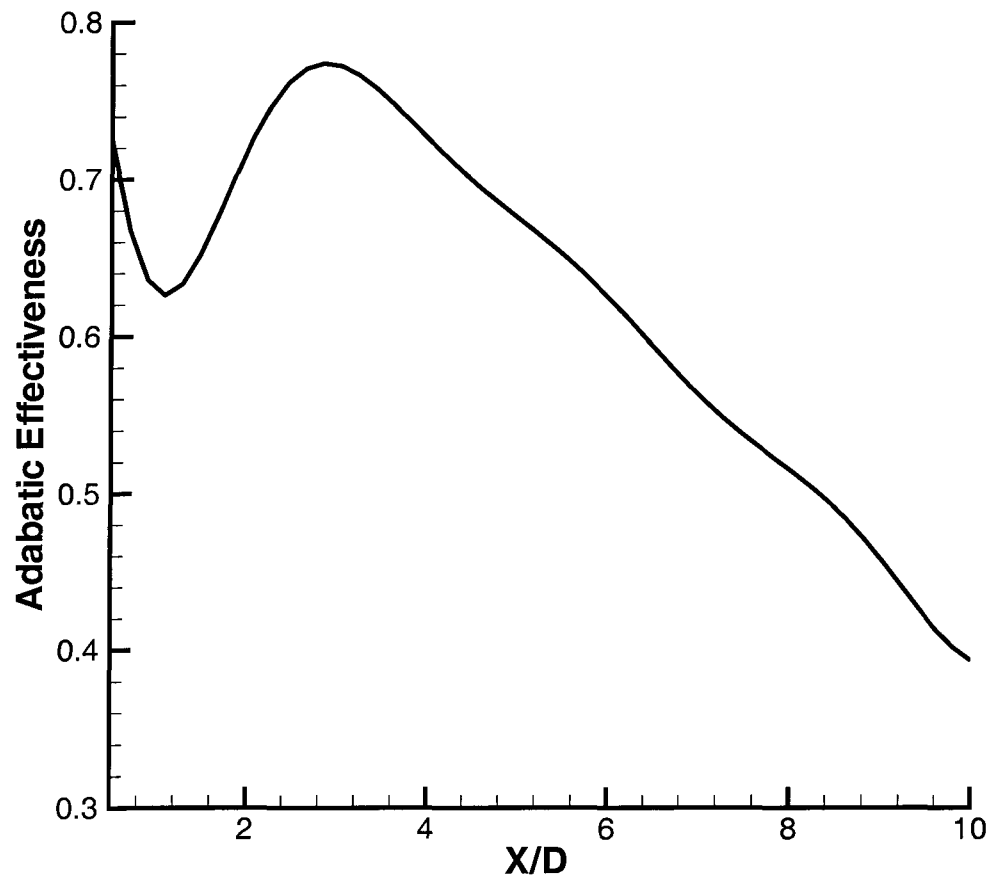


Figure 8.9 The plot of adiabatic effectiveness following the center line of the flat plate, where density ratio $DR = 2.0$, blowing ratio $BR = 0.5$ and free stream turbulence level $Tu = 0.0$.

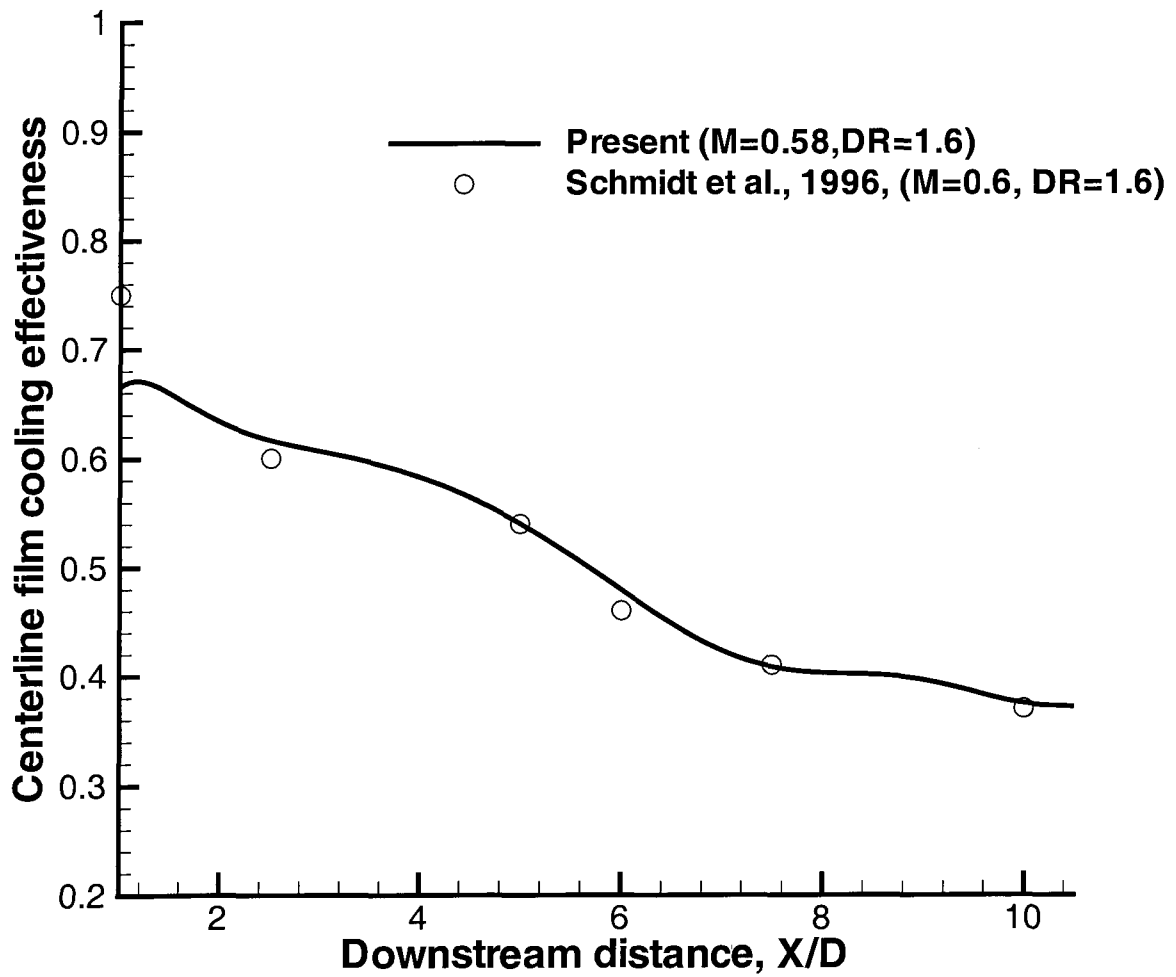


Figure 8.10 The plot of adiabatic effectiveness following the center line of the flat plate, where density ratio $DR = 1.6$, blowing ratio $BR = 0.362$, mass flow ratio $MR = 0.58$, and free stream turbulence level $Tu = 0.0$.

CHAPTER 9. CONCLUSIONS AND RECOMMENDATIONS

A summary of the dissertation is given in section 9.1. Also the significant contributions are outlined in section 9.1. Recommendations for the future study are proposed in the section 9.2.

9.1 Summary and Contributions

Several contributions were made to the fields of CFD, fluid physics, and applied mathematics.

In the area of CFD:

A novel numerical algorithm for solving the compressible Navier-Stokes equations at low Mach numbers was proposed. Calculating the compressible Navier-Stokes equations at the low Mach number limit is a challenge to CFD. Pressure-based methods like the fractional step method or SIMPLE method work for the simulation of the incompressible Navier-Stokes equations but lag some terms of the energy equation in time, which limit the application of the pressure-based methods in the simulation of turbulence with strong heat transfer. The density-based method can solve the energy equation but has a limit on the low Mach number calculation. Although some semi-implicit schemes have been developed for the calculation of the compressible Navier-Stokes equations, the method proposed in this dissertation brings a new idea to handle this problem. The numerical results show that the method is faster than the density-based method for the simulation of low Mach number flows.

Also, two boundary conditions: a dynamic recycling method and a characteristic boundary condition were formulated. The dynamic recycling method provides a robust way to establish the downstream turbulence. Compared with the previous inflow generator, the method helps

to reduce the starting transient. The characteristic boundary condition is a modification of Poinso and Lele (1992)'s early work.

In the area of fluid physics:

The mechanism regarding the anisotropy and non-homogeneity has been studied. The contribution of this study is twofold: theoretical part and numerical part. In the theoretical part, the dissertation proves that the strong fully developed anisotropic turbulence cannot be globally homogeneous without external forcing. Moreover, it was proven that the small scale structures satisfy the incremental homogeneity. This answers Frisch *et al.* (2005)'s paradox about the concept of the local homogeneity. In the numerical part, the three dimensional two-point correlations and the one-point turbulent structure tensors are formulated. The results indicated that the Reynolds stress and the hairpin vortices cause the rotation and asymmetry of the two-point correlations of R_{ww} , but such a rotation has not been found for R_{vv} . The rotation angle of R_{ww} is a function of the normal distance from the wall. And the tails of the two-point correlations decay faster than the power functions. Furthermore, the numerical results indicate that turbulent production makes the major contribution to the anisotropy of the anisotropic tensor b_{ij} compared with the turbulent dissipation and transport.

The PDF of velocities has been studied. The dissertation focuses on the formulation and the mechanism of the PDF. Results show that for the two-dimensional turbulent boundary layer, the PDF of the spanwise velocity is Gaussian, the PDF of the normal velocity fluctuations is approximately a Gaussian distribution, and the PDF of the streamwise velocity fluctuations is a beta distribution. Furthermore, the mechanism for the generation of the PDFs in the wall shear flows is relevant to the sign and the strength of vortices.

A comparison study among three different turbulent boundary layers was conducted, which are a supersonic turbulent boundary layer at Mach number 1.8, a subsonic turbulent boundary layer with heated wall $T_w = 1.58T_e$ at Mach number 0.06, and a subsonic turbulent boundary layer without heated transfer at Mach number 0.06. The influence of the compressibility and variable density effects on the turbulence statistics are discussed. The strong Reynolds analogy, Van Driest transformation, and the applicability of Morkovin's hypothesis were tested.

In the area of pure and applied mathematics:

A numerical algorithm for a class of nonlinear equations including elliptic and parabolic types was proposed, (see appendix C), which is different from the previous methods. The method is a Newton-like method, but the Jacobian operator is perturbed through the Fredholm alternative theorem. The advantage of the method is not in the numerical simulation but in the theoretical analysis because this algorithm provides a way to construct the Cauchy sequence of the solutions. In this sense, this algorithm enables us to conduct the existence and regularity study for nonlinear equations.

From chapter 2 to chapter 8, each of them, indeed, is a journal or conference paper.

9.2 Recommendations for Future Work

The following section describes recommendations for future work. Section 9.2.1 pertains to the work presented in this dissertation. Section 9.2.2 includes the author's opinions of areas that require attention.

9.2.1 Future Work Relate to This Dissertation

In the area of CFD, some modifications could be made to improve the fractional step method proposed by this dissertation. Although no difficulties were observed for the flows considered in this dissertation, it may be advantageous to include a more efficient pressure solver for some flows with complex geometry. The use of unstructured meshes may also extend the limits of the code. The modifications associated with the unstructured mesh should be formulated. The treatment of the scheme at the block interfaces could be improved.

The pressure boundary condition should be improved not only for the inflow but also for the outflow even though the free stream pressure gradient is zero. For the subsonic flows, the numerical outlet pressure condition should be given for the LUSGS scheme or the proposed fractional step method. Conversely, for the supersonic flows, the numerical inlet pressure condition should be considered. However, when the energy equation is solved, the change of the pressure consists in the variation of temperature and density because of the equation of

state. This feature may help to close the numerical pressure conditions. How to formulate the numerical pressure condition by using the equation of state is an interesting problem.

In the area of fluid physics, there are a couple of situations that could be improved. Presently, the Euler statistics including the mean, rms, skewness, flatness, spectrum, Euler PDF, and Reynolds stress budgets are done well. Agreement with previous DNS and experimental results are good. However, the Lagrangian statistics should be improved. An accurate way to trace the particles should be determined. For the wall shear flow, the better way to take the Lagrangian statistic is to use the unstructured or nonuniform mesh so that the longitudinal spacing of the mesh is a function of normal distance from the wall. In this manner, the particle can travel to the next cell at each time step regardless of the normal distance from the wall.

The LES model could be improved. Presently, the dynamic SGS model is utilized. The method is based on the Smagorinsky assumption: which says that the SGS terms are symmetric. i.e.

$$\tau_{ij} - \frac{1}{3}q^2\delta_{ij} = -2C_d\rho D^2\Delta^2 S(S_{ij} - \frac{1}{3}S_{kk}\delta_{ij}) \quad (9.1)$$

Although C_d is variable, for any given specific time and location, the right hand side of the above identity is symmetric, i.e., τ_{ij} is symmetric. However, this is not true for any filter. This is a fundamental problem for the application of LES modeling. A novel LES model is desired such that the anisotropy of turbulence can be taken into account.

9.2.2 Future Studies

The simulation of turbulence subjected to complex geometry will be one of highlights for future research in the CFD area. CFD is ready for the simulation of realistic flows. For this purpose, the unstructured technique should be developed for the simulation of turbulence. A volume-based finite element method may be a good candidate for this. Once the finite element method is selected as the fluid solver, the following issues should be taken into account:

- 1) Accuracy: The comparison study between the finite volume method and finite element method should be conducted.

- 2) Robustness: The influence of the boundary and initial conditions on the convergence should be studied.
- 3) Mesh: The labeling of the mesh, the remesh process, and mesh resolution should be taken into account.
- 4) Efficiency: The numerical solver could be improved in term of the numerical cost.

In the area of fluid physics, the principle mechanism relating to the distributions of PDF and coherent structures needs to be explored. The correlations among the different moments of distributions should be formulated because these features represent the determination of the nonlinear systems. Also, the mechanism relevant to the non-Gaussian distribution should be discussed in detail.

**APPENDIX A. GOVERNING EQUATION FOR REYNOLDS STRESS
ANISOTROPIC TENSOR b_{ij}**

By the definition $b_{ij} = \frac{\langle u_i u_j \rangle}{2k} - \frac{\delta_{ij}}{3}$, where k is the turbulent kinetic energy, $k = \frac{\langle u_i u_i \rangle}{2}$.

Thus,

$$\frac{\partial b_{ij}}{\partial t} + U_k \frac{\partial b_{ij}}{\partial x_k} = \frac{1}{2k} \left[\frac{\partial \langle u_i u_i \rangle}{\partial t} + U_k \frac{\partial \langle u_i u_i \rangle}{\partial x_k} - \frac{\langle u_i u_j \rangle}{k} \left(\frac{\partial k}{\partial t} + U_k \frac{\partial k}{\partial x_k} \right) \right]$$

Due to the equation (4.8),

$$\frac{\partial \langle u_i u_j \rangle}{\partial t} + U_k \frac{\partial \langle u_i u_j \rangle}{\partial x_k} = P_{ij} + T_{ij} + D_{ij} + \Pi_{ij} - \varepsilon_{ij} \quad (\text{A.1})$$

and the turbulent kinetic energy equation,

$$\frac{\partial k}{\partial t} + U_k \frac{\partial k}{\partial x_k} = P_{ii} + T_{ii} + D_{ii} + \Pi_{ii} - \varepsilon_{ii} \quad (\text{A.2})$$

it turns out that

$$\begin{aligned} \frac{\partial b_{ij}}{\partial t} + U_k \frac{\partial b_{ij}}{\partial x_k} &= \frac{1}{2k} \left[(P_{ij} + T_{ij} + D_{ij} + \Pi_{ij} - \varepsilon_{ij}) - \frac{\langle u_i u_j \rangle}{k} (P_{kk} + T_{kk} + D_{kk} + \Pi_{kk} - \varepsilon_{kk}) \right] \\ &= \frac{1}{2k} \left[(P_{ij} + T_{ij} + D_{ij} + \Pi_{ij} - \varepsilon_{ij}) - (2b_{ij} + \frac{2\delta_{ij}}{3}) (P_{kk} + T_{kk} + D_{kk} + \Pi_{kk} - \varepsilon_{kk}) \right] \end{aligned}$$

Let

$$\overline{P_{ij}} = P_{ij} - \frac{\delta_{ij}}{3} P_{ss}$$

$$\overline{T_{ij}} = T_{ij} - \frac{\delta_{ij}}{3} T_{ss}$$

$$\overline{D_{ij}} = D_{ij} - \frac{\delta_{ij}}{3} D_{ss}$$

$$\overline{\Pi_{ij}} = \Pi_{ij} - \frac{\delta_{ij}}{3} \Pi_{ss}$$

$$\overline{\varepsilon_{ij}} = \varepsilon_{ij} - \frac{\delta_{ij}}{3} \varepsilon_{ss}$$

It ends up with

$$\frac{\partial b_{ij}}{\partial t} + U_k \frac{\partial b_{ij}}{\partial x_k} = \frac{1}{2K} [(\overline{P}_{ij} + \overline{T}_{ij} + \overline{D}_{ij} + \overline{\Pi}_{ij} - \overline{\varepsilon}_{ij}) - (2b_{ij} + \frac{\delta_{ij}}{3})(P_{ss} + T_{ss} + D_{ss} + \Pi_{ss} - \varepsilon_{ss})]$$

APPENDIX B. LU-SGS SCHEME

The lower-upper symmetric Gauss-Seidel (LU-SGS) scheme was originally developed by Yoon and Jameson (1987) for the Euler and Navier-Stokes system without preconditioning. Dailey and Pletcher (1996) reformulated the LU-SGS scheme by using the preconditioning technique. Usually, the dual time step was utilized by the LU-SGS scheme. The pseudo-time derivative was discretized with a first-order Euler backward difference, and the physical time derivative was discretized with a second order or higher order Euler backward difference. Hence,

$$\left\{ \frac{\Omega}{\Delta\tau} [I] + [\Gamma]^{-1} [T] \frac{3}{2} \frac{\Omega}{\Delta t} + [\Gamma]^{-1} \sum_{\beta=1}^6 [([A]_{nx} + [B]_{ny} + [C]_{nz}) S]_{\beta} \right\}_m \Delta \mathbf{W} = -\mathfrak{R}_m \quad (\text{B.1})$$

where m is the pseudo-time step, $[\Gamma]$ is the preconditioning matrix, $[A] = \partial E_i / \partial W$, $[B] = \partial F_i / \partial W$ and $[C] = \partial G_i / \partial W$ are linearized inviscid flux vectors in x , y and z directions, respectively. \mathbf{W} is the vector of variance and \mathfrak{R} is the preconditioned residual. The viscous stresses and sub-grid scale stresses were lagged as the values of the previous pseudo time step and included in the preconditioned residual. The surface index is defined as shown in Fig. B.1. The inviscid flux Jacobians on each face are defined as

$$\begin{aligned} [\hat{A}] &= ([A]_{nx} + [B]_{ny} + [C]_{nz})_{S=1,3} \\ [\hat{B}] &= ([A]_{nx} + [B]_{ny} + [C]_{nz})_{S=2,4} \\ [\hat{C}] &= ([A]_{nx} + [B]_{ny} + [C]_{nz})_{S=5,6} \end{aligned} \quad (\text{B.2})$$

where n_x , n_y , and n_z are the projection of the normal direction of the surface on the x , y and z directions.

Substituting inviscid flux Jacobian by using Eq. B.2, the linearized equation, Eq. B.1, can be reduced to

$$\left\{ [\Gamma]^{-1} [T] \frac{3}{2} \frac{\Omega}{\Delta t} + [\Gamma]^{-1} \left[[\hat{A}]_1 S_1 - [\hat{A}]_3 S_3 + [\hat{B}]_2 S_2 - [\hat{B}]_4 S_4 + [\hat{C}]_5 S_5 - [\hat{C}]_6 S_6 \right] \right\} \Delta \mathbf{W} = -\mathfrak{R} \quad (\text{B.3})$$

The pseudo-time step, $\Delta \tau$, was set to infinity, corresponding to a Newton iteration that drives the Newton linearization error to zero in each physical time step. In the above, the Γ is the preconditioning matrix. In this study, the preconditioning matrix Γ is given by Eq. 2.32. Thus, it turns out that:

$$[\tilde{A}] = [\Gamma]^{-1} [\hat{A}], \quad [\tilde{B}] = [\Gamma]^{-1} [\hat{B}], \quad [\tilde{C}] = [\Gamma]^{-1} [\hat{C}] \quad (\text{B.4})$$

To achieve the diagonal dominance of the solver, the shifting operator was used. In this manner, the flux Jacobian were split as

$$[\tilde{A}] = [\tilde{A}]^+ + [\tilde{A}]^-, \quad [\tilde{B}] = [\tilde{B}]^+ + [\tilde{B}]^-, \quad [\tilde{C}] = [\tilde{C}]^+ + [\tilde{C}]^- \quad (\text{B.5})$$

where

$$\begin{aligned} [\tilde{A}]^\pm &= \frac{1}{2} \left([\tilde{A}] \pm \left| \lambda_{[\tilde{A}]} \right| [I] \right) \\ [\tilde{B}]^\pm &= \frac{1}{2} \left([\tilde{B}] \pm \left| \lambda_{[\tilde{B}]} \right| [I] \right) \\ [\tilde{C}]^\pm &= \frac{1}{2} \left([\tilde{C}] \pm \left| \lambda_{[\tilde{C}]} \right| [I] \right) \end{aligned} \quad (\text{B.6})$$

The quantities $\lambda_{[\tilde{A}]}$, $\lambda_{[\tilde{B}]}$ and $\lambda_{[\tilde{C}]}$ are the maximum eigenvalues of the flux Jacobian $[\tilde{A}]$, $[\tilde{B}]$ and $[\tilde{C}]$, respectively. For the preconditioned system, the maximum eigenvalues are

$$\begin{aligned} \lambda_{[\tilde{A}]} &= \frac{1}{2R} \left[(R+1)|\tilde{u}| + \sqrt{(R-1)^2 \tilde{u}^2 + 4Rc^2} \right] \\ \lambda_{[\tilde{B}]} &= \frac{1}{2R} \left[(R+1)|\tilde{v}| + \sqrt{(R-1)^2 \tilde{v}^2 + 4Rc^2} \right] \\ \lambda_{[\tilde{C}]} &= \frac{1}{2R} \left[(R+1)|\tilde{w}| + \sqrt{(R-1)^2 \tilde{w}^2 + 4Rc^2} \right] \end{aligned} \quad (\text{B.7})$$

where R is the gas constant, c is the speed of sound and \tilde{u} , \tilde{v} and \tilde{w} are the Cartesian velocity components in the x , y and z directions, respectively.

Thereby, the flux Jacobians on the surface of the control volume were approximated as

$$\begin{aligned}
([\Gamma][\tilde{A}]\Delta W)_1 &= ([\Gamma][\tilde{A}]^+\Delta W)_{i,j,k} + ([\Gamma][\tilde{A}]^-\Delta W)_{i+1,j,k} \\
([\Gamma][\tilde{A}]\Delta W)_3 &= ([\Gamma][\tilde{A}]^+\Delta W)_{i-1,j,k} + ([\Gamma][\tilde{A}]^-\Delta W)_{i,j,k} \\
([\Gamma][\tilde{B}]\Delta W)_2 &= ([\Gamma][\tilde{B}]^+\Delta W)_{i,j,k} + ([\Gamma][\tilde{B}]^-\Delta W)_{i,j+1,k} \\
([\Gamma][\tilde{B}]\Delta W)_4 &= ([\Gamma][\tilde{B}]^+\Delta W)_{i,j-1,k} + ([\Gamma][\tilde{B}]^-\Delta W)_{i,j,k} \\
([\Gamma][\tilde{C}]\Delta W)_5 &= ([\Gamma][\tilde{C}]^+\Delta W)_{i,j,k} + ([\Gamma][\tilde{C}]^-\Delta W)_{i,j,k+1} \\
([\Gamma][\tilde{C}]\Delta W)_6 &= ([\Gamma][\tilde{C}]^+\Delta W)_{i,j,k-1} + ([\Gamma][\tilde{C}]^-\Delta W)_{i,j,k}
\end{aligned} \tag{B.8}$$

After substituting Eq. B.4 and Eq. B.8 into Eq. B.3, it turns out:

$$([L] + [D] + [U])\Delta \mathbf{W} = -\mathfrak{R} \tag{B.9}$$

where the matrices $[L]$, $[D]$ and $[U]$ are

$$\begin{aligned}
[L] &= -[\Gamma]^{-1} \left[([\Gamma][\tilde{A}]^+)_{i-1,j,k} S_3 \right. \\
&\quad \left. + ([\Gamma][\tilde{B}]^+)_{i,j-1,k} S_4 + ([\Gamma][\tilde{C}]^+)_{i,j,k-1} S_6 \right]
\end{aligned} \tag{B.10}$$

$$\begin{aligned}
[D] &= [\Gamma]^{-1} [T] \frac{3}{2} \frac{\Omega}{\Delta t} + [\Gamma]^{-1} \left[([\Gamma][\tilde{A}]^+)_{i,j,k} S_1 - ([\Gamma][\tilde{A}]^-)_{i,j,k} S_3 \right. \\
&\quad + ([\Gamma][\tilde{B}]^+)_{i,j,k} S_2 - ([\Gamma][\tilde{B}]^-)_{i,j,k} S_4 \\
&\quad \left. + ([\Gamma][\tilde{C}]^+)_{i,j,k} S_5 - ([\Gamma][\tilde{C}]^-)_{i,j,k} S_6 \right]
\end{aligned} \tag{B.11}$$

$$\begin{aligned}
[U] &= [\Gamma]^{-1} \left[([\Gamma][\tilde{A}]^-)_{i+1,j,k} S_1 \right. \\
&\quad \left. + ([\Gamma][\tilde{B}]^-)_{i,j+1,k} S_2 + ([\Gamma][\tilde{C}]^-)_{i,j,k+1} S_5 \right]
\end{aligned} \tag{B.12}$$

Note that $[D]$ was only a function of quantities defined at the center points, $[L]$ was only a function of quantities defined at the lower points, and $[U]$ was only a function of quantities defined at the upper points.

Due to the splitting of the flux Jacobian,

$$[\Gamma][\tilde{A}]^+ - [\Gamma][\tilde{A}]^- = \left| \lambda_{[\tilde{A}]} \right| \tag{B.13}$$

$$[\Gamma][\tilde{B}]^+ - [\Gamma][\tilde{B}]^- = \left| \lambda_{[\tilde{B}]} \right| \tag{B.14}$$

$$[\Gamma][\tilde{C}]^+ - [\Gamma][\tilde{C}]^- = \left| \lambda_{[\tilde{C}]} \right| \tag{B.15}$$

Furthermore, it was assumed that $S_1 \approx S_3$, $S_2 \approx S_4$, and $S_5 \approx S_6$. Thus, the matrix $[D]$ can be reduced to

$$[D] = \frac{3}{2} \frac{\Omega}{\Delta t} [\Gamma]^{-1} [T] + \left(\left| \lambda_{[\tilde{A}]} \right| S_{13} + \left| \lambda_{[\tilde{B}]} \right| S_{24} + \left| \lambda_{[\tilde{C}]} \right| S_{56} \right) [I] \quad (\text{B.16})$$

where

$$S_{13} = \frac{1}{2}(S_1 + S_3), S_{24} = \frac{1}{2}(S_2 + S_4), S_{56} = \frac{1}{2}(S_5 + S_6)$$

Because the product of $[\Gamma]^{-1}[T]$ is a diagonal matrix, the matrix $[D]$ is also diagonal. Equation Eq. B.9 can be approximately factored as

$$([L] + [D])[D]^{-1}([D] + [U])\Delta \mathbf{W} = -\mathfrak{R} \quad (\text{B.17})$$

and efficiently solved in three steps as follows:

$$\begin{aligned} \text{Step1 :} \quad & ([L] + [D])\Delta \mathbf{W}^* = -\mathfrak{R} \\ & \Delta \mathbf{W}^* = [D]^{-1}(-\mathfrak{R} - [L]\Delta \mathbf{W}^*) \\ \text{Step2 :} \quad & ([D] + [U])\Delta \mathbf{W} = [D]\Delta \mathbf{W}^* \\ & \Delta \mathbf{W} = \Delta \mathbf{W}^* - [D]^{-1}[U]\Delta \mathbf{W} \\ \text{Step3 :} \quad & \mathbf{W}^{m+1} = \mathbf{W}^m + \Delta \mathbf{W} \end{aligned}$$

Since $[D]$ is diagonal matrix except for the control volumes in the center region of the pipe, the inversion of $[D]$ required a trivial amount of work and hence the LU-SGS scheme is still very efficient compared to other implicit schemes.

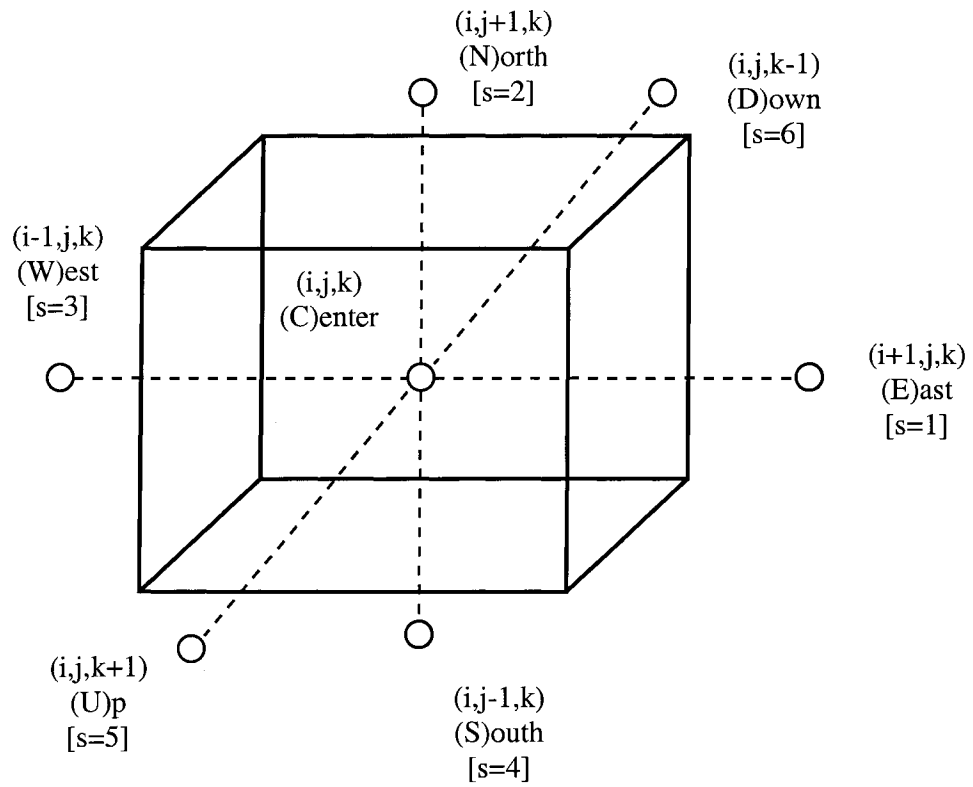


Figure B.1 Main control volume with cell center, (i,j,k) , and six neighboring cell centers, labeled as E, W, N, S, U, and D.

APPENDIX C. EXISTENCE OF A STRONG SOLUTION FOR A CLASS OF NONLINEAR PARABOLIC SYSTEMS

C.1 Introduction

We study the Cauchy-Dirichlet problem of strong solution for a class of nonlinear parabolic partial difference equations

$$\frac{\partial u}{\partial t} + f(u, x, Du, D^2U) = f_0 \quad (\text{C.1})$$

$$u(0, x) = g(x) \quad , \quad u(t, x) = h(t; x) \quad \text{when } x \in \partial U. \quad (\text{C.2})$$

in the domain $[0, T] \times U$, where the nonlinear function f is a polynomial of linear operators and can be represented by

$$f(u, x, Du, D^2U) = Lu - L_1u. \quad (\text{C.3})$$

Here, Lu is a linear part of f obeying

$$Lu := -D_i(a^{ij}(x)D_ju) + b(x)u, \quad (\text{C.4})$$

and L_1u is the high order part of f given by

$$L_1u = \sum_{i=2}^M \sum_{n=1}^{N_i} \prod_{j=1}^i F_{i,j,n}(u). \quad (\text{C.5})$$

We assume that the Dirichlet problem of the system (C.1)-(C.2) hold following conditions:

(A1), U is a bounded connected open set in \mathbb{R}^N satisfying $C^{m+2s+2,1}$ -regularity property, and there exists a $m + 2s + 2$ -smooth one to one transform of U onto disk(0,1), where $\infty > m > N/2$, $\infty > s > 0$, and N is a positive integer.

(A2), $a^{ij}(x) \in C^{m+2s+1,1}(\bar{U})$ and $b(x)$ are non-negative. L is self-adjoint, bounded and strong elliptic. i.e. there exist positive number γ_1 , γ_2 , and a non-negative number γ_3 such

that $a^{ij} = a^{ji}$,

$$|a^{ij}(x)\xi_i\xi_j| \geq \gamma_1 |\xi|^2, \quad \forall x \in U, \xi \in \mathbb{R}^N, \quad (\text{C.6})$$

$$\sum |a^{ij}(x)|^2 \leq \gamma_2, \quad \forall x \in U, \quad (\text{C.7})$$

and

$$\infty > b(x) \geq \gamma_3 \geq 0, \quad \forall x \in U. \quad (\text{C.8})$$

Moreover, $g \in H^{m+2s+1}(\bar{U})$, $h \in C^1(0, T; H^{m+2s+1}(\partial\bar{U})) \cap C^0(0, T; H^{m+2s+3}(\partial\bar{U}))$, and $f_0 \in H^{m+2s}(\bar{U})$ is a force independent of u .

(A3), each $F_{i,j,n}$ is a linear operator from $C^j(0, T; H^{a+p_{i,j,n}}(U))$ into $C^j(0, T; H^a(U))$ so that

$$\|F_{i,j,n}(u)\|_{C^j(0,T;H^a(U))} \leq a_{i,j,n} \|u\|_{C^j(0,T;H^{a+p_{i,j,n}}(U))} \quad (\text{C.9})$$

where $m + 2s + 1 \geq \alpha \geq 0$, $s \geq j \geq 0$, $1 \geq p_{i,j,n} > -\infty$, and the space $C^j(0, T; H^a(U))$ is defined by definition 4.

f is uniformly elliptic, but may not be convex or proper because of the condition (A2) and (A3). When the condition (A1) and (A2) are held, the eigenvalues of operator Lu are positive and the eigenfunctions $\varphi_{\lambda_i} \in H_0^1(U) \cap H^{m+2s+2}(U)$ span a Hilbert space $H(U)$ (theorem 8.37, Gilbarg and Trudinger (2001)). Moreover, $F_{i,j,n}$ can be convolution, scalar multiplication, differential or integral operator etc. Nonlinear parabolic equation (C.1) is a general representation of reaction-diffusion equation and Burger's equation etc. Here, the i is the order of the nonlinear operator $\prod_{j=1}^i F_{i,j,n}$ and the N_i is the maximum number of the nonlinear operator

$\prod_{j=1}^i F_{i,j,n}$ with the order i .

There are some dramatic efforts carried out in the study of the fully nonlinear partial difference equations including the elliptic and parabolic types during the last three decades. Two main methods have been developed for solving fully nonlinear elliptic equations. One approach is to prove the existence of classical solutions of the Dirichlet problem in a smooth bounded domain $U \in \mathbb{R}^N$ directly using the continuity method (Evans (1982) and Krylov (1983), and Caffarelli and Huang (2003)). For this, one needs to prove a priori estimates for solutions in the

space $C^{2,\alpha}(\bar{U})$ for some $0 < \alpha < 1$. The second approach called viscosity solution method is to prove the existence of some sort of generalized solutions and then to achieve their uniqueness and regularity (Evans (1978), Crandall and Lions (1983), and Crandall *et al.* (1992)). A major breakthrough in the theory of viscosity solutions was made by Jensen (1988), who proved a comparison principle which turned out the uniqueness of viscosity solutions of the Dirichlet problem for

$$f(D^2u, x) = 0$$

at least for f independent of x , but the existence of solutions of the Dirichlet problem is not proved. Indeed, our knowledge about the existence and high order regularity of fully nonlinear PDEs remains elusive, particularly for the nonlinear PDEs which are not convex or proper. A typical case is the Navier-Stokes equation. Although the existence of the weak solution (Leray (1934), Caffarelli *et al.* (1982)) and mild solution Kato (1984) of Navier-Stokes equation are known, the global existence of the strong solution still remains open.

The objective of this paper is to prove the Dirichlet problem of the strong global solution in the space $[0, T] \times U$ for a class of nonlinear parabolic systems (C.1)-(C.2) under the condition (A1), (A2), and (A3), where the system may not be convex.

C.2 Notation and Main Ideas

C.2.1 Notation

Definition 4 Denote $C^s(0, T; H^m(U))$ by a vector space consists of all functions u such that

$$\|u\|_{C^s(0, T; H^m(U))} := \sum_{0 \leq j \leq s} \max_{0 \leq t \leq T} \left\| \frac{\partial^j u}{\partial t^j} \right\|_{H^m(U)} < \infty$$

where $U \in \mathbb{R}^N$.

Definition 5 Denote $B_m^{s,q}(0, T; U)$ by a vector space consists of all functions u ,

$$u \in \cap_{j=0}^s C^{s-j}(0, T; H^{m+qj}(U)) \quad (\text{C.10})$$

where $U \in \mathbb{R}^N$ and $q \geq 2$. $\|u\|_{C^s(0, T; H^m(U))}$ is defined by

$$\|u\|_{B_m^{s,q}(0, T; U)} = \sum_{0 \leq j \leq s} \|u\|_{C^{s-j}(0, T; H^{m+qj}(U))}$$

Definition 6 Let the constant ε^* be arbitrary in the domain $[\frac{1}{4}, \frac{1}{2}]$, $\theta = \frac{4C_\gamma}{\varepsilon^*}$,

$$C_\gamma = 2N^{m+2(s+1)} \max(1, \frac{\sqrt{T}}{\sqrt{\gamma_1}}, \min(T, \frac{\sqrt{T}}{\sqrt{\gamma_3}})),$$

$$C_\theta = M2^M C_*^M \sum_{i=2}^M \sum_{n=1}^{N_i} [(i-1) \prod_{l=1}^i (a_{i,l,n})],$$

$$\lambda = \min(1, \frac{\varepsilon^*}{4MC_\gamma \max(1, C_*^M) \sum_{i=2}^M \sum_{n=1}^{N_i} (\prod_{l=1}^i a_{i,l,n})}), \quad (\text{C.11})$$

and

$$\beta = \min(\frac{1}{4}, \frac{(1-\varepsilon^*)}{2\theta \|r_0\|_{B_{m+2s}^{1,2}(0,T;U)}}, \frac{(1-\varepsilon^*)^2}{4C_\theta \theta^2 \|r_0\|_{B_{m+2s}^{1,2}(0,T;U)}}) \quad (\text{C.12})$$

respectively. Here, C_* is a constant given by lemma 7, r_0 is given by C.13.

C.2.2 The Idea of Construction

The main idea of this paper is to construct a Cauchy sequence $\{u_k\}$ to approach the global solution of nonlinear parabolic equation (C.1) in the space $B_{m+1}^{s+1,2}(0,T;U)$. The theorems 5 and 6 will show that $B_{m+1}^{s+1,2}(0,T;U)$ is complete.

Assume that u_k is not the solution. It must have a nontrivial residue r_k , where r_k is defined by

$$r_k := (\frac{\partial}{\partial t} + L)u_k - f_0 - L_1 u_k. \quad (\text{C.13})$$

Let $\rho_k s_k := u_{k+1} - u_k$, where ρ_k is a constant less than 1. Since $f(u_{k+1})$ is a polynomial of linear functional on u_{k+1} , identity (C.1) can be decomposed into three parts;

$$r_{k+1} = r_k + F_1(\rho_k s_k) + F_2(\rho_k s_k) \quad (\text{C.14})$$

where $F_1(\rho_k s_k)$ is given by

$$F_1(\rho_k s_k) := (\frac{\partial}{\partial t} + L)(\rho_k s_k) - \sum_{i=2}^M \sum_{n=1}^{N_i} \sum_{j=1}^i F_{i,j,n}(\rho_k s_k) (\prod_{l=1, l \neq j}^{i-1} F_{i,l,n}(u_k)) \quad (\text{C.15})$$

and $F_2(\rho_k s_k)$ is denoted by

$$\begin{aligned} F_2(\rho_k s_k) & : = r_{k+1} - r_k - F_1(\rho_k s_k) \\ & = - \sum_{i=2}^M \sum_{j=2}^i \binom{i}{j} \left(\prod_{l=1}^j F_{i,j_l,n}(\rho_k s_k) \right) \left(\prod_{t=1, j_l \neq j_t}^{i-j} F_{i,j_t,n}(u_k) \right) \end{aligned} \quad (\text{C.16})$$

where j_l and j_t form a partition of set $\{1, 2, \dots, i\}$. Clearly, $F_1(\rho_k s_k)$ is a linear operator of ρs_k , more precisely,

$$F_1(\rho s_k) = \rho_k F_1(s_k)$$

And $F_2(\rho s_k)$ is a nonlinear operator of ρs_k but is homogenous with order larger than 1.

In order to achieve the monotonic convergence of the residue r_k , we want

$$\|r_{k+1}\|_{B_{m+2s}^{1,2}(0,T;U)} \leq (1 - \beta) \|r_k\|_{B_{m+2s}^{1,2}(0,T;U)} \quad (\text{C.17})$$

for some fixed constant $\beta \in (0, 1)$. Since we want $\{u_k\}$ to be Cauchy, we attempt to control the step length, $\rho_k s_k$, by

$$\|\rho_k s_k\|_{B_{m+2s+1}^{1,2}(0,T;U)} \leq \rho_k \theta \|r_k\|_{B_{m+2s}^{1,2}(0,T;U)} \quad (\text{C.18})$$

where θ is independent of k and $0 < \rho_k \leq 1$.

However, there may not be an s_k such that

$$F_1(s_k) = -r_k \quad (\text{C.19})$$

The idea here is to seek a perturbation R_k of r_k such that

$$\|R_k - r_k\|_{B_{m+2s}^{1,2}(0,T;U)} \leq \varepsilon^* \|r_k\|_{B_{m+2s}^{1,2}(0,T;U)} \quad (\text{C.20})$$

for some small ε^* , and there exists an s_k such that

$$F_1(s_k) = -R_k. \quad (\text{C.21})$$

The method to construct such a R_k is proposed by theorem 10. This theorem proves the existence of R_k and s_k and the regularity of the solution $\{s_k\}$.

In conclusion, we perturb r_k such that equation (C.21) has a solution satisfying condition (C.17) and (C.18). The inequality (C.17) and (C.18) will guarantee the convergence of the Cauchy sequence $\{u_k\}$ in $B_{m+2s+1}^{1,2}(0, T; U)$ for any T .

C.3 Main Theorems

C.3.1 Preliminaries

We will show that the space $C^s(0, T; H^m(U))$ and $B_m^{s,q}(0, T; U)$ are the Banach space for any finite $s, m \geq 0$ and $q \geq 2$.

Theorem 5 *The space $C^s(0, T; H^m(U))$ is a Banach space if $U \subset \mathbb{R}^N$ satisfies the cone condition and $m > N/2$.*

Proof. (1) *Clearly, $C^s(0, T; H^m(U))$ is a norm space. We will show next that it is complete. Suppose that $\{u_n\}$ is Cauchy in $C^s(0, T; H^m(U))$. For every given t , $\{\frac{\partial^j}{\partial t^j} u_n\}$ is Cauchy in $H^m(U)$, where $0 \leq j \leq s$, because for any pair of u_{n_1} and u_{n_2} , we have*

$$\begin{aligned} \left\| \frac{\partial^j u_{n_1}}{\partial t^j} - \frac{\partial^j u_{n_2}}{\partial t^j} \right\|_{H^m(U)}(t) &\leq \max_{t \in [0, T]} \left\| \frac{\partial^j u_{n_1}}{\partial t^j} - \frac{\partial^j u_{n_2}}{\partial t^j} \right\|_{H^m(U)} \\ &\leq \|u_{n_1} - u_{n_2}\|_{C^s(0, T; H^m(U))} \end{aligned}$$

Following the fact that $H^m(U)$ is closed, for any given t , $\frac{\partial^j}{\partial t^j} u_n$ converges to function $v_j(t, x)$ in $H^m(U)$ and $v_j(t, x) \in C^0(0, T; H^m(U))$.

(2) *In this step, we will show that $v_j(t, x) = \frac{\partial v_{j-1}}{\partial t}$ in the space $C^0(0, T; C_B^r(U))$ for any $0 < j \leq s$. By the imbedding theorem, $H^m(U) \rightarrow C_B^r(U)$ where r is the largest integer less than $m - N/2$. i.e., there exists a constant k such that*

$$\max_{|\alpha| \leq r} \sup_{x \in U} \left| D^\alpha \left(\frac{\partial^j u_{n_1}}{\partial t^j} - \frac{\partial^j u_{n_2}}{\partial t^j} \right) \right| = \left\| \frac{\partial^j u_{n_1}}{\partial t^j} - \frac{\partial^j u_{n_2}}{\partial t^j} \right\|_{C_B^r(U)}(t) \quad (\text{C.22})$$

$$\begin{aligned} &\leq k \left\| \frac{\partial^j u_{n_1}}{\partial t^j} - \frac{\partial^j u_{n_2}}{\partial t^j} \right\|_{H^m(U)}(t) \quad (\text{C.23}) \\ &\leq k \|u_{n_1} - u_{n_2}\|_{C^s(0, T; H^m(U))} \end{aligned}$$

where k is independent of j, n , and t . Thus, $\{\frac{\partial^j u_n}{\partial t^j}\}$ uniformly converge to v_j in $C^0(0, T; C_B^r(U))$ and $u_n, v_j \in C^0(0, T; C_B^r(U))$ for any $0 \leq j \leq s$.

For every given x in U , by the uniform convergence and differentiation theorem (theorem 7.17, Rudin (1976)), we have $\frac{\partial}{\partial t} v_{j-1}(t, x) = v_j(t, x)$ for this given x . Since x is arbitrary, we conclude that $\frac{\partial}{\partial t} v_{j-1}(t, x) = v_j(t, x)$ in $C^0(0, T; H^m(U))$.

(3) Now, we are going to show that $v_j(t, x) = \frac{\partial v_{j-1}}{\partial t}$ in the space $C^0(0, T; H^m(U))$ for any $0 < j \leq s$. Let $\Phi \in C_c^\infty(U)$ be an arbitrary test function. Owing to the facts that $\lim_n \frac{\partial^{j-1} u_n}{\partial t^{j-1}} = v_{j-1}$, $\lim_n \frac{\partial^j u_n}{\partial t^j} = v_j$, and $u_n \in C^s(0, T; H^m(U))$, we have

$$\begin{aligned} \left(\frac{\partial v_{j-1}}{\partial t} - v_j(t, x), D^{r+1} \Phi \right) &= \lim_n \left(\frac{\partial}{\partial t} \frac{\partial^{j-1} u_n}{\partial t^{j-1}} - \frac{\partial^j u_n}{\partial t^j}, D^{r+1} \Phi \right) \\ &= \lim_n (-1)^{r+1} \left(D^{r+1} \frac{\partial}{\partial t} \frac{\partial^{j-1} u_n}{\partial t^{j-1}} - D^{r+1} \frac{\partial^j u_n}{\partial t^j}, \Phi \right) \\ &= 0. \end{aligned}$$

Since j and r are arbitrary, we complete the proof. ■

Indeed, the step 1 of the preceding theorem proves that the space $C^0(0, T; H^m(\mathbb{R}^N))$ is a Banach space. The Cauchy sequence in the space $C^0(0, T; H^m(\mathbb{R}^N))$ will converge to a limit in $C^0(0, T; H^m(\mathbb{R}^N))$. Therefore, the IVP of the system (C.1)-(C.2) can be established in $C^0(0, T; H^m(\mathbb{R}^N))$. It is not clear whether $C^s(0, T; H^m(\mathbb{R}^N))$ is a Banach space or not. However, once the existence of solution of the system (C.1)-(C.2) in $C^0(0, T; H^m(U))$ for any arbitrary U in \mathbb{R}^N is proved, one can easily conclude that the solution is also in the space $C^1(0, T; H^{m-2}(U))$ for some large enough m because it obeys the nonlinear heat equation (C.1). Again, the solution shall be in $C^s(0, T; H^{m-2s}(U))$ if the initial (or boundary) conditions are smooth enough. Owing to this facts, the solution of the system (C.1)-(C.2) should be in the space $B_m^{s,q}(0, T; U)$.

Theorem 6 *The space $B_m^{s,q}(0, T; U)$ is a Banach space if $U \subset \mathbb{R}^N$ satisfies the cone condition and $m > N/2$.*

Proof. Suppose sequence $\{u_n\}$ is Cauchy in $B_m^{s,q}(0, T; U)$. By theorem 5, sequence $\{u_n\}$ converges to v_{s-j} in $C^{s-j}(0, T; H^{m+qj}(U))$ for each $0 \leq j \leq s$. To prove the theorem, it suffices to show that $v_{s-j} \in C^{s-j-1}(0, T; H^{m+qj+q}(U))$ for each $0 \leq j \leq s$. Since $C^{s-j}(0, T; H^{m+qj}(U)) \subset C^{s-j-1}(0, T; H^{m+qj}(U))$, we obtain

$$v_{s-j} \in C^{s-j-1}(0, T; H^{m+qj}(U))$$

Thus, for any t and k , where $0 \leq k \leq s - j - 1$, $\frac{\partial^k u_n}{\partial t^k}$ converges to $\frac{\partial^k v_{s-j}}{\partial t^k}$ in $H^{m+qj}(U)$ uniformly. Since $\{u_n\}$ is Cauchy in $B_m^{s,q}(0, T; U)$ and $q \geq 1$, sequence $\left\{ \frac{\partial}{\partial x} \frac{\partial^k u_n}{\partial t^k} \right\}$ converge in

$H^{m+qj}(U)$ uniformly. For any $0 \leq k \leq s - j - 1$ and $0 \leq r \leq m + qj + q$,

$$\begin{aligned} \left(\frac{\partial^k v_{s-j}}{\partial t^k}, D^r \Phi \right) &= \lim_n \left(\frac{\partial^k u_n}{\partial t^k}, D^r \Phi \right) \\ &= \lim_n (-1)^r \left(D^r \frac{\partial^k u_n}{\partial t^k}, \Phi \right). \end{aligned}$$

where $\Phi \in C_c^\infty(U)$ is an arbitrary test function. We know that $\lim_n D^r \frac{\partial^k u_n}{\partial t^k}$ exists in H^{m+qj+q} for each t and k . Thus,

$$v_{s-j} \in C^{s-j-1}(0, T; H^{m+qj+q}(U))$$

This completes the proof. ■

As a prelude to existence considerations we derive now some lemmas.

Lemma 7 Let $u_1, u_2 \in C^s(0, T; W^{m,p}(U))$ and $u_3, u_4 \in B_{m,p}^{s,q}(0, T; U)$. Let U be a set in \mathbb{R}^N satisfying a cone property. For each $\infty > pm > N$, $q > 1$, and $\infty > s \geq 0$, there exists a constant $C_* = C_*(N, U, m, p, s)$ such that

$$\|u_1 u_2\|_{C^s(0, T; W^{m,p}(U))} \leq C_* \|u_1\|_{C^s(0, T; W^{m,p}(U))} \|u_2\|_{C^s(0, T; W^{m,p}(U))}, \quad (\text{C.24})$$

$$\|u_1 u_2\|_{W^{s,\infty}(0, T; W^{m,p}(U))} \leq C_* \|u_1\|_{W^{s,\infty}(0, T; W^{m,p}(U))} \|u_2\|_{W^{s,\infty}(0, T; W^{m,p}(U))}, \quad (\text{C.25})$$

and

$$\|u_3 u_4\|_{B_{m,p}^{s,q}(0, T; U)} \leq C_* \|u_3\|_{B_{m,p}^{s,q}(0, T; U)} \|u_4\|_{B_{m,p}^{s,q}(0, T; U)}. \quad (\text{C.26})$$

Proof. Suppose $u_1, u_2 \in C^s(0, T; W^{m,p}(U))$. Let γ be such that $s \geq \gamma \geq 0$, then $\frac{\partial^\gamma u_1}{\partial t^\gamma}, \frac{\partial^{s-\gamma} u_2}{\partial t^{s-\gamma}} \in W^{m,p}(U)$. Note that U holds a cone property and $\infty > pm > N$. Due to the theorem 4.39 of Adams (2003), there exists a constant c_1 such that for any $pm > N$,

$$\left\| \frac{\partial^\gamma u_1}{\partial t^\gamma} \frac{\partial^{s-\gamma} u_2}{\partial t^{s-\gamma}} \right\|_{W^{m,p}(U)} \leq c_1(U, N, m, p) \left\| \frac{\partial^\gamma u_1}{\partial t^\gamma} \right\|_{W^{m,p}(U)} \left\| \frac{\partial^{s-\gamma} u_2}{\partial t^{s-\gamma}} \right\|_{W^{m,p}(U)}$$

where c_1 only depends U, N, m and p .

The boundedness of $u_1 u_2$ in $C^s(0, T; W^{m,p}(U))$ follows:

$$\begin{aligned} \|u_1 u_2\|_{C^s(0, T; W^{m,p}(U))} &= \max_{0 \leq t \leq T} \left\| \frac{\partial^s}{\partial t^s} u_1 u_2 \right\|_{W^{m,p}(U)} \\ &\leq \max_{0 \leq t \leq T} \sum_{\gamma=0}^s \binom{s}{\gamma} c_1 \left\| \frac{\partial^\gamma u_1}{\partial t^\gamma} \right\|_{W^{m,p}(U)} \left\| \frac{\partial^{s-\gamma} u_2}{\partial t^{s-\gamma}} \right\|_{W^{m,p}(U)}. \end{aligned}$$

Note that for each given $t \in [0, T]$, $\left\| \frac{\partial^\gamma u_1}{\partial t^\gamma} \right\|_{W^{m,p}(U)}$ and $\left\| \frac{\partial^{s-\gamma} u_2}{\partial t^{s-\gamma}} \right\|_{W^{m,p}(U)}$ are in $L^\infty([0, T])$. Therefore, $\|u_1 u_2\|_{C^s(0,T;W^{m,p}(U))}$ is bounded. Furthermore, there exists a constant C'_* , which is independent of T , such that

$$\|u_1 u_2\|_{C^s(0,T;W^{m,p}(U))} \leq C'_* \|u_1\|_{C^s(0,T;W^{m,p}(U))} \|u_2\|_{C^s(0,T;W^{m,p}(U))}.$$

By repeating above deduction, we conclude that for each $0 \leq j \leq s$, there exists a constant c_j such that

$$\|u_3 u_4\|_{C^{s-j}(0,T;W^{m+qj,p}(U))} \leq c_j \|u_3\|_{C^{s-j}(0,T;W^{m+qj,p}(U))} \|u_4\|_{C^{s-j}(0,T;W^{m+qj,p}(U))}.$$

Let $C_* = \max(c_j, c, C'_*)$, we obtain:

$$\|u_3 u_4\|_{B_{m,p}^{s,q}(0,T;U)} \leq C_* \|u_3\|_{B_{m,p}^{s,q}(0,T;U)} \|u_4\|_{B_{m,p}^{s,q}(0,T;U)}$$

and

$$\|u_1 u_2\|_{C^s(0,T;W^{m,p}(U))} \leq C_* \|u_1\|_{C^s(0,T;W^{m,p}(U))} \|u_2\|_{C^s(0,T;W^{m,p}(U))}.$$

In the same way, we can prove the inequality (C.25). ■

Preceding lemma enables us to bound the norm of a polynomial by the corresponding polynomial of norm. With these inequalities, we can easily prove that the nonlinear operator F_2 is bounded by r_k .

Remark 1 Suppose φ_i to be the normalized eigenfunctions of the Dirichlet problem for the operator Lu denoted by (C.4). The solution of generated Dirichlet problem of the heat equation

$$u_t + Lu = f,$$

$$u(0, U) = g(U) \quad , \quad u(t, \partial U) = h(t; \partial U),$$

is given by

$$u = \sum_{i=1}^{\infty} e^{-\lambda_i t} \varphi_i \left(\int_U g_i \varphi_i + \int_0^t e^{\lambda_i \tau} \int_U \varphi_i(\xi) f(\tau; \xi) d\xi d\tau - \int_0^t \int_{\partial U} h \frac{\partial \varphi_i(\xi)}{\partial \xi_n} d\xi d\tau \right).$$

Denote

$$\psi(t; x|\tau; \xi) = \sum_{i=1}^{\infty} e^{-\lambda_i(t-\tau)} \varphi_i(x) \varphi_i(\xi), \quad (\text{C.27})$$

It yields

$$u = \int_0^t \int_U \psi(t; x | \tau; \xi) f(\tau; \xi) d\xi d\tau + \int_U \psi(t; x | 0; \xi) g(\xi) d\xi - \int_0^t \int_{\partial U} h \frac{\partial \psi}{\partial \xi_n}.$$

Here, $\psi(t; x | \tau; \xi)$ is the Dirichlet heat kernel. The regularity of $\psi(t; x | \tau; \xi)$ depends on the smoothness of the domain U and the coefficients of operator L .

Lemma 8 Under condition (A1) and (A2), the operator Lu has a set of eigenfunctions $\{\varphi_{\lambda_i}\}$ obeying (1) $\{\varphi_{\lambda_i}\}$ form an orthonormal basis of a Hilbert space $H(U)$, (2) $\varphi_{\lambda_i} \in H_0^\beta(U)$ and the eigenvalues λ_i hold

$$0 < \lambda_1 < \dots < \lambda_n < \dots, \quad (\text{C.28})$$

and (3) $\forall 0 \leq \beta \leq m + 2(1 + s)$ and $\varphi_i, \varphi_j \in \{\varphi_{\lambda_i}\}$,

$$\langle D^\beta \varphi_i, D^\beta \varphi_j \rangle = 0, \quad \text{if } i \neq j \quad (\text{C.29})$$

$$\langle D^\beta \varphi_i, D^\beta \varphi_i \rangle \leq \frac{\lambda_i - \gamma_3}{\gamma_1} \langle D^{\beta-1} \varphi_i, D^{\beta-1} \varphi_i \rangle \quad (\text{C.30})$$

where γ_1 is given by condition (A2).

Proof. It is known that the eigenfunctions $\varphi_{\lambda_i}^1 \in H^{m+2(s+1)}(U) \cap H_0^1(U)$ of operator Lu span a Hilbert space $H(U)$, and the corresponding eigenvalues hold (C.28) (Theorem 8.37 and 9.19, Gilbarg and Trudinger (2001)). Denote $\varphi_{\lambda_i} = \lim_{\varepsilon \rightarrow 0} \eta_\varepsilon \otimes \varphi_{\lambda_i}^2$ where η_ε is a standard mollifier and

$$\begin{aligned} \varphi_{\lambda_i}^2 &= \varphi_{\lambda_i}^1, & \text{when } x \in U, \\ \varphi_{\lambda_i}^2 &= 0, & \text{when } x \in \mathbb{R}^N \setminus U. \end{aligned}$$

Since U is a bounded open set in \mathbb{R}^N , $\varphi_{\lambda_i} \in H_0^{m+2(s+1)}(\bar{U})$ and $\varphi_{\lambda_i} = \varphi_{\lambda_i}^1$ in $H^{m+2(s+1)}(U) \cap H_0^1(U)$. Then, $\{\varphi_{\lambda_i}\}$ span $H(U)$. Meanwhile, eigenvalues of φ_{λ_i} is equivalent to that of $\varphi_{\lambda_i}^1$. Thus, (C.28) is satisfied. The orthogonality of $\{\varphi_{\lambda_i}\}$ in $H(U)$ immediately follows the orthogonality of $\{\varphi_{\lambda_i}^1\}$ in $H(U)$. The reminded problem is to show the orthogonality of $\{D^\beta \varphi_{\lambda_i}\}$ for any $0 < \beta \leq m + 2(1 + s)$. Suppose that φ_i, φ_j are arbitrary in $\{\varphi_{\lambda_i}\}$ and $i \neq j$. The Green's first identity Gilbarg and Trudinger (2001) and the facts $\varphi_i, \varphi_j \in H_0^{m+2(s+1)}(\bar{U})$ immediately

follow

$$\begin{aligned}\lambda_j \langle D^{\beta-1} \varphi_i, D^{\beta-1} \varphi_j \rangle &= \langle D^{\beta-1} \varphi_i, LD^{\beta-1} \varphi_j \rangle \\ &= \langle \alpha^{ij} D^\beta \varphi_i, D^\beta \varphi_j \rangle + \langle b D^{\beta-1} \varphi_i, D^{\beta-1} \varphi_j \rangle\end{aligned}$$

where operator L is defined by the condition (A2). Together with the strong elliptic condition (C.6)-(C.8), we obtain:

$$\lambda_j \langle D^{\beta-1} \varphi_i, D^{\beta-1} \varphi_j \rangle \geq \gamma_1 \langle D^\beta \varphi_i, D^\beta \varphi_j \rangle + \gamma_3 \langle D^{\beta-1} \varphi_i, D^{\beta-1} \varphi_j \rangle.$$

It is clear that $\lambda_j > \gamma_3$ because

$$\lambda_j \geq \min_{\|u\|=1, u \in H_0^1(U)} \langle u, Lu \rangle \geq \min_{\|u\|=1, u \in H_0^1(U)} \gamma_1 \|Du\| + \gamma_3. \quad (\text{C.31})$$

Thus, $\langle D^\beta \varphi_i, D^\beta \varphi_j \rangle \leq \frac{\lambda_j - \gamma_3}{\gamma_1} \langle D^{\beta-1} \varphi_i, D^{\beta-1} \varphi_j \rangle = \left(\frac{\lambda_j - \gamma_3}{\gamma_1}\right)^\beta \langle \varphi_i, \varphi_j \rangle$. This proves the inequality (C.30). ■

The following theorem deals with the upper bound of the heat kernel.

Theorem 9 Denote $F(g) := \int_0^t \int_U \psi(0; x | \tau; y) g(t - \tau; y) d\tau d\xi$ and let X_1 to be the space $W^{1,2}(0, T; H^{r-1}(U)) \cap L^2(0, T; H^{r+1}(U)) \cap L^\infty(0; H^r(U))$. Under condition (A1) and (A2), for any $\gamma \geq 1$, if $g \in X_1$, then

(1) there exist follow inequalities;

$$\|F(g)\|_{C^1(0, T; H^r(U))} \leq C_1 \|g_t\|_{W^{1,2}(0, t; H^{\gamma-1}(U))} + C_2 \|g_t(0; x)\|_{H^\gamma(U)} \quad (\text{C.32})$$

and

$$\|F(g)\|_{C^0(0, T; H^{r+2}(U))} \leq C_1 \|g_t\|_{L^2(0, t; H^{\gamma+1}(U))} \quad (\text{C.33})$$

where $C_1 = N^{\gamma+1} \max\left(\frac{1}{\sqrt{2\gamma_1}}, \min\left(\sqrt{T}, \frac{1}{\sqrt{2\gamma_3}}\right)\right)$ and $C_2 = N^{\gamma+1}$.

(2) $F(g)$ is a compact linear operator from X_1 into $B_{\gamma, 2}^{1,2}(0, T; U)$.

Proof. (1) Firstly, we estimate the upper bound of $\|F(g)\|_{C^1(0, T; H^r(U))}$. It suffices to show that, for any $0 \leq \beta \leq \gamma$, $\|D^\beta \frac{\partial}{\partial t} F(g_t)\|_{C^0(0, T; L^2(U))}$ is bounded by $\|g_t\|_{W^{1,2}(0, t; H^{\gamma-1}(U))}$ and

$\|g_l\|_{L^2(0,t;H^{\gamma+1}(U))}$. According to the Leibnitz integral rule, we compute

$$\begin{aligned} \left\| D^\beta \frac{\partial}{\partial t} F(g_l) \right\|_{L^2(U)} &= \left\{ \int_U dx \left| \frac{\partial}{\partial t} \int_0^t d\tau \int_U D^\beta \psi(0; x|\tau; y) g_l(t - \tau; y) dy \right|^2 \right\}^{1/2} \\ &\leq \left\{ \int_U dx \left| \int_0^t d\tau \int_U D^\beta \psi(0; x|\tau; y) \frac{\partial}{\partial t} g_l(t - \tau; y) dy \right|^2 \right\}^{1/2} + \\ &\quad \left\{ \int_U dx \left| \int_U D^\beta \psi(0; x|t; y) g_l(0; y) dy \right|^2 \right\}^{1/2}. \end{aligned}$$

It follows from the identity (C.27),

$$\begin{aligned} \left\| D^\beta \frac{\partial}{\partial t} F(g_l) \right\|_{L^2(U)} &\leq \left\{ \int_U dx \left| \int_0^t d\tau \sum_{i=1}^{\infty} e^{-\lambda_i \tau} D^\beta \varphi_i(x) \left\langle \varphi_i(\xi), \frac{\partial g_l}{\partial t} \right\rangle \right|^2 \right\}^{1/2} \\ &\quad + \left\{ \int_U \left[\sum_{i=1}^{\infty} D^\beta \varphi_i(x) e^{-\lambda_i t} \langle \varphi_i(\xi), g_l(0; y) \rangle \right]^2 \right\}^{1/2} \\ &=: I + II. \end{aligned} \tag{C.34}$$

where

$$\begin{aligned} I &= \left\{ \int_U dx \left| \int_0^t d\tau \sum_{i=1}^{\infty} e^{-\lambda_i \tau} D^\beta \varphi_i(x) \left\langle \varphi_i(\xi), \frac{\partial g_l}{\partial t} \right\rangle \right|^2 \right\}^{1/2} \\ &= \left\{ \int_U dx \left| \sum_{i=1}^{\infty} D^\beta \varphi_i(x) \left[\int_0^t e^{-\lambda_i \tau} \left\langle \varphi_i(\xi), \frac{\partial g_l}{\partial t} \right\rangle \right] \right|^2 \right\}^{1/2} \end{aligned}$$

Here, $[\int_0^t e^{-\lambda_i \tau} \langle \varphi_i(\xi), \frac{\partial g_l}{\partial t} \rangle]$ is a function of time, and can be treated as the coefficient of the orthogonal basis $D^\beta \varphi_i(x)$ of $H(U)$ (lemma 8). Without loss of generality, we discuss the case $\beta \geq 1$ firstly. Since $D^\beta \varphi_i(x)$ are orthogonal, thus,

$$I = \left\{ \sum_{i=1}^{\infty} \left\| D^\beta \varphi_i(x) \right\|_{L^2(U)}^2 \left[\int_0^t e^{-\lambda_i \tau} \left\langle \varphi_i(\xi), \frac{\partial g_l}{\partial t} \right\rangle \right]^2 \right\}^{1/2}.$$

The inequality (C.30) follows that

$$I \leq \left\{ \sum_{i=1}^{\infty} \frac{(\lambda_i - \gamma_3)}{2\gamma_1 \lambda_i} \left\| D^{\beta-1} \varphi_i(x) \right\|_{L^2(U)}^2 \left[\int_0^t \sqrt{2\lambda_i} e^{-\lambda_i \tau} \left\langle \varphi_i(\xi), \frac{\partial g_l}{\partial t} \right\rangle \right]^2 \right\}^{1/2}.$$

Clearly, $\frac{(\lambda_i - \gamma_3)}{2\gamma_1 \lambda_i} \leq \frac{1}{2\gamma_1}$. By the Hölder's inequality,

$$\begin{aligned} I &\leq \frac{1}{\sqrt{2\gamma_1}} \left\{ \sum_{i=1}^{\infty} \left\| D^{\beta-1} \varphi_i(x) \right\|_{L^2(U)}^2 \int_0^t 2\lambda_i e^{-2\lambda_i \tau} \int_0^t \left\langle \varphi_i(\xi), \frac{\partial g_l}{\partial t} \right\rangle^2 \right\}^{1/2} \\ &\leq \frac{1}{\sqrt{2\gamma_1}} \left\{ \int_0^t \sum_{i=1}^{\infty} \left\| D^{\beta-1} \varphi_i(x) \right\|_{L^2(U)}^2 \left\langle \varphi_i(\xi), \frac{\partial g_l}{\partial t} \right\rangle^2 \right\}^{1/2} \\ &= \frac{1}{\sqrt{2\gamma_1}} \left\| D^{\beta-1} \frac{\partial g_l}{\partial t} \right\|_{L^2(0,t;L^2(U))} \end{aligned}$$

because

$$\frac{\partial g_l}{\partial t} = \sum_{i=1}^{\infty} \left\langle \varphi_i(\xi), \frac{\partial g_l}{\partial t} \right\rangle \varphi_i(x)$$

Thus

$$D^{\beta-1} \frac{\partial g_l}{\partial t} = \sum_{i=1}^{\infty} \left\langle \varphi_i(\xi), \frac{\partial g_l}{\partial t} \right\rangle D^{\beta-1} \varphi_i(x)$$

Considering that $D^{\beta-1} \varphi_i(x)$ are orthogonal,

$$\left\| D^{\beta-1} \frac{\partial g_l}{\partial t} \right\|_{L^2(0,t;L^2(U))} = \left\{ \int_0^t \sum_{i=1}^{\infty} \left\| D^{\beta-1} \varphi_i(x) \right\|_{L^2(U)}^2 \left\langle \varphi_i(\xi), \frac{\partial g_l}{\partial t} \right\rangle^2 \right\}^{1/2}$$

In the same way for I , we have

$$\begin{aligned} II &= \left\{ \sum_{i=1}^{\infty} \left\| D^{\beta} \varphi_i(x) \right\|_{L^2(U)}^2 e^{-2\lambda_i t} \left\langle \varphi_i(\xi), g_l(0; y) \right\rangle^2 \right\}^{1/2} \\ &\leq \left\| D^{\beta} g_l(0; y) \right\|_{L^2(U)}. \end{aligned} \quad (\text{C.35})$$

because $0 < e^{-2\lambda_i t} \leq 1$ and $D^{\beta} \varphi_i(x)$ are orthogonal. Thus, for any $t \in [0, T]$,

$$\left\| \frac{\partial}{\partial t} \frac{\partial^{\beta}}{\partial x^{\beta}} F(g_l) \right\|_{L^2(U)} \leq \frac{1}{\sqrt{2\gamma_1}} \left\| D^{\beta-1} \frac{\partial g_l}{\partial t} \right\|_{L^2(0,t;L^2(U))} + \left\| D^{\beta} g_l(0; y) \right\|_{L^2(U)} \quad (\text{C.36})$$

For the case $|\beta| = 0$, by the analogous method with above, we deduce

$$\begin{aligned} \left\| \frac{\partial}{\partial t} F(g_l) \right\|_{L^2(U)} &\leq \left\{ \sum_{i=1}^{\infty} \left\| \varphi_i \right\|_{L^2(U)}^2 \left[\int_0^t e^{-\lambda_i \tau} \left\langle \varphi_i(\xi), \frac{\partial g_l}{\partial t} \right\rangle^2 \right]^{1/2} + \left\| g_l(0; y) \right\|_{L^2(U)} \right. \\ &\leq \left\{ \sum_{i=1}^{\infty} \left\| \varphi_i \right\|_{L^2(U)}^2 \int_0^t \left\langle \varphi_i, \frac{\partial g_l}{\partial t} \right\rangle^2 \int_0^t e^{-2\lambda_i \tau} \right\}^{1/2} + \left\| g_l(0; y) \right\|_{L^2(U)}. \end{aligned}$$

In the lemma 8, we prove that $\lambda_i > \gamma_3$. Hence, $\sqrt{\int_0^T e^{-2\lambda_i \tau}} \leq \min(\sqrt{T}, \frac{1}{\sqrt{2\gamma_3}})$. Thereby,

$$\left\| \frac{\partial}{\partial t} F(g_l) \right\|_{L^2(U)} \leq \min(\sqrt{T}, \frac{1}{\sqrt{2\gamma_3}}) \left\| \frac{\partial g_l}{\partial t} \right\|_{L^{\infty}(0,t;H(U))} + \left\| g_l(0; y) \right\|_{L^2(U)}.$$

In summary,

$$\begin{aligned} \|F(g)\|_{C^1(0,T;H^r(U))} &\leq \frac{1}{\sqrt{2\gamma_1}} \sum_{1 \leq |\beta| \leq \gamma} \left\| D^{\beta-1} \frac{\partial g_l}{\partial t} \right\|_{L^2(0,t;H(U))} + \sum_{1 \leq |\beta| \leq \gamma} \left\| D^{\beta} g_l(0; x) \right\|_{L^2(U)} \\ &\quad + \min(\sqrt{T}, \frac{1}{\sqrt{2\gamma_3}}) \left\| \frac{\partial g_l}{\partial t} \right\|_{L^2(0,t;H(U))} + \left\| g_l(0; y) \right\|_{L^2(U)} \\ &\leq \|g_l\|_{W^{1,2}(0,t;H^{\gamma-1}(U))} \sum_{|\beta| \leq \gamma} \max\left(\frac{1}{\sqrt{2\gamma_1}}, \min(\sqrt{T}, \frac{1}{\sqrt{2\gamma_3}})\right) + \\ &\quad \left\| g_l(0; x) \right\|_{H^{\gamma}(U)} \sum_{|\beta| \leq \gamma} 1 \\ &\leq C_1 \|g_l\|_{W^{1,2}(0,t;H^{\gamma-1}(U))} + C_2 \|g_l(0; x)\|_{H^{\gamma}(U)} \end{aligned}$$

where $C_1 = N^{\gamma+1} \max(\frac{1}{\sqrt{2\gamma_1}}, \min(\sqrt{T}, \frac{1}{\sqrt{2\gamma_3}}))$ and $C_2 = N^{\gamma+1}$. This proves inequality (C.32).

(2), We will show the inequality (C.33) in this part. For the case $|\beta| > 0$. In the same way for above, we have

$$\begin{aligned} \|D^\beta F(g_l)\|_{L^2(U)} &= \left\{ \int_U dx \left| \int_0^t d\tau \sum_{i=1}^{\infty} e^{-\lambda_i \tau} D^\beta \varphi_i(x) \langle \varphi_i(\xi), g_l \rangle \right|^2 \right\}^{1/2} \\ &\leq \left\{ \sum_{i=1}^{\infty} \frac{1}{2\lambda_i} \|D^\beta \varphi_i(x)\|_{L^2(U)}^2 \int_0^t 2\lambda_i e^{-2\lambda_i \tau} \int_0^t \langle \varphi_i(\xi), g_l \rangle^2 \right\}^{1/2} \\ &\leq \frac{1}{\sqrt{2\gamma_1}} \left\{ \sum_{i=1}^{\infty} \|D^{\beta-1} \varphi_i(x)\|_{L^2(U)}^2 \int_0^t 2\lambda_i e^{-2\lambda_i \tau} \int_0^t \langle \varphi_i(\xi), g_l \rangle^2 \right\}^{1/2} \\ &\leq \frac{1}{\sqrt{2\gamma_1}} \|D^{\beta-1} g_l\|_{L^2(0,t;L^2(U))}. \end{aligned}$$

For the case $\beta = 0$,

$$\begin{aligned} \|F(g_l)\|_{L^2(U)} &= \left\{ \int_U dx \left| \int_0^t d\tau \sum_{i=1}^{\infty} e^{-\lambda_i \tau} \varphi_i(x) \langle \varphi_i(\xi), g_l \rangle \right|^2 \right\}^{1/2} \\ &\leq \min(\sqrt{T}, \frac{1}{\sqrt{2\gamma_3}}) \left\{ \sum_{i=1}^{\infty} \|\varphi_i(x)\|_{L^2(U)}^2 \int_0^t \langle \varphi_i(\xi), g_l \rangle^2 \right\}^{1/2} \\ &= \min(\sqrt{T}, \frac{1}{\sqrt{2\gamma_3}}) \|g_l\|_{L^2(0,t;L^2(U))}. \end{aligned}$$

Thus,

$$\|F(g)\|_{C^0(0,T;H^{r+2}(U))} \leq C_1 \|g_l\|_{L^2(0,t;H^{\gamma+1}(U))}.$$

(3), Now, we shall prove that F is a compact linear operator.

Let g_t be a bounded sequence in $W^{1,2}(0,T;H^{\gamma-1}(U)) \cap L^2(0,T;H^{\gamma+1}(U))$. Let $0 < \beta \leq \gamma - 1$ when $\alpha = 1$ and $0 < \beta \leq \gamma + 1$ when $\alpha = 0$. By the Banach-Alaoglu theorem and Cantor diagonalization argument, g_t have a weakly convergence subsequence g_l such that (a) $D^{\beta-1} \frac{\partial^\alpha}{\partial t^\alpha} g_l(t, x)$ is a weakly convergence subsequence in $L^2(0, t; L^2(U))$ and (b) $D^\beta g_l(0; x)$ weakly converge in $L^2(U)$. i.e. for any $\varepsilon > 0$, there exists a l_ε , when $l_1, l_2 > l_\varepsilon$.

$$\left\| D^{\beta-1} \frac{\partial^\alpha}{\partial t^\alpha} (g_{l_1} - g_{l_2}) \right\|_{L^2(0,t;L^2(U))} < c_4 \varepsilon \quad (\text{C.37})$$

and

$$\left\| D^\beta (g_{l_1} - g_{l_2})(0; x) \right\|_{L^2(U)} < c_4 \varepsilon \quad (\text{C.38})$$

Here, c_4 is a constant. Now, denote Δg_l by $g_{l_1} - g_{l_2}$. The inequality (C.33) follows

$$\|F(\Delta g)\|_{C^0(0,T;H^{r+2}(U))} \leq C_3 \|\Delta g_l\|_{L^2(0,t;H^{\gamma+1}(U))}$$

The inequality (C.32) implies that

$$\|F(\Delta g_l)\|_{C^1(0,t;H^r(U))} \leq C_1 \|\Delta g_l\|_{W^{1,2}(0,T;H^{\gamma-1}(U))} + C_2 \|\Delta g_l(0;x)\|_{H^\gamma(U)}.$$

Above inequalities together with (C.37) and (C.38) indicate that F is a compact linear operator.

■

C.3.2 The Existence of Global and Local Solutions in $B_{m+1}^{s+1,2}(0,T;U)$

Equation (C.19) is the linearization of the nonlinear parabolic partial difference equation (??), which reads

$$\frac{\partial s_k}{\partial t} + Ls_k = -r_k + \sum_{i=2}^M \sum_{n=1}^{N_i} \sum_{j=1}^i F_{i,j,n}(s_k) \left(\prod_{l=1, l \neq j}^{i-1} F_{i,l,n}(u_k) \right). \quad (\text{C.39})$$

The solution of above equation with respect to the boundary and initial condition (C.45) and (C.46) in $[0, T] \times U$ can be represented by

$$s_k(t;x) = \int_0^t \int_U \psi(t;x|\tau;y) \left[-r_k + \sum_{i=2}^M \sum_{n=1}^{N_i} \sum_{j=1}^i F_{i,j,n}(s_k) \left(\prod_{l=1, l \neq j}^{i-1} F_{i,l,n}(u_k) \right) \right] dy d\tau \quad (\text{C.40})$$

where $\psi(t;x|\tau;y)$ is the heat kernel.

Above representation can be simplified to

$$s_k = A(s_j^k) + f \quad (\text{C.41})$$

where

$$A(s_j^k) := \int_0^t \int_U \psi(0;x|\tau;y) \sum_{i=2}^M \sum_{n=1}^{N_i} \sum_{j=1}^i F_{i,j,n}(s_k) \left(\prod_{l=1, l \neq j}^{i-1} F_{i,l,n}(u_k) \right) (t-\tau;y) dy d\tau \quad (\text{C.42})$$

and function f is defined by

$$f := - \int_0^t \int_U \psi(0;x|\tau;y) r_k^*(t-\tau;y) dy d\tau. \quad (\text{C.43})$$

As we described above, equation (C.19) may not have a regular solution $\{s_k\}$. By the following theorem, we will show that, regardless of r_k , there is a perturbation R_k of r_k such that

$$F_1 s_k = -R_k$$

where

$$\|R_k - r_k\|_{B_{m+2s}^{1,2}(0,T;U)} \leq \varepsilon^* \|r_k\|_{B_{m+2s}^{1,2}(0,T;U)}$$

for some small ε^* . The theorem concerning to the solvability of linearized equation follows.

Theorem 10 *Under condition (A1), (A2), and (A3), if $r_k \in B_{m,2}^{s+1,2}(0,T;U)$, $u_k \in B_{m+1}^{s+1,2}(0,T;U)$, and $\|u_k\|_{B_{m+2s+1}^{1,2}(0,T;U)} \leq \lambda$, then there exists a function $R_k \in B_{m,2}^{s+1,2}(0,T;U)$ satisfying*

$$\|R_k - r_k\|_{B_{m+2s}^{1,2}(0,T;U)} \leq \varepsilon^* \|r_k\|_{B_{m+2s}^{1,2}(0,T;U)}$$

such that the system

$$F_1(s_k) = -R_k \tag{C.44}$$

$$s_k(0, U) = 0 \tag{C.45}$$

$$s_k(t, \partial U) = 0 \tag{C.46}$$

has a solution $s_k \in B_{m+1}^{s+1,2}(0,T;U)$. And such a solution obeys

$$\|s_k\|_{B_{m+2s+1}^{1,2}(0,T;U)} \leq \theta \|r_k\|_{B_{m+2s}^{1,2}(0,T;U)} \tag{C.47}$$

where θ is independent of r_k and s_k .

Proof. Step 1: the existence and regularity of solution.

(1), Define X_1 by $W^{1,2}(0,T;H^{m+2s}(U)) \cap L^2(0,T;H^{m+2s+2}(U)) \cap C^0(0;H^{m+2s+1}(U))$ and X by $X := B_{m+2s+1}^{1,2}(0,T;U)$. We assert that $A(s_j^k)$, which is given by the identity (C.42), is a compact linear operator from X into itself. It suffices to show that

$$\sum_{i=2}^M \sum_{n=1}^{N_i} \sum_{j=1}^i F_{i,j,n}(s_k) \left(\prod_{l=1, l \neq j}^{i-1} F_{i,l,n}(u_k) \right) \in X_1$$

because the theorem 9 indicates that $A(s_j^k)$ is a compact linear operator from X_1 into X .

Clearly,

$$\begin{aligned} & \left\| \sum_{i=2}^M \sum_{n=1}^{N_i} \sum_{j=1}^i F_{i,j,n}(s_k) \left(\prod_{l=1, l \neq j}^{i-1} F_{i,l,n}(u_k) \right) \right\|_{W^{1,2}(0,T;H^{m+2s}(U))} \\ & \leq \sqrt{T} \left\| \sum_{i=2}^M \sum_{n=1}^{N_i} \sum_{j=1}^i F_{i,j,n}(s_k) \left(\prod_{l=1, l \neq j}^{i-1} F_{i,l,n}(u_k) \right) \right\|_{W^{1,\infty}(0,T;H^{m+2s}(U))}. \end{aligned}$$

The condition (A3) and the lemma 7 follow

$$\begin{aligned} & \left\| \sum_{i=2}^M \sum_{n=1}^{N_i} \sum_{j=1}^i F_{i,j,n}(s_k) \left(\prod_{l=1, l \neq j}^{i-1} F_{i,l,n}(u_k) \right) \right\|_{W^{1,\infty}(0,T;H^{m+2s}(U))} \\ & \leq \sum_{i=2}^M \sum_{n=1}^{N_i} C_*^i \sum_{j=1}^i a_{i,j,n} \|s_k\|_{W^{1,\infty}(0,T;H^{m+2s+p_{i,j,n}}(U))} \left(\prod_{l=1, l \neq j}^{i-1} a_{i,l,n} \|u_k\|_{W^{1,\infty}(0,T;H^{m+2s+p_{i,l,n}}(U))} \right) \\ & \leq \sum_{i=2}^M \sum_{n=1}^{N_i} C_*^i \sum_{j=1}^i a_{i,j,n} \|s_k\|_{W^{1,\infty}(0,T;H^{m+2s+1}(U))} \left(\prod_{l=1, l \neq j}^{i-1} a_{i,l,n} \|u_k\|_{W^{1,\infty}(0,T;H^{m+2s+1}(U))} \right) \end{aligned}$$

because $p_{i,j,n} \leq 1$. Likewise,

$$\begin{aligned} & \left\| \sum_{i=2}^M \sum_{n=1}^{N_i} \sum_{j=1}^i F_{i,j,n}(s_k) \left(\prod_{l=1, l \neq j}^{i-1} F_{i,l,n}(u_k) \right) \right\|_{L^2(0,T;H^{m+2s+2}(U))} \\ & \leq \sqrt{T} \sum_{i=2}^M \sum_{n=1}^{N_i} C_*^i \sum_{j=1}^i a_{i,j,n} \|s_k\|_{L^\infty(0,T;H^{m+2s+3}(U))} \left(\prod_{l=1, l \neq j}^{i-1} a_{i,l,n} \|u_k\|_{L^\infty(0,T;H^{m+2s+3}(U))} \right) \\ & = \sqrt{T} \sum_{i=2}^M \sum_{n=1}^{N_i} C_*^i \sum_{j=1}^i a_{i,j,n} \|s_k\|_{C^0(0,T;H^{m+2s+3}(U))} \left(\prod_{l=1, l \neq j}^{i-1} a_{i,l,n} \|u_k\|_{C^0(0,T;H^{m+2s+3}(U))} \right). \end{aligned}$$

The initial condition s_k is zero, i.e. $s_k(0, x) = 0$, it turns out that

$$\begin{aligned} & \left\| \sum_{i=2}^M \sum_{n=1}^{N_i} \sum_{j=1}^i F_{i,j,n}(s_k) \left(\prod_{l=1, l \neq j}^{i-1} F_{i,l,n}(u_k) \right) \right\|_{L^\infty(0;H^{m+2s+2}(U))} \\ & \leq \sum_{i=2}^M \sum_{n=1}^{N_i} C_*^i \sum_{j=1}^i a_{i,j,n} \|s_k\|_{L^\infty(0;H^{m+2s+3}(U))} \left(\prod_{l=1, l \neq j}^{i-1} a_{i,l,n} \|u_k\|_{L^\infty(0;H^{m+2s+3}(U))} \right) \\ & = 0. \end{aligned}$$

Above deductions indicate that $A(s_j^k)$ is a compact linear operator from X into itself.

The inequality (C.32) and (C.33) immediately turn out that

$$\begin{aligned}
& \|f\|_{B_{m+2s+1}^{1,2}(0,T;U)} \\
&= \|f\|_{C^1(0,T;H^{m+2s+1}(U))} + \|f\|_{C^0(0,T;H^{m+2s+3}(U))} \\
&\leq C_1(\|r_k\|_{W^{1,2}(0,t;H^{m+2s}(U))} + \|r_k\|_{L^2(0,t;H^{m+2s+2}(U))}) + C_2 \|r_k(0; x)\|_{H^{m+2s+1}(U)} \\
&\leq C_1(\|r_k\|_{W^{1,2}(0,t;H^{m+2s}(U))} + \|r_k\|_{L^2(0,t;H^{m+2s+2}(U))}) + C_2 \|r_k(0; x)\|_{H^{m+2s+1}(U)} \\
&\leq 2\sqrt{T}C_1(\|r_k\|_{C^{1,\infty}(0,t;H^{m+2s}(U))} + \|r_k\|_{C^0(0,t;H^{m+2s+2}(U))}) + C_2 \|r_k(0; x)\|_{H^{m+2s+1}(U)}.
\end{aligned}$$

Since $r_k \in B_{m+2s}^{1,2}(0, T; U)$, we conclude

$$\|f\|_{B_{m+2s+1}^{1,2}(0,T;U)} \leq C_\gamma \|r_k\|_{B_{m+2s}^{1,2}(0,T;U)}. \quad (\text{C.48})$$

where C_γ is given by the definition (6). This proves that $f \in X$.

(2), In this part, we will prove that there exist η and $s_k \in B_{m+2s+1}^{1,2}(0, T; U)$ such that

$$|\eta - 1| \leq \varepsilon_1 < \frac{1}{2} \quad (\text{C.49})$$

$$\eta s_i^k = A(s_j^k) + f \quad (\text{C.50})$$

and

$$\|(A - \eta)s_k\|_{B_{m+2s+1}^{1,2}(0,T;U)} \geq \varepsilon_1 \|s_k\|_{B_{m+2s+1}^{1,2}(0,T;U)} \quad (\text{C.51})$$

Since $B_{m+2s+1}^{1,2}(0, T; U)$ is a Banach space, so the only limit of eigenvalues of A is zero. By using the Fredholm alternative theorem Gilbarg and Trudinger (2001), we can find out a pair of η_1 and η_2 , which are in the resolvent of A , hold (C.49) and $|\eta_1 - \eta_2| \geq 2\varepsilon_1 - \varepsilon_2$ for any small ε_2 satisfying $0 < \varepsilon_2 \leq \varepsilon_1$. If

$$\|(A - \eta_1)s_k\|_{B_{m+2s+1}^{1,2}(0,T;U)} \geq \varepsilon_1 \|s_k\|_{B_{m+2s+1}^{1,2}(0,T;U)}, \quad (\text{C.52})$$

we assign η to be η_1 . Otherwise,

$$\|(A - \eta_1)s_k\|_{B_{m+2s+1}^{1,2}(0,T;U)} < \varepsilon_1 \|s_k\|_{B_{m+2s+1}^{1,2}(0,T;U)}.$$

We compute

$$\begin{aligned}
\|(A - \eta_2)s_k\|_{B_{m+2s+1}^{1,2}(0,T;U)} &\geq \left| \|(\eta_1 - \eta_2)s_k\|_{B_{m+2s+1}^{1,2}(0,T;U)} - \|(A - \eta_1)s_k\|_{B_{m+2s+1}^{1,2}(0,T;U)} \right| \\
&> |2\varepsilon_1 - \varepsilon_2 - \varepsilon_1| \|s_k\|_{B_{m+2s+1}^{1,2}(0,T;U)}.
\end{aligned}$$

Considering that ε_2 is arbitrary, thus, such a η_2 enables

$$\|(A - \eta_2)s_k\|_{B_{m+2s+1}^{1,2}(0,T;U)} \geq \varepsilon_1 \|s_k\|_{B_{m+2s+1}^{1,2}(0,T;U)}. \quad (\text{C.53})$$

Now, we assign η to be η_2 . Since $s_k \in B_{m+2s+1}^{1,2}(0,T;U)$ and $s, m \geq 1$, s_k is a strong solution. i.e.

$$\frac{\partial s_k}{\partial t} + Ls_k + \frac{1}{\eta}r_k - \frac{1}{\eta} \left(\sum_{i=2}^M \sum_{n=1}^{N_i} \sum_{j=1}^i F_{i,j,n}(s_k) \left(\prod_{l=1, l \neq j}^{i-1} F_{i,l,n}(u_k) \right) \right) \equiv 0. \quad (\text{C.54})$$

Let $R_k := r_k - (1 - \eta) \left(\frac{\partial}{\partial t} + L \right) s_k$, we have

$$\frac{\partial s_k}{\partial t} = -Ls_k - R_k + \sum_{i=2}^M \sum_{n=1}^{N_i} \sum_{j=1}^i F_{i,j,n}(s_k) \left(\prod_{l=1, l \neq j}^{i-1} F_{i,l,n}(u_k) \right). \quad (\text{C.55})$$

By taking a derivative $\frac{\partial}{\partial t}$ to the both sides of identity (C.55), the right hand side of (C.55) is in $C^0(0, T; H^{m+2s-1}(U))$. Thus $\frac{\partial^2 s_k}{\partial t^2} \in C^0(0, T; H^{m+2s-1}(U))$. This implies that $s_k \in C^2(0, T; H^{m+2s-1}(U))$. Taking a derivative $\frac{\partial^2}{\partial t^2}$ to the both sides of identity (C.55) yields $s_k \in C^3(0, T; H^{m+2(s-1)-1}(U))$, and so on. By induction, we obtain $s_k \in B_{m+1}^{s+1,2}(0, T; U)$.

Step 2: the upper bound of solution.

(3), In this part, we are going to estimate the $B_{m+2s+1}^{1,2}(0, T; U)$ norm of s_k .

Equation (C.50) reads

$$\eta s_i^k = A(s_j^k) + f. \quad (\text{C.56})$$

Hence,

$$\left\| A(s_j^k) - \eta s_i^k \right\|_{B_{m+2s+1}^{1,2}(0,T;U)} = \|f\|_{B_{m+2s+1}^{1,2}(0,T;U)}.$$

Owing to inequality (C.51) and (C.48),

$$\|s_k\|_{B_{m+2s+1}^{1,2}(0,T;U)} \leq \frac{C_\gamma}{\varepsilon_1} \|r_k\|_{B_{m+2s}^{1,2}(0,T;U)}. \quad (\text{C.57})$$

(4), Since $R_k := r_k - (1 - \eta) \left(\frac{\partial}{\partial t} + L \right) s_k$, we have

$$\begin{aligned} & \|R_k - r_k\|_{B_{m+2s}^{1,2}(0,T;U)} \\ & \leq \left\| (1 - \eta) \left(\frac{\partial s_k}{\partial t} + Ls_k \right) \right\|_{B_{m+2s}^{1,2}(0,T;U)} \\ & \leq \left\| \frac{(1 - \eta)}{\eta} \left(-r_k + \sum_{i=2}^M \sum_{n=1}^{N_i} \sum_{j=1}^i F_{i,j,n}(s_k) \left(\prod_{l=1, l \neq j}^{i-1} F_{i,l,n}(u_k) \right) \right) \right\|_{B_{m+2s}^{1,2}(0,T;U)}. \end{aligned}$$

Considering $|1 - \eta| \leq \varepsilon_1 < \frac{1}{2}$,

$$\begin{aligned}
& \|R_k - r_k\|_{B_{m+2s}^{1,2}(0,T;U)} \\
& \leq \frac{\varepsilon_1}{\eta} (\|r_k\|_{B_{m+2s}^{1,2}(0,T;U)} + \left\| \sum_{i=2}^M \sum_{n=1}^{N_i} \sum_{j=1}^i F_{i,j,n}(s_k) \left(\prod_{l=1, l \neq j}^{i-1} F_{i,l,n}(u_k) \right) \right\|_{B_{m+2s}^{1,2}(0,T;U)}) \\
& \leq \frac{\varepsilon_1}{\eta} (\|r_k\|_{B_{m+2s}^{1,2}(0,T;U)} + \sum_{i=2}^M \sum_{n=1}^{N_i} C_*^i \sum_{j=1}^i a_{i,j,n} \|s_k\|_{B_{m+2s+1}^{1,2}(0,T;U)} \\
& \quad \prod_{l=1, l \neq j}^{i-1} a_{i,l,n} \|u_k\|_{B_{m+2s+1}^{1,2}(0,T;U)}) \\
& \leq \frac{\varepsilon_1}{\eta} (\|r_k\|_{B_{m+2s}^{1,2}(0,T;U)} + \|s_k\|_{B_{m+2s+1}^{1,2}(0,T;U)} \\
& \quad [M \max(1, C_*^M) \sum_{i=2}^M \sum_{n=1}^{N_i} (\prod_{l=1}^i a_{i,l,n}) \|u_k\|_{B_{m+2s+1}^{1,2}(0,T;U)}^{i-1}]).
\end{aligned}$$

Updating the right hand side of above inequality by using the inequality (C.57) and the condition $\|u_k\|_{B_{m+2s+1}^{1,2}(0,T;U)} \leq \lambda \leq 1$, it yields

$$\begin{aligned}
& \|R_k - r_k\|_{B_{m+2s}^{1,2}(0,T;U)} \\
& \leq \frac{\varepsilon_1}{\eta} (\|r_k\|_{B_{m+2s}^{1,2}(0,T;U)} (1 + \frac{C_\gamma}{\varepsilon_1} [M \max(1, C_*^M) \sum_{i=2}^M \sum_{n=1}^{N_i} (\prod_{l=1}^i a_{i,l,n}) \|u_k\|_{B_{m+2s+1}^{1,2}(0,T;U)}^{i-1}]) \\
& \leq \frac{\varepsilon_1}{\eta} \|r_k\|_{B_{m+2s}^{1,2}(0,T;U)} (1 + \frac{C_\gamma}{\varepsilon_1} \lambda M \max(1, C_*^M) \sum_{i=2}^M \sum_{n=1}^{N_i} (\prod_{l=1}^i a_{i,l,n})).
\end{aligned}$$

Note that $0 < \frac{1}{\eta} < 2$ and

$$\lambda = \min(1.0, \frac{\varepsilon^*}{4MC_\gamma \max(1, C_*^M) \sum_{i=2}^M \sum_{n=1}^{N_i} (\prod_{l=1}^i a_{i,l,n})}),$$

above inequality is reduced to

$$\|R_k - r_k\|_{B_{m+2s}^{1,2}(0,T;U)} \leq \|r_k\|_{B_{m+2s}^{1,2}(0,T;U)} \left(\frac{\varepsilon_1}{\eta} + \frac{\varepsilon^*}{2} \right).$$

Recall that ε_1 is arbitrary. Assign $\varepsilon_1 = \varepsilon^*/4$. We have

$$\|R_k - r_k\|_{B_{m+2s}^{1,2}(0,T;U)} \leq \varepsilon^* \|r_k\|_{B_{m+2s}^{1,2}(0,T;U)}. \quad (\text{C.58})$$

With this ε_1 , inequality (C.57) can be rewritten as

$$\|s_k\|_{B_{m+2s+1}^{1,2}(0,T;U)} \leq \frac{4C_3}{\varepsilon^*} \|r_k\|_{B_{m+2s}^{1,2}(0,T;U)} = \theta \|r_k\|_{B_{m+2s}^{1,2}(0,T;U)} \cdot$$

where θ is function of ε^* , N, U, s, m, T , and λ . It is easy to check $R_k \in B_{m,2}^{s+1,2}(0,T;U)$. ■

The preceding theorem proves the existence and regularity of the linearized problem of system (??).

By the following lemma, we will show the monotonic convergence of r_k and the boundedness of the nonlinear operator $F_2(s_k)$ by r_k in $B_{m+2s}^{1,2}(0,T;U)$.

Lemma 11 *Let*

$$\alpha = C_\theta \theta^2 \|r_0\|_{B_{m+2s}^{1,2}(0,T;U)}. \quad (\text{C.59})$$

Under condition (A1), (A2), and (A3), if i) for every $0 < l \leq k$, $r_l \in B_{m,2}^{s+1,2}(0,T;U)$ obeys

$$\|r_l\|_{B_{m+2s}^{1,2}(0,T;U)} \leq (1 - \beta) \|r_{l-1}\|_{B_{m+2s}^{1,2}(0,T;U)} \quad (\text{C.60})$$

where r_l are given by (C.13).

ii) there exists a function $R_k \in B_{m,2}^{s+1,2}(0,T;U)$ such that the equation $F_1(s_k) = -R_k$ has a solution s_k and

$$\|s_k\|_{B_{m+2s+1}^{1,2}(0,T;U)} \leq \theta \|r_k\|_{B_{m+2s}^{1,2}(0,T;U)} \quad (\text{C.61})$$

where

$$\|R_k - r_k\|_{B_{m+2s}^{1,2}(0,T;U)} \leq \varepsilon^* \|r_k\|_{B_{m+2s}^{1,2}(0,T;U)} \cdot$$

iii) $u_k \in B_{m+1}^{s+1,2}(0,T;U)$ and $\|u_k\|_{B_{m+2s+1}^{1,2}(0,T;U)} < \lambda$.

Then there exists a ρ_k such that

$$\|F_2(\rho_k s_k)\|_{B_{m+2s}^{1,2}(0,T;U)} \leq \rho_k^2 \alpha \|r_k\|_{B_{m+2s}^{1,2}(0,T;U)} \quad (\text{C.62})$$

and

$$\|r_{k+1}\|_{B_{m+2s}^{1,2}(0,T;U)} \leq (1 - \beta) \|r_k\|_{B_{m+2s}^{1,2}(0,T;U)}$$

where $i = 1, \dots, N$, $u_{k+1} = u_k + \rho_k s_k$, $p^{k+1} = p^k + \rho_k s_{N+1}^k$.

Proof. (1) we shall estimate $\|F_2(\rho_k s_k)\|_{B_{m+2s}^{1,2}(0,T;U)}$ in the first part. Considering that U is a bounded set in \mathbb{R}^N satisfying a cone condition and $2m > N$, by the lemma 7,

$$\begin{aligned} & \|F_2(\rho_k s_k)\|_{B_{m+2s}^{1,2}(0,T;U)} \\ &= \left\| \sum_{i=2}^M \sum_{n=1}^{N_i} \sum_{j=2}^i \binom{i}{j} \left(\prod_{l=1}^j F_{i,j_l,n}(\rho_k s_k) \right) \left(\prod_{t=1, j_t \neq j}^{i-j} F_{i,j_t,n}(u_k) \right) \right\|_{B_{m+2s}^{1,2}(0,T;U)} \\ &\leq \sum_{i=2}^M \sum_{n=1}^{N_i} \sum_{j=2}^i (C_*)^i \binom{i}{j} \prod_{l=1}^j (\|F_{i,j_l,n}(\rho_k s_k)\|_{B_{m+2s}^{1,2}(0,T;U)}) \\ &\quad \prod_{t=1, j_t \neq j}^{i-j} (\|F_{i,j_t,n}(u_k)\|_{B_{m+2s}^{1,2}(0,T;U)}). \end{aligned}$$

Owing to the condition (A3),

$$\begin{aligned} & \|F_2(\rho_k s_k)\|_{B_{m+2s}^{1,2}(0,T;U)} \\ &\leq \sum_{i=2}^M \sum_{n=1}^{N_i} \sum_{j=2}^i (C_*)^i \binom{i}{j} \prod_{l=1}^j (a_{i,j_l,n} \|\rho_k s_k\|_{B_{m+2s+1}^{1,2}(0,T;U)}) \\ &\quad \prod_{t=1, j_t \neq j}^{i-j} (a_{i,j_t,n} \|u_k\|_{B_{m+2s+1}^{1,2}(0,T;U)}) \\ &\leq 2^M C_*^M \sum_{i=2}^M \sum_{n=1}^{N_i} \prod_{l=1}^i (a_{i,l,n}) \sum_{j=2}^i \|\rho_k s_k\|_{B_{m+2s+1}^{1,2}(0,T;U)}^j \|u_k\|_{B_{m+2s+1}^{1,2}(0,T;U)}^{i-j}. \end{aligned}$$

Since $\|u_k\|_{B_{m+2s+1}^{1,2}(0,T;U)} < \lambda \leq 1$, it turns out that

$$\|F_2(\rho_k s_k)\|_{B_{m+2s}^{1,2}(0,T;U)} \leq 2^M C_*^M \sum_{i=2}^M \sum_{n=1}^{N_i} \prod_{l=1}^i (a_{i,l,n}) \sum_{j=2}^i \|\rho_k s_k\|_{B_{m+2s+1}^{1,2}(0,T;U)}^j.$$

Due to the inequality (C.61),

$$\|F_2(\rho_k s_k)\|_{B_{m+2s}^{1,2}(0,T;U)} \leq 2^M C_*^M \sum_{i=2}^M \sum_{n=1}^{N_i} \prod_{l=1}^i (a_{i,l,n}) \sum_{j=2}^i (\rho_k \theta \|r_k\|_{B_{m+2s}^{1,2}(0,T;U)})^j.$$

Note that the inequality (C.60) is satisfied provided $l \leq k$, thus

$$\|r_k\|_{B_{m+2s}^{1,2}(0,T;U)} \leq (1 - \beta)^k \|r_0\|_{B_{m+2s}^{1,2}(0,T;U)}. \quad (\text{C.63})$$

Hence, we compute

$$\begin{aligned} \|F_2(\rho_k s_k)\|_{B_{m+2s}^{1,2}(0,T;U)} &\leq [2^M C_*^M \sum_{i=2}^M \sum_{n=1}^{N_i} \prod_{l=1}^i (a_{i,l,n}) \sum_{j=0}^{i-2} (\rho_k \theta \|r_k\|_{B_{m+2s}^{1,2}(0,T;U)})^j] \times \\ &\quad \rho_k^2 \theta^2 \|r_k\|_{B_{m+2s}^{1,2}(0,T;U)}^2. \end{aligned}$$

Let $\rho_k = \min(\frac{2}{3}, \frac{1}{\theta \|r_0\|_{B_{m+2s}^{1,2}(0,T;U)}}, \frac{(1-\varepsilon^*)(1-\beta)}{2\alpha})$. We have

$$\|F_2(\rho_k s_k)\|_{B_{m+2s}^{1,2}(0,T;U)} \leq \rho_k^2 C_\theta \theta^2 \|r_k\|_{B_{m+2s}^{1,2}(0,T;U)}^2 \quad (\text{C.64})$$

where

$$C_\theta = M 2^M C_*^M \sum_{i=2}^M \sum_{n=1}^{N_i} [(i-1) \prod_{l=1}^i (a_{i,l,n})].$$

Due to the fact $0 < \beta < 1$ and the inequality (C.63), it turns out that

$$\begin{aligned} \|F_2(\rho_k s_k)\|_{B_{m+2s}^{1,2}(0,T;U)} &\leq \rho_k^2 C_\theta \theta^2 (1-\beta)^k \|r_0\|_{B_{m+2s}^{1,2}(0,T;U)} \|r_k\|_{B_{m+2s}^{1,2}(0,T;U)} \\ &\leq \rho_k^2 \alpha \|r_k\|_{B_{m+2s}^{1,2}(0,T;U)} \end{aligned}$$

where α is given by (C.59). This proves the inequality (C.62).

(2), By the identity (C.14), r_{k+1} can be decomposed into three parts;

$$r_{k+1} = r_k + F_1(\rho_k s_k) + F_2(\rho_k s_k).$$

For simplification, denote $\mathbf{h}_i^k := F_1(s_k) + r_k$. Hence

$$r_{k+1} = r_k + \rho_k (\mathbf{h}_i^k - r_k) + F_2(\rho_k s_k). \quad (\text{C.65})$$

Taking a $B_{m+2s}^{1,2}(0, T; U)$ norm to both sides of the (C.65), it yields

$$\begin{aligned} &\|r_{k+1}\|_{B_{m+2s}^{1,2}(0,T;U)} \\ &= \left\| r_k + \rho_k (\mathbf{h}_i^k - r_k) + F_2(\rho_k s_k) \right\|_{B_{m+2s}^{1,2}(0,T;U)} \\ &\leq |1 - \rho_k| \|r_k\|_{B_{m+2s}^{1,2}(0,T;U)} + \rho_k \left\| \mathbf{h}_i^k \right\|_{B_{m+2s}^{1,2}(0,T;U)} + \|F_2(\rho_k s_k)\|_{B_{m+2s}^{1,2}(0,T;U)}. \end{aligned}$$

Owing to the inequality (C.62),

$$\|r_{k+1}\|_{B_{m+2s}^{1,2}(0,T;U)} \leq (|1 - \rho_k| + \rho_k^2 \alpha) \|r_k\|_{B_{m+2s}^{1,2}(0,T;U)} + \rho_k \left\| \mathbf{h}_i^k \right\|_{B_{m+2s}^{1,2}(0,T;U)}. \quad (\text{C.66})$$

Note that $\mathbf{h}_i^k := -R_k + r_k$, thereby,

$$\left\| \mathbf{h}_i^k \right\|_{B_{m+2s}^{1,2}(0,T;U)} = \|r_k - R_k\|_{B_{m+2s}^{1,2}(0,T;U)} \leq \varepsilon^* \|r_k\|_{B_{m+2s}^{1,2}(0,T;U)}.$$

Inequality (C.66) can be reduced to

$$\|r_{k+1}\|_{C^1(0,T;H^{m+2s}(U))} \leq [1 - \rho_k + \rho_k^2 \alpha + \rho_k \varepsilon^*] \|r_k\|_{C^1(0,T;H^{m+2s}(U))}.$$

Note that $\rho_k = \min(\frac{2}{3}, \frac{1}{\theta \|r_0\|_{B_{m+2s}^{1,2}(0,T;U)}}, \frac{(1-\varepsilon^*)(1-\beta)}{2\alpha})$,

$$\begin{aligned} |1 - \rho_k| + \rho_k^2 \alpha + \rho_k \varepsilon^* &= 1 + \rho_k(-1 + \varepsilon^* + \rho_k \alpha) \\ &\leq 1 + \rho_k(-1 + \varepsilon^* + \frac{(1-\varepsilon^*)(1-\beta)}{2\alpha} \alpha) \\ &\leq 1 + \rho_k(-1 + \varepsilon^* + (1-\varepsilon^*) \frac{(1-\beta)}{2}). \end{aligned}$$

Consider that $0 < \beta < 1$ and $\varepsilon^* \in [\frac{1}{4}, \frac{1}{2}]$, $\frac{(1-\varepsilon^*)}{2} \geq \frac{3}{8}$. Hence,

$$\begin{aligned} |1 - \rho_k| + \rho_k^2 \alpha + \rho_k \varepsilon^* &\leq 1 - \rho_k \left(\frac{1 - \varepsilon^*}{2} \right) \\ &\leq 1 - \min\left(\frac{1}{4}, \frac{(1-\varepsilon^*)}{2\theta \|r_0\|_{B_{m+2s}^{1,2}(0,T;U)}}, \frac{(1-\varepsilon^*)^2}{4\alpha}\right) \\ &= 1 - \beta. \end{aligned}$$

This proves

$$\|r_{k+1}\|_{B_{m+2s}^{1,2}(0,T;U)} \leq (1 - \beta) \|r_k\|_{B_{m+2s}^{1,2}(0,T;U)}.$$

■

The preceding lemma shows the monotonic convergence of the residue sequence. By the following theorem, we will prove the existence of regular solution of the nonlinear parabolic equation (C.1).

Theorem 12 *Under condition (A1), (A2), and (A3), if there exists an initial guess $u_0 \in B_{m+1}^{s+1,2}(0,T;U)$ satisfying the boundary and initial conditions such that $r_0 \in B_{m,2}^{s+1,2}(0,T;U)$ and*

$$\|u_0\|_{B_{m+2s+1}^{1,2}(0,T;U)} + \frac{\theta}{\beta} \|r_0\|_{B_{m+2s}^{1,2}(0,T;U)} \leq \lambda, \quad (\text{C.67})$$

then the nonlinear parabolic system (C.1)-(C.2) has a solution u^ in $B_{m+1}^{s+1,2}(0,T;U)$.*

Proof. (1), If $\|r_0\|_{B_{m+2s}^{1,2}(0,T;U)} = 0$, then the initial guess u_0 is the solution of the nonlinear parabolic system (C.1)-(C.2). This proves the theorem. So, without loss of generality, we assume $\|r_0\|_{B_{m+2s}^{1,2}(0,T;U)} > 0$.

(2), When $k = 0$. By theorem 10, there exists a function R_0 such that

$$F_1(s_0) = -R_0$$

has a solution s_0 in $[0, T] \times U$, where s_0 and R_i^0 hold

$$\|R_0 - r_0\|_{B_{m+2s}^{1,2}(0,T;U)} \leq \varepsilon^* \|r_0\|_{B_{m+2s}^{1,2}(0,T;U)}, \quad (\text{C.68})$$

$$\|s_0\|_{B_{m+2s+1}^{1,2}(0,T;U)} \leq \theta \|r_0\|_{B_{m+2s}^{1,2}(0,T;U)}. \quad (\text{C.69})$$

Denote ρ_k by

$$\rho_k = \min\left(\frac{2}{3}, \frac{1}{\theta \|r_0\|_{B_{m+2s}^{1,2}(0,T;U)}}, \frac{(1 - \varepsilon^*)(1 - \beta)}{2C_\theta\theta^2 \|r_0\|_{B_{m+2s}^{1,2}(0,T;U)}}\right). \quad (\text{C.70})$$

Let $u_1 = u_0 + \rho_k s_0$, we have

$$\begin{aligned} \|u_1\|_{B_{m+2s+1}^{1,2}(0,T;U)} &= \|u_0 + \rho_k s_0\|_{B_{m+2s+1}^{1,2}(0,T;U)} \\ &\leq \|u_0\|_{B_{m+2s+1}^{1,2}(0,T;U)} + \|s_0\|_{B_{m+2s+1}^{1,2}(0,T;U)}. \end{aligned}$$

Owing to the inequality (C.69), (C.67), and the fact $0 < \beta < 1$ (identity (C.12)), we have

$$\begin{aligned} \|u_1\|_{B_{m+2s+1}^{1,2}(0,T;U)} &\leq \|u_0\|_{B_{m+2s+1}^{1,2}(0,T;U)} + \frac{\theta}{\beta} \|r_0\|_{B_{m+2s}^{1,2}(0,T;U)} \\ &\leq \lambda. \end{aligned}$$

The identity (C.65) implies that

$$r_1 = r_0 + \rho_k(\mathbf{h}_i^0 - r_0) + F_2(\rho_k s_0).$$

Taking the $B_{m+2s}^{1,2}(0, T; U)$ norm to both sides of above identity and taking into account the inequality (C.62) and (C.68) yield

$$\|\mathbf{r}^1\|_{B_{m+2s}^{1,2}(0,T;U)} \leq \|r_0\|_{B_{m+2s}^{1,2}(0,T;U)} [|1 - \rho_k| + \rho_k(\varepsilon^* + \rho_k C_\theta \theta^2 \|r_0\|_{B_{m+2s}^{1,2}(0,T;U)})].$$

Furthermore, considering the identity (C.70), we have

$$\begin{aligned} &1 + \rho_k(-1 + \varepsilon^* + \rho_k C_\theta \theta^2 \|r_0\|_{B_{m+2s}^{1,2}(0,T;U)}) \\ &\leq 1 + \rho_k(-1 + \varepsilon^* + \frac{1 - \varepsilon^*}{2C_\theta\theta^2 \|r_0\|_{B_{m+2s}^{1,2}(0,T;U)}} C_\theta \theta^2 \|r_0\|_{B_{m+2s}^{1,2}(0,T;U)}) \\ &\leq 1 - \rho_k\left(\frac{1 - \varepsilon^*}{2}\right) \\ &\leq 1 - \min\left(\frac{1}{4}, \frac{(1 - \varepsilon^*)}{2\theta \|r_0\|_{B_{m+2s}^{1,2}(0,T;U)}}, \frac{(1 - \varepsilon^*)^2}{4C_\theta\theta^2 \|r_0\|_{B_{m+2s}^{1,2}(0,T;U)}}\right). \end{aligned}$$

This implies that

$$[1 + \rho_k(-1 + \varepsilon^* + \rho_k C_\theta \|r_0\|_{B_{m+2s}^{1,2}(0,T;U)})] \leq (1 - \beta). \quad (\text{C.71})$$

Thus,

$$\begin{aligned} \|r_1\|_{B_{m+2s}^{1,2}(0,T;U)} &\leq (1 - \beta) \|r_0\|_{B_{m+2s}^{1,2}(0,T;U)}, \\ \|u_1\|_{B_{m+2s+1}^{1,2}(0,T;U)} &\leq \lambda, \\ \|s_0\|_{B_{m+2s+1}^{1,2}(0,T;U)} &\leq \theta \|r_0\|_{B_{m+2s}^{1,2}(0,T;U)}. \end{aligned}$$

(2), Without loss of generality, we assume that, for any $1 < \sigma \leq k$,

$$\begin{aligned} \|r_\sigma\|_{B_{m+2s}^{1,2}(0,T;U)} &\leq (1 - \beta) \|r_{\sigma-1}\|_{B_{m+2s}^{1,2}(0,T;U)}, \\ \|u_\sigma\|_{B_{m+2s+1}^{1,2}(0,T;U)} &\leq \lambda, \\ \|s_{\sigma-1}\|_{B_{m+2s+1}^{1,2}(0,T;U)} &\leq \theta \|r_{\sigma-1}\|_{B_{m+2s}^{1,2}(0,T;U)}. \end{aligned}$$

By theorem 10, there exists a function $R_k \in B_{m+2s}^{1,2}(0, T; U)$ such that the system $F_1(s_k) = -R_k$ has a solution $\{s_k\}$ in $[0, T] \times U$. Such a solution satisfies that

$$\begin{aligned} \|R_k - r_k\|_{B_{m+2s}^{1,2}(0,T;U)} &\leq \varepsilon^* \|r_k\|_{B_{m+2s}^{1,2}(0,T;U)}, \\ \|s_k\|_{B_{m+2s+1}^{1,2}(0,T;U)} &\leq \theta \|r_k\|_{B_{m+2s}^{1,2}(0,T;U)}. \end{aligned}$$

By lemma 11, we have

$$\|r_{k+1}\|_{B_{m+2s+1}^{1,2}(0,T;U)} \leq (1 - \beta) \|r_k\|_{B_{m+2s}^{1,2}(0,T;U)}.$$

Assign $u_{k+1} = u_k + \rho_k s_k$. We compute:

$$\begin{aligned} \|u_{k+1}\|_{B_{m+2s+1}^{1,2}(0,T;U)} &\leq \|u_k + \rho_k s_k\|_{B_{m+2s+1}^{1,2}(0,T;U)} \\ &\leq \left\| u_0 + \sum_{n=0}^k \rho_k s_n \right\|_{B_{m+2s+1}^{1,2}(0,T;U)} \\ &\leq \|u_0\|_{B_{m+2s+1}^{1,2}(0,T;U)} + \sum_{n=0}^k \|\rho_k s_n\|_{B_{m+2s+1}^{1,2}(0,T;U)}. \end{aligned}$$

Since $0 < \beta, \rho_k < 1$,

$$\begin{aligned}
\|u_{k+1}\|_{B_{m+2s+1}^{1,2}(0,T;U)} &\leq \|u_0\|_{B_{m+2s+1}^{1,2}(0,T;U)} + \sum_{n=0}^k \|s_n\|_{B_{m+2s+1}^{1,2}(0,T;U)} \\
&\leq \|u_0\|_{B_{m+2s+1}^{1,2}(0,T;U)} + \theta \sum_{n=0}^k \|r_k\|_{B_{m+2s+1}^{1,2}(0,T;U)} \\
&\leq \|u_0\|_{B_{m+2s+1}^{1,2}(0,T;U)} + \theta \|r_0\|_{B_{m+2s+1}^{1,2}(0,T;U)} \sum_{n=0}^k (1-\beta)^n \\
&\leq \lambda.
\end{aligned}$$

Likewise, we can prove that $\left\| \frac{\partial u_{k+1}}{\partial t} \right\|_{B_{m+2s-1}^{1,2}(0,T;U)} \leq \lambda_2$.

By induction, we conclude that, for any $k > 0$,

$$\begin{aligned}
\|r_{k+1}\|_{B_{m+2s}^{1,2}(0,T;U)} &\leq (1-\beta) \|r_k\|_{B_{m+2s}^{1,2}(0,T;U)}, \\
\|u_{k+1}\|_{B_{m+2s+1}^{1,2}(0,T;U)} &\leq \lambda, \\
\|s_k\|_{B_{m+2s+1}^{1,2}(0,T;U)} &\leq \theta \|r_k\|_{B_{m+2s}^{1,2}(0,T;U)}.
\end{aligned}$$

Considering that β is a nonzero constant independent of k and $0 < \beta < 1$, sequence r_{k+1} monotonically converges to 0 in $B_{m+2s}^{1,2}(0,T;U)$.

(3), Obviously, the sequence u_k is Cauchy in the space $B_{m+2s+1}^{1,2}(0,T;U)$. This implies that u_* where $u_* := \lim_{k \rightarrow \infty} u_k$, is the solution of the nonlinear parabolic equation (??). Note that $m > N/2$ and $s > 0$, it is a strong solution in $B_{m+1}^{s+1,2}(0,T;U)$.

(4), Clearly, u_* satisfies the initial and boundary conditions because u_0 satisfies the initial and boundary conditions and

$$s_k(0, U) = 0, \quad s_k(t, \partial U) = 0.$$

Finally, we accomplish the proof. ■

The inequality (C.67) is a sufficient condition for the global existence of the strong solution. In the case that the inequality (C.67) fails, we will seek a rescaling of variables such that the inequality (C.67) is held. The rescaling shown by the table C.1 will transfer the system (C.1)-(C.2) into

$$\frac{\partial \bar{u}}{\partial \bar{t}} - D_i(\bar{a}^{ij}(x)D_j \bar{u}) + \bar{b}\bar{u} = \bar{f}_0 + \sum_{i=2}^M \sum_{n=1}^{N_i} \prod_{j=1}^i \bar{F}_{i,j,n}(\bar{u}), \quad (\text{C.72})$$

$$\bar{u}(0, U) = \bar{g}(U) = \zeta^\pi g(U) \quad , \quad \bar{u}(\bar{t}, \partial U) = \bar{h}(\bar{t}; \partial U) = \zeta^\pi h(\zeta^{\pi-\sigma} t; \partial U). \quad (\text{C.73})$$

where ζ is a constant, $\pi, \sigma > 0$.

Table C.1 The relationship between the rescaled system and original system

| | | | | | | | |
|--------|----------------------------------|---------------|-----------------------------|-------------------------------|---|--|---------------------------------|
| Ori. | t | x | $u(t; x)$ | f_0 | $\alpha_{i,j,n}$ | a^{ij} | b |
| Res. | \bar{t} | \bar{x} | $\bar{u}(\bar{t}; \bar{x})$ | \bar{f}_0 | $\bar{\alpha}_{i,j,n}$ | \bar{a}^{ij} | \bar{b} |
| Relat. | $\bar{t} = t/\zeta^{\sigma-\pi}$ | $\bar{x} = x$ | $\bar{u} = u\zeta^\pi$ | $\bar{f}_0 = f_0\zeta^\sigma$ | $\bar{\alpha}_{i,j,n} = \zeta^{(\sigma-i\pi)/i} \alpha_{i,j,n}$ | $\bar{a}^{ij} = a^{ij} \zeta^{\sigma-\pi}$ | $\bar{b} = b\zeta^{\sigma-\pi}$ |

Note that the rescaling changes the norm but does not change the arguments x . The residual \bar{r} corresponding to the rescaled system obeys

$$\bar{r} = \zeta^\sigma r \quad (\text{C.74})$$

because

$$\begin{aligned} \bar{r} & : = \frac{\partial \bar{u}}{\partial \bar{t}} - D_i(\bar{a}^{ij}(x) D_j \bar{u}) + \bar{b} \bar{u} - \bar{f}_0 - \sum_{i=2}^M \sum_{n=1}^{N_i} \prod_{j=1}^i \bar{F}_{i,j,n}(\bar{u}) \\ & = \zeta^\sigma \left[\frac{\partial u}{\partial t} - D_i(a^{ij}(x) D_j u) + bu - f_0 - \sum_{i=2}^M \sum_{n=1}^{N_i} \prod_{j=1}^i F_{i,j,n}(u) \right] \\ & = \zeta^\sigma r. \end{aligned}$$

For the rescaled system, the condition (A2)-(A3) and the definition 6 are updated to:

(B2), $\bar{a}^{ij}(x) \in C^{m+2s+1,1}(\bar{U})$ and \bar{b} is a non-negative constant. L is self-adjoint, bounded and strong elliptic. i.e. there exist positive number $\bar{\gamma}_1$, $\bar{\gamma}_2$, and a non-negative constant $\bar{\gamma}_3$ such that $\bar{a}^{ij} = \bar{a}^{ji}$,

$$|\bar{a}^{ij}(x) \xi_i \xi_j| \geq \bar{\gamma}_1 |\xi|^2, \quad \forall x \in U, \xi \in \mathbb{R}^N. \quad (\text{C.75})$$

$$\sum |\bar{a}^{ij}(x)|^2 \leq \bar{\gamma}_2, \quad \forall x \in U. \quad (\text{C.76})$$

$$\infty > \bar{b}(x) \geq \bar{\gamma}_3 \geq 0, \quad \forall x \in U. \quad (\text{C.77})$$

where $\bar{\gamma}_1 = \zeta^{\sigma-\pi} \gamma_1$, $\bar{\gamma}_2 = \zeta^{\sigma-\pi} \gamma_2$ and $\bar{\gamma}_3 = \zeta^{\sigma-\pi} \gamma_3$, and $\bar{a}^{ij} = a^{ij}$. Moreover, $\bar{g} \in H^{m+2(1+s)}(\bar{U})$, $\bar{h} \in C^1(0, T; H^{m+2s}(\partial \bar{U})) \cap C^0(0, T; H^{m+2(1+s)}(\partial \bar{U}))$, and $\bar{f}_0 \in H^{m+2s}(\bar{U})$ is a force independent of \bar{u} .

(B3), each $\bar{F}_{i,j}$ is a linear operator from $C^j(0, T; H^{a+p_{i,j,n}}(U))$ into $C^j(0, T; H^a(U))$ so that

$$\|\bar{F}_{i,j,n}(\bar{u})\|_{C^j(0,T;H^a(U))} \leq \bar{a}_{i,j,n} \|\bar{u}\|_{C^j(0,T;H^{a+p_{i,j,n}}(U))} = \zeta^{(\sigma-i\pi)/i} \alpha_{i,j,n} \|\bar{u}\|_{C^j(0,T;H^{a+p_{i,j,n}}(U))}, \quad (\text{C.78})$$

where $m + 2s + 1 \geq \alpha \geq 0$, $s \geq j \geq 0$ and $1 \geq p_{i,j,n} > -\infty$.

Definition 7 Let the constant ε^* to be arbitrary constant in the domain $[\frac{1}{4}, \frac{1}{2}]$, $\bar{\theta} = \frac{4\bar{C}_\gamma}{\varepsilon^*}$,

$$\bar{C}_\gamma = 2N^{m+2(s+1)} \max(1, \frac{\sqrt{T}}{\sqrt{\gamma_1}}, \min(T, \frac{\sqrt{T}}{\sqrt{\gamma_3}})),$$

$$\bar{C}_\theta = M2^M C_*^M \sum_{i=2}^M \sum_{n=1}^{N_i} [(i-1) \prod_{l=1}^i (\bar{a}_{i,l})],$$

$$\bar{\lambda} = \min(1.0, \frac{\varepsilon^*}{4M\bar{C}_\gamma \max(1, C_*^M) \sum_{i=2}^M \sum_{n=1}^{N_i} (\prod_{l=1}^i \bar{a}_{i,l,n})}) \quad (\text{C.79})$$

and

$$\bar{\beta} = \min(\frac{1}{4}, \frac{(1-\varepsilon^*)}{2\bar{\theta} \|\bar{r}_0\|_{B_{m+2s}^{1,2}(0,T;U)}}, \frac{(1-\varepsilon^*)^2}{4\bar{C}_\theta \bar{\theta}^2 \|\bar{r}_0\|_{B_{m+2s}^{1,2}(0,T;U)}}). \quad (\text{C.80})$$

Obviously, the rescaling is identified by the coefficient σ and π . By the following theorem, we will show that regardless of the initial guess u_0 , we can always find out a pair of σ , π , and T^* such that the inequality (C.67) is satisfied.

Theorem 13 Under condition (A1), (A2), and (A3), if there exists an initial guess $u_0 \in B_{m+1}^{s+1,2}(0, T; U)$ satisfying the boundary and initial conditions, then there is a T^* such that the nonlinear parabolic system (C.1)-(C.2) has a solution u^* in $B_{m+1}^{s+1,2}(0, T^*; U)$, where

$$T^* = \min(1, \zeta^{M-1} \gamma_1, T), \quad (\text{C.81})$$

$$\zeta = \min(\frac{(\|u_0\|_{B_{m+2(s+1),2}^{1,2}(0,T;U)} + \frac{\theta}{\bar{\beta}} \|r_0\|_{B_{m+2s}^{1,2}(0,T;U)})}{\min(1.0, \frac{\varepsilon^*}{4MC_\gamma \max(1, C_*^M) \sum_{i=2}^M \sum_{n=1}^{N_i} (\prod_{l=1}^i a_{i,l,n})}}, 1.0), \quad (\text{C.82})$$

and the constant M is maximum order of the identity (C.5).

Proof. Assign $\sigma = M$ and $\pi = 1$. Define $T^* = \min(1, \zeta^{M-1}\gamma_1, T)$ where ζ is given by (C.82). It is easy to check that $\bar{C}_\theta \leq C_\theta$ because

$$\bar{C}_\gamma = 2N^{m+2(s+1)} \max\left(1, \frac{\sqrt{T^*}}{\sqrt{\gamma_1}}, \min\left(T^*, \frac{\sqrt{T^*}}{\sqrt{\gamma_3}}\right)\right) = 2N^{m+2(s+1)} \leq C_\gamma.$$

Furthermore, $\bar{\theta} \leq \theta$. Considering that $0 < \zeta \leq 1$, we have

$$\begin{aligned} \bar{\lambda} &= \min\left(1.0, \frac{\varepsilon^*}{4M\bar{C}_\gamma \max(1, C_*^M) \sum_{i=2}^M \sum_{n=1}^{N_i} \left(\prod_{l=1}^i \bar{a}_{i,l,n}\right)}\right) \\ &\geq \min\left(1.0, \frac{\varepsilon^*}{4MC_\gamma \max(1, C_*^M) \sum_{i=2}^M \sum_{n=1}^{N_i} \left(\prod_{l=1}^i a_{i,l,n}\right)}\right) \\ &\geq \lambda(T) \end{aligned}$$

and

$$\begin{aligned} \frac{1}{\bar{\beta}} &= \max\left(4, \frac{2\bar{\theta} \|\bar{r}_0\|_{B_{m+2s}^{1,2}(0,T;U)}}{(1-\varepsilon^*)}, \frac{4\bar{C}_\theta \bar{\theta}^2 \|\bar{r}_0\|_{B_{m+2s}^{1,2}(0,T;U)}}{(1-\varepsilon^*)^2}\right) \\ &\leq \max\left(4, \frac{2\theta \|r_0\|_{B_{m+2s}^{1,2}(0,T;U)} \zeta^M}{(1-\varepsilon^*)}, \frac{4C_\theta \theta^2 \|r_0\|_{B_{m+2s}^{1,2}(0,T;U)} \zeta^M}{(1-\varepsilon^*)^2}\right) \\ &\leq \frac{1}{\beta}. \end{aligned}$$

Note that C_* is independent of T which is proved by lemma 7. Therefore, by the identity (C.82) and (C.79),

$$\begin{aligned} &\|\bar{u}_0\|_{B_{m+2s+1}^{1,2}(0,T^*;U)} + \frac{\bar{\theta}}{\beta} \|\bar{r}_0\|_{B_{m+2s}^{1,2}(0,T^*;U)} \\ &\leq \|\bar{u}_0\|_{B_{m+2s+1}^{1,2}(0,T;U)} + \frac{\bar{\theta}}{\beta} \|\bar{r}_0\|_{B_{m+2s}^{1,2}(0,T;U)} \\ &\leq \zeta \left(\|u_0\|_{B_{m+2s+1}^{1,2}(0,T^*;U)} + \frac{\theta}{\beta} \|r_0\|_{B_{m+2s}^{1,2}(0,T^*;U)} \zeta^{M-1} \right) \\ &\leq \min\left(1.0, \frac{\varepsilon^*}{4MC_\gamma \max(1, C_*^M) \sum_{i=2}^M \sum_{n=1}^{N_i} \left(\prod_{l=1}^i a_{i,l,n}\right)}\right) \\ &\leq \bar{\lambda}. \end{aligned}$$

Hence, by theorem 12, we prove the existence of the strong solution in $B_{m+1}^{s+1,2}(0, T^*; U)$. ■

Above theorem prove the local existence of the Dirichlet problem of nonlinear system (C.1)-(C.2).

C.4 Conclusion

This paper proposes a monotonic method to approach the strong solutions of nonlinear parabolic system (C.1)-(C.2). By this method, we prove that if the initial data satisfies inequality (C.67), then the global solution of system (C.1)-(C.2) exists in $B_{m+1}^{s+1,2}(0, T; U)$. Otherwise, there exists a T^* such that the solution exists in $B_{m+2,2}^{s+1,2}(0, T^*; U)$. And theorem 13 gives a time interval that the solution will not blow up.

BIBLIOGRAPHY

- Adams, R. A. (2003). Sobolev Space. *Ed.2*, New York: Academic Press
- Antonia, R.A., Dienidi, L., and Spalert, P.R. (1994). Anisotropy of dissipation tensor in a turbulent boundary layer. *Phys. Fluids*, 7, 2475–2479.
- Arad, I., L'vov, V.S., and Procaccia, I. (1999). Correlation functions in isotropic and anisotropic turbulence: The role of the symmetry group. *Phy. Rev. E.*, 59, 6753–6765.
- Aris, R. (1989). *Vectors, tensors and the basic equation of fluid Mechanics*. Chapter 4, 76–97. Mineola: Dover.
- Barrett, M. J. and Hollingsworth, D. K. (2003). Correlation friction velocity in turbulent boundary layers subjected to freestream turbulence. *AIAA J.*, 41(8), 1444–1451.
- Barrett, M. J. and Hollingsworth, D. K. (2003). Heat transfer in turbulent boundary layers subjected to free-stream turbulence, part I: experimental results. *J. Turbomachinery*, 125(Apr.), 232–241.
- Barrett, M. J. and Hollingsworth, D. K. (2001). On the calculation of length scales for turbulent heat transfer correlation. *J. Heat Transfer*, 123, 878–883.
- Batchelor, G.K. (1953). Theory of homogenous turbulence. *Cambridge University Press*, New York.
- Batchlor, G. K. (2000). *An introduction to fluid dynamics*, Chapter 3.1, 131–137. London: Cambridge Univ. Press.

- Benzi, R., Struglia, M.V. and Tripiccione, R. (1996). Extended self-similarity in numerical simulation of three-dimensional anisotropic turbulence. *Phys. Rev. E.*, *53*, 5565–5568.
- Biferale, L. and Vergassola, M. (2001) Isotropy vs anisotropy in small-scale turbulence. *Phys. Fluids*, *13*, 2139–2141.
- Biferale, L. and Toschi, F. (2001). Anisotropic homogenous turbulence: hierarchy and intermittency of scaling exponents in the anisotropic sectors. *Phys. Rev. Lett.*, *86*, 4831–4834.
- Biferale, L., Daumont, I., Lanotte, A., and Toschi, F. (2002). Anomalous and dimensional scaling in anisotropic turbulence. *Phys. Rev. E*, *66*, 056306.
- Biferale, L., Daumont, I., Lanotte, A. and Toschi, F. (2004). Theoretical and numerical study of highly anisotropic turbulent flows. *Europ. J. Mech.*, *23*, 401–414.
- Bijl, H. and Wesseling, P. (1998). A unified method for computing incompressible and compressible flows in boundary fitted coordinates, *J. Comput. Phys.* *141*, 153.
- Blair, M. F. (1983). Influence of free-stream turbulence on turbulent boundary layer heat transfer and mean profile development, part II-analysis of results. *J. Heat Transfer*, *105*, 41–47.
- Boltzmann, L. (1964). Lecture on gas theory, Univ. of California Press, Berkeley.
- Bradshaw, P. (1974). The effect of mean compressible or dilatation on the turbulent structure of supersonic boundary layers. *J. Fluid Mech.* *63*: 449–464.
- Bradshaw, P. (1977). Compressible turbulent shear layers. *Ann. Rev. Fluid. Mech.*, *9*, 33–54.
- Burd, S. W., Kaszeta, R. W., and Simon, T. W. (1996). Measurements in film cooling flows: hole L/D and turbulence intensity effects. *ASME*. 96-WA/HT-7.
- Caffarelli, L., Kohn, R., and Nirenberg, L. (1982). Partial regularity of suitable weak solutions of the nonlinear parabolic equations. *Comm. Pure Appl. Math.* *35*, 771–831.

- Caffarelli, L. and Huang, Q. (2003). Estimates in the generalized Campanato-John-Nirenberg spaces for fully nonlinear elliptic equations. *Duke Math. J.* 118, 1–17.
- Cebeci, T. and Smith, A. M. O. (1974). *Analysis of turbulent boundary layers*. New York: Academic Press.
- Cebeci, T. and Bradshaw, P. (1977). *Momentum transfer in boundary layer*, Hemisphere.
- Choi, K.-S. and Lumley, J.L. (2001). The return to isotropic of homogenous turbulence, *J. Fluid Mech.* 436, 59–84.
- Choi, H. and Moin, P. (1994). Effects of the computational time step on numerical solutions of turbulent flow. *J. Comput. Phys.*, 113, 1–4.
- Chorin, A. J. (1968). Numerical solution of the Navier-Stokes equations. *Math. Comp.*, 22, 745–762.
- Crandall, M.G. and Lions, P. L. (1983). Viscosity solutions of Hamilton-Jacobi equations. *Trans. Amer. Math. Soc.* 227, 1–42.
- Crandall, M.G., Ishii, H., and Lions, P. L. (1992). User's guide to viscosity solutions of second order partial differential equations. *Bull. Amer. Math. Soc.* 1992, 1–67.
- Croteau, T., and Ronis, D. (2002). Nonequilibrium velocity distributions in liquid: Systems under shear. *Phys. Rev. E* 66, 066109.
- Dailey, L. and Pletcher, R. H. (1996). Evolution of multigrid acceleration for preconditioned time-accurate Navier-Stokes algorithms. *Computers & Fluids*, 25, 791–811.
- DeGraaff, D. B. and Eaton, J. K. (2000). Reynolds-number scaling of the flat-plate turbulent boundary layer. *J. Fluid Mech.* 422, 319–346.
- Dennis, J. E., and Schnabel, R. B. (1996). *Numerical methods for unconstrained optimization and nonlinear equations*. Philadelphia: SIAM.

- Durbin, P. A. and Zeman, O. (1992). Rapid distortion theory for homogenous compressed turbulence with application to modeling. *J. Fluid Mech.* 242: 349–370.
- Evans, L. C. (1982). Classical solutions of fully nonlinear, convex, second-order elliptic equations. *Comm. Pure Appl. Math.* 35, 333–363.
- Evans, L. C. (1978). A convergence theorem for solutions of nonlinear second-order elliptic equations. *Indiana Univ. Math.J.* 27, 875–887.
- Falkovich, G., and Lebedev, V. (1997). Single-point velocity distribution in turbulence, *Phys. Rev. Lett.* 79 (21), 4159–4161.
- Favre, A. (1983). Turbulence: space-time statistical properties and behavior in supersonic flows. *Physics of Fluids*, 26, 2851–2863.
- Freire, A. P., Cruz, D. O. A. and Pellegrini, C. C. (1995). Velocity and temperature distributions in compressible turbulent boundary layers with heat and mass transfer. *Int. J. Heat Mass Transfer.*, 38(13), 2507–2515.
- Frisch, U. (1995). Turbulence. The legacy of A. N. Kolmogorov. *Cambridge University Press*, Cambridge.
- Frisch, U., Bec, J., and Aurell, E. (2005). "Local homogeneous turbulence": Is it an inconsistent framework? *Phys. Fluids*, 17, 081706(1)–081706(4).
- Ganapathisubramani, B., Hutchins, N., Hambleton, W.T., Longmire, E.K., and Marusic, I. (2005). Investigation of large-scale coherence in a turbulent boundary layer using two-point correlations, *J. Fluid. Mech.* 524, 57–80.
- Germano, M., Piomelli, U., Moin, P., and Cabot, W. H. (1991). A dynamic subgrid-scaled eddy viscosity model. *Phys. of Fluids*, A 3, 1760–1765.
- Gilbarg, D. and Trudinger, N. S. (2001). Elliptic partial differential equations of second order
New York: Springer

- Gille, S. T., and Smith, S. G. L. (2000). Velocity probability density functions from altimetry. *J. Phys. Oceanograph.* 30, 125–136.
- Goldstein, R. J., Eckert, E. R. G., and Burggraf, F. (1974). Effects of hole geometry and density on three-dimensional film cooling. *Int. J. Heat Mass Transfer*, 17, 595–607.
- Grossmann, S., Heydt, A., and Lohse, D. (2001). Scaling exponents in weakly anisotropic turbulence from the Navier-Stokes equation, *J. Fluid Mech.*, 440, 381–390.
- Guarini, S. E., Moser, R. D., Shariff, K. and Wray, A., (2000). Direct numerical simulation of a supersonic turbulent boundary layer at Mach 2.5. *J. Fluid Mech.*, 414, 1–33.
- Hancock, P. E. and Bradshaw, P. (1983). Effect of free-stream turbulence on turbulent boundary layer. *J. Fluids Eng.*, 105(Sep.), 284–289.
- Hill, R.J. (1997). Applicability of Kolmogorov's and Monin's equations of turbulence, *J. Fluid Mech.* 353, 67–81.
- Hill, R.J. (2001). Equations relating structure functions of all orders, *J. Fluid Mech.*, 434, 379–388.
- Hinz, J. O. (1975). *Turbulence*, Ed. 2. New York: McGraw-Hill, Ed. 2.
- Hoffmann, J. A. and Mohammadi, K. (1991). Velocity profiles for turbulent boundary layer under freestream turbulence. *J. Fluids Eng.*, 113(Sep.), 399–404.
- Huang, P. G., Bradshaw, P., and Coakley, T. J. (1993). Skin friction and velocity profile family for compressible turbulent boundary layers. *AIAA J.*, 31(9), 33–54.
- Iritani, Y., Kasagi, N., and Hirata, M. (1985). Heat transfer mechanism and associated turbulent boundary structure in the near-wall region of a turbulent boundary layer. *Turbulent Shear Flows 4.*, edited by L.J.S. Bradbury, F.Durst, B.E.Lauder, F.W.Schmidt and J.H.Whitelaw. Beilin: Springer-Verlag, 223–234.

- Jacob, B., Biferale, L., Luso, G., and Casciola, C. M. (2004). Anisotropic fluctuations in turbulent shear flows, *Phys. Fluids*, *16*, 4135–4142.
- Jayesh and Warhaft, Z. (1991). Probability distribution of a passive scalar in grid-generated turbulence, *Phys. Rev. Lett.* *67* (25), 3503–3506.
- Jensen, R. (1988). The maximum principle for viscosity solutions of fully nonlinear second order partial differential equations. *Arch. Rational Mech. Anal.*. *101*, 1–27.
- Kato, T. (1984). Strong L^p solution of the nonlinear parabolic equations in R^m with application. *Math.Z.*. *187*, 471–480.
- Kadar, B. A. (1981). Temperature and concentration profiles in fully turbulent boundary layers. *Int. J. Heat Mass Transfer*, *24*(9), 1541–1544.
- Karki, K. C. and Patankar, S. V. (1989). Pressure based calculation procedure for viscous flows at all speeds in arbitrary configurations, *AIAA J.* *27*, 1167.
- Kim, J. and Moin, P. (1985). Application of a fractional step method to incompressible flows. *J. Comput. Phys.*, *59*, 308–323.
- Kolmogorov, A.N. (1941). The local structure function of turbulence in incompressible viscous fluids for very large Reynolds number, *C.R. Acad. Sci. USSR.* *30*, 301–305.
- Kong, H., Choi, H. and Lee, J. S. (2000). Direct numerical simulation of turbulent thermal boundary layers. *Phys. of Fluids*, *12*, 2555–2568.
- Krylov, N. V. (1983). Boundedly inhomogeneous elliptic and parabolic equations *Izv. Akad. Nauk. SSSR Ser. Mat.* . *46*, 487–523 (Russian); English transl., *Math. USSR-Izv.* *20* (1983), 459–492.
- Kudrolli, A., and Henry, J. (2000). Non-Gaussian velocity distributions in excited granular matter in the absence of clustering, *Phys. Rev. E.* **62**, 1486–1492.

- Kurien, S. and Screenivasan, K.R. (2000). Anisotropic scaling contributions to high-order structure functions in high-Reynolds-number turbulence, *Phys. Rev. E*, *62*, 2206–2212.
- Lee, S., Lele, S. K. and Moin, P. (1992). Simulation of spatially evolving turbulence and the applicability of Taylor’s hypothesis in compressible flow. *Phys. Fluids A*, *4*, 1521–1530.
- Lee, M.J., Oh, B.D., and Kim, Y.B. (2001). Canonical fractional-step methods and consistent boundary conditions for the incompressible Navier-Stokes equations. *J. Comput. Phys.* *168*, 73–100.
- Lele, S.K. (1994). Compressible Effects on Turbulence. *Ann. Rev. Fluid Mech.*, *26*:211–254.
- Leray, J. (1934). Sur le mouvement d’un liquide visqueux emplissant l’espace. *Acta Math.* *63*, 193–248.
- Ligrani P. M. , Wigle J. M. , Ciriello S. and Jackson S. M. (1994). Film-cooling from holes with compound angle orientations: Part 1-Results downstream of two staggered rows of holes with 3d spanwise spacing. *J. Heat Transfer*, *116*, 341–352.
- Ligrani P. M. , Wigle J. M. and Jackson S. M. (1994). Film-cooling from holes with compound angle orientations: Part 2-Results downstream of two staggered rows of holes with 6d spanwise spacing. *J. Heat Transfer*, *116*, 353–362.
- Lilly, D. K. (1992). A proposed modification of the Germano subgrid-scale closure method. *Phys. of Fluids A*, *4*, 633–635.
- Liu, K. and Pletcher, R. H. (2004). A procedure to establish inflow conditions for LES of spatially developing turbulent boundary layers, *ASME Heat Transfer/Fluids Engineering Summer Conferences*, *HT-FED2004*.
- Liu, K, and Pletcher, R. H. (2006). A new fractional step method for the calculation of compressible Navier-Stokes equations, accepted by *J. Comp. Phys.* (Also see chapter 2)

- Liu, K, and Pletcher, R. H. (2006). Inflow conditions for the large eddy simulation of turbulent boundary layers: a dynamic recycling procedure, submitted. (Also see chapter 3)
- Lumley, J.L. and Newman, G.R. (1977). The return to isotropic of homogenous turbulence, *J. Fluid Mech.*, 82, 161-178.
- Lundgren, T.S. (1969). Model equation for nonhomogenous turbulence, *Phys. Fluids*, 12, 485-497.
- Lund, T. S., Wu, X. and Squires, K. D. (1998). Generation of turbulent inflow data for spatially-developing boundary layer simulation. *J. Comput. Phys.*, 140, 233–258.
- Meignen, R. and Berthoud, G. (1998). A mixing length model for strongly heated subsonic turbulent boundary layers. *Int. J. Heat Mass Transfer*, 41, 3373–3385.
- Moin, P. and Kim, J. (1985). The structure of the vorticity field in turbulence channel flow. Part 1. analysis of instantaneous and statistical correction, *J. Fluid Mech.* 155, 441–464.
- Moin, P., Squires, K., Cabot, W., and Lee, S. (1991). A dynamic subgrid-scale model for compressible turbulence and scalar transport. *Physics of Fluids A*, 3, 2746–2757.
- Moin, P. and Mahesh, K. (1998). Direct numerical simulation: A tool in turbulent research. *Annu. Rev. Fluid Mech.*, 30, 539–578.
- Monin, A.S. and Yaglom, A.M. (1975). Statistical fluid mechanics: Mechanics of turbulence, Vol2. *MIT Press*, Combridge.
- Morinishi, Y., Tamano, S., and Nakabayashi, K. (2004). Direct numerical simulation of compressible turbulent channel flow between adiabatic and isothermal walls. *J. Fluid Mech.* 502: 273–308.
- Morkvin, M. V. (1962). Effects of compressibility on turbulent flows. In *Mécanique de la Turbulence* (ed. A. Favre) CNRS, 367–380.

- Nasir H., Ekkad S. V. and Acharya S. (2003). Flat surface film cooling from cylindrical holes with discrete tabs. *J. Thermophysics and Heat Transfer*, 17(3), 304–312.
- Nicoud, N. and Bradshaw, P. (2000). A velocity transformation for heat and mass transfer. *Physics of Fluids*, 12, No.1, 237–238.
- Oberlack, M. (1997) Non-isotropic dissipation in non-homogeneous turbulence, *J. Fluid Mech.* 350, 351–374.
- Patankar, S. V. and Spalding, D. B. (1972). A calculation procedure for heat, mass and momentum transfer in three-dimensional parabolic flows. *Int. J. Heat mass Transfer*, 15, 1787–1806.
- Perot, J. B. (1993). An analysis of the fractional step method. *J. Comput. Phys.* 108, 51–58.
- Perot, J. B. (1995). Comments on the fractional step Method, *J. Comput. Phys.*, 121, 190–191.
- Pope, S. B. (2000). *Turbulent flows*. Cambridge: Univ. Cambridge Press.
- Pope, S.B. (1994). Stochastic Lagrangian models for turbulence. *Annual Reviews of Fluid Mechanics*, Vol. 26, 23–63.
- Pope, S.B. (1994). On the relationship between stochastic Lagrangian models of turbulence and second-moment closures. *Phys. Fluids*, 6, 973–985.
- Pope, S.B. (2002). A stochastic Lagrangian model for acceleration in turbulent flows. *Phys. Fluids*, 14, 2360–2375.
- Pope, S.B. (2002). Stochastic Lagrangian models of velocity in homogeneous turbulent shear flow. *Phys. Fluids*, 14, 1696–1702.
- Pletcher, R. H. and Chen, K. H. (1993). On solving the compressible Navier-Stokes equations for unsteady flows at very low Mach numbers. *AIAA Paper 93-3368-CP*.
- Poinsot, T. J. and Lele, S. K. (1992). Boundary conditions for direct simulations of compressible viscous flows. *J. Comput. Phys.*, 101, 104–129.

- Pumir, A. (1996). Turbulence in homogeneous shear flows, *Phys. Fluids*, 8, 3112–3127.
- Rai, M. M. and Moin, P. (1993). Direct numerical simulation of transition and turbulence in a spatially evolving turbulence. *J. Comput. Phys.*, 109, 169–192.
- Rhodes, R. P. (1975). A probability distribution function for turbulent flows. In *Turbulent mixing in nonreactive and reaction flows*, ed. S. N. B. Murthy, 235–241. New York/London: Plenum.
- Rudin, W. (1976). Principle of mathematical analysis. *Ed.3*, New York: McGraw-hill.
- Sawford, B.L., and Yeung, P.K. (2000). Eulerian acceleration statistics as a discriminator between Lagrangian stochastic models in uniform shear flow, *Phys. Fluids*, 12, 2033–2045.
- Sawford, B.L., and Yeung, P.K. (2001). Lagrangian statistics in uniform shear flow: Direct numerical simulation and Lagrangian stochastic models. *Phys. Fluids*, 13, 2627–2634.
- Schlüter, J. U., Pitsch, H. and Moin, P. (2003). On boundary conditions for LES in coupled simulations. *AIAA Paper 0069*.
- Schmidt D. L. , Sen B. and Bogard D. G. (1996). Film-cooling with compound angle holes: Adiabatic effectiveness. *J. Turbomachinery*, 118, 807–813.
- Sen B., Schmidt D. L. and Bogard D. G. (1996). Film-cooling with compound angle holes: Heat transfer. *J. Turbomachinery*, 118, 800–806.
- Serio, C. (1998). Probability density of velocity increments in weakly turbulent pipe flow, *Europhys. Lett.* 42 (6), 605–609.
- Simonich, J. C and Bradshaw, P. (1978). Effect of free-stream turbulence on heat transfer through a turbulent boundary layer. *J. Heat Transfer*, 100, 671–677.
- Simonich, J. C and Bradshaw, P. (1983). Influence of free-stream turbulence on turbulent boundary layer heat transfer and mean profile development, Part II-analysis of results. *J. Heat Transfer*, 105, 41–53.

- Smith, C. R. and Metzler, S. P. (1983). The characteristics of low-speed streaks in the near-wall region of a turbulent boundary layer. *J. Fluid Mech.*, 129, 27–46.
- Smith, C.R., Walker, J.D.A., Haidari, A.H., and Soburn, U. (1991). On the dynamics of near-wall turbulence, *Phil. Trans. R. Soc. Lond. A* 336, 131-175.
- Sorriso-Valvo, L., Carbone, V., and Veltri, P. (1999). Intermittancy in the solar wind turbulence through probability distribution functions of fluctuations. *Geophysical Res. Lett.* 26, (13), 1801–1804.
- Sorriso-Valvo, L., Carbone, V., Veltri, P., Politano, H., and Pouquet, A. (2000). Non-Gaussian velocity distribution functions in two dimensional magnetohydrodynamic turbulence. *Europhys. Lett.* 51 (5), 520–526.
- Spalart, P. R. (1988). Direct numerical simulation of turbulent boundary layer up to $Re_{\theta} = 1410$. *J. Fluid Mech.*, 187, 61–98.
- Spalding, S. B. and Chi, S. W. (1964). The drag of a compressible turbulent boundary layer on a smooth flat plate with and without Heat Transfer. *J. Fluid Mech.* 18: 117–143.
- Speziale, C.G. (1991). Analytic method for the development of Reynolds-stress closures in turbulence, *Annu. Rev. Fluid Mech.* 23, 107–157.
- Spille-Kohoff, A. and Kaltenbach, H.-J. (2001). Generation of turbulent inflow data with a prescribed shear-stress profile. *Third AFOSR Conf.*, Arlington, Texas, 319–326.
- Stakgold, I. (2000). Boundary value problems of mathematics physics, *Vol 2*. SIAM, Philadelphia.
- Tatekawa, T. (2005). Non-Gaussianity of one-point distribution functions in extended Lagrangian perturbation theory, *J. Cosmology Astroparticle Phys.*, 04, 018.
- Temam, R. (1969). Sur l'approximation de la solution des équations de Navier-Stokes par la méthode des pas fractionnaires ii". *Arch. Rat. Mech. Anal.* , 33, 377–385.

- Tennekes, H. and Lumley, J.L. (1972). A first course in turbulence, *MIT Press*, Cambridge.
- Thole, K. A. and Bogard, D. G. (1996). High freestream effects on turbulent boundary layer. *J. Fluids Eng.*, 118(June), 276–284.
- Tomboulides, A. G. and Orzag, S. A. (1998). A quasi-two-dimensional benchmark problem for low Mach number compressible codes. *J. Comput. Phys.*, 146, 691–706.
- Turkel, E. (1999). Preconditioning techniques in computational fluid dynamics. *Annu. Rev. Fluid Mech.*, 31, 385–416.
- Varga, R. S. (2000). *Matrix iterative analysis*, New York: Springer-Verlag, Chapter 3. 64–103.
- Vreman, A. W., Geurts, B. J., and Kuerten, H. (1995). Subgrid-modeling in les of computational flow. *Applied Scientific Research*, 54, 191–203.
- Wang, W. and Pletcher, R.H. (1996). On the large eddy simulation of a turbulent channel flow with significant heat transfer *Phys. Fluids* 8, 3354–3366.
- Wall, C., Pierce, C.D. and Moin, P. (2002). A semi-implicit method for resolution of acoustic waves in low mach number flows. *J. Comput. Phys.* 181, 545–563.
- Xu, X., Lee, J. S. and Pletcher, R. H. (2005). A compressible finite volume formulation for large eddy simulation of turbulent pipe flows at low Mach number in Cartesian coordinates. *J. Comput. Phys.*, 203, 22–24.
- Yakhot, V. (2001). Mean-field approximation and a small parameter in turbulent theory, *Phys. Rev. E.* 63, 026307.
- Yoon, S. and Jameson, A. (1987). An LU-SGS scheme for the Euler and Navier-Stokes equations, *AIAA paper 87-600*
- Zhou, J., Adrian, R. J., Balachandar, S., and Kendall, T.M. (1999). Mechanisms for generating coherent packets of hairpin vortices in channel flow, *J. Fluid Mech.* 387, 353–396.

ACKNOWLEDGEMENTS

I would like to take this opportunity to express my thanks to those who helped me with various aspects of conducting research and the writing of this dissertation. First and foremost, Dr. Richard H. Pletcher for his guidance, patience and support throughout this research and the writing of this dissertation. I would also like to thank my committee members for their efforts and contributions to this work: Dr. Eric Weber, Dr. Francine Battaglia, Dr. John C. Tannehill and Dr. Michael G. Olsen. I would additionally like to thank Dr. Xiaofeng Xu, Dr. Joon Seng Lee, Ms. Xiaohang Wang, Mr. Zhaohui Qin, Ms. Wan Wang, Mr. Yuanhong Li, Mr. Jin Sun, Ms. Nan Xie, Mr. Anup, Mr. Madu, etc. for their help and friendship during these years.

My parents, Dakuan and Cuihua, and wife, Jie, deserve a special thanks for their undivided attention and moral support.